Self-assembly and properties of nano-organized multimaterial films with complex anisotropies

Jean Muller

University of Strasbourg

UNIVERSITE DE STRASBOURG

École doctorale Physique, chimie-physique ED 182 Université de Strasbourg

ÉCOLE DOCTORALE Physique, Chimie-Physique (ED 182)

Institut Charles Sadron (UPR 22)

THÈSE

présentée par

Jean MULLER

Soutenue le : **9 décembre 2021**

Pour obtenir le grade de : **Docteur de l'Université de Strasbourg**

Discipline/Spécialité : Chimie Physique

Self-assembly and properties of nano-organized multimaterial films with complex anisotropies

THÈSE dirigée par :

M. Olivier FELIX	Chargé de recherche, Université de Strasbourg
M. Gero DECHER	Professeur, Université de Strasbourg

RAPPORTEURS EXTERNES :

Mme. Regine VON KLITZING	Professeur, Technische Universität Darmstadt
M. Serge RAVAINE	Professeur, Université de Bordeaux

EXAMINATEUR :

M. Laurent HEUX	Directeur de recherche, Université Grenoble Alpes

---

INVITE :

M. Matthias PAULY	Maître de conférences, Université de Strasbourg

Index

Acknowledgements

First of all, I would like to express my deep gratitude to Dr. Olivier Félix, Dr. Matthias Pauly and Pr. Gero Decher for their availability, support, advices and countless discussions during my whole doctoral research. I also would like to warmly thank Olivier Félix for letting me supervise different Master students that was definitely a very enriching experience for me. I also would like to thank Michel Tschopp for his help on my research topic and for his happiness and motivation.

I would like to sincerely thank all the members of ICS that helped me in many different ways. I am very grateful to Alain Carvalho for the time he spent for training me on SEM and for all the discussions related to microscopic data analyses as well as Damien Favier for the mechanical characterization of the films. I would like to also thank Christophe Contal for the AFM training and for giving me the opportunity to use the equipment independently. My thanks also go to Vincent Le Houerou for his help and involvement during my work. I would like to thank the group of Andreas Fery from the Leibniz-Institut for Polymerforschung in Dresden and especially Anik Kumar Ghosh for having accepted to collaborate on my work for the in-situ microscopic study on the stretchable samples and for the discussions on the data.

I would like to thank Pr. Regine Von Klitzing, Pr. Serge Ravaine and Dr. Laurent Heux for having accepted to act as referees for my thesis work.

My gratitude also goes to the different students I had the opportunity to supervise. I thank Giovanni, Matthieu and especially Pavithra for her great work, help and her motivation during my last year of PhD. I really found it interesting, motivating and enriching to work with different people and sharing ideas and knowledge in order to progress together on a specific topic.

Finally, besides the working part, I would like to thank different people that I had the opportunity to meet during these 3 years including Imen, Eirini, Javid, Eulalie, Nicolas, Randy, Charchit, Justine, Othmene, Vaibhav, Fedir, Anastasia, Ricardo, Marion, Duncan and Quentin. It was a real pleasure to share lunch and coffee breaks but also

pleasant moments outside of the lab life including BJC events and parties. I also thank all the players that I had the opportunity to play with during the football games.

Last but not least, I would like to dedicate this thesis to my whole family, especially my parents and Luisiana. Without your help, motivation and support, this would not have been possible.

List of abbreviations

AFM	Atomic Force Microscopy
AgNWs	Silver nanowires
CD	Circular dichroism
CNCs	Cellulose nanocrystals
CNFs	Cellulose nanofibrils
CNTs	Carbon nanotubes
CVD	Chemical vapor deposition
DMA	Dynamical mechanical analysis
DNA	Deoxyribonucleic acid
EBL	Electron beam lithography
GIS	Grazing incidence spraying
LbL	Layer-by-layer
OTS	Octadecyltrichlorosilane
PAH	Poly(allylamine hydrochloride)
PDDA	Poly(diallyl dimethylammonium chloride)
PDMS	Poly(dimethyl siloxane)
PEI	Poly(ethyleneimine)
PMMA	Poly(methylmethacrylate)
PSS	Poly(sodium 4-styrene sulfonate)
PVAl	Poly(vinylalcohol)
PVAm	Poly(vinylamine)
RMS	Root mean square
RH	Relative humidity
SEM	Scanning Electron Microscopy
TEM	Transmission electron microscopy
UV-Vis-NIR	Ultraviolet-visible-near infrared

Introduction

Nature is undoubtedly an unlimited and fascinating source of inspiration for human as it has developed through evolution nanocomposite materials composed of a limited number of components with complex structures and remarkable properties.[1] For instance, the fibrillar helical architecture, one of the most complicated structures to assemble, is widely found in animal and plant kingdoms. This helicoidal arrangement of oriented fibers, also known as Bouligand structure,[2] can be found for example (i) in the secondary layers of wood cell walls conferring high toughness and strength to wood[3] and (ii) in the arthropod exoskeleton showing an exceptional mechanical robustness.[4] It was shown that the helicoidal structure and the combination of hard and soft elements interact synergistically to make the composite tougher in any direction against crack propagation in comparison to a nonhelicoidal composite.[5,6] Not only enhanced mechanical properties but also interesting optical phenomena are associated to helicoidal structures in biological materials, it is for instance the source of the structural colors of some plant leaves, fruits and animal exoskeleton.[7,8] An interesting example is the exoskeleton of many beetles displaying a helicoidal structure of chitin fibers providing both an exceptional mechanical resistance and a selective reflection of polarized light. The intimate relationships between structure and properties of biological materials have inspired researchers towards the preparation of nanocomposite materials with superior performance. Nevertheless, the fabrication of high-performance bio-inspired materials requires first a precise and detailed analysis of natural materials to understand their structure-properties relations at all length scales.[9]

The first chapter of this thesis will provide a general overview on the diversity of biological materials and will present the structure-property relationships in these materials by focusing on two main examples namely arthropods exoskeleton and plant cell walls. Human-made materials inspired from these biological materials will then be reviewed as well as their corresponding properties.

One key point towards the fabrication of high-performance bio-inspired materials is the control of their composition and architecture at the nanoscale level. Several top-down and bottom-up methods have been developed to address this point. Among all

methods used for the fabrication of such nanostructured materials, the layer-by-layer (LbL)[10] assembly has established itself as a simple and versatile technique to design multifunctional multimaterial films with a high level of control over the structure and the composition using a large number of building blocks. Its use for the preparation of nanocellulose-based films with complex anisotropies will be presented and their corresponding mechanical and optical properties be described.
Finally, stretchable strain sensors will be introduced as they could be used as an alternative approach for determining the mechanical properties of anisotropic materials. In the present work we developed a multidirectional strain sensor based on the anisotropic optical properties of a unidirectionally oriented silver nanowire (AgNW) monolayer deposited on a stretchable poly(dimethysiloxane) (PDMS) substrate.

The first aim of this thesis (chapter 3) is to show how we took inspiration from the nature and more specifically from the plant cell walls to prepare nanocellulose-based multilayer films with interesting mechanical and optical properties. The influence of the composition and structure of these wood-inspired composite materials was investigated in order to study the structure-property relationships in these nanocomposites. Cellulose nanocrystals (CNCs) and nanofibrils (CNFs) extracted from different sources were used for the preparation of wood-inspired materials. Isotropic cellulose-based films were first prepared by dip-assisted LbL assembly. The influence of the pH and concentration of the solutions as well as the source of nanocellulose on the film build-up was investigated. To design more complex structures such as helicoidal ones found in biological materials, the LbL methodology was combined with the grazing incidence spraying (GIS)[11] allowing the independent unidirectional in-plane alignment of cellulose nanoparticles in each layer. The optical and mechanical properties of the fabricated wood-inspired films were finally determined by circular dichroism (CD) and by nanoindentation and dynamic mechanical analysis (DMA) respectively. While a different optical response could clearly be observed for CNC-based LbL films with various anisotropies (unidirectional and helicoidal), mechanical properties of these films were surprisingly similar independently of their anisotropy and the applied stress direction.

In addition to resistant bio-sourced nanocomposite materials, stretchable and wearable strain sensors have attracted tremendous attention in recent years due to

their interest in applications on the human body.[12] Towards the fabrication of efficient strain sensors, various materials, manufacturing strategies and sensing mechanisms have already been elaborated and will be discussed in chapter 1.[13] Nevertheless, most of them are not sensitive to the stretching direction. In order to monitor multidimensional strains, the fabrication of sensors with anisotropic properties is definitely needed. Among the possible materials with anisotropic properties, silver nanowires are interesting candidates. The optical properties of the AgNWs will be presented as well as the possible strategies to orient them.

The chapter 4 describes the preparation of a direction-sensitive strain sensor using the anisotropic optical properties of an oriented silver nanowire monolayer upon mechanical stretching. The aim of this part was to exploit the optical anisotropic properties of aligned silver nanowires to design a multidimensional sensor. The AgNWs were aligned using GIS and deposited on a stretchable PDMS substrate. The influence of the stretching direction and light polarization on the optical properties was investigated by linearly polarized UV-Vis-NIR spectroscopy. Using a simple mathematical model, we were able to retrieve both the local strain and the direction of the deformation from the optical measurements. This study demonstrates the potential of this optical anisotropic sensor, capable of detecting an applied strain and its directionality, for probing multidimensional strains.

Chapter 1 – State of the art

1.1 Biological materials

1.1.1 Nature, an amazing source of efficient functional structures

Materials found in nature are surprisingly only composed of a limited number of chemical elements produced under mild conditions.[1] Nevertheless, these biological materials display remarkable structures and properties generating a wide diversity of interesting functions.

Lotus leaves, for instance, have become the archetype when speaking about self-cleaning properties since the introduction of the “lotus effect”.[14] Indeed, these leaves present remarkable superhydrophobic properties that can be explained by their hierarchical rough structures. The epidermis of lotus leaves is composed of papillae covered with hydrophobic wax tubules as depicted in Figure 1.1(C). The small diameter, comprised between 4 and 12 µm, of these papillae provides a reduced contact area between the leaf and water. An average contact angle of 163° (Figure 1.1(B)) was determined for lotus leaves proving their superhydrophobic behaviour.[15]

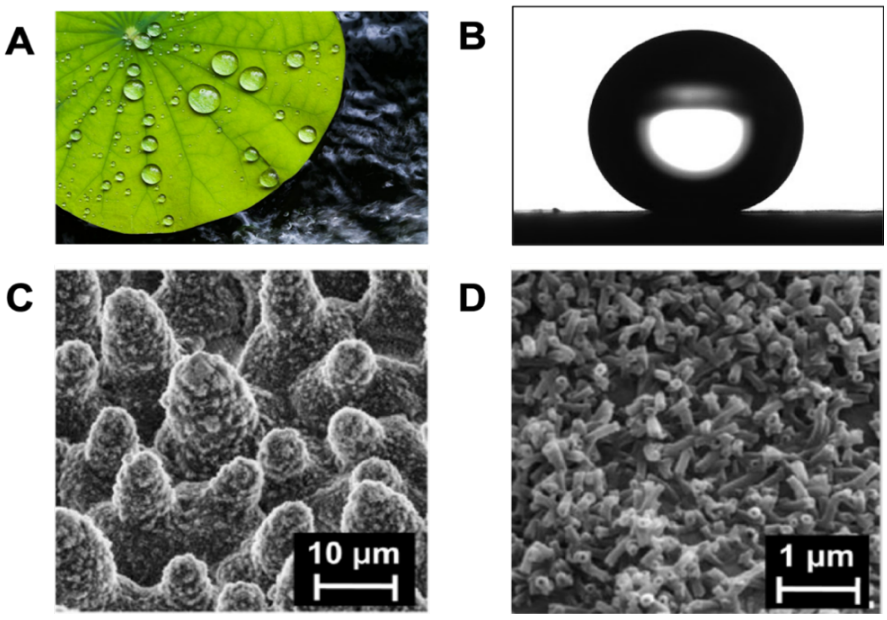

Figure 1.1: (A) Photograph of a lotus leaf. (B) Image of a water drop deposited on a lotus leaf highlighting a high contact angle. (C) SEM image of the upper leaf side showing the hierarchical surface structure consisting of papillae covered with wax tubules. (D) SEM picture representing multiple wax tubules.[14]

In the case of lotus leaves, the adhesion between water and the surface was further reduced by varying the height of the different papillae.[16] Moreover, X-ray diffraction analyses proved the presence of non-polar methyl groups in the wax significantly limiting the interactions between the leaf and water.[17] To summarize, the clever architecture of the lotus leaf, combining non-polar groups with a rough structure, allows the rolling of water drops on its surface.

Another striking example of biological materials displaying hierarchical structures is the silk produced by spiders that is used for various purposes including the building of their webs or the capturing of the preys.[18] These functions are possible thanks to outstanding mechanical properties such as a tensile strength of 1.1 GPa.[18] This value is similar to the one of steel (1.5 GPa) but considering the density of the material (1.3 g/cm^3 for silk compared to 7.8 g/cm^3 for steel),[19] spider silk is more than four times stronger than steel per mass unit. Moreover, silk presents a high elasticity (50%) combined with an important toughness. This combination of outstanding properties can be explained by analysing the silk structure, a hierarchical fibrous material.[19] At the microscale level, the silk fibers can be decomposed in a skin-core structure with the fibrils forming the core (Figure 1.2(A)). At the nanoscale level, protein-based silk fibrils, comprising crystalline regions with β-sheets interconnected with amorphous chains via hydrogen bonds, bound together to form micron size fibers as shown in Figure 1.2(B). The stretchable amorphous matrix gives the silk a high elasticity while the rigid crystalline segments are responsible for the high strength and toughness of the material.

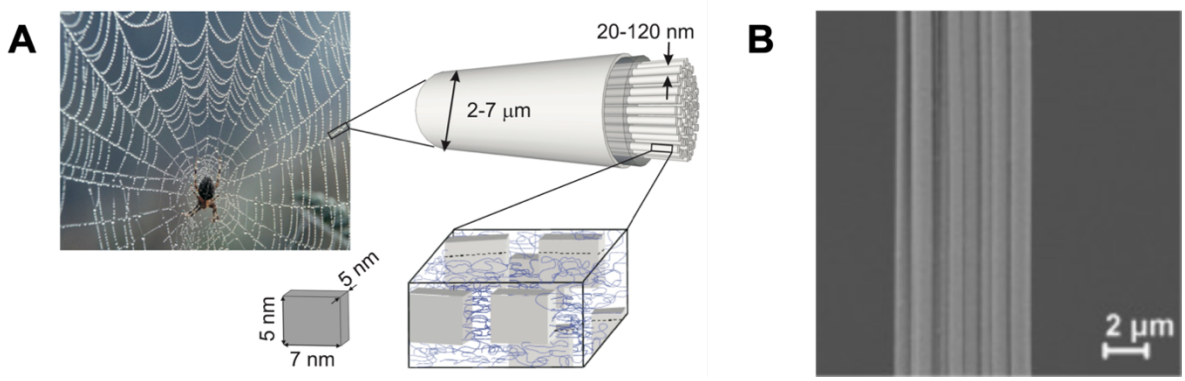

Figure 1.2: (A) Picture of a spider silk web with a schematic representation of the hierarchical organization of silk.[20] (B) SEM image showing connected silk fibers from *A.avicularia* spider.[21]

Remarkable optical properties can also be found in biological materials. One of the most well-known examples is the Morpho butterfly wings displaying structural colors arising from interference and diffraction phenomena (Figure 1.3(A)). Indeed, the multi-layered ridge structure (Figure 1.3(B)) on the butterfly wings provides only the strong and selective reflection in the blue while the sub-wavelength spacing between the ridges induces light diffraction.[22] This light scattering explains the angle-dependent color of the butterfly also known as iridescence.

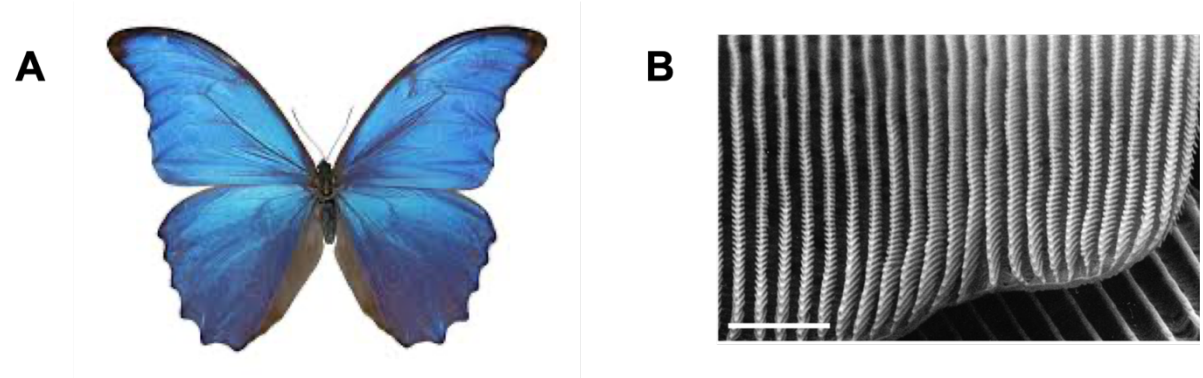

Figure 1.3: (A) Picture of a Morpho butterfly displaying wings with an intense blue color. (B) Microscopy image showing the multi-layered structure of ridges. Scale bar corresponds to 3 µm.[23]

From nacre composed of strong calcium carbonate platelets glued together with a softer organic matrix[24] to the toucan beak exhibiting a high-resistant and lightweight structure of stiff keratin units with a ductile collagen foam,[25] the diversity of natural materials is truly remarkable.[1] The exceptional properties of these materials arise from their hierarchical structure with a specific organization of the constitutive building blocks at different length scales. Before mimicking the biological structures found in nature, the first step is to thoroughly analyse the structure-function-property relationships in these materials. The next section will focus on the intimate link between the structure and the mechanical properties of two specific biological materials namely arthropods exoskeleton and plant cell walls.

1.1.2 Structure and properties of arthropod exoskeleton

Arthropod exoskeleton and plant cell walls are both biological materials combining strong anisotropic building blocks with a soft matrix.

All arthropods are covered by a multifunctional skeleton allowing the support of their body, the resistance to mechanical loadings and the protection to environmental conditions. This skeleton, known as exoskeleton, is composed of chitin-protein fibers embedded in a mineral matrix of calcium carbonate ($CaCO_3$))[26] and its well-defined hierarchical organization at different structural levels was first precisely studied by Raabe and co-workers.[27] This hierarchical and highly ordered arrangement can be seen for instance in the exoskeleton of the lobster *Homarus Americanus* (Figure 1.4). At the molecular level, chitin chains are forming small fibrils with a length of 300 nm and a diameter of 3 nm. These fibrils are wrapped with proteins (Figure 1.4(III)) to form fibers with a diameter of about 60 nm and embedded in a mineral phase. These fibers then bound together into bundles that are forming horizontal planes arranged in a helicoidal pattern, also known as Bouligand structure or twisted plywood (Figure 1.4(V)).[28]

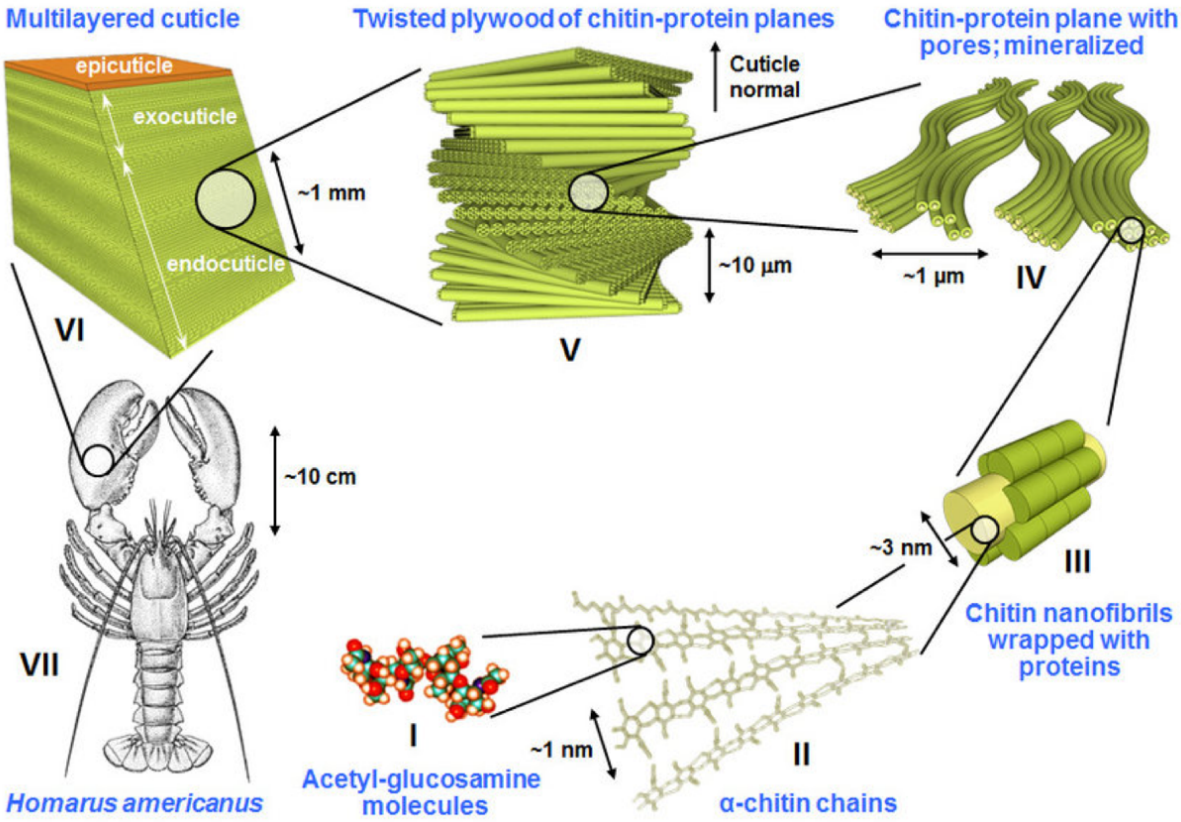

Figure 1.4: Schematic illustration of the hierarchical organization of the endocuticle of *Homarus Americanus* lobster with the arrangement of chitin-protein fibers in a Bouligand structure.[6]

Concerning the mechanical properties of such structures, Raabe et al.[29] investigated the evolution of the stiffness and hardness of the *Homarus Americanus* cuticle by micro indentation. They found out that the exocuticle layer (outer layer) presented a very dense helicoidal stacking of chitin-protein fibers leading to high stiffness values comprised between 8.5 and 9.5 GPa. The hardness was also measured and increased progressively within the exocuticle layer between the surface region (130 MPa) and the region close to the endocuticle (270 MPa). On the other hand, the endocuticle layer displayed a significant lower stiffness comprised between 3 and 4.5 GPa attributed to a less dense stacking. The hardness in the endocuticle (between 30 and 55 MPa) was also much smaller than in the exocuticle.

Another striking feature of this nanocomposite material is its well-defined pore canal system in the direction normal to the surface (see Figure 1.4(IV)) allowing the efficient transport of ions and nutriments during the building of the exoskeleton. This porous architecture can be ascribed to a honeycomb-like structure[27] and leads to the increase of the toughness and strain to fracture of the material.

It was shown that the helicoidal stacking of chitin layers found in arthropods exoskeleton provides several toughening mechanisms that hamper the catastrophic propagation of cracks within the material.[4] The helicoidal arrangement indeed forces the cracks to propagate following a helicoidal path between the chitin fibers, which dissipates a higher amount of energy than a crack propagating in a straight line.

1.1.3 Structure and properties of plant cell walls

The plant cell walls are composed of only four main building blocks that are cellulose, hemicellulose, lignin and pectin. Depending on the type of plant, the structure and composition (the percentage of the four main constituents) of these cell walls varies significantly. For instance, a closed-cell foam architecture can be found in cells of potatoes while a honeycomb-like cellular structure is observed in wood.[30] Even if the diversity of structure and composition of plant cell walls is important, the common point is the presence of cellulose fibers reinforcing a matrix of hemicellulose and either lignin or pectin. Different mechanical properties can be found in plants ranging from very elastic stems to strong tree trunks.

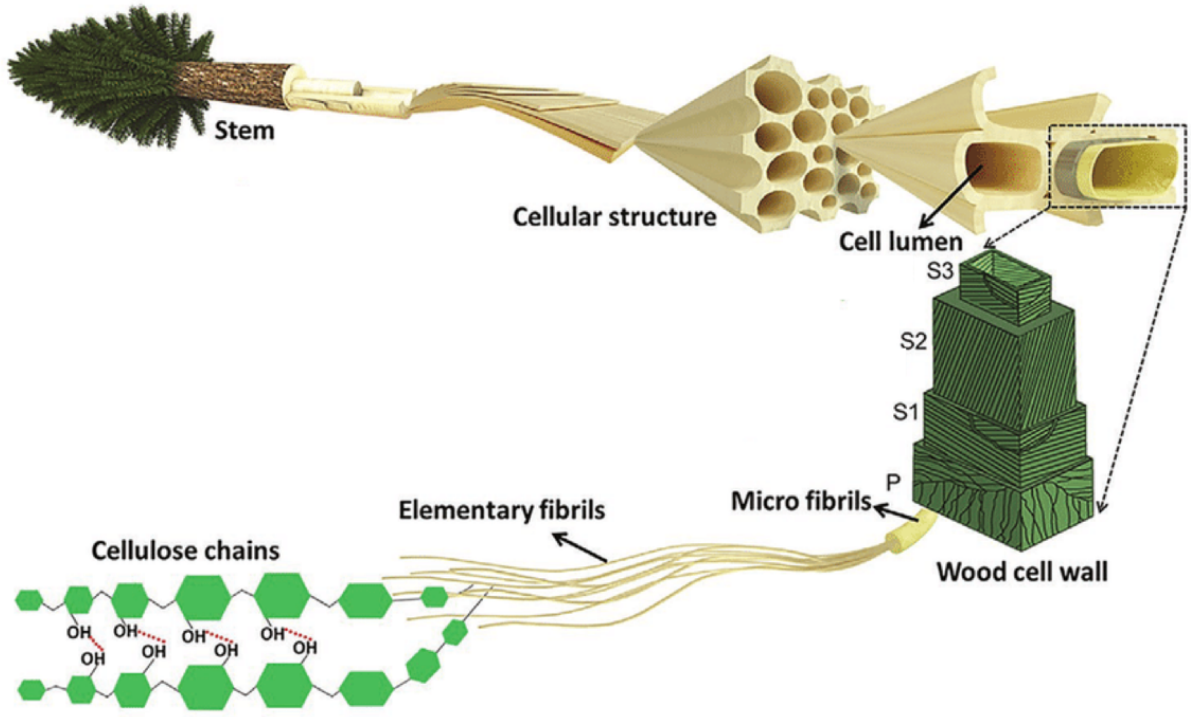

Figure 1.5: Schematic illustration of the hierarchical organization of cellulose in wood highlighting the isotropic and anisotropic arrangement of cellulose nanofibrils in the wood cell wall.[31]

These remarkable properties can be explained by the hierarchical organization of cellulose at different length scales including the one observed in wood illustrated in Figure 1.5.

The basic building block of wood is cellulose, a polysaccharide composed of glucose monomer units, that presents very interesting mechanical properties with a tensile strength close to 1 GPa and a Young's modulus around 130 GPa. At the microscale level, these cellulose molecules are forming micro-fibrils comprising amorphous and crystalline domains. They can bound together to form cellulose bundles or macrofibrils with a diameter around tens of nanometers. These cellulose macrofibrils glued with hemicellulose and lignin constitute the cell wall of wood. Cellulose has a high strength while hemicellulose and lignin have a Young's modulus of 8 and 4 GPa respectively. Wood can thus be considered as a nanocomposite material with strong cellulose chains embedded in a soft matrix of hemicellulose and lignin providing toughness and flexibility.[28]

Interestingly, cellulose fibrils possess a defined organization and orientation in each layer of the wood cell wall. For instance, they are randomly distributed in the primary layer (P). The secondary cell wall consists in three different layers (S1, S2 and S3) with the S2 layer being the thickest one and defining the mechanical properties of wood including stiffness, strength and toughness.[33] The cellulose fibrils within this layer are arranged in a helicoidal pattern[34] and it has been shown that the mechanical properties of the cell wall are greatly affected by the angle between the fibrils orientation and the main axis of the wood cell.[35] Moreover, Gibson et al.[36] demonstrated that stiffness and strength of wood were significantly more important along the cells compared to the perpendicular direction meaning that wood is an anisotropic material. The porous architecture of wood cell walls also provides a good strength-to-weight ratio to wood.

The hierarchical organization of high-strength chitin and cellulose units found in arthropod exoskeleton and plant cell walls respectively is responsible for the remarkable mechanical properties of these materials. The implementation of such types of organizations could be particularly interesting towards the preparation of synthetic nanocomposite materials with high performance.

1.2 Bio-inspired materials

Nature is a rich and unlimited source of knowledge and inspiration and human life has definitely progressed by taking inspiration from biological systems to find solutions to encountered problems. One of the first example of bio-inspired materials is Velcro, invented in 1941, that is taking inspiration from the structure of burdock burrs possessing hooks which allow the seeds to catch on to things like fabrics, which have tiny loops. Since then, a plurality of natural materials has already inspired engineers and researchers towards the preparation of efficient and multifunctional structures. In that section, we will focus on materials taking inspiration from the hierarchical organization of chitin and cellulose molecules respectively present in arthropod exoskeleton and plant cell walls.

1.2.1 Materials inspired from arthropods exoskeleton

As demonstrated previously, the exoskeleton of many arthropods displays remarkable mechanical properties arising from the helicoidal arrangement of chitin-proteins fibers embedded in a mineral matrix. Lu et al.[37] were among the first researchers to employ chitin as a nano-reinforcing agent. They prepared a nanocomposite material composed of chitin whiskers associated to a soy protein as a polymer matrix. The incorporation of chitin units provided a significant improvement of the mechanical properties of the soy matrix. Indeed, after 30% blending of chitin whiskers, the tensile strength increased from 3.3 MPa to 8.4 MPa while the Young's modulus rose from 26 MPa to 158 MPa. The remarkable improvement of the material's mechanical properties was attributed to strong interactions between the soy matrix and chitin units.

In order to improve the mechanical properties of these nanocomposites, a key development was the extraction of long chitin nanofibers. Ifuku et al.[38] used very long chitin nanofibers in combination with chitosan and studied the mechanical properties of the film (Figure 1.6). Their work highlights the improvement of mechanical properties by progressively incorporating chitin nanofibers into the film. Interestingly, the Young's modulus (Figure 1.6(B)) and tensile strength increased respectively by 65% and 94% after blending with only 10% of chitin nanofibers.

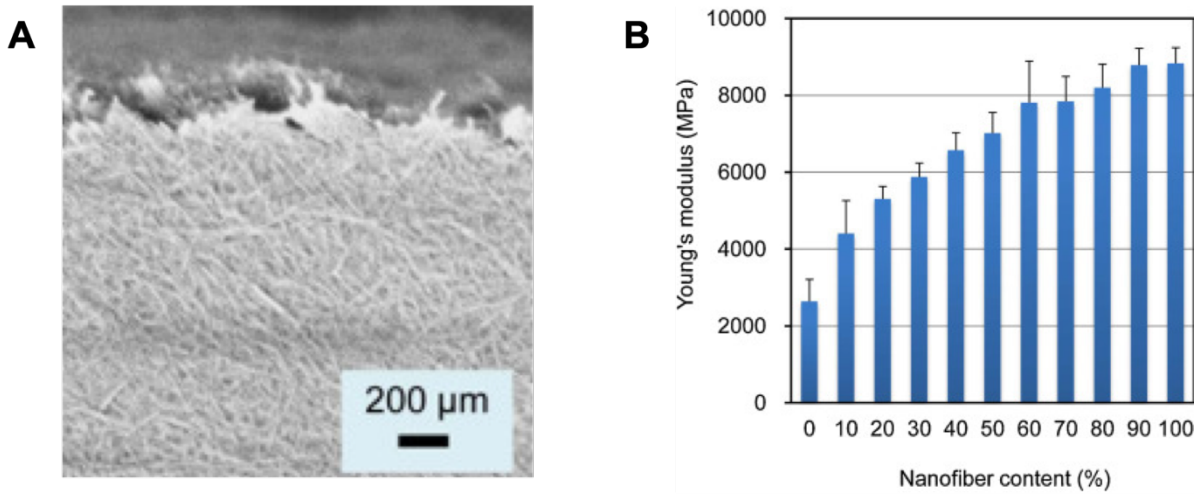

Figure 1.6: (A) Microscopic image of the chitin nanofiber-based transparent film with a nanofiber content of 100% and (B) Young's modulus of nanocomposite films containing an increasing content of chitin nanofibers.[38]

Many other studies reported the association of chitin nanofibers with different polymers. Nevertheless, these nanocomposites made use of chitin without considering their alignment within the material. Uddin et al.[39] took inspiration from the oriented chitin nanofibers in arthropod exoskeleton in order to improve the performance of polymer films. Chitin whiskers were aligned by gel spinning and were embedded in a poly(vinyl alcohol) (PVAl) polymer matrix. The Young's modulus of the nanocomposite material reached 50 GPa after incorporation of 30% chitin whiskers. Moreover, both Young's modulus and tensile strength of the film could be tuned by tailoring the amount of chitin incorporated in the film.

Recently Oh et al.[40] were able to mimic the helicoidal hierarchical structure found in arthropod exoskeleton by exploiting a chemical approach using calcium ions (Ca^{2+}) that are generally found in chitin-based exoskeletons and bind strongly with chitin (Figure 1.7).

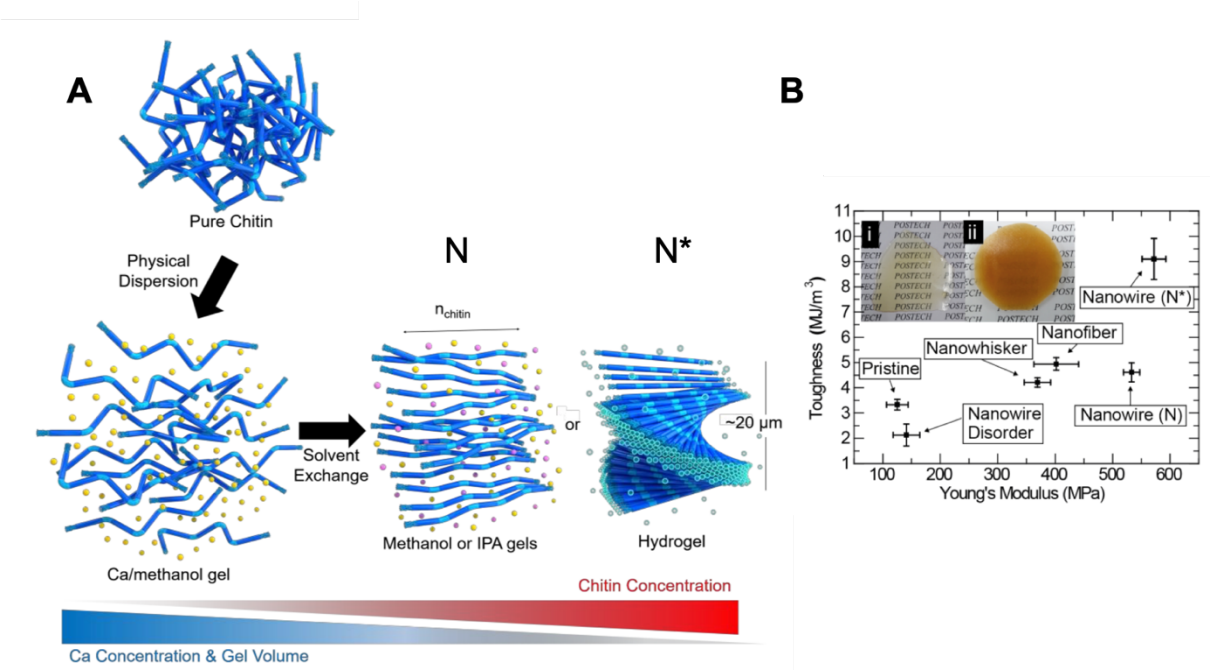

Figure 1.7: (A) Calcium-saturated methanol disintegrates chitin nanofibrils generating a Ca-methanol gel (disordered) (bottom-left panel). Ca^{2+} ions are removed from the Ca/methanol gel by washing with alcohol (methanol or isopropyl alcohol (IPA)) generating alcohol gels (N phase, bottom-middle panel) or by washing in water generating hydrogel (N* phase, bottom-right panel). (B) Tensile toughness and Young's modulus from pristine and different chitin epoxy composites.[40]

In absence of Ca^{2+}, chitin nanofibrils agglomerate randomly via strong hydrogen bonding. When added to pure chitin, Ca^{2+} surround chitin nanofibrils and screen the hydrogen bonding between leading to a separated disordered network (Figure 1.7(A)). Ca^{2+} are then removed by solvent exchange using 3 different solvents. As alcohols (IPA and methanol) display lower binding affinities to Ca^{2+} than water, the quantity of calcium ions screening the hydrogen bonding between chitin nanofibrils is more important in alcohol gels resulting in nematic liquid crystal structures (N). On the other hand, as the binding between calcium ions and chitin is less important in water, chitin nanofibrils arrange in a chiral nematic liquid phase (N*).

The mechanical properties of these gels were then characterized. Both toughness and Young's modulus increased when highly ordered structures were formed either in alcohol (N phase) and in water (N* phase). Nevertheless, no significant Young's modulus difference was observed between N and N* phases. On the other hand, the toughness was much higher in N* phase (chiral nematic liquid crystal structure) than in N phase (achiral nematic liquid crystal structure) (Figure 1.7(B)) indicating that the chiral nematic phase structure redirects the crack direction and prevents crack propagation in the composite.

1.2.2 Wood-inspired materials

The composition and structure of plant cell walls provide inspiration for the preparation of materials with superior mechanical properties due to the high strength, stiffness and sustainability of cellulose fibers. One main challenge is to design structures combining lightweight and mechanical resistance. Sehaqui et al.[41] associated these properties in a cellulose-based nanopaper presenting a Young's modulus of 1.4 GPa and a tensile strength of 84 MPa while being very porous (56% of porosity). Interestingly, the mechanical properties of this material were better than for many thermoplastics and with a lower density.

Although wood presents exceptional mechanical properties, it is also flammable, hygroscopic and doesn't conduct electricity. In order to overcome wood's flammability, Merk et al.[42] reported the preparation of a fire-retardant composite by consecutive

vacuum-assisted impregnations in $CaCl_2$ and $NaHCO_3$ solutions. This treatment provided the deep insertion of calcium carbonate ($CaCO_3$) in the cellular structure of wood as depicted in Figure 1.8.

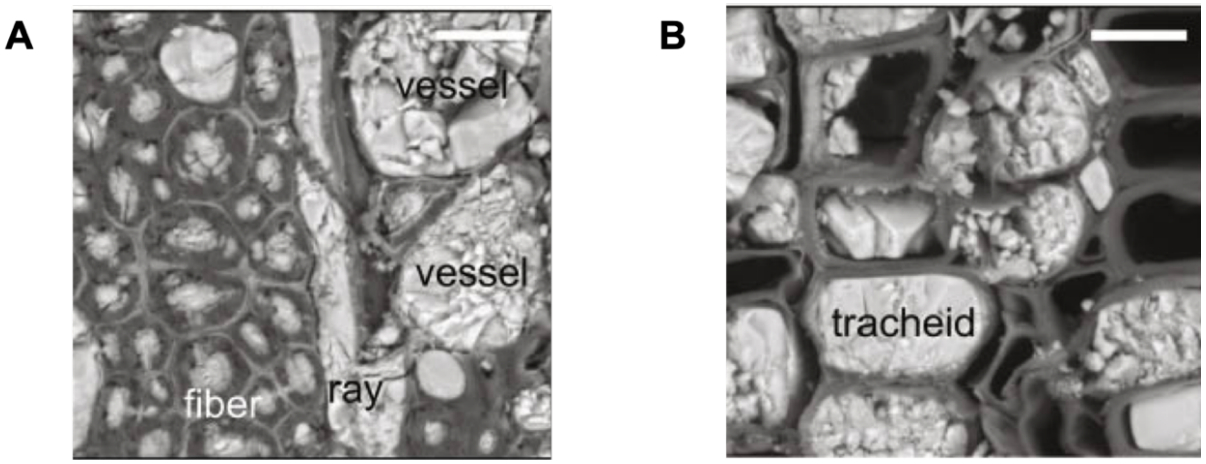

Figure 1.8: Cross-sectional SEM images of $CaCO_3$/wood composites with (A) beech wood and (B) spruce wood. Scale bars correspond to 20 microns.[42]

One interesting advantage of this process is the ability to control the degree of mineralization by the number of impregnation cycles. Moreover, different mineral compositions can be obtained by employing different cations and anions. Finally, calorimetry experiments were conducted and demonstrated an improved fire resistance of the material arising from the addition of incombustible $CaCO_3$.

Chen et al.[43] combined cellulose nanofibrils with silver nanowires to obtain conductive sponges by directional freeze-drying. The aligned metallic nanowires and synergistic effect between AgNWs and CNFs lead to anisotropic electrical conductivity properties. The final material presented a maximum electrical conductivity of 1.52 S/cm and a compressive stress of 24.5 kPa. This method opens up new opportunities towards the preparation of bio-inspired materials with interesting mechanical and electrical properties that are more and more sought after for various applications.

Mittal et al.[44] finally took inspiration from the alignment of cellulose fibers in wood cell walls. Indeed, they reported the organization of CNFs into macroscale fibers by flow-assisted assembly (Figure 1.9) yielding to a tensile strength of 1.57 GPa and a Young's modulus of 86 GPa.

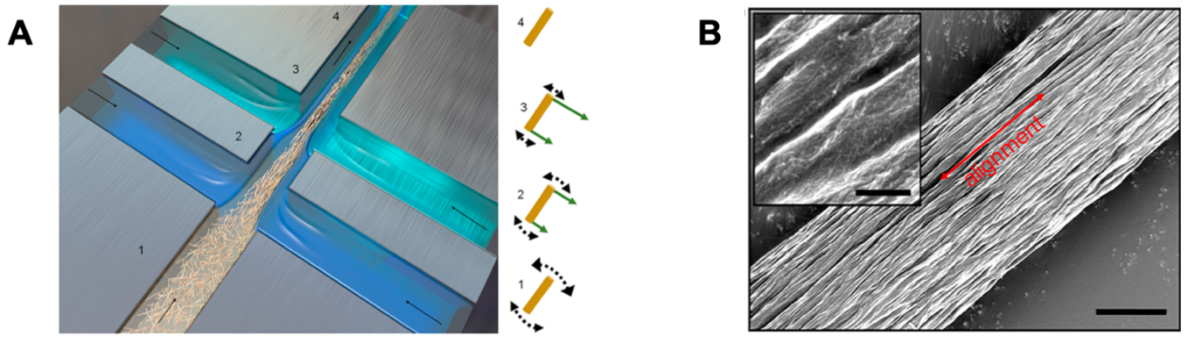

Figure 1.9: (A) Schematic illustration of the nanostructured CNFs by flow-assisted assembly and (B) SEM image of the surface of the fiber with the alignment direction highlighted by the red double arrow. Scale bars correspond to 3 µm in the main image and to 400 nm in the inset.[44]

These mechanical properties are remarkable as they are surpassing those from metals and polymeric fibers. Different parameters including the fibril's length, the surface charge and the crosslinking were studied. It was demonstrated that the strength and stiffness of the material did not depend much on the surface charge of the fibrils whereas their length had a major influence. Indeed, as the length of the fibrils is reduced, the alignment becomes lower and induces a decrease in strength and stiffness. This work highlights the importance of an efficient stress transfer from the micro to the nanofibrils to develop high performance materials. This stress transfer can be tuned by the degree of alignment of the fibrils and the interactions between them.

To conclude this section, Shamshina et al.[45] reported the electrospinning of chitin-cellulose composites and demonstrated a 2-fold improvement in hardness and 3-fold improvement in elasticity compared to the pure chitin material. This study opens up new perspectives towards the low-cost preparation of chitin/cellulose composites with improved mechanical properties.

1.3 Nanostructured materials

As already discussed previously, nature is definitely an unlimited source of inspiration for the fabrication of synthetic nanocomposite materials. Biological materials often exhibit multi-layered structures combining a soft polymer matrix with hard anisotropic building blocks. Towards the preparation of such types of architectures, the main

challenge is to produce multilayers with a precise control of the composition, the structure and the anisotropy at the nanoscale level. Different techniques for the fabrication of nanostructured materials have been developed and can be divided into two main groups referred to as top-down and bottom-up approaches (Figure 1.10). As top-down approaches rely on the miniaturization of a bulk material into the desired size and shape up to the nanoscale, bottom-up approaches provide the assembly of small constituents (atoms, molecules) into larger nanostructures.

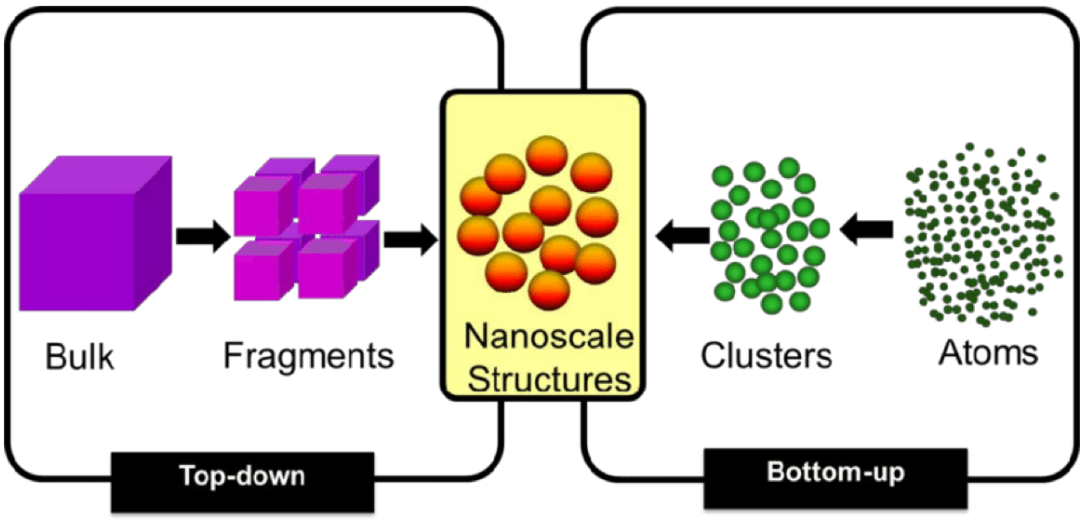

Figure 1.10: Schematic illustration of the top-down and bottom-up approaches.[46]

1.3.1 Top-down approaches

Top-down approaches consist in the physical transformation of a bulk material into well-defined structures at the nanoscale level. Feynman[47] in 1959 was the first to suggest the use of a top-down approach for the design of nanostructures, also referred to as miniaturization process. Since then, different techniques exploiting this approach have been discovered with the common goal of patterning a material by using interactions between a surface or thin film and particles or photons. Among all top-down approaches, photolithography (Figure 1.11), consisting in the design of a pattern with the use of light, is surely one of the most famous and powerful examples. A photoresist layer is first coated on a metal film and covered with a mask before being exposed to light. A chemical change is then induced by exposure to light and the photoresist is consequently being removed by a special solution called “developer”. A positive photoresist for instance becomes soluble in the developer when exposed

regions are soluble in the developer. The accessible metal areas are finally etched away and the photoresist is removed.

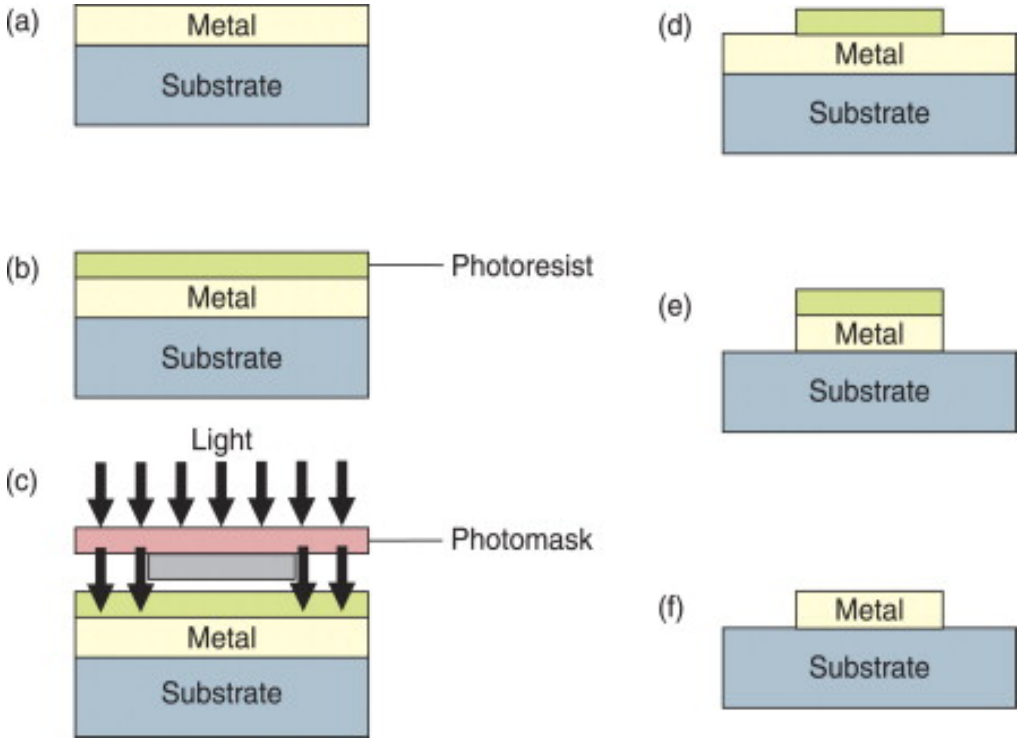

Figure 1.11: Schematic illustration of the photolithography process with a positive photoresist.[48]

This top-down approach is widely used in the microelectronic field but suffers from a limited resolution due to light diffraction. Later on, other techniques were developed to improve the patterning resolution such as electron-beam lithography (EBL).[49] The working principle of EBL is similar to photolithography but in that case, a focused electron beam is used instead of light. For instance, Cumming et al.[50] prepared NiCr wires with a diameter of 3 nm on a silicon substrate by electron-beam lithography with a PMMA resist. This technique allows the preparation of high-resolution patterns without diffraction limitations but remains very expensive.

Dip-pen nanolithography is another technique relying on the use of an AFM tip coated with a chemical compound put in contact with the substrate surface. It was used for instance to create a pattern of Fe_2O_3 nanocrystals on mica and silica substrates.[51] Nano-imprint lithography finally is a method based on the use of a mould embossing the resist with the adequate pattern. The main advantage of this technique is its capability of producing features with a resolution down to 10 nm combined with its

easiness and low-cost. Yang et al.[52] employed this technique to prepare polymer solar cells with a precise control on the orientation of the molecules.

The top-down approaches presented above are all well-adapted at the microscale level and allow the preparation of structures with different shapes. However, for most of them, their downscaling at the nanoscale level remains complicated, expensive and time demanding limiting their use towards the preparation of complex nanostructures on large areas.

1.3.2 Bottom-up approaches

Bottom-up approaches are exploiting physical and chemical transformations at the nanoscale level to assemble building blocks into larger structures. Nature has already developed and handled physical and chemical reactions to create specific atoms and molecules that can assemble into more complex structures exhibiting remarkable functionalities.[53] Structure-properties relationships of these biological materials have inspired researchers for the development of synthetic materials using similar approaches.

The sol-gel method for instance, inspired from diatoms which are able to elaborate silica shells from dissolved silica under mild conditions, is commonly applied for the preparation of solid materials such as glass, ceramics and organo-mineral hybrid compounds from metal oxide precursors in solution and at room temperature.[54] This process can be used in various fields such as particle synthesis, encapsulation and elaboration of porous/dense materials, but it finds its main application in the realization of coatings. This method involves the hydrolysis of a metal oxide precursor and then its condensation to form a gel. Marikkannan et al.[55] exploited this approach to prepare transparent and conductive tin oxide films on glass substrates. Even if this versatile technique operates at low temperature for the production of oxides, non-oxides and hybrid organic-inorganic materials, the time required, the difficulty to attain large monolithic pieces and the cost of precursor materials limit its use.
Another common bottom-up approach is Chemical Vapor Deposition (CVD) which is a vacuum-based deposition method used to produce high quality, high-performance,

solid materials, especially thin films. Typically, the substrate is exposed to one or more volatile precursors, which react and/or decompose on the substrate surface to produce the desired deposit. Cheung et al.[56] used for instance CVD to make carbon nanotubes grow on a silicon tip. TEM analyses showed the formation of a single carbon nanotube with a diameter of a few nanometer (Figure 1.12(A)). Although CVD allows the coating of various and complex structures, it requires the use of vacuum and high temperatures.

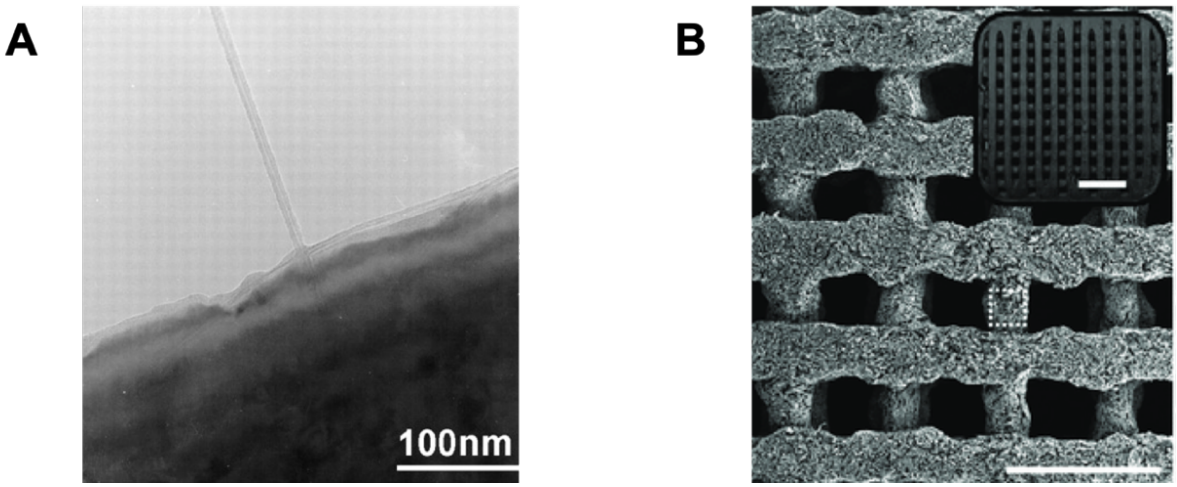

Figure 1.12: (A) TEM image of a single carbon nanotube obtained by CVD.[56] (B) SEM image of a 3D-printed graphene aerogel lattice covered with MnO_2. Scale bar corresponds to 1 mm.[57]

DNA origami is another emerging technique based on the folding of a single-stranded DNA template into a specific shape due to multiple interactions with staple strands. Torelli et al.[58] designed a cylindrical nanorobot with a diameter of 14 nm and a length of 48 nm by employing this technique. This technology enables the preparation of complex nanostructures with incredible accuracy but its downsides are typically low yield, small production scale, cost of synthetic DNA and lack of chemical diversity as the used DNA scaffold is a biological material.

More recently, 3D printing has gained increasing interest because it allows the printing of materials with a wide variety of structures. A computer is first utilized to design the exact structure of the desired object and a program then converts it into layers that will be stacked by printing to form the object. Yao et al.[57] exploited this technique to prepare a porous graphene oxide structure coated with MnO_2 as it can be seen in

Figure 1.12(B). 3D printing enables the fast design of complex nanostructured materials but it is restricted to a small group of components, limited in its ability to yield uniformly aligned materials over large areas, and does not allow depositing layers with a nanoscale precision.

To summarize, compared to top-down approaches, bottom-up approaches are more adapted to produce very precise nanostructured materials. Moreover, these strategies provide the preparation of materials with less defects and with a more homogeneous chemical composition on larger scales/areas without using heavy equipment.[52]

1.4 Layer-by-Layer (LbL) assembly

Layer-by-Layer (LbL) assembly has gained great interest for the preparation of multilayer films thanks to its experimental easiness, low-cost fabrication and versatility. This section will provide a presentation of this well-known bottom-up approach including its principle, key parameters and applications.

1.4.1 History and principle of the LbL assembly

The first work referring to the alternative deposition of oppositely charged building blocks, negatively charged silica particles and positively charged alumina fibrils, was suggested in 1966 by Iler.[59] Some years later, Fromherz[60] explored the assembly of proteins with polyelectrolytes assuming a charge inversion after each deposition step. Due to the lack of characterization methods at this time, this assumption could not be proved before Decher and Hong[61] fully characterized the film construction in 1991. The popularity and the use of the technique were revived with the work of Decher[10] in 1997 presenting a green and easy way to build polyelectrolyte films by exploiting electrostatic interactions.

The construction of such multilayer films requires the use of oppositely charged polyelectrolyte solutions (polyanion and polycation) and a solid charged substrate as depicted in Figure 1.13(A).

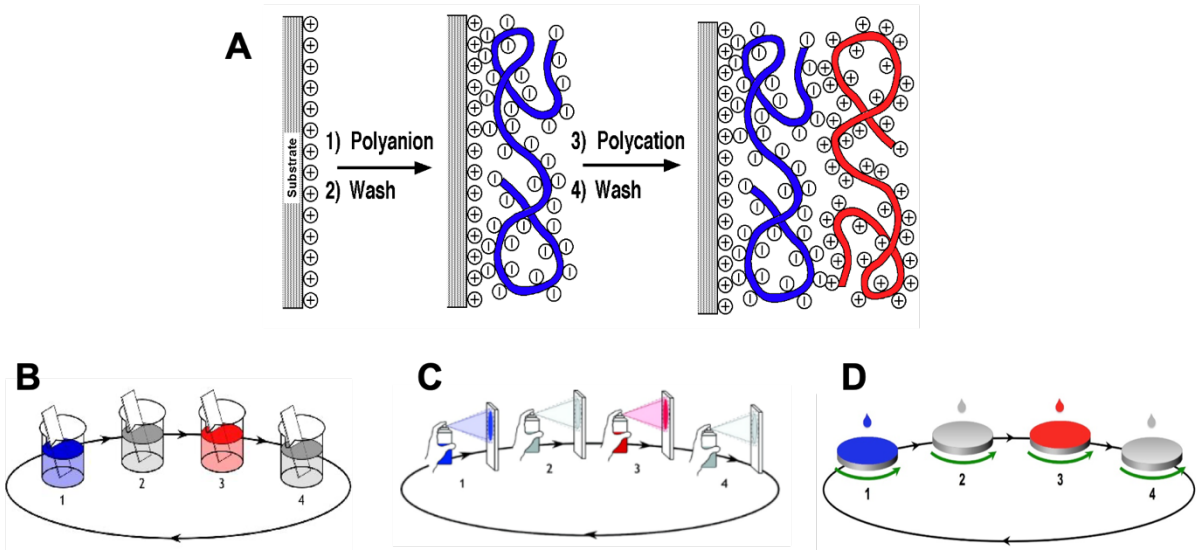

Figure 1.13: (A) Schematic illustration of the alternative deposition of a polyanion (blue) and polycation (red) on a positively charged surface[10] by dip-assisted (B), orthogonal spray-assisted (C) and spin-assisted (D) LbL assembly.

Dipping was the first used deposition method and presents several steps starting from the immersion of a positively charged substrate into the polyanion solution (see Figure 1.13(B)). Negatively charged polyelectrolyte chains adsorb on the substrate thanks to electrostatic interactions and the release of counter anions causing the reversal of the surface charge. The adsorption time per layer is typically about 15 minutes corresponding to the adsorption plateau where the surface coverage is maximum. Rinsing and drying steps are then completed to remove the weakly adsorbed chains before immersing the film into the polycation solution. Once again, this second dipping is followed by rinsing and drying steps. This polycation/polyanion deposition step can then be repeated as many times as wanted until the desired film thickness is reached.

Nevertheless, dip-assisted LbL assembly is a very time-consuming process as the deposition of one layer requires around 15 min limiting its use for industrial applications. In order to speed up the film growth, spray-assisted[62] (Figure 1.13(C)) and spin-assisted[63] (Figure 1.13(D)) assemblies have been developed. Spray-assisted deposition consists in the sequential spraying of oppositely charged solutions

perpendicular to a receiving substrate with intermediate rinsing steps. For spin-assisted deposition, several drops of the different solutions are deposited at the center of a rapidly rotating substrate. The centrifugal force created by the rotating substrate provides the liquid to spread on the substrate surface. In both cases, the time needed to deposit a layer is only about a few seconds.

Two main growth regimes were defined for LbL films depending on the diffusion of the components in the film. In absence of diffusion a steady (linear) growth of the film thickness is observed. If at least one of the components diffuses in the film a superlinear ("exponential") growth of the film thickness is seen. In this case the film acts as a reservoir that will store and release an increasing amount of extra charges available for ion-pairing at each deposition step explaining the continuous speed up of the thickness growth.

The build-up principle of polyelectrolyte multilayers prepared by LbL assembly has been discussed in this section. We will now see how the film growth can be tuned.

1.4.2 Control of the LbL build-up

The composition, structure and properties of films prepared by LbL assembly can be controlled by varying various parameters such as for example pH, temperature, component concentration, ionic strength, and exposure time.[64]
Mérindol et al.[65] for instance reported the preparation of cellulose-based multilayer films by dip-assisted LbL assembly. The film build-up was carried out by associating anionic CNFs with cationic PVAm at different pH values. The growth of the film, monitored by ellipsometry, was faster at higher pH values (Figure 1.14(A)). Indeed, the degree of ionization of PVAm chains decreases as the pH increases meaning that a higher amount of polyelectrolyte is needed to compensate the negative charges of CNFs. As the film composition can be adjusted by a pH variation, the corresponding mechanical properties can consequently be tailored as shown in Figure 1.14(B). As the amount of PVAm in the film increases, more bridges are created between adjacent cellulose nanofibrils and the reinforcing efficiency of each fibril increases (films become more brittle).

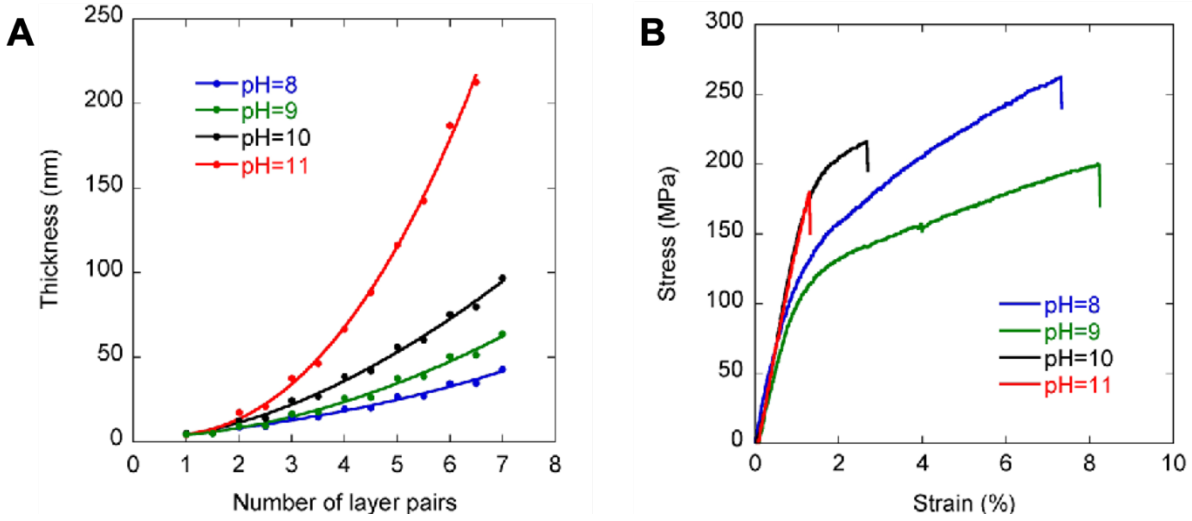

Figure 1.14: (A) Build-up of $(PVAm/CNF)_n$ LbL films monitored by ellipsometry as function of the pH of the PVAm solution and the number of layer pairs. (B) Stress strain curves obtained for micron thick $(PVAm/CNF)_n$ films built with PVAm solutions at pH values between 8 and 11.[65]

Dodoo et al.[66] studied the influence of the ionic strength and the type of ions on the build-up of LbL multilayer films composed of poly(sodium 4-styrene sulfonate) (PSS) and poly(diallyl dimethylammonium chloride) (PDDA). They showed that the film thickness increases by raising the ionic strength and ion size. At low salt concentration, the polymer chains were stretched due to the low charge screening whereas for high salt concentration, the polymer chains adopt a coiled conformation inducing a higher thickness increment.

Although pH and ionic strength are some of the most studied parameters, the solvent can also affect the growth of a multilayer film and consequently its properties. For multilayer films comprising PSS and poly(allylamine hydrochloride) (PAH), increasing the quantity of ethanol in the polyelectrolyte solutions leads to an increase of the film growth.[67] Beyond the great diversity of tunable parameters, a wide variety of building blocks can also be employed in LbL assembly including polymers, proteins, lipids or nanoparticles.[68] Podsiadlo et al.[69] for example prepared nanocomposite films by LbL assembly with montmorillonite (MTM) nanosheets and PVAl resulting in a multilayered architecture (Figure 1.15(A)). The remarkable stiffness (modulus of 106 GPa) and tensile strength (400 MPa) of the cross-linked materials were attributed to the hydrogen and covalent bonding between the polymer and the nanosheets (Figure 1.15(B)).

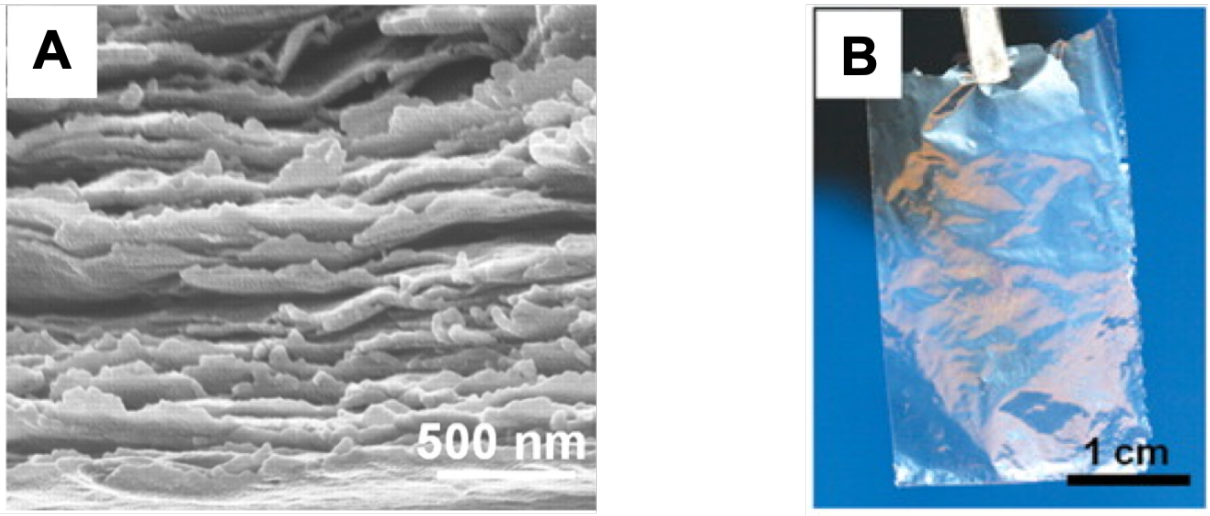

Figure 1.15: (A) SEM cross-section image of a thick $(PVAl/MTM)_{300}$ film showing the multilayered architecture and (B) photograph of the corresponding freestanding film presenting high transparency.[69]

Although LbL multilayer films have been initially assembled using electrostatic interactions, other types of interactions have also been used such as hydrogen bonding,[70] hydrophobic interactions,[71] charge transfer interactions,[72] covalent bonding,[73] host-guest interactions[74] or donor/acceptor interactions.[75]

To conclude, LbL assembly is an easy, robust and versatile method towards the preparation of multifunctional nanomaterials with a control over the structure and composition at the nanoscale level. Therefore, it is a promising technique for assembling nanostructured materials mimicking those found in nature including plant cell walls. In the next section, the nanocellulose building blocks will first be introduced before presenting the use of LbL assembly for the fabrication of nanocellulose-based materials.

1.5 Nanocellulose-based LbL materials

Cellulose is the most abundant polymer on Earth and the main constituent of the cell walls of plants. Apart from plants, cellulose can also be found in marine animals, bacteria, fungi and algae.[76] Structurally speaking, cellulose is a polysaccharide

consisting of a linear chain of repetitive anhydroglucose units (AGU) linked to each other via β-1,4-glycosidic bonds (Figure 1.16).

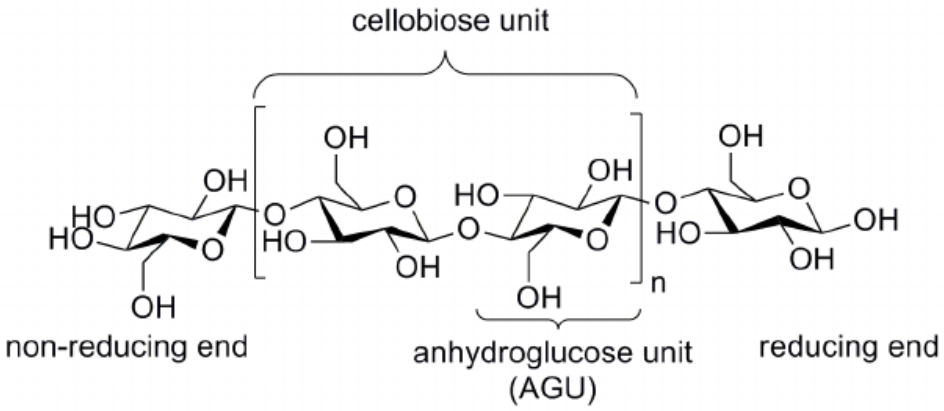

Figure 1.16: Representation of a cellulose chain showing the repetitive anhydroglucose units (AGU) linked by β-1,4 glycosidic bonds.

Two types of nanocellulose namely cellulose nanofibrils (CNFs) and nanocrystals (CNCs) can be obtained from elementary fibrils and will first be presented in this section.

1.5.1 Cellulose nanofibrils (CNFs)

Cellulose nanofibrils (CNFs), composed of alternating amorphous and crystalline parts, are generally extracted from cellulose microfibers by various mechanical methods such as high-pressure homogenization,[77] high-intensity ultrasonication[78] or grinding.[79] The generation of these shear forces induces the cellulose microfibers to split apart from each other and leads to long, flexible and entangled nanofibrils which are not soluble in water. As these mechanical routes are generally associated to a high energy consumption, different pre-treatments have been developed including enzymatic hydrolysis, chemical functionalization (e.g. carboxymethylation) or TEMPO-mediated oxidation reactions to produce soluble cellulose nanofibrils. Pääkkö et al.[80] for instance reported the preparation of homogeneous CNFs by combining enzymatic hydrolysis with high-pressure homogenization. Depending on the selected preparation method and its processing conditions, CNFs with a diameter comprised between 5 and 50 nm and a length of a few micrometers can be obtained.

1.5.2 Cellulose nanocrystals (CNCs)

The first investigations concerning cellulose nanocrystals have been reported by Rånby et al.[81] who obtained rod-like CNCs after sulfuric acid hydrolysis of wood cellulose fibers. Since then, this type of hydrolysis remained the most common preparation of CNCs. Typically, amorphous regions of cellulose fibers are prone to acid hydrolysis while crystalline parts remain intact because of their higher resistance to hydrolysis. During hydrolysis with sulfuric acid, the reaction between acid and part of the hydroxyl groups of the CNCs provides the formation of anionic sulfate ester groups promoting their stable dispersion in aqueous media. As the acid-hydrolysis treatment is controlled by diffusion, a broad dimension distribution of CNCs is generally observed. It is important to note that the surface and morphological properties of CNCs highly depend on the source, the isolation process and its conditions[82] as illustrated in Table 1.1.

Table 1.1: Overview of the dimensions and aspect ratio of different nanocrystals depending on the source and preparation method.

Source	Preparation method	Length (nm)	Width (nm)	Aspect ratio	Reference
Ramie	H_2SO_4 hydrolysis	70-200	5-15	12	[83]
Cotton	HCl hydrolysis	100-150	5-10	10-30	[84]
Wood	H_2SO_4 hydrolysis	100-300	3-5	20-100	[85]
Sisal	H_2SO_4 hydrolysis	100-300	60	60	[86]
Bacteria	H_2SO_4 hydrolysis	100-1000	10-50	2-100	[87]
Tunicates	H_2SO_4 hydrolysis	> 1000	10-20	100	[88]

Moreover, CNCs also exhibit high crystallinity ranging from 54% to 88% depending on the source,[89] low density (1.6 g/cm^3) and very interesting mechanical properties including high stiffness (150 GPa) and high tensile strength (7.5 GPa).[90] These mechanical properties make CNCs ideal candidates for the preparation of reinforced polymer nanocomposites. Beside their outstanding mechanical properties, crystalline cellulose also presents remarkable optical properties. Revol et al.[91] first described the self-organization of CNCs into a chiral nematic crystalline phase in solution. This liquid crystalline behaviour coupled with the birefringence of CNCs lead to interesting optical

properties. Interestingly, this chiral structure with CNCs arranged in a helicoidal pattern was retained after solvent evaporation and iridescent films were observed.

Thanks to their interesting properties, both nanocellulose types have been associated with polymers to form multilayer films using LbL assembly. Podsiadlo et al.[92] in 2005 were the first to incorporate nanocellulose within a multilayer film by combining anionic CNCs with PDDA. Since then, research on cellulose-based films gained tremendous attention due to the natural origin of cellulose, its sustainability and the possibility to exploit multiple interactions between nanocellulose and polymers. In this section, we will focus on the preparation of nanocellulose-based materials prepared by LbL assembly.

1.5.3 Preparation and properties of isotropic cellulose-based LbL films

The preparation of isotropic LbL films is generally performed by sequential dipping of a substrate in solutions containing anionic and cationic components, one of which being an anisotropic nano-object like CNF or CNC. A statistical orientation of the anisotropic nano-objects in the corresponding layers is observed as no preferential object alignment is induced by the dipping method based on the free diffusion of the molecules and nano-objects.

Both CNFs and CNCs have already been used in association with many different polycations in dip-assisted LbL assembly such as PDDA,[92] PAH[93] or poly (ethyleneimine) (PEI).[94] Nevertheless, as indicated previously, the film build-up is not only restricted to electrostatic interactions and hydrogen bonding has also been exploited between anionic CNCs and xyloglucan, a neutral polysaccharide.[95] Moreover, the surface morphology of these films depends significantly on the crystallinity and aspect ratio of the nanoparticles. Podsiadlo et al.[94] reported the dip-assisted LbL assembly of long and rigid CNCs on PEI (Figure 1.17(A)). They observed a low density of nanoparticles with a high surface roughness resulting in a porous architecture. On contrary, Wågberg et al.[93] demonstrated the formation of a dense

fibrillar network with a low surface roughness when employing flexible CNFs (Figure 1.17(B)).

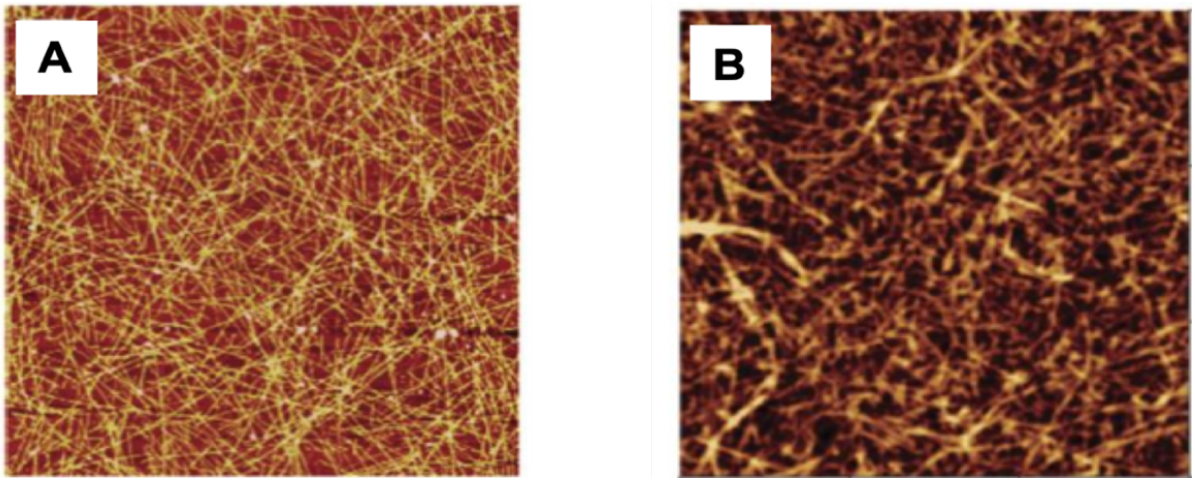

Figure 1.17: AFM images of (A) a single PEI / tunicate CNCs layer pair[94] (10 × 10 µm²) and (B) a single PEI / CNFs layer pair[93] (1.5 × 1.5 µm²) deposited by dipping on silicon wafers.

As already shown previously, the ionic strength of the polymer solutions can greatly affect the structure and properties of the multi-layered film. Moreau et al.[96] for instance demonstrated the deposition of CNCs in a double layer when combined with PAH with a concentration of 1 mol/L of NaCl. Indeed, in the presence of salt, PAH chains adopt a coiled conformation leading to their interpenetration in the first CNC layer and displaying extra cationic charges promoting the deposition of a second CNC layer (Figure 1.18(B)). Moreover, upon drying, hydrogen bonding can be developed between the two CNC layers.

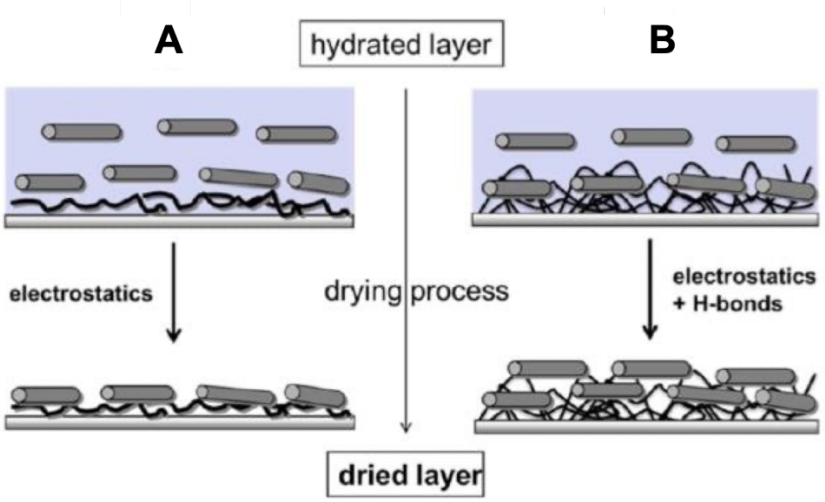

Figure 1.18: Schematic representation of the CNC adsorption on a single layer of PAH (A) without and (B) with salt.[96]

On the other hand, Wågberg et al.[93] reported the growth of CNF-based multilayer films with different polycations and ionic strengths. They demonstrated a significant influence of the selected polycation and the pH of the solution on the film growth.

After the preparation of nanocellulose-based multilayer films, their mechanical and optical properties have been characterized on supported and freestanding films using various methods. For instance buckling mechanics (Figure 1.19(A)) was employed to determine the Young's modulus of supported multilayer films comprising PEI and CNFs.[97] Interestingly, the authors demonstrated a significant influence of the humidity on the mechanical properties of the film with a Young's modulus of 1.5 GPa at 50% RH that increased to 17.2 GPa at 0% RH.

A

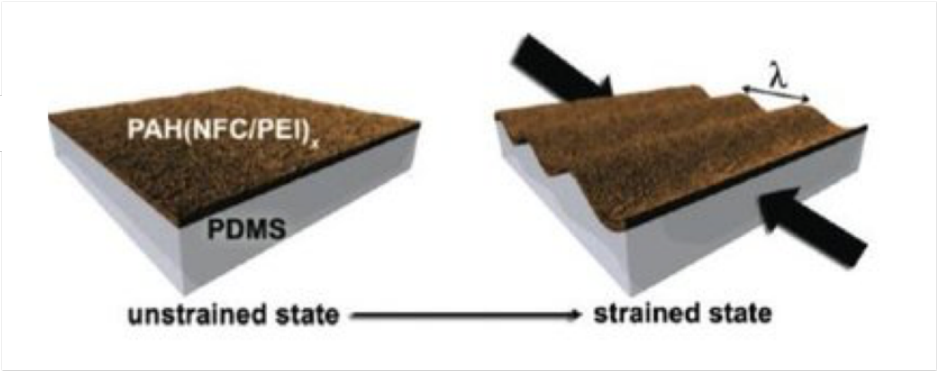

B

	0% R.H. (SEM)	50% R.H. (optical microscope)
film thickness	67 ± 8 nm	71 ± 8 nm[a]
buckling wavelength	5.7 ± 0.2 μm	2.65 ± 0.09 μm
Young's modulus (E_f)	17.2 ± 1.2	1.5 ± 0.2

Figure 1.19: (A) Schematic representation of the buckling observed for a CNF-based multilayer film on a stretchable PDMS substrate. (B) Young's modulus dependence on the relative humidity for PAH (CNF/PEI)$_{15.5}$ films.[97]

Additionally, Eita et al.[98] showed the possibility to tailor the mechanical properties of multilayer films composed of CNFs by incorporating silica nanoparticles. Indeed, the Young's modulus of (PVAm/CNF) films doubled from 1 to 2 GPa by embedding silica nanoparticles in the films. Karabulut et al.[99] were able to prepare freestanding films, built on hydrophobic substrates, allowing the direct measurements of the mechanical

properties of these films using a tensile strength apparatus. They reported a Young's modulus of 9.3 GPa at 0% RH for $(PEI/CNF)_{150}$ films. Ghanadpour et al.[100] finally reported the fabrication of pure cellulose films by associating cationic modified CNFs with anionic CNFs. The freestanding films were also characterized by tensile tests resulting in a Young's modulus of 9 GPa at 50% RH proving the possibility to prepare highly resistant films only composed of cellulose.

Podsiadlo et al.[94] exploited the porous architecture of (PEI/CNC) films (Figure 1.20(A)) for the preparation of antireflective coatings. Indeed, in order to exhibit antireflective properties, films built on glass should have a thickness of ¼ of the incident light wavelength while presenting a refractive index of around 1.22. These conditions can only be satisfied thanks to the porous structure of the randomly distributed long CNCs within the film. The monitoring of the light transmittance in the visible range (Figure 1.20(B)) during the film growth demonstrated a linear increase characteristic of multi-layered antireflective coatings.

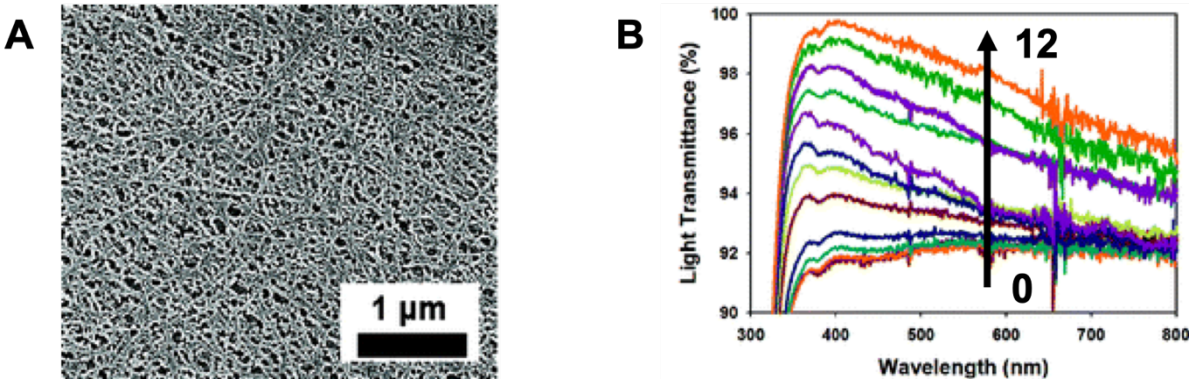

Figure 1.20: (A) Microscopy image of a $(PEI/CNC)_{12}$ film showing its porous structure and (B) light transmittance spectra measured for the first 12 bilayers.[94]

Beside mechanical and optical properties, cellulose nanoparticles have also been used to fabricate films with fire-retardant,[100] adhesive,[101] thermo-responsive[102] or gas barrier properties.[103]

All the examples mentioned previously demonstrate the possibility to prepare reproducibly films with tunable structures and compositions by LbL dip-assisted assembly. Nevertheless, this technique does not allow any control over the orientation

of the anisotropic cellulose nanoparticles. This is a main limiting point as the preparation of oriented films with anisotropic mechanical and optical properties is highly sought for many applications ranging from optical polarizers to photovoltaic devices or even to cell culture.

1.5.4 Preparation and properties of anisotropic cellulose-based LbL films

Unidirectional alignment

A variety of methods based on the application of external fields (mechanical, electrical, or magnetic) or epitaxial growth (templating) have been suggested for the in-plane alignment of anisotropic nano-object like nanocelluloses in thin films.[104] Among them spin-coating has been intensively employed to prepare oriented films composed of nanocelluloses (CNFs or CNCs).

Cranston et al.[105] studied for instance the in-plane alignment of cotton CNCs by spin-coating (Figure 1.21(A)).

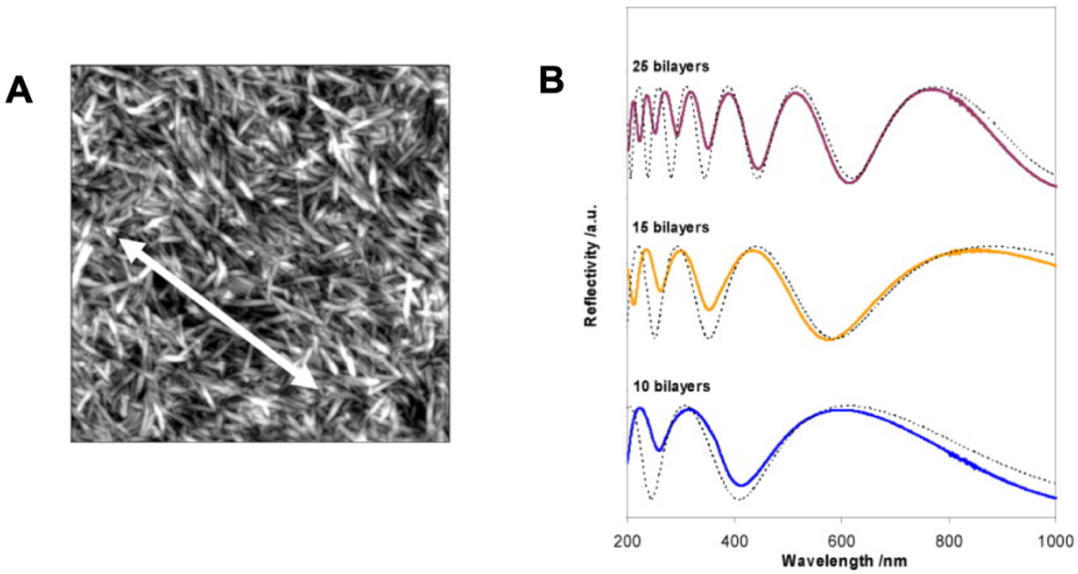

Figure 1.21: (A) Microscopy image showing the in-plane alignment of cotton cellulose nanocrystals by spin-coating with the white double arrow indicating the main orientation direction. (B) Reflectivity as function of the wavelength for $(PAH/CNC)_n$ multilayer films with different number of layer pairs.[105]

Films containing cellulose nanocrystals and PAH were prepared with various numbers of bilayers and showed birefringence arising from the optical anisotropy of the oriented CNCs. Optical reflectometry (Figure 1.21(B)) was used to prove the thickness dependence of the film birefringence but also allowed the determination of the refractive indices along (1.595) and across (1.534) the CNC alignment direction.

Mérindol et al.[106] reported recently the preparation of micrometric (PVAm/CNF) films with highly oriented CNFs by spin-assisted LbL assembly. The degree of alignment of the nanofibrils was investigated by AFM and was proven to increase from the center to the edge of the sample. They demonstrated anisotropic mechanical properties (Figure 1.22) with the highest Young's modulus (33 GPa) and strength (490 MPa) values measured along the alignment direction of the fibrils. Moreover, a significant improvement of the mechanical properties could be observed by aligning CNFs when compared to randomly distributed nanofibrils.

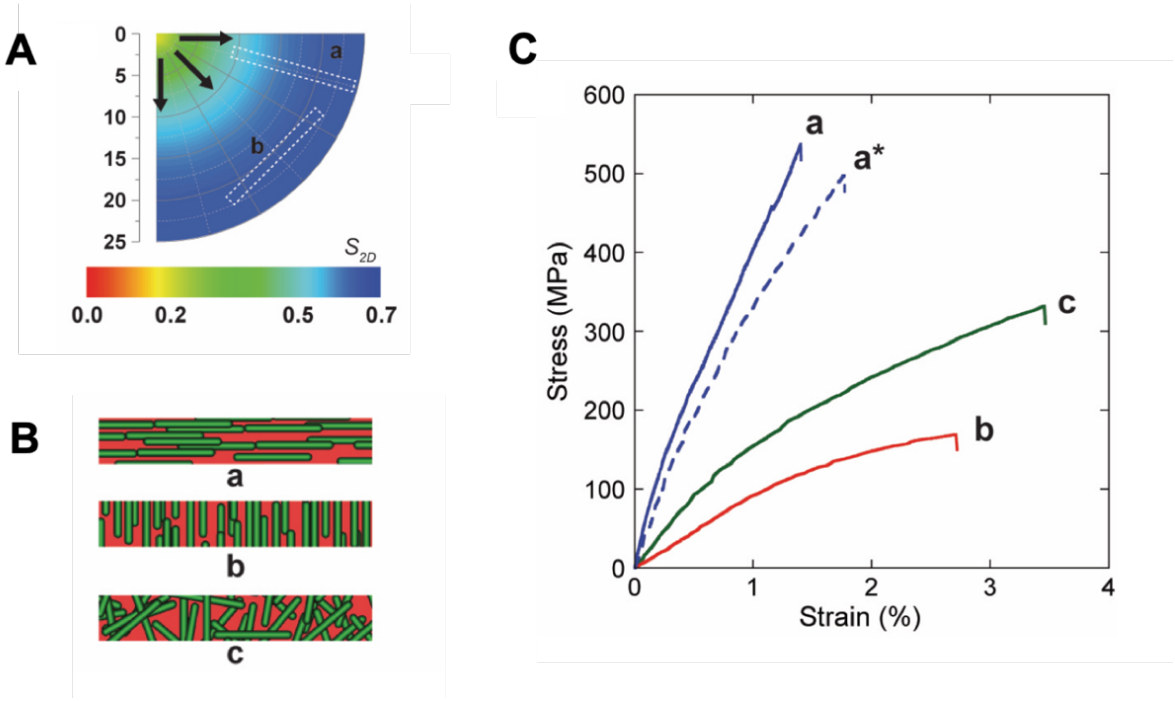

Figure 1.22: (A) Schematic illustration showing the oriented sample (parallel (a) and perpendicular (b) to the CNF alignment) for mechanical tests from films prepared by spin-assisted assembly. (B) Simplified sketch of the relative organization of the CNFs in oriented (a, b) and random (c) samples. (C) Stress-strain curves measured for thick CNF-based multilayers prepared by dipping (c) and spin-assisted LbL assembly at 8000 (a*, b) and 10000 rpm (a).[106]

Spin-coating was not the only method used for aligning cellulose nanocrystals. Jean et al.[107] prepared oriented CNC films by dipping the substrate in an ordered liquid crystal CNC suspension. AFM followed by Fourier transformation of the images demonstrated a uniaxial orientation of the crystals after 20 min of dipping. Cranston et al.[108] finally immerged a silicon substrate in a chiral nematic liquid crystal phase of CNCs and observed the orientation of the nanocrystals after the application of a strong magnetic field.

Complex structures

Spin-assisted LbL assembly allows the in-plane alignment of anisotropic nanoparticles in each layer, but it is impossible to vary their alignment in consecutive layers of the film. This limits its use towards the preparation of more complex structures namely helicoidal structures that are found in biological materials. Recently, the orderly integration of 1D micro- or nano-scale building blocks into macroscopic 3D bio-inspired anisotropic hierarchical architectures possessing outstanding mechanical properties was demonstrated using either 3D printing techniques[109,110] or a brushing-induced assembly method.[111] While this published work compellingly underlines the interest in such materials, such methods do not allow producing such helicoidal composites with nanoscale dimensions. A key development in the LbL field towards the preparation of complex structures is the introduction of the grazing incidence spraying (GIS) technique in our group which allows to control the in-plane alignment of anisotropic nano-objects in the spraying direction.[11] Instead of spraying the nanoparticle solution with an angle of 90° against a receiving surface resulting in randomly distributed nanoparticles in each layer, they sprayed CNFs with a small angle onto the surface inducing the in-plane alignment of the nanofibrils in the spraying direction (Figure 1.23).

The combination of GIS with LbL assembly allowed the build-up of nanocomposite films with unidirectional, cross-ply and helicoidal arrangements of cellulose nanofibrils.[112] Specific attention has been given to the preparation of helicoidal structures (Figure 1.24(A)). This chiral architecture (left and right helices) was confirmed by circular dichroism (CD) spectroscopy (Figure 1.24(B)) while the mechanical properties of helicoidal films were investigated by nanoindentation as the area with homogeneous thickness were too small for tensile testing. As expected, the

characterization of the helicoidal sample with an anisotropic Knoop indenter resulted in no significant difference among either the modulus and hardness measured at different azimuthal angles.

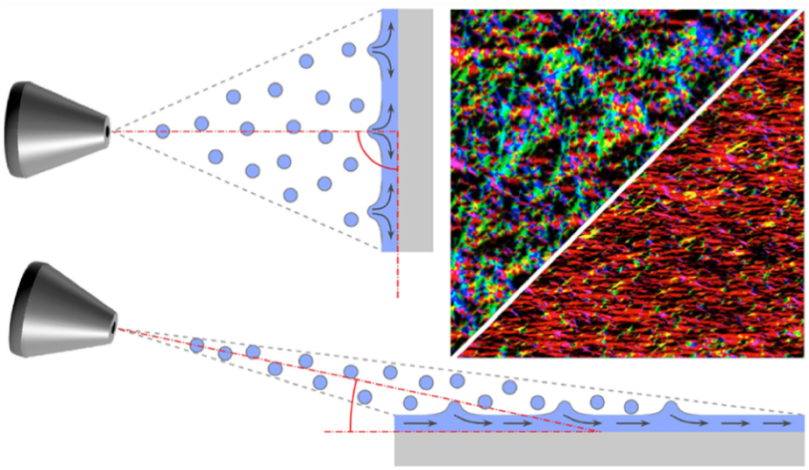

Figure 1.23: Schematic illustration of the CNFs sprayed in an orthogonal direction to the substrate (top image) providing randomly distributed nanofibrils with multiple colors indicating no preferential orientation direction. Grazing incidence spraying (GIS) of CNFs at a small angle with respect to the substrate (bottom image) resulting in highly oriented nanofibrils as demonstrated by the homogeneously colored nanofibrils.[11]

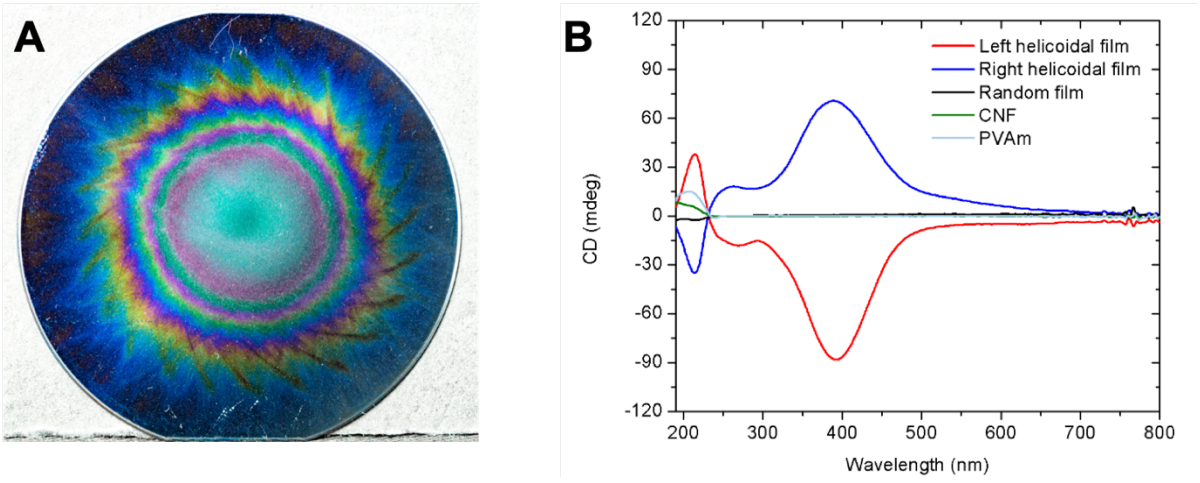

Figure 1.24: (A) Optical photograph of a CNF multilayer helicoidal film composed of 72-layer pairs with 3 turns and an angle of 15° between each (CNF/PVAm) layer pair. (B) CD spectra of right- and left-handed helicoidal films compared to the spectra of a random film prepared by dipping and CNF and PVAm solutions.[112]

This study demonstrates the possibility of fabricating complex structures including Bouligand architectures of CNFs by combining LbL assembly with GIS. The handedness and pitch of the helical arrangement of CNFs can be tailored by the direction of spraying and the rotation angle between consecutive layer pairs.

The topics presented in the previous sections showed the necessity to develop efficient strategies to prepare hierarchical bio-based nanomaterials with interesting properties to target highly demanded applications. The first aim of the present work was to take inspiration from the plant cell walls to design wood-inspired nanomaterials. In that perspective, the layer-by-layer (LbL) assembly was employed to combine various cellulose nanoparticles with a polymer matrix of PVAm. Different structures were fabricated using several deposition techniques and are presented in Chapter 3. The characterization of the optical and mechanical properties was also discussed and presented to evaluate the structure-property relationships of the obtained nanomaterials.

In addition to bio-based highly resistant materials, materials displaying anisotropic optical properties are also currently highly demanded in a wide variety of applications including in strain sensors. In that perspective, the next section will focus on the topic concerning the strain sensors and describe the most important points including the sensing and supporting materials as well as the possible manufacturing strategies.

1.6 Stretchable strain sensors

Stretchable and wearable strain sensors have attracted tremendous attention in recent years due to their facile applications on the human body for different purposes including health monitoring,[113] human motion detection,[114] artificial skins[115] and soft robotics.[116] These sensors, transducing a mechanical stimulus into a measurable signal, are generally composed of a sensing material associated with a flexible matrix allowing the stretching. This section will first provide an overview on the different types of strain sensors and their main characteristics. The different sensing and supporting materials will then be discussed as well as the possible manufacturing strategies to design these strain sensors.

1.6.1 Different types of sensors

Stretchable strain sensors are all converting a mechanical deformation into a measurable signal. Depending on their working mechanisms, they can be mainly categorized into resistive, capacitive and optical strain sensors.[12] Resistive-type strain sensors are based on the variation of the electrical resistance when subjected to a mechanical deformation. The electrical resistance R of a conducting material is the inverse of electrical conductance and can be expressed using Equation 1.1.

$$R = \rho \times \frac{L}{A} \qquad \textbf{Equation 1.1}$$

With ρ the resistivity in Ω·m, L the length of the conductor in m and A the cross-sectional area of the conductor in m2 (Figure 1.25(A)).

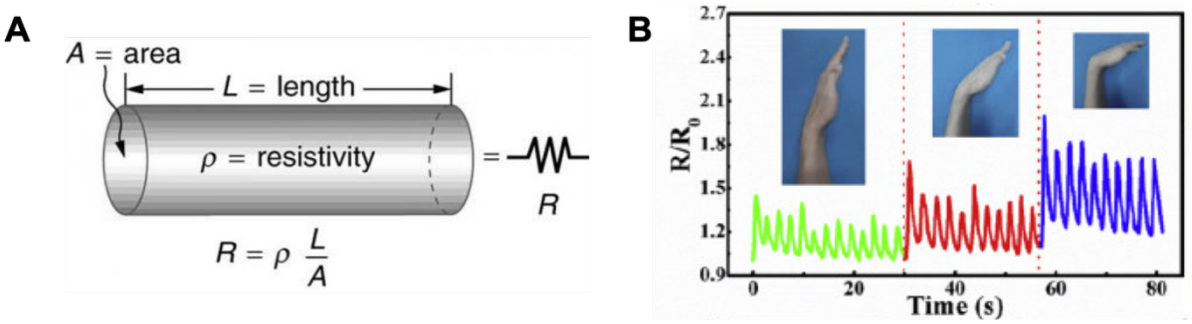

Figure 1.25: (A) Schematic illustration of a conductor. (B) Electrical resistance change of a resistive strain sensor as a function of time measured for different hand movements.[117]

Wang et al.[117] for instance prepared a flexible resistive strain sensor based on reduced graphene oxide deposited on thermoplastic polyurethane fibers and reported a change of the electrical resistance upon stretching for different hand movements as it can be seen in Figure 1.25(B).

Capacitive-type strain sensors are frequently prepared by inserting a dielectric layer between two electrodes (Figure 1.26(A)).

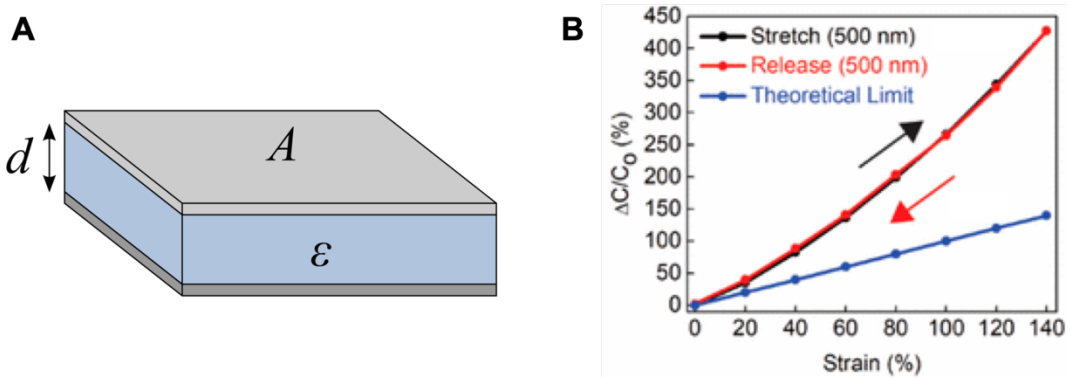

Figure 1.26: (A) Schematic illustration of a parallel plate capacitor showing two electrodes (in grey) separated by a dielectric layer (in blue). (B) Capacitance change of a strain sensor as function of the applied strain showing good reversibility upon stretching and release.[118]

Electrical capacitance is defined as the ability of a material to store an electric charge when a voltage is applied and can be expressed for a parallel-plate capacitor using Equation 1.2.

$$C = \varepsilon \times \frac{A}{d} \qquad \textbf{Equation 1.2}$$

With C the capacitance in farad, ε the permeability of the dielectric layer, A the area of the electrodes in m^2 and d the distance between the electrodes in m.

Nur et al.[118] fabricated a capacitive strain sensor based on gold film electrodes separated by a dielectric layer and showed a reversible electrical capacitance variation after several stretch-release cycles. As the traditional parallel plate capacitors (Figure 1.26(A)) present a limited sensitivity arising from their inherent structure, this work demonstrates the improvement of the sensitivity by inducing wrinkles in the film.

Optical-type strain sensors, finally, are based on the variation of light transmission or reflection during mechanical deformation. Gu et al.[119] reported the fabrication of an optical strain sensor with carbon nanotubes embedded in a silicone elastomer (Figure 1.27(A)). Upon stretching, they observed a change in the optical transmittance (Figure 1.27(B)) of the material that was attributed to the formation and propagation of

microcracks. They employed this sensor to monitor the bending of the finger of a robot arm.

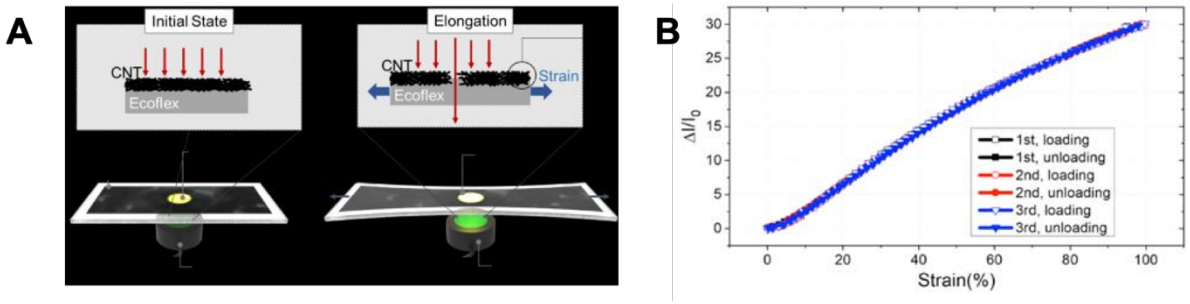

Figure 1.27: (A) Schematic illustration of the stretching of the optical strain sensor based on CNT-embedded Ecoflex film and (B) the optical transmittance change of the strain sensor upon several stretching and release cycles.[119]

Among the various strain sensors that have been presented, resistive and capacitive strain sensors were initially intensively studied due to their high stretchability and simple fabrication process.[13] More recently, optical strain sensors have attracted increasing interest because of their high resistance to temperature[120] and humidity as well as their low sensitivity to electromagnetic interference.[121] Moreover, compared to resistive and capacitive strain sensors, optical sensors don't need to be connected to a power supply. We will now present the main performance parameters characterizing the different types of strain sensors.

1.6.2 Performance parameters of strain sensors

The sensing properties of a strain sensor can be characterized by various parameters namely its stretchability, sensitivity and durability. The first important parameter when considering the preparation of a strain sensor is referred as stretchability. This corresponds to the maximum strain that the sensor can withstand while keeping its integrity and sensing properties. The stretchability of a sensor depends essentially on the sensing and supporting materials but also on the selected fabrication method. The stretchability of the strain sensors reported in the literature varies from a few percent (around 3%) to 1000%.[122,123] It can also be seen that generally, the stretchability of the strain sensors can be improved by using nanoparticles with an important aspect ratio

providing the formation of a resistant percolation network bearing important strains.

The sensitivity is another important variable when designing a strain sensor. It corresponds to the ratio of the relative change of a measurable variable to the applied strain[124] and is quantified by the gauge factor (GF). For resistive-type strain sensors, GF is defined as function of the relative change of electric resistance and applied strain (Equation 1.3).

$$GF = \frac{\Delta R}{R_0 \times \varepsilon} \qquad \textbf{Equation 1.3}$$

With $\Delta R/R_0$ and ε corresponding respectively to the relative change of the electric resistance and to the applied strain. Similarly, the relative change of electrical capacitance $\Delta C/C_0$ and light transmittance $\Delta I/I_0$ is generally used to respectively determine the GF for capacitive and optical strain sensors. Independently from the type of strain sensors, the higher the GF, the more sensitive is the sensor.

As these strain sensors are expected to be applied on the human body with large and dynamic strains,[125] a crucial point is also their durability. Indeed, the strain sensor should withstand multiple stretch-release cycles while keeping its sensing performance. Kim et al.[126] for example reported the fabrication of a resistive strain sensor with remarkable durability at very high strains (10 000 cycles at 150% of strain). In order to improve this durability, yarn-based strain sensors were developed more recently and displayed durability up to 300 000 stretching-releasing cycles.[127]

A strain sensor can be characterized by several performance parameters that depend significantly on the used sensing mechanisms. The next section will provide an overview on the main sensing mechanisms that can be found in the different types of strain sensors.

1.6.3 Strain sensing mechanisms

In this section, the main strain sensing mechanisms being exploited in resistive,

capacitive and optical strain sensors will be presented in details. Generally, capacitive and optical strain sensors are based on geometrical variations while resistive strain sensors rely on multiple sensing mechanisms including the formation of microcracks.

Geometrical structure change

The geometrical effect plays a significant role on the control of the sensing properties of strain sensors. Indeed, the cross-sectional area of the supporting material varies upon stretching due to its Poisson's ratio ϑ that is defined (Equation 1.4) as the contraction of the material in the direction perpendicular to the stretching direction as illustrated in Figure 1.28.

$$\vartheta = -\frac{dl/l_0}{dL/L_0} = -\frac{(l - l_0)/l_0}{(L - L_0)/L_0} \qquad \textbf{Equation 1.4}$$

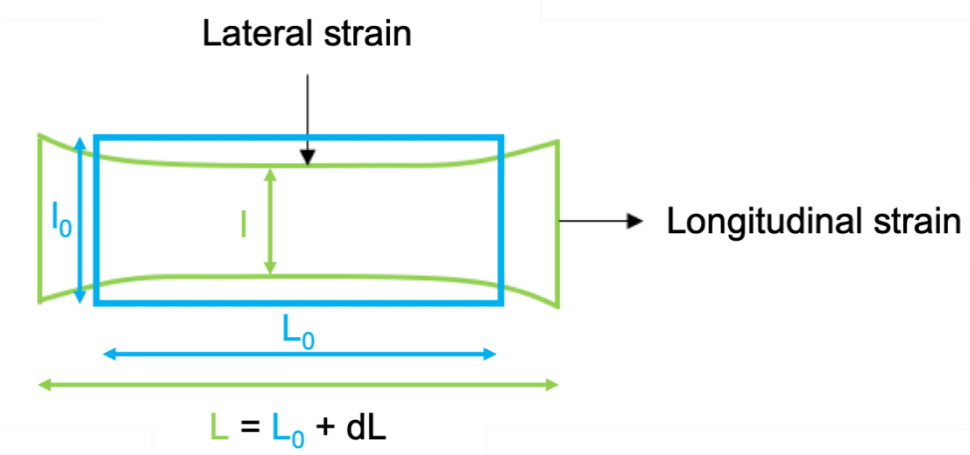

Figure 1.28: Schematic illustration of the uniaxial stretching of a material highlighting its contraction in the direction perpendicular to the stretching direction.

This geometrical change has already been intensively utilized for the preparation of different types of strain sensors.[118,128,129,130] Concerning capacitive sensors, electrical capacitance depends on both the cross-sectional area and thickness of the dielectric layer. Nur et al.[118] exploited the thickness reduction of the dielectric layer upon stretching providing a capacitance change. Guo et al.[130] reported the preparation of an optical waveguide whose length increased upon stretching as depicted in Figure

1.29(A). The optical loss induced by the length variation of the PDMS fiber doped with Rhodamine B dye was exploited to monitor the strain change (Figure 1.29(B)).

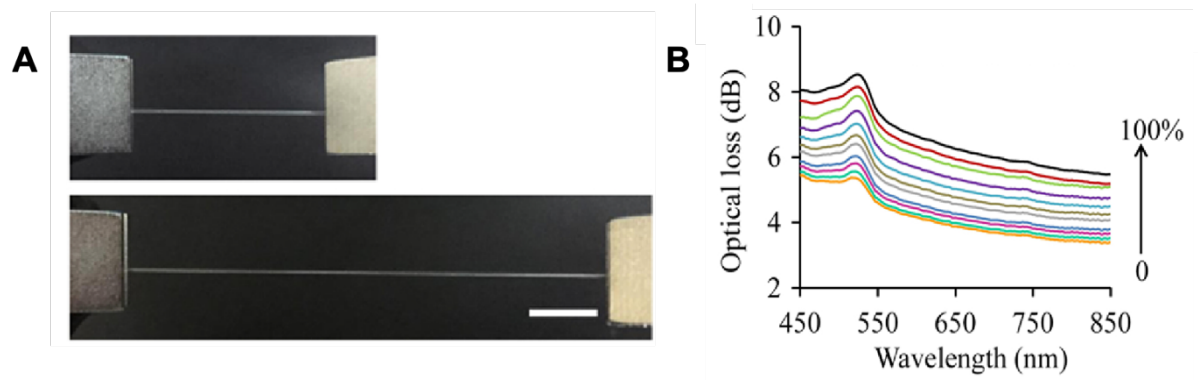

Figure 1.29: (A) Photographs of the optical waveguide before (top) and after stretching (down). Scale bar corresponds to 1 cm. (B) Attenuation spectra of the sensor between 0 and 100% of strain illustrating the increase of the optical loss.[130]

Disconnection mechanism

In the case of resistive strain sensors, the flow of electrons is possible through a conducting network only if the sensing components are connected. However, when subjected to a mechanical deformation, some sensing materials can disconnect from each other because of the stiffness difference between the sensing and supporting materials. As the number of conductive pathways decreases, the electrical resistance increases. This mechanism has been intensively employed with nanowires and especially with silver nanowires. Amjadi et al.[114] for instance reported the preparation of a strain sensor with AgNWs embedded in a PDMS matrix and demonstrated an electrical resistance increase upon stretching arising from the disconnection of adjacent AgNWs as illustrated in Figure 1.30.

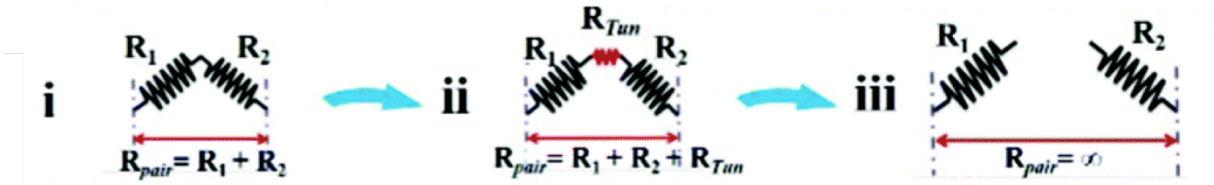

Figure 1.30: Schematic representation of different electrical interconnection scenarios between 2 adjacent AgNWs (represented by springs) upon stretching: (i) a complete connection with no contact resistance, (ii) a tunneling current between AgNWs (iii) and a complete disconnection.[114]

Microcracks formation

When brittle films are deposited on top of a flexible substrate, mechanical deformation induces the formation of cracks upon stretching due to the different mechanical properties of the sensing and supporting materials. These microcracks generate a discontinuity in the conductive paths and consequently lead to an increase of the electrical resistance. Even if the formation of these cracks is not targeted, they were used multiple times to design highly sensitive strain sensors. Wang et al.[131] for example reported the preparation of a crack-based strain sensor with carbon nanotubes deposited on PDMS allowing the detection of strains as low as 0.007%

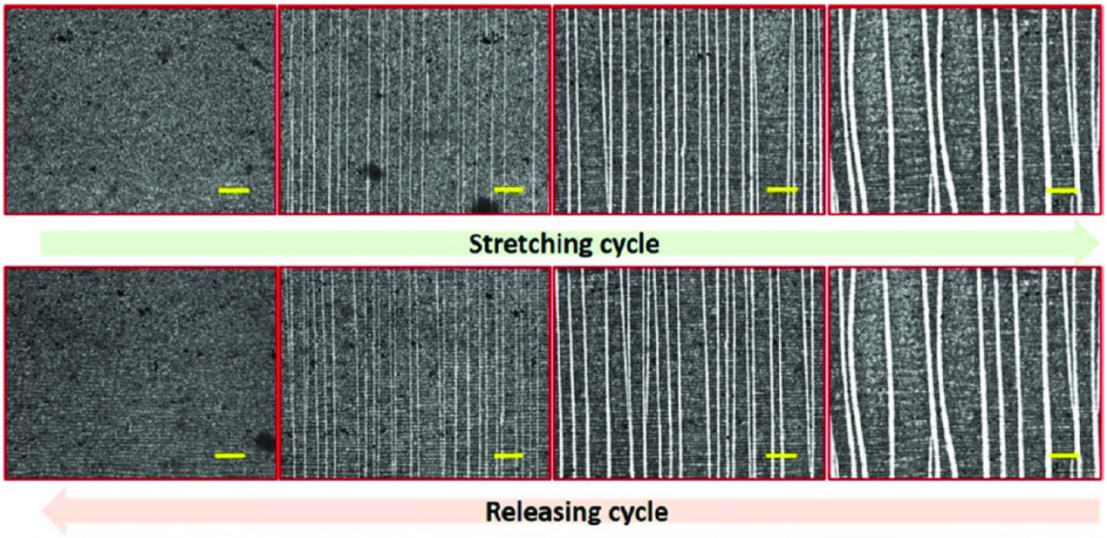

Figure 1.31: Morphology change of the graphite film deposited on an elastomer under a stretch-release cycle from 0 (left) to 100% (right) of strain highlighting the formation of parallel micro-cracks in the perpendicular direction of the applied strain. Scale bars correspond to 100 microns.[132]

while presenting a high stretchability (100%). Graphite films deposited on an Ecoflex elastomer were also employed for the preparation of a highly sensitive sensor (maximum GF value of 11344) based on microcracks formation (Figure 1.31).[132]
The stretchability and sensitivity of this sensor could be tuned by the size of the generated microcracks. The graphite nanoparticles were reconnected after the film release and induced the recovery of the electrical resistance.

These main sensing mechanisms will significantly affect the response and behavior of the sensors and consequently their properties. However, the targeted mechanism will also depend on the employed materials. The next section will present the different sensing and supporting materials that can be used and how they can be associated.

1.6.4 Fabrication of strain sensors

Towards the preparation of high-performance strain sensors, one crucial step is the selection of adequate sensing and supporting materials combined with easy and scalable fabrication methods.

Nanomaterials have significantly led to tremendous progress in the research of strain sensors. Indeed, compared to metal foils and semiconductors allowing only very small strains,[133] low dimensional nanomaterials can be used for a broader range of applied strains. In order to obtain strain sensors with excellent sensitivity, a wide variety of sensing components has been used including carbon nanotubes (CNTs),[134] graphene,[135] conductive polymers,[136] gold nanoparticles (AuNPs)[137] and nanowires (AuNWs),[138] silver nanowires (AgNWs),[139] or copper nanowires (CuNWs).[140] Concerning the flexible and supporting materials, silicone elastomers[141,142] (PDMS and Ecoflex) but also natural fibers[143,144] have already been utilized in association with different sensing materials.

Various manufacturing strategies have already been utilized to design stretchable strain sensors. Cai et al.[145] for instance reported the preparation of a composite strain sensor by spray-assisted LbL assembly by combining CNTs with two-dimensional titanium carbide $Ti_3C_2T_X$ MXene nanosheets. The association of conductive and

stretchable CNTs with highly sensitive $Ti_3C_2T_X$ MXene nanostacks provided a material with high stretchability (130%) and high sensitivity. Chemical Vapor Deposition (CVD) was also employed to obtain highly sensitive strain sensor. Liu et al.[146] reported the fabrication of a freestanding graphene woven fabrics by CVD that was then transferred on a PDMS substrate (see Figure 1.32).

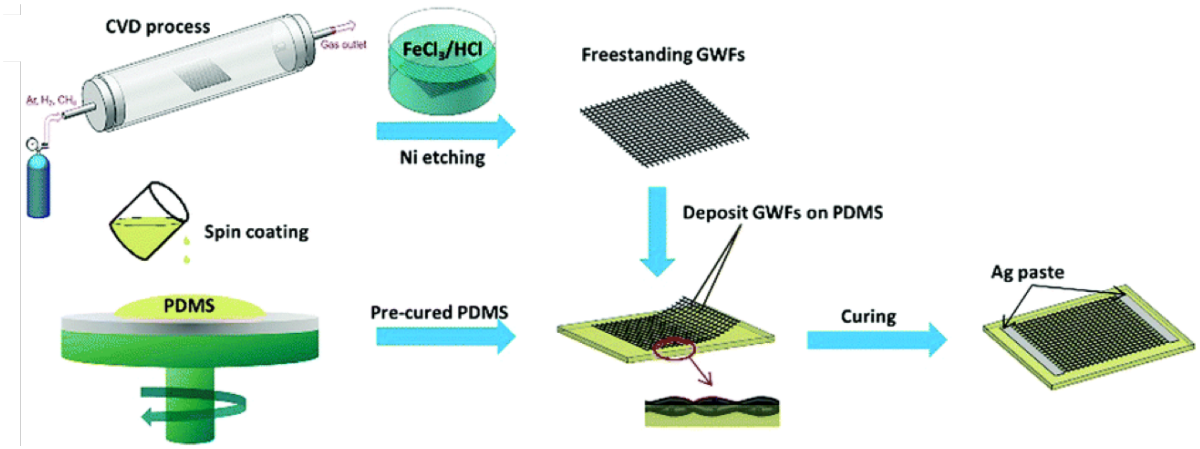

Figure 1.32: Schematic illustration of the preparation of a strain sensor based on a freestanding graphene woven fabrics grown by CVD.[146]

Laser direct writing[147] or etching and stamping techniques[135] have also been utilized. Finally, Zhang et al.[148] prepared a strain sensor by printing silver nanoparticles in repeated segments of serpentine structures on a polyurethane acrylate substrate such as depicted in Figure 1.33.

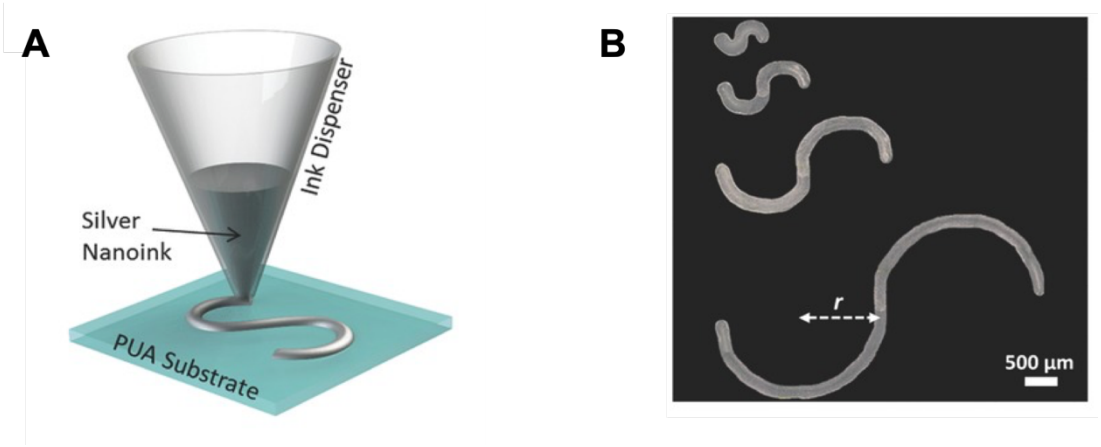

Figure 1.33: (A) Schematic illustration of the printing of silver nanoparticles on a polyurethane acrylate substrate in (B) serpentine structures with different radius *r* as seen by microscopy.[148]

They demonstrated a strong dependence of both stretchability and resistance change on the serpentine radius, referred as *r*. This serpentine structure allowed the formation of a strain sensor with higher stretchability (compared to a straight line of deposited silver nanoparticles) and remarkable gauge factors. Indeed, a serpentine feature with a radius of 200 µm displayed a record gauge factor of 10^7 at 12% that was attributed to an exceptional strain relieving attributed to the specific serpentine structure of the silver nanoparticles.

A wide variety of manufacturing strategies has been developed, especially in the recent years, in order to prepare strain sensors combining high stretchability with high sensitivity. The selected fabrication process significantly affects the interactions between the sensing and the supporting materials as well as the architecture of the strain sensor. Although these preparation methods provide strain sensors with high performance and various structures, they only allow the detection of a strain applied in a single direction. In order to monitor multidimensional strains, flexible strain sensors with anisotropic properties are highly desired.

To build anisotropic structures, many fabrication methods have been developed recently. Zeng et al.[149] for instance reported the preparation of an anisotropic porous structure composed of multiwalled CNTs by freeze-drying.
An electrospinning approach was employed by Lee et al.[150] to obtain highly aligned

carbon nanofibers as demonstrated in Figure 1.34(A).

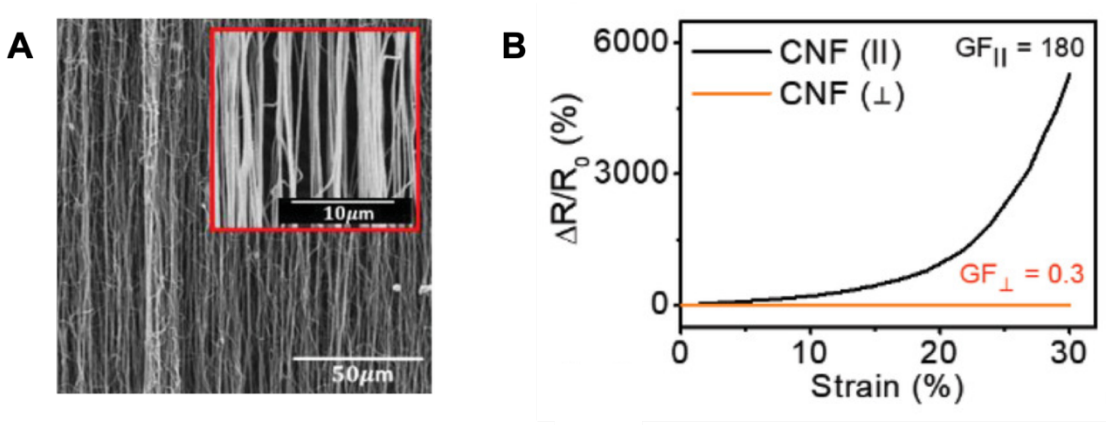

Figure 1.34: (A) SEM image showing the oriented carbon nanofibers aligned by electrospinning and the (B) anisotropic electrical properties upon stretching of the strain sensor with strains applied parallel and perpendicular to the fiber alignment direction.[150]

The corresponding strain sensor displayed high transparency, durability and exceptional anisotropic strain sensing properties (Figure 1.34(B)). Indeed, as a load applied perpendicular to the fiber alignment provided a low sensitivity (GF = 0.3), a strain applied along the fiber alignment considerably enhanced the sensitivity of the strain sensor (GF = 180).

Mousavi et al.[151] used 3D-printing to prepare a CNT reinforced polylactic acid composite (PLA/CNT) deposited on thermoplastic polyurethane as illustrated in Figure 1.35(A). Interestingly, the sensitivity and anisotropy of the sensor could be tailored by controlling the gap between the adjacent printed tracks and the temperature of the heated receiving surface (Figure 1.35(B)). The corresponding sensor was utilized for detecting the bending deformation and the angle of deformation in different directions.

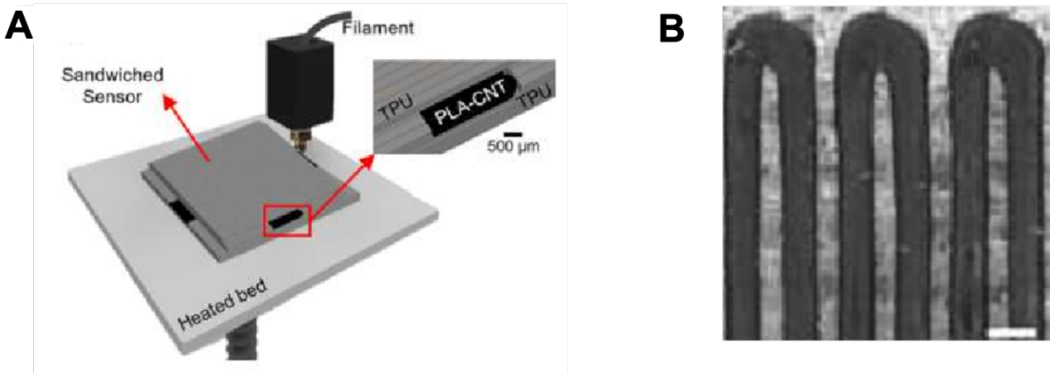

Figure 1.35: (A) Schematic illustration of the 3D-printing of the PLA/CNT composite on thermoplastic polyurethane (TPU) and the (B) microscopic image of the PLA/CNT sensor with the scale bar corresponding to 500 nm.[151]

Due to the increasing need to develop multidimensional strain sensors, various manufacturing strategies have been developed recently to orient nanomaterials. These techniques allow the preparation of sensors with properties that are highly depending on the mechanical deformation direction. Nevertheless, these strategies usually require specific nanomaterials or complicated equipment or are time-consuming.

Among the broad range of sensing materials presented previously, metallic nanoparticles and especially AgNWs are very promising candidates for the preparation of strain sensors due to their excellent anisotropic optical and electrical properties. In the next part, we will first discuss the optical properties of metallic nanoparticles and the possible ways to tailor them. In a second time, we will present different methods to prepare anisotropic AgNW networks and then demonstrate the potential of these nanowires towards the design of optical anisotropic strain sensors.

1.6.5 Properties of metallic nanoparticles

Metallic nanoparticles have received increasing interest due to their applications in sensing, imaging, biology and medicine.[152] One of the most striking and studied properties of metallic nanoparticles is their Localized Surface Plasmon Resonance (LSPR)[150] corresponding to the collective oscillation of the electron cloud near the surface of the metal when interacting with light (Figure 1.36).

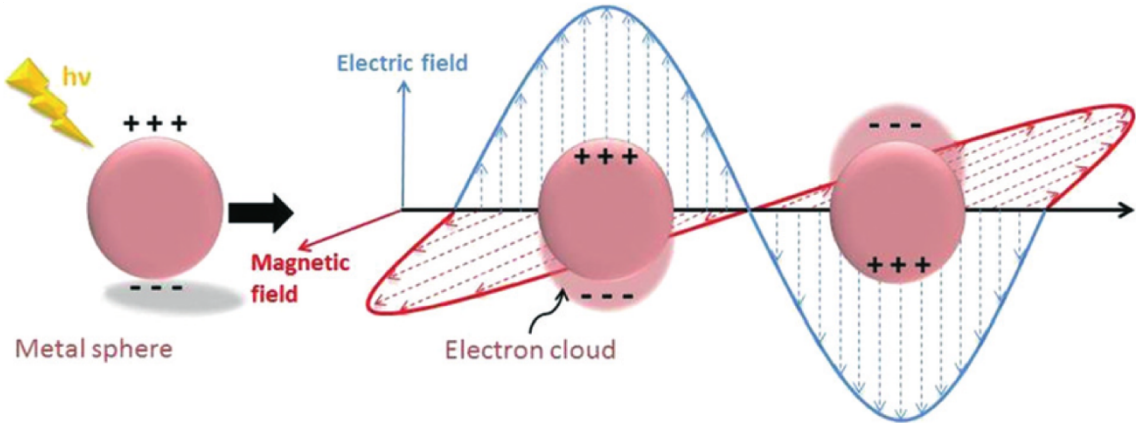

Figure 1.36: Schematic illustration of the Localized Surface Plasmon Resonance (LSPR) for a metallic sphere when interacting with light.[154]

In particular, the LSPR frequency of a nanoparticle can be modulated by different parameters including the nature of the metal but also the size and shape of the particle as well as the dielectric properties of the surrounding medium.[155] Chen et al.[156] for instance reported the influence of the shape and size of gold nanoparticles on their optical properties. As it can be seen in Figure 1.37, gold nanorods displayed significant higher LSPR wavelengths compared to gold nanospheres and as the aspect ratio of the nanorods increased, the LSPR peak redshifted.

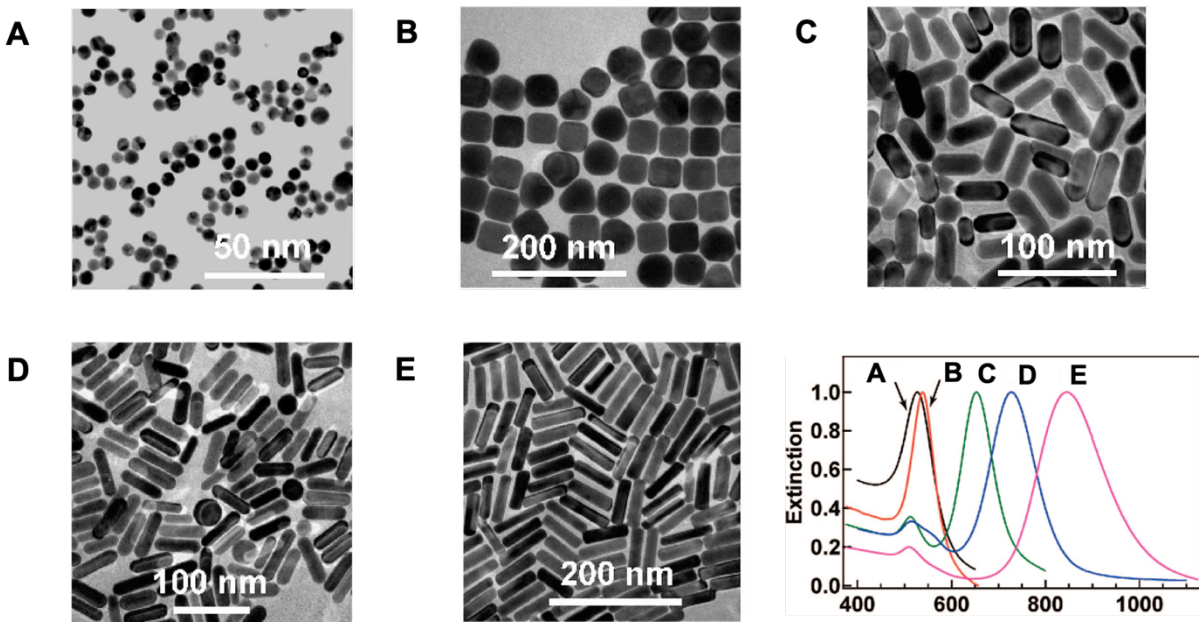

Figure 1.37: (A-E) TEM images and (F) normalized extinction spectra of Au nanoparticles of different shapes and sizes: (A) Nanospheres, (B) nanocubes, (C) nanorods with aspect ratio 2.4, (D) nanorods with aspect ratio 3.4 and (E) nanorods with aspect ratio 4.6.[156]

Interestingly, we can notice that gold nanospheres and nanocubes are displaying a single peak at around 530 nm. This can be explained by the fact that spheres are isotropic particles (same geometry regardless of the direction) displaying a single plasmon absorption mode. On the other hand, anisotropic nanoparticles reveal multiple plasmon absorption bands that are depending on their morphology.[157] For nanorods, two plasmonic modes can be observed with a first band corresponding to the electronic oscillation in the direction of the rod diameter (transverse surface plasmon resonance) and a second band associated to the oscillation of the electrons in the direction of the rod length (longitudinal surface plasmon resonance). Depending on the aspect ratio of rods, the wavelength shift between both peaks can be tuned precisely as illustrated in Figure 1.37(E).

Furthermore, anisotropic nanoparticles absorb light differently depending on the light polarization. For a nanorod, if the light is polarized in the same direction than the nanorod orientation, the longitudinal mode will be excited preferentially. When the light is polarized perpendicular to the nanorod orientation, the transverse mode will be mainly excited. Consequently, the orientation of the nanoparticles plays a significant role on the plasmon resonance of the system. To conclude, it is possible to tailor the

optical properties of anisotropic nanoparticles by playing on their dimension and orientation.
In the next section, we will see why AgNWs are highly interesting candidates to fabricate strain sensors and how they can be prepared.

1.6.6 Preparation of AgNW networks

Among the existing anisotropic metallic nanoparticles, AgNWs networks are very promising candidates due to their remarkable optical and electrical properties[158] that have been exploited in many applications such as in solar cells,[159] touch screens,[160] organic light-emitting diodes[161] or strain sensors.[114] A broad range of fabrication strategies has already been employed to prepare such kind of networks including spray-coating,[162] drop-casting[159] or rod coating.[163] Nevertheless, these techniques often suffer from low reproducibility and do not allow any control over the orientation of the nanowires. This last point is a severe limiting point towards the preparation of high-performance materials with anisotropic physical properties.

In order to align AgNWs in the plane, different methods have already been proposed including Langmuir-Blodgett technique,[128] substrate stretching,[164] capillary printing,[165] heat-assisted dip-coating[166] or the use of an electric field.[167] However, these strategies are limited to the deposition of AgNWs on small areas and/or require the use of complicated and expensive equipment. Moreover, the density as well as the uniformity of AgNW deposits are often limited.
To overcome the drawbacks induced by these preparation strategies, grazing incidence spraying (GIS) was recently developed in our team to efficiently align different 1D-nanoparticles in the plane such as cellulose nanofibrils and silver nanowires.[168] Hu et al.[169] reported the preparation of highly oriented films of AgNWs using this technique and demonstrated the possibility to tune the orientation and density of the nanowires (Figure 1.38).

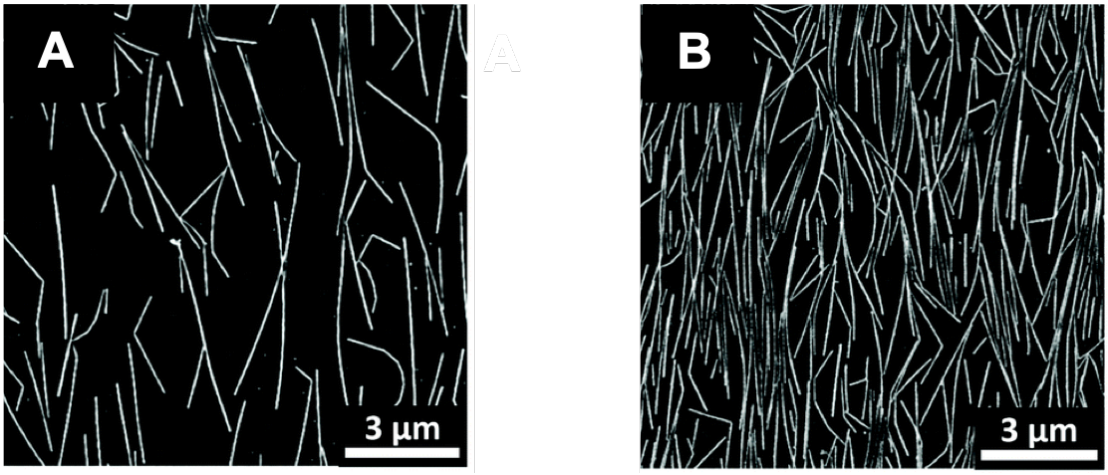

Figure 1.38: SEM images of AgNW monolayers deposited by GIS for (A) 10 s and (B) 50 s.[169]

Moreover, the resulting thin films displayed optical anisotropic properties that were measured by polarized UV-Vis-NIR spectroscopy. Indeed, the use of polarized light enabled the selective excitation of the transverse and longitudinal plasmon resonances of the AgNWs as depicted in Figure 1.39.

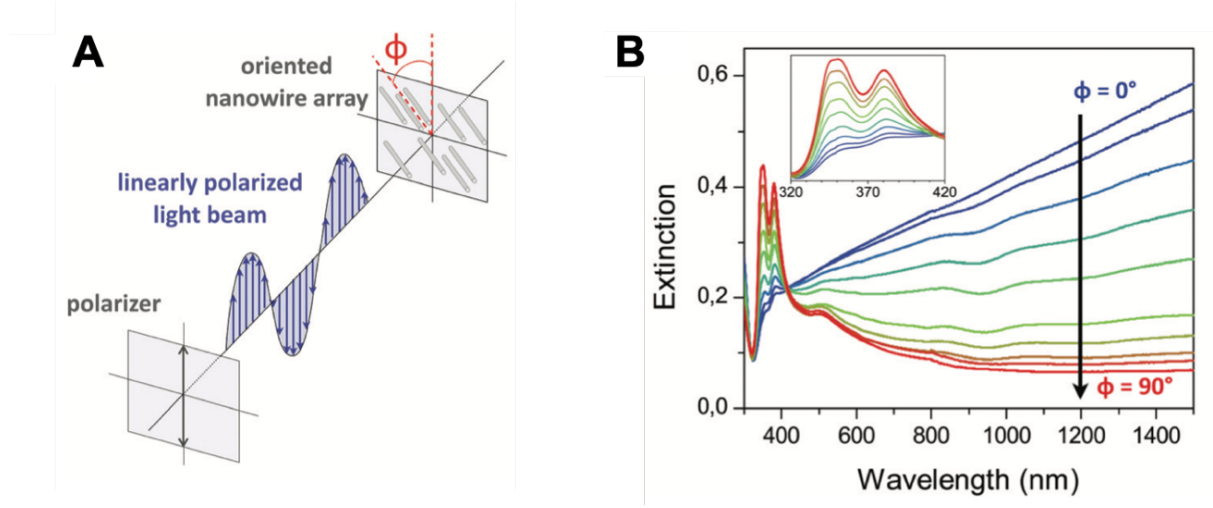

Figure 1.39: (A) Schematic illustration of the polarized UV-Visible-NIR extinction measurements highlighting the angle ϕ between the nanowire orientation direction and the light polarization plane. (B) UV-Visible-NIR extinction spectra of an oriented AgNW monolayer for different polarization angles.[169]

This work demonstrates the use of a fast, simple and inexpensive approach to prepare well aligned monolayers of AgNWs on large areas and displaying anisotropic optical

properties that are currently highly desired especially towards the preparation of multidimensional optical strain sensors.

Chapter 2 – Materials and methods

2.1 Materials and solution preparation

2.1.1 Materials

Chemically modified (sulfuric acid hydrolysis) suspensions of cellulose nanocrystals (CNCs) extracted from tunicate (t-CNCs, 0.4 wt.% in H_2O) and wood (w-CNCs, 6 wt.% in H_2O) and carboxymethylated cellulose nanofibrils (CNFs) as powders were purchased from Cellulose Lab (Fredericton, Canada). A chemically modified (sulfuric acid hydrolysis) t-CNC suspension (0.7 wt.% in H_2O) was also supplied by Bruno Jean from CERMAV (Grenoble, France). Silver nanowires (AgNWs) were purchased from Novarials (Woburn, USA) at a concentration of 10 mg/mL in isopropanol.
Poly(vinyl amine) (PVAm, tradename Lupamin 9095, 20 wt.% in water, $\overline{M_w} \approx$ 340,000 g/mol) was freely provided by BASF (Ludwigshafen, Germany). Poly(ethyleneimine) (PEI, 50 wt.% in water, $\overline{M_w} \approx$ 750,000 g/mol), poly(vinyl alcohol) (PVAl) (tradename Moviol 10-98, PVAl, $\overline{M_w} \approx$ 61,000 g/mol), sodium hydroxide (NaOH) pellets (> 97%) and reference standard buffers (pH 4.00 ± 0.01, 7.00 ± 0.01 and 10.00 ± 0.01) were purchased from Sigma-Aldrich (Lyon, France).
Montmorillonite clays EXM 2039 were provided by Clariant Produkte GmbH (Moosburg, Germany) as a powder.
Octadecyltrichlorosilane (OTS, 95%) was purchased from Acros-Organics. Toluene was obtained from VWR Chemical (Strasbourg, France).
Ultrapure water with a resistivity of 18.2 MΩ was obtained with a Milli-Q Advantage A10 water purification system from Merk-Millipore (Molsheim, France).
A silicon-based elastomer Bluesil RTV 141 A/B was purchased from Elkem Silicones (Saint-Fons, France) and a silicon-based dye (Holcosil) was purchased from Holland Colours Europe B.V (Apeldoorn, The Netherlands).

(100) silicon wafers of a diameter of 200 mm were purchased from WaferNet Inc. (San José, CA, USA) and were cut at the desired size and used as substrates for the preparation of LbL films. 5 cm diameter silicon wafers were used for the fabrication of LbL films by spin-assisted assembly. Quartz slides (25 x 25 x 1 mm) were purchased from Agar Scientific Ltd (Stansted, UK). Poly(dimethylsiloxane) (PDMS) sheets with a

thickness of 0.25 mm were purchased from Specialty Manufacturing Inc. (SMI) (Saginaw, USA) and were cut at the desired size and shape and used as substrates for the preparation of stretchable thin films of AgNWs.

2.1.2 Preparation of polyelectrolyte solutions

PEI and PVAm were diluted in Milli-Q water to obtain solutions at respectively 2.5 g/L and 1 g/L. The pH of the PVAm solution was adjusted by using solutions of NaOH or HCl at a concentration of 0.5 mol/L in Milli-Q water. PVAl was dissolved in Milli-Q water to obtain a solution at 5 g/L. In order to completely dissolve the PVAl, the solution was vigorously stirred and heated at a temperature around 70°C.

2.1.3 Preparation of nanoparticle solutions

Montmorillonite clay EDX 2039 was suspended at a concentration of 10 g/L in Milli-Q water during 2 days under magnetic stirring. The suspension was then centrifuged at 9500 rpm during 1 h. The resulting supernatant was used without any dilution.
The commercial CNC suspensions extracted from wood and tunicate were diluted in Milli-Q water to obtain solutions at 0.4 g/L. The CNFs, received as a powder, were first dispersed in Milli-Q water before being sonicated with a sonic dismembranor model 505 (Fischer Scientific, USA) for 20 min at an amplitude of 30%. The suspension was then centrifuged during 1h at 9500 rpm in a ROTINA 420R centrifuge (Hettich Zentrifugen, Germany). The resulting supernatant was finally filtered on cotton wool and then with 5-micron PVDF syringe filters Millex-SV (Merck, Germany) in order to remove the biggest particles. AgNWs solutions were prepared at a concentration of 0.2 g/L by diluting the commercial solution 50 times in Milli-Q water.

2.2 Sample preparation

2.2.1 Substrate cleaning

The silicon wafers and quartz slides were cleaned in a solution of EtOH/Milli-Q water (volume ratio 1:1) during 10 min in an ultrasound bath before being dried with

compressed air. The surface of the substrates was activated in a Plasma Cleaner PDC-002 (Harrick Plasma, USA) for 3 min at high RF power (~30 W). The PDMS sheets were cut in the desired shape (rectangular or dog bone) with a length of about 3 cm and a width of about 1 cm using a scalpel. To remove any organic contamination or dust particle, the PDMS substrates were dipped 30 s in a pure ethanol solution and then 30 s in a Milli-Q water solution. The substrates were then dried with compressed air prior to use.

2.2.2 Preparation of hydrophobic substrates

After being activated by plasma cleaning, the silicon substrates were immerged in a freshly prepared solution of octadecyltrichlorosilane (OTS) in toluene (volume fraction of 0.1%) during 1 h. They were then rinsed in a toluene solution and then in a solution of ethanol/Milli-Q water (volume ratio 1:1). After drying with compressed air, the substrates were first dipped in a PVAl solution (5 g/L) for 10 min followed by three rinsing steps in Milli-Q water during 2 min each time. This dipping step was repeated for MTM clay EXM 2039 and PEI (2.5 g/L) solutions to obtain the multilayer sequence PVAl/Clay/PEI. The construction of the multilayered cellulose-based films was then carried out starting with the deposition of a cellulose layer (CNCs or CNFs).

2.2.3 Preparation of coloured PDMS substrates

To color PDMS to ascertain the density change during film stretching, a bi-component silicon base elastomer Bluesil RTV 141 A/B was used. The curing was completed by mixing the polymer base with the curing agent (weight ratio of monomer to curing agent of 10:1). Afterwards, few drops of silicone-based dye were added to the PDMS mixture and thoroughly mixed. The red colored PDMS mixture was then slowly poured onto a clean glass Petri dish and degassed in a vacuum desiccator multiple times (3-4 times) to remove the air bubbles from the mixture. Finally, the Petri dish filled up with the colored PDMS mixture was kept in a heating oven at 70 ± 5°C for 4 h. After curing, the PDMS sample was carefully peeled off from the Petri dish and cut in a rectangular shape (3 cm x 1 cm).

2.2.4 Dip-assisted LbL assembly

For all multilayer films built by dipping, the following procedure was completed. After plasma cleaning, the substrate was dipped in a PEI solution for 10 min before being rinsed three times in Milli-Q water for 2 min each. The substrate was then dried with compressed air and the thickness of the film was measured by ellipsometry. The substrate was then successively dipped into a negatively charged suspension of CNCs or CNFs and positively charged PVAm solution for 10 min with the same intermediate rinsing steps. This deposition cycle was repeated until the desired film thickness was obtained. A home-made dipping robot with three motorized arms was used for the preparation of thick multilayer films. A multi-axis controller from ISEL (Houdan, France), a drying station with compressed air and a LabView program were used to control the assembly including the substrate movements, the drying steps and dipping times.

2.2.5 Spin-assisted LbL assembly

A spin coater (Laurell Technology Corporation, North Wales, PA) was used to prepare spin-assisted multilayer films. The substrate was first spun at a defined rotating speed and acceleration. Once this speed was reached, a specific volume (0.3 or 1.2 mL) of the polyelectrolyte/CNC solutions was deposited dropwise at the center of the rotating substrate. 1 mL of Milli-Q water was then added to rinse the surface. The substrate was left rotating until it was dried before depositing the next layer.

2.2.6 Spray-assisted LbL assembly

Orthogonal spray-assisted LbL assembly was completed using AIR-BOY spraying bottles (Carl Roth GmbH, Karlsruhe, Germany). Polyelectrolyte and nanoparticle solutions were poured in the bottles that were then pressurized manually. Each solution was sprayed alternately for 5 s perpendicularly to the receiving surface. An intermediate rinsing step was performed by spraying Milli-Q water during 10 s before a drying step was carried out with compressed air. This deposition process was repeated until the desired film thickness was reached.

Grazing Incidence Spraying (GIS) was performed with a homemade spraying system. The suspensions of CNFs, CNCs and AgNWs were pumped by a liquid handling pump M50 (VICI AG, Schenkon, Switzerland) through fluorinated ethylene-propylene microfluidic tubing until a stainless-steel air atomizing nozzle (Spraying Systems, Glendale Heights, IL, USA) which was supplied with compressed air piloted by gas flow controllers Red-y (Vögtlin Instruments GmbH, Aesch, Switzerland). The substrate was kept in vertical position on a rotating platform thanks to a rubber stopper and pulling vacuum. The spraying direction was pointed downward and the angle of the nozzle with respect to the substrate was fixed at 10°. The software Kynon (Galaad, France) was used to control the x and y positions of the platform and its rotation around the z-axis. The spraying was controlled via a LabView program allowing the control of all parameters including rates of the liquid and air flow and the spraying time. The spraying of polyelectrolyte solutions and Milli-Q water was manually completed using AIR-BOY spraying bottles.

The nanocellulose suspensions were typically sprayed during 60 s with an airflow rate of 40 L/min, a liquid flow rate of 1 mL/min. AgNWs suspensions were sprayed during 50 s with an airflow rate of 30 L/min, a liquid flow rate of 1 mL/min.

2.3 Methods

2.3.1 Ellipsometry

Ellipsometry is a non-destructive optical technique based on the change of the light polarization after reflection on the surface of a sample. The polarization state of an incident light can be decomposed into s- and p-components with the s-component oscillating parallel to the surface and the p-component oscillating perpendicular to it. These components display variations in amplitude and phase upon light reflection on the sample transforming a linearly polarized light into an elliptically polarized light (Figure 2.1). Ellipsometry measures the ratio ρ of amplitude reflection coefficients for p- and s-polarizations that is defined with Equation 2.1.

$$\rho = \frac{r_P}{r_S} = \frac{(E_{rp} \,/\, E_{ip})}{(E_{rs} \,/\, E_{is})} = tan(\psi) \times exp\,(i\,\Delta) \qquad \textbf{Equation 2.1}$$

Where $tan(\psi)$ corresponds to the amplitude change and Δ corresponds to the phase shift upon reflection. Nevertheless, the determination of ψ and Δ is not sufficient to directly extract the optical constants and thickness of the sample. To do so, the construction of a physical model is required including the layer sequence and the optical constants of the individual layers. The measured data are then fitted to the physical model providing the determination of the film thickness and optical constants.

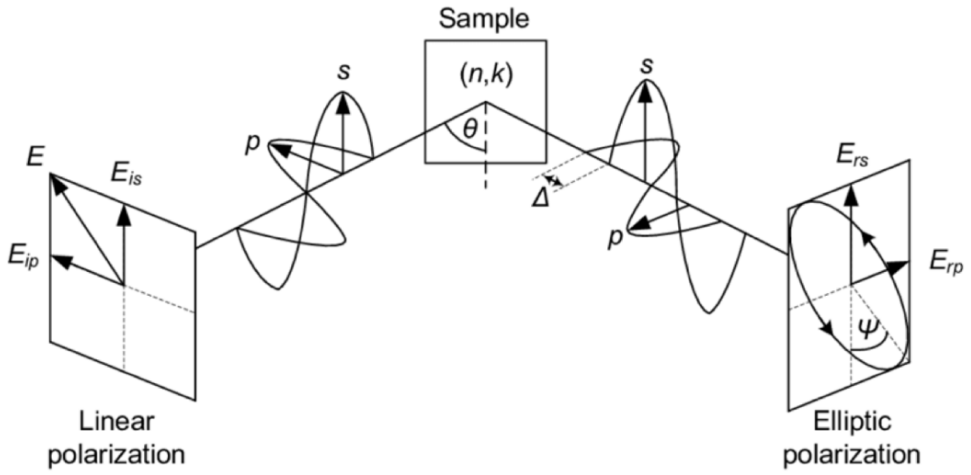

Figure 2.1: Schematic illustration of the principle of ellipsometry with the reflection of a linear polarized light on a sample surface.[170]

For thickness measurements of thin films, a Plasmos SD 2300 ellipsometer was employed at a single wavelength of 632.8 nm and an incident angle of 70°. The thickness of films was determined by taking the average of 10 measurements at random positions on the silicon wafer. The error bars reported in this work correspond to the standard deviation of the measurements. The film thickness values determined by ellipsometry are not absolute values but represented a quick estimation of the film growth and homogeneity. Concerning thicker films, the thickness determination was carried out on a spectroscopic ellipsometer SENpro (SENTECH Instruments GmbH, Germany) operating between 400 and 800 nm and with an angle of incidence of 70°. The determination was completed using a model composed of 3 layers with the deposited cellulose-based multilayer films with a refractive index of 1.559 (Figure 2.2).

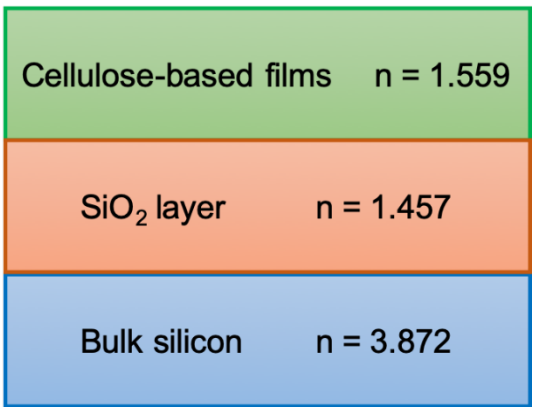

Figure 2.2: Optical model composed of 3 layers used for the thickness measurements of thick films with the spectroscopic ellipsometer.

2.3.2 UV-Visible-NIR spectroscopy

UV-Vis-NIR spectroscopy is a quantitative and non-destructive technique allowing the absorbance measurement of solutions and transparent substrates from the UV to the NIR domain (between 180 and 3300 nm). These measurements were carried out on a Cary 5000 UV-Vis-NIR spectrophotometer (Agilent Technologies, Inc., USA). This spectrophotometer is using a double beam with an incident light being separated into 2 beams: one beam will pass through the sample to characterize whereas the other one will pass through the reference. The detector then collects the light intensity I transmitted through the sample and the light intensity I_0 transmitted through the reference. The absorbance A and the percentage of transmittance $\%T$ can then be expressed as function of light intensities transmitted through the sample and through the reference (Equations 2.2 and 2.3).

$$A = -log_{10}\left(\frac{I}{I_0}\right) \qquad \textbf{Equation 2.2}$$

$$\%T = \left(\frac{I}{I_0}\right) \times 100 \qquad \textbf{Equation 2.3}$$

Films deposited on quartz or glass substrates were fixed on a sample holder with a 5 mm aperture diameter and the baseline was carried out using bare substrates.

For the acquisition of optical properties of oriented AgNW monolayers upon stretching, a home-made stretching device was built with two metallic clamps whose movement was controlled by a single screw providing the same displacement and strain in both directions (Figure 2.3(A)). Each PDMS films coated with oriented AgNWs was fixed at the two jaws of the device. The stretching device was then mounted in the Cary 5000 UV-Visible-NIR spectrophotometer. A spectrum was acquired for each applied strain and a Glan-Taylor polarizer was used for performing UV-Visible-NIR spectroscopy with linearly polarized light (Figure 2.3(B)). In that case, the polarizer was placed in front of the analyzed sample and the angle to the vertical axis was adjusted using a controllable acquisition program.

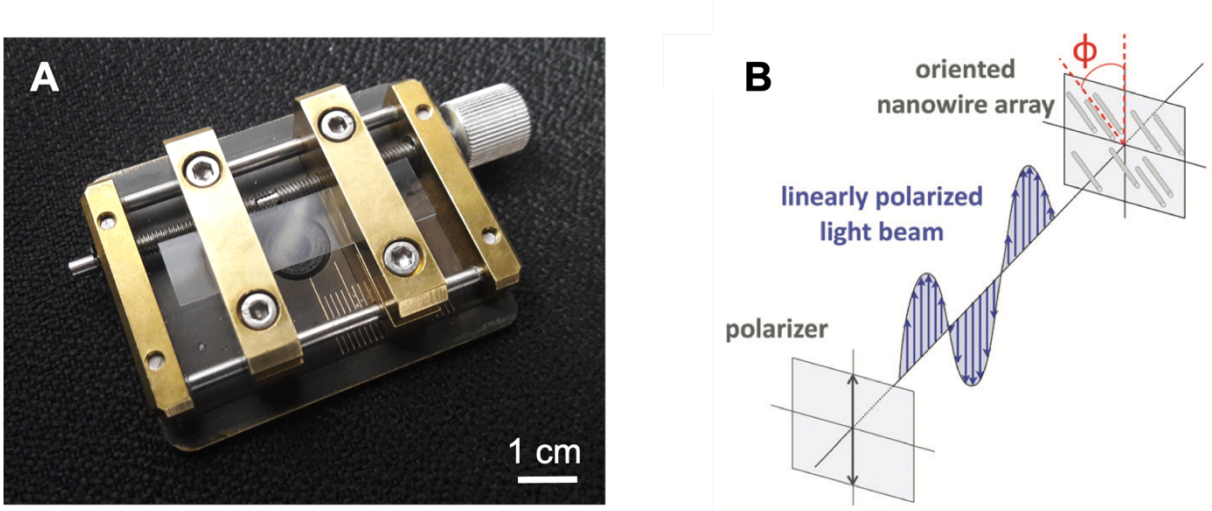

Figure 2.3: (A) Optical photograph of an oriented AgNW monolayer deposited on PDMS and mounted on the home-made stretching device. (B) Schematic representation illustrating the polarized UV-Vis-NIR extinction measurement with an angle ϕ between the light polarization and the nanowire orientation.[169]

2.3.3 Circular Dichroism (CD) spectroscopy

CD spectroscopy is a very useful and powerful technique to analyze the chirality of a sample and is based on the measurement of the difference in absorbance between left and right circularly polarized light (respectively L-CPL and R-CPL).[172] Indeed, the propagation speed of the L-CPL and R-CPL through a chiral sample is different. Consequently, a chiral sample will preferentially absorb one of the directions of the

circularly polarized light compared to the other one leading to an absorbance difference (Equation 2.4).

$$\Delta A = A_{LCPL} - A_{RCPL} \qquad \textbf{Equation 2.4}$$

Where A_{LCPL} and A_{RCPL} correspond respectively to the absorbance of L-CPL and R-CPL. The CD signal reported in spectra is often reported in degrees of ellipticity (θ) that measures the ellipticity of the polarization and can be expressed as function of the absorbance difference (Equation 2.5).

$$[\theta] = \Delta A \times \left(\frac{ln\,10}{4}\right) \times \left(\frac{180}{\pi}\right) \qquad \textbf{Equation 2.5}$$

The circular dichroism spectra of films prepared on quartz slides were recorded on a Jasco J1700 CD spectrophotometer (JASCO, Tokyo, Japan) between 190 and 800 nm at a scan rate of 100 nm/min. The samples were fixed on a sample holder with a 1 mm aperture diameter and the baseline was performed using a bare quartz substrate.

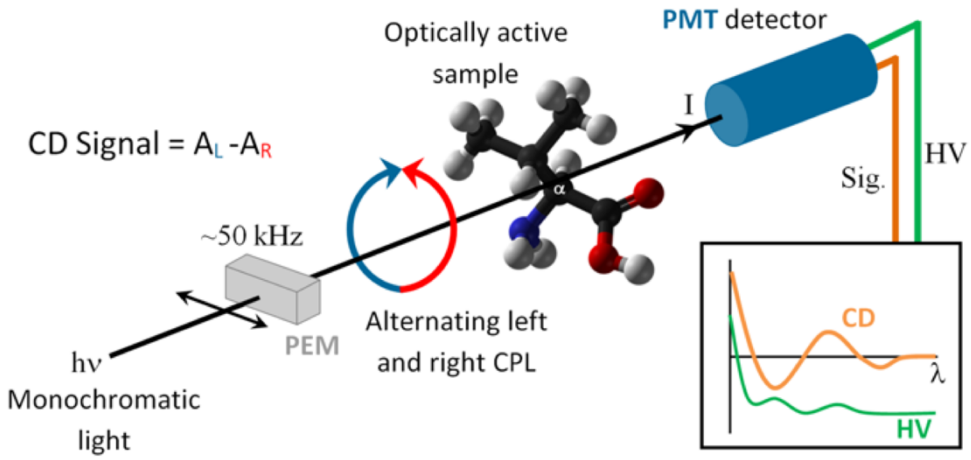

Figure 2.4: Schematic representation illustrating the principle of CD spectroscopy with a Photo Elastic Modulator (PEM) converting linearly polarized light into left and right circularly polarized light alternatively and a Photo Multiplier Tube (PMT) detector probing the absorbance difference.[171]

2.3.4 Zeta potential

Any charged particle in a liquid is surrounded by a liquid layer that can be decomposed into two layers: an inner region with the ions being strongly bound to the particle and an outer diffuse region with less firmly associated ions. The electric potential of this double layer corresponds to the zeta potential. If the particles present a large negative or positive zeta potential, they will tend to repel each other and thus lead to stable suspensions. However, unstable suspensions will be obtained with particles presenting low zeta potential values.
The zeta potential is consequently an important physical property and can be used to optimize the formulations of suspensions, the formation of films and coatings but also to predict the interactions of a given solution with surfaces.

All the zeta potential measurements have been performed on a Zetasizer Nano-ZS device (Malvern Instrument, Ltd., UK) with a scattering angle of 173° and a wavelength of 632.8 nm and at 25°C. For the measurement of the zeta potential of the different solutions, standard disposable cuvettes were first rinsed with Milli-Q water. The solutions were then introduced in the cuvettes and three measurements were completed for each sample.

2.3.5 Atomic Force Microscopy (AFM)

Atomic Force Microscopy (AFM) was discovered by Binnig et al. in 1986 after their studies completed on Scanning Tunnelling Microscopy (STM). AFM is based on the interactions between a tip and the sample surface.[172] A sharp tip, generally composed of silicon, scans the sample surface in a raster pattern with a nanometric precision. The nanoscale tip is attached at the extremity of a cantilever that acts as a small spring (Figure 2.5(A)). In contact mode, when the distance between the tip and the surface decreases, forces applied on the cantilever increases resulting in its bending as illustrated in Figure 2.5(B). On the other hand, as the sample gets further from the tip, forces applied on the cantilever decreases providing the cantilever to relax in order to keep contact with the surface. The cantilever deflection is indicative of interaction forces between the tip and the sample and is detected by the laser reflection

displacement on a photodetector. The displacement of the laser on this detector therefore allows the imaging of the topography of the sample surface.

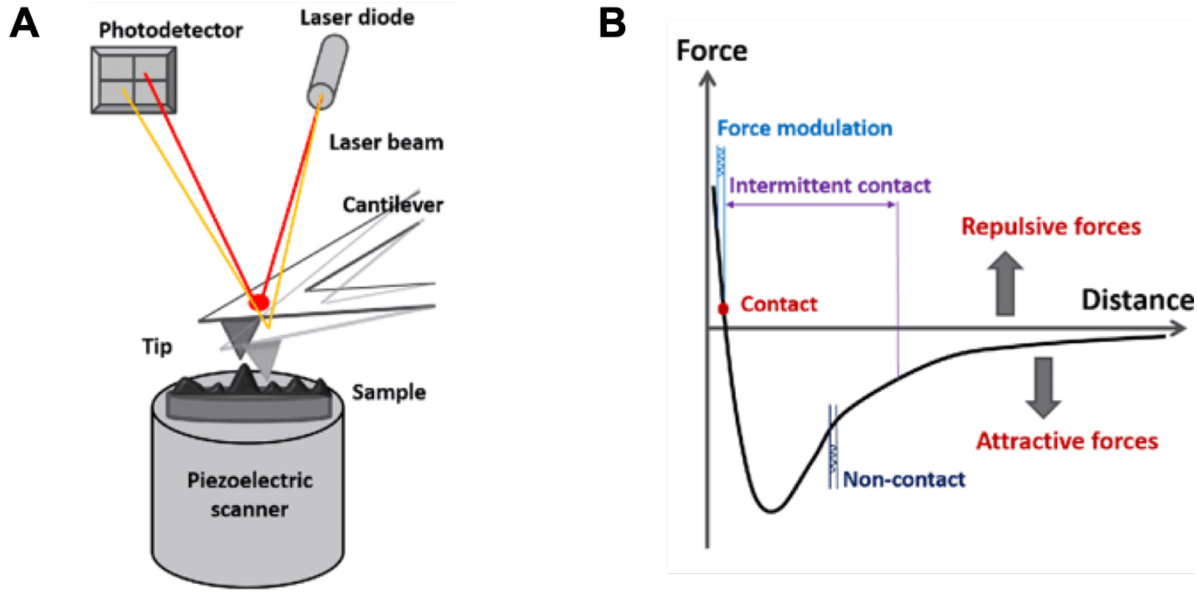

Figure 2.5: (A) Schematic representation of an Atomic Force Microscope and (B) the different interactions acting between the tip and the substrate.[173]

Nevertheless, the application of constant forces on the substrate in contact mode can induce damages on fragile/soft samples. To avoid surface damages, tapping mode was developed in which the cantilever oscillates and interacts with the surface near its resonant frequency (around 200-300 kHz). When the tip interacts with the surface, the oscillation amplitude of the cantilever changes and is used as feedback parameter. Consequently, the variations of the oscillation amplitude measured on the photodetector are indicative of the surface topography. Thanks to the limited contact time between the tip and the surface and the low applied forces, the imaged samples are less prone to damage. However, imaging can still remain challenging, as the operator has to tune the cantilever before imaging and should also adjust the feedback gains during imaging.

To overcome these limitations, Peak Force Tapping Mode was developed in the 2010s.[173] The tip-sample interactions are modulated by a sinusoidal motion at a frequency around 2 kHz, far away from the resonant frequency. In that case, the peak

force between the tip and the sample is maintained constant and force curves can be obtained for every pixel of the picture.

AFM images during this work were obtained in Peak Force Tapping mode on a Bruker AFM Dimension Icon (Bruker, USA) with a Nanoscope V controller. The AFM cantilevers present a nominal resonant frequency of 70 kHz, a nominal spring constant of 0.4 N/m. Height and phase images were recorded simultaneously using a scan rate of 1.0 Hz and a resolution of 512 × 512 pixels. For the morphological characterization of CNCs and CNFs, 0.1 mL of diluted suspensions were deposited on PEI-coated silicon wafers, washed and dried to air. The samples were then fixed on a metallic support using super glue (Loctite Super Glue-3).

2.3.6 Scanning Electron Microscopy (SEM)

Scanning Electron Microscopy (SEM) consists in the scanning of the surface of a sample with a focused electron beam with a resolution at the nanometer scale.[174] Electrons are first generated at the top of the column (electron gun), they are then accelerated and passed through diverse lenses in order to produce a focused electron beam (Figure 2.6(A)). When the focused electron beam interacts with the surface of the sample, different types of electrons are emitted namely backscattered (BSE) and secondary electrons (SE) and provide information about the topography and composition of the sample (Figure 2.6(B)).

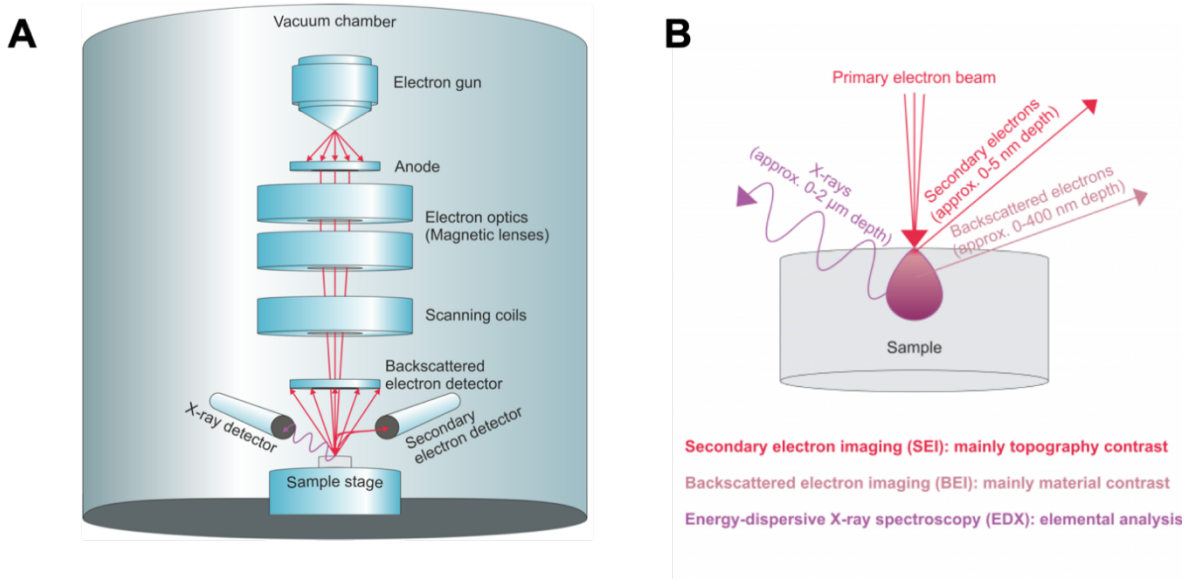

Figure 2.6: (A) Schematic illustration of a scanning electron microscope and (B) the different types of electrons emitted after interactions between the sample surface and the primary electron beam providing various information about the sample.[174]

The main detector is employed to collect the low-energy secondary electrons (SE) arising from inelastic interactions between incident electrons and the surface of the sample. As these electrons are coming from the surface of the sample, they provide information about the topography of the surface. The second type of electrons that can be detected are known as backscattered electrons (BSE) resulting from elastic interactions between the primary electrons and the specimen. Atoms presenting a high atomic number have an important positive net charge on their nucleus and consequently generate more BSE. These electrons are thus highly sensitive to the atomic number of the surface and provide information about the sample composition.

During this doctoral thesis, a Scanning Electron Microscope SU8010 (Hitachi, Japan) has been used with a detector collecting the secondary electrons (SE) at an accelerating voltage of 1.0 kV for the samples prepared on silicon wafers. The sample was glued horizontally thanks to conductive carbon adhesive tape (Agar Scientific, UK) in order to image the top of the sample surface. To determine the film thickness, the imaging of the cross-section of multilayer films was required. The film was fractured mechanically and then glued vertically on a cross-section holder using carbon cement.

For the characterization of AgNW monolayers prepared on PDMS substrates, a NEON 40 FIB-SEM workstation (Carl Zeiss Microscopy GmbH, Oberkochen, Germany) was used under an accelerating voltage of 3.0 kV. All the micrographs were captured in SE2 mode. A constant clamping torque value of 4.5 cN.m was applied to avoid torsion upon stretching. The fabricated sample with a length of 3 cm and a width of 1 cm was stretched in-situ (Figure 2.7) using an integrated stretching device at a constant speed of 1 mm/min from 0% to 40% of its length, with an intermediate step of 10%.

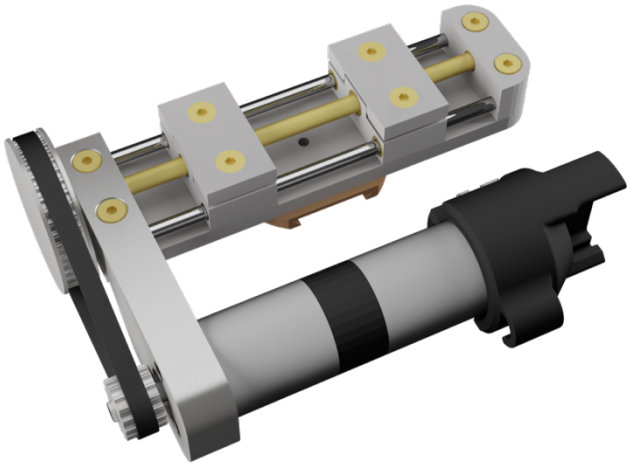

Figure 2.7: Optical photograph of the stretching device that was used to stretch the AgNW monolayers deposited on PDMS in the SEM workstation.

2.3.7 Polarized light microscopy

Polarizing microscopy is a commonly used technique to evaluate the optical anisotropy of a material. A polarized light microscope is composed of a first polarizer before the sample and a second polarizer (analyser) located after the sample (Figure 2.8). The first polarizer allows the passage of the incident light in a single direction while the second one will select the transmitted light in a single direction.

Anisotropic materials display optical properties that vary with the orientation of the incident light and possess refractive indices depending on the propagation direction of light. Birefringent materials will divide the incident light into two orthogonal wave components with different velocities. These velocities depend on the propagation direction of the light through the material. Consequently, these components will emerge from the material with a retardation and combine with either constructive or

destructive interferences. Depending on the angle of in-plane rotation, the intensity of transmitted light will change and reach a maximum or a minimum value. The light intensity that is transmitted through the sample depends on the angle of rotation. On the other hand, the incident light will propagate at the same speed through isotropic samples as they present a single refractive index thus inducing no change in the light intensity.

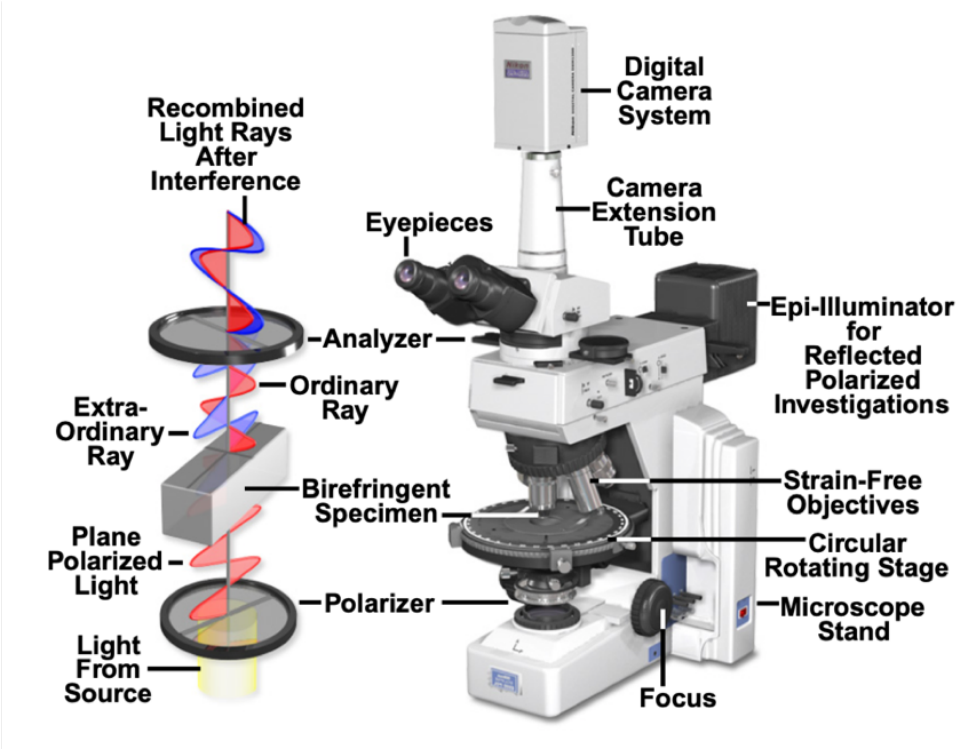

Figure 2.8: Optical photograph of a polarized light microscope and a schematic illustration of a polarized light arriving on a birefringent specimen.[175]

In the present work, a Leica DM-RX microscope was employed to ascertain the anisotropy of the prepared multi-layered films. The polarizer and the analyser were oriented perpendicular to each other. The micrographs were acquired at every 45° of in-plane rotation using an objective with 40× magnification and a CMOS camera TrueChrome AF (Tucsen Photonics, China). The images were taken using the same camera settings for all samples. The grey intensities of the different micrographs were measured using the ImageJ (National Institute of Health, USA) software to evaluate the relative brightness of every sample as function of the in-plane rotation.

2.3.8 Orientation analysis

The alignment of AgNWs, CNFs and CNCs was determined by the analysis of SEM and AFM images obtained on monolayers. The degree of orientation of the deposited nanoparticles was quantified using the plug-in OrientationJ[176] (Biomedical Imaging Group, EPFL, Switzerland) developed for ImageJ.[177] Based on the analysis of the structure tensor in the local neighbourhood of every pixel of the image, it allows the visualization of the main direction of orientation (main color) and the degree of orientation (color intensity) of the images.

The distribution of the angle θ between each nanoparticle main axis and the main orientation of the sample can be extracted. A 2D nematic order parameter (S_{2D}) can then be calculated from this angular distribution using Equation 2.6.

$$S_{2D} = \langle 2\ \cos^2(\theta) - 1 \rangle \qquad \textbf{Equation 2.6}$$

With the chevrons denoting the weighted average over the distribution of θ. S_{2D} is comprised between 0 and 1 with 0 corresponding to a random distribution (isotropic films) with all angles being equally represented and 1 corresponding to perfectly aligned nanoparticles (anisotropic films).

The degree of alignment of CNFs and CNCs was determined using AFM images. These images were first flattened and then analysed using OrientationJ and several parameters were adjusted. AgNWs were imaged by SEM and the surface coverage of the deposited layers and the nanowire alignment were determined after thresholding the greyscale images in ImageJ. In this work, a Gaussian window of 1 pixel was set because it corresponds to the diameter of the smallest nanoparticles. Pixels with coherency and energy values below 1% were not included in the analysis calculation as they are often isotropic pixels. The distribution of the nanofibril and nanowire orientation was centered to 0 in order to calculate the order parameter.

2.3.9 Nanoindentation

Nanoindentation is a method to characterize the mechanical properties of a material by driving a hard indenter tip on the sample surface. This method was first proposed

by Oliver et al.[178] in 1992 and was then intensively used to determine the elastic modulus and hardness of materials. During a nanoindentation measurement, the load is provided by a tip on the sample surface that induces an elastic deformation. As the applied load increases with the progressive penetration of the tip, a plastic deformation occurs and leads to a residual indentation on the surface of the sample (Figure 2.9(A)). Typical load-displacement curves during a nanoindentation measurement can be seen in Figure 2.9(B) with one portion corresponding to the loading and the other one to the unloading of the tip.

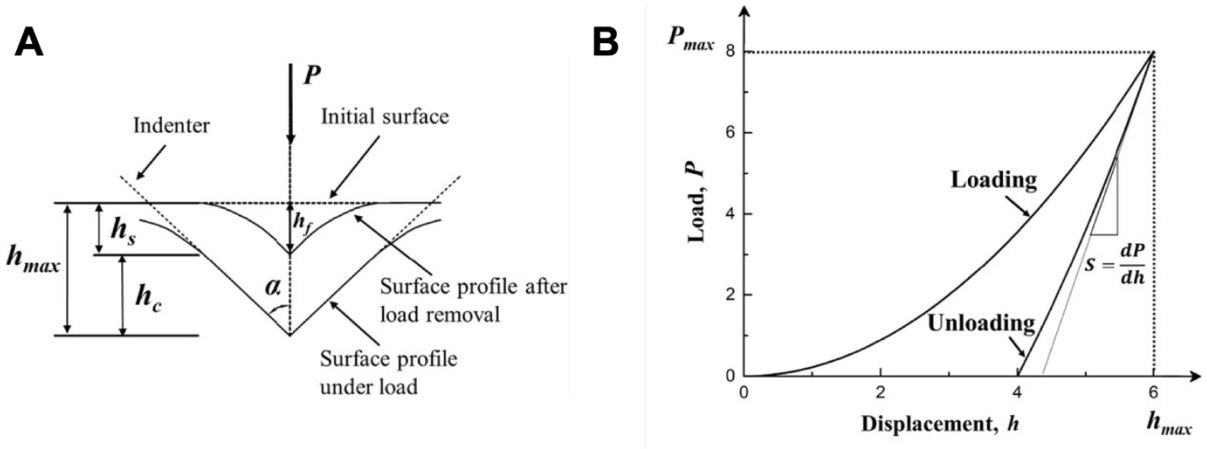

Figure 2.9: (A) Schematic diagram of the parameters during a nanoindentation measurement with h_s the displacement of the surface, h_c he maximum contact depth and h_f the depth after unloading and (B) a typical load-displacement curve.[179]

These curves are particularly useful to extract the mechanical properties of the material. The hardness H and equivalent modulus E_r of the material can be expressed by Equations 2.7 and 2.8.

$$H = \frac{P_{max}}{A} \qquad \textbf{Equation 2.7}$$

$$E_r = \frac{S\sqrt{\pi}}{2\sqrt{A}} \qquad \textbf{Equation 2.8}$$

Where P_{max} corresponds to the maximum applied load, A to the projected area of contact under load and S to the contact stiffness.

An important point in this model is the possibility to determine the projected area of contact (A) as function of the contact depth (h_C) in case of a perfect Berkovich tip (Equation 2.9).

$$A = 24.5\ h_C \qquad \textbf{Equation 2.9}$$

Knowing the maximum applied load P_{max} and the contact area A, the hardness H of the material can be determined using Equation 2.7.
The contact stiffness can be calculated from the slope of the unloading curve presented in Figure 2.9(B) using Equation 2.10.

$$S = \frac{dP}{dh} \qquad \textbf{Equation 2.10}$$

The equivalent modulus E_r of the material can then be calculated using Equation 4. The elastic modulus of the tested material (E) can finally be calculated (Equation 2.11).

$$\frac{1}{E_r} = \frac{1-\vartheta^2}{E} + \frac{1-\vartheta_i^2}{E_i} \qquad \textbf{Equation 2.11}$$

Where E_i and ϑ_i are respectively the elastic modulus and Poisson's ratio of the tip material.

Usually, the influence of the substrate is supposed to be negligible for penetration depths that are smaller than 10% of the film thickness.[180] In this work, thick cellulose-based multilayer films (minimum thickness of 3 μm) were measured using an Ultra Nano Hardness Tester (UNHT-Anton Paar Instruments) with a Berkovich pyramidal tip having three faces to determine the elastic modulus values. Each sample was loaded with a force increasing linearly until the maximum penetration depth (10% of the film thickness) was reached. This force was held during 30 seconds and then released. An average elastic modulus of each film was determined after the measurement of 10 points.

2.3.10 Dynamical mechanical analysis (DMA)

DMA is a useful technique to measure mechanical and viscoelastic properties of a broad range of materials.[181] Compared to traditional tensile tests focusing only on the elastic component of a material, DMA allows the determination of the viscoelastic properties. During a DMA measurement, the sample is typically subjected to a sinusoidal stress (or strain) and the resultant sinusoidal strain (or stress) is measured. For a purely elastic material subjected to a tensile deformation, the stress σ and strain ε can be related by the elastic or Young's modulus E using the Hooke's law (Equation 2.12).

$$\sigma = E \times \varepsilon \qquad \textbf{Equation 2.12}$$

On the other hand, for a purely viscous material with a viscosity η, Newton's law can be used to describe its response to an applied stress (Equation 2.13).

$$\sigma = \eta \times \frac{d\varepsilon}{dt} \qquad \textbf{Equation 2.13}$$

For a viscoelastic material, an oscillating stress σ is generally applied to a sample at a specific frequency ω and can be expressed as function of time (Equation 2.14).

$$\sigma(t) = \sigma_0 \times sin(\omega t) \qquad \textbf{Equation 2.14}$$

The resulting response of a viscoelastic material presents a phase difference δ because it dissipates part of the energy upon stretching (Figure 2.10(A)) and can be expressed using Equation 2.15.

$$\varepsilon(t) = \varepsilon_0 \times sin(\omega t + \delta) \qquad \textbf{Equation 2.15}$$

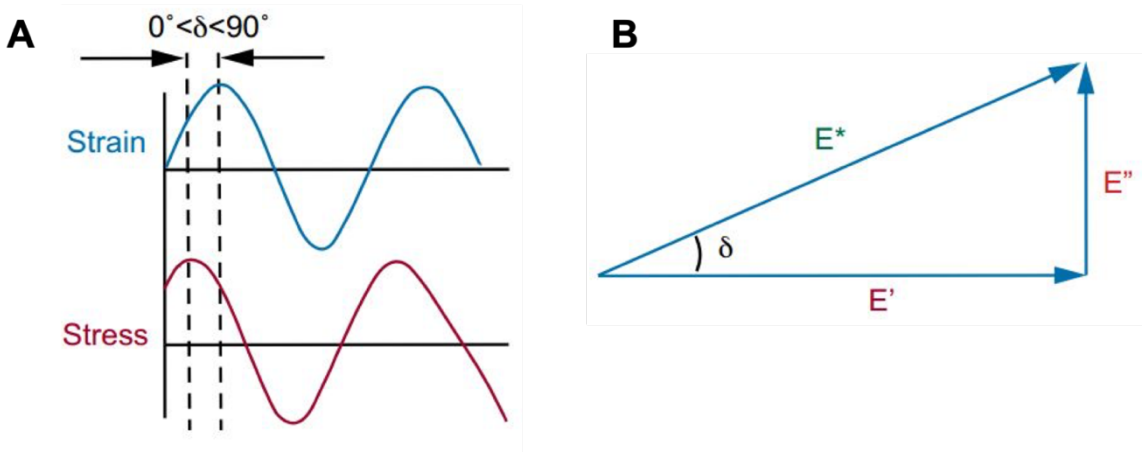

Figure 2.10: (A) Curves of the sinusoidal strain and stress of a viscoelastic material exhibiting a phase angle δ comprised between 0 and 90°. (B) Schematic illustration of the phase angle, the storage, loss and complex moduli for a viscoelastic material.[182]

A viscoelastic material displays mechanical properties that are comprised between the ones of a purely elastic material and the ones of a purely viscous material. Therefore, the response of a viscoelastic material presents an elastic and a viscous component. The storage modulus measuring the energy stored by the sample and the loss modulus corresponding to the energy dissipated by the sample can be related (Equation 2.16).

$$E^* = E' + iE'' = \sqrt{(E')^2 + (E'')^2} \qquad \textbf{Equation 2.16}$$

The phase difference corresponding to the sample damping can be expressed as function of the storage and loss moduli (Equation 2.17) as it is illustrated in Figure 2.10(B).

$$tan(\delta) = \frac{E''}{E'} \qquad \textbf{Equation 2.17}$$

The phase angle measured between the stress and the strain gives information about the viscoelasticity of the material. For instance, a small phase angle indicates that the material is very elastic whereas a highly viscous material displays an important phase angle. During a DMA experiment, the storage modulus E' and the sample damping $tan(\delta)$ are usually measured. The complex modulus measured by DMA

represents the stiffness of the material and combines the elastic and viscous components.

After the preparation of thick multilayer films, the characterization of the mechanical properties by DMA measurements was completed. To do so, LbL films were cut from silicon wafers in stripes with dimensions of approximately 15 mm in length and 5 mm in width using a scalpel blade. Stripes were then detached from each substrate using a piece of tape. After their detachment, they were attached at the two jaws of the DMA instrument using a paper support (Figure 2.11(A)). Thick freestanding films were tested by Dynamical Mechanical Analysis (DMA 1 Star System, Mettler Toledo), with a sinusoidal strain at a frequency of 1 Hz (amplitude varied from 0.5 to 50 μm by 20 increments), using a pre-load ranging from 0.4 to 3 N to adjust the film straight between the clamps, under a constant relative humidity (RH) value between 40 and 50% and at room temperature (22°C).

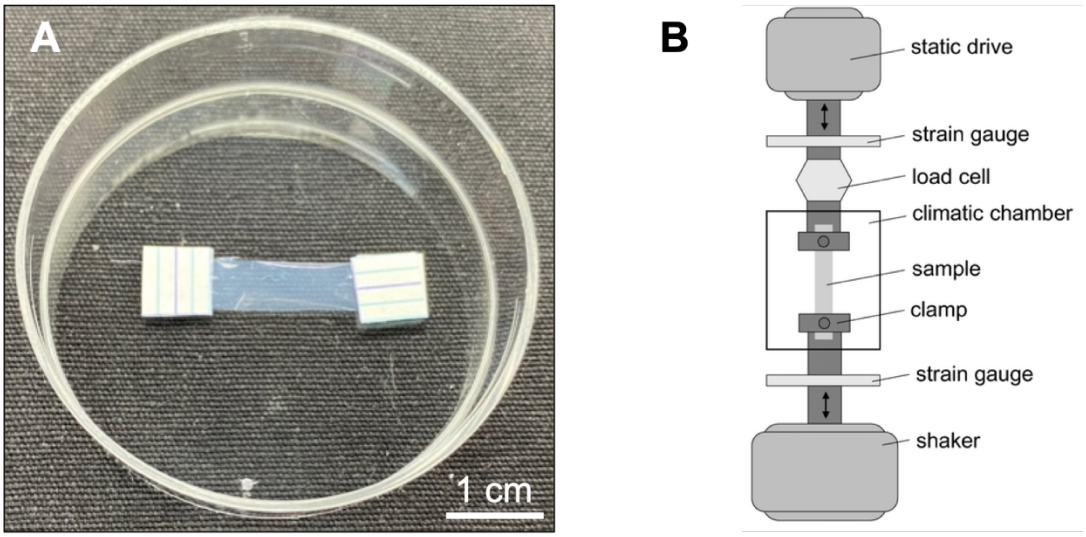

Figure 2.11: (A) Optical photograph of a micron thick film attached on a paper support. (B) Schematic illustration of the DMA.[182]

Chapter 3 – Cellulose-based multilayer films

As indicated in chapter 1, the composition of cell walls of plants including wood consists of cellulose fibrils embedded in a polymer matrix. The hierarchical organization of these anisotropic building blocks is a key point to explain the remarkable mechanical properties of wood.[3] Taking inspiration from the precise arrangement of cellulose units in wood at the nanoscale level, we prepared bio-based cellulose nanocomposite films with various compositions and architectures using layer-by-layer (LbL) assembly[10] and grazing incidence spraying (GIS).[11] In this chapter, we first investigated the fabrication of isotropic multi-layered films employing different types of cellulose nanoparticles, namely cellulose nanofibrils (CNFs) and cellulose nanocrystals (CNCs) from different sources (wood and tunicate). Anisotropic CNC-based films were then prepared by orienting CNCs using spin-assisted assembly. As this method does not allow varying the alignment direction of the anisotropic constituents in each individual layer, we combined LbL assembly with GIS to design more complex structures including the helical architecture found in the secondary layers of wood cell walls. The optical and mechanical properties of the obtained films were finally characterized as function of the film composition and structure and preparation conditions.

3.1 Morphological characterization

Prior to the preparation of multi-layered films, dimensions and charge of different types of cellulose nanoparticles, namely cellulose nanofibrils (CNFs), cellulose nanocrystals extracted from tunicate (t-CNCs) and from wood (w-CNCs), have first been determined. These cellulose nanofibers and nanocrystals were characterized by AFM on sub-monolayers deposited on PEI-precoated silicon wafers (Figure 3.1). The diameter of the CNFs and CNCs was determined by measuring their height and length using the Nanoscope Analysis software because of the tip-sample broadening. The average dimensions were obtained from analysing a series of AFM images like the ones shown in Figure 3.1(A), 3.1(B) and 3.1(C).

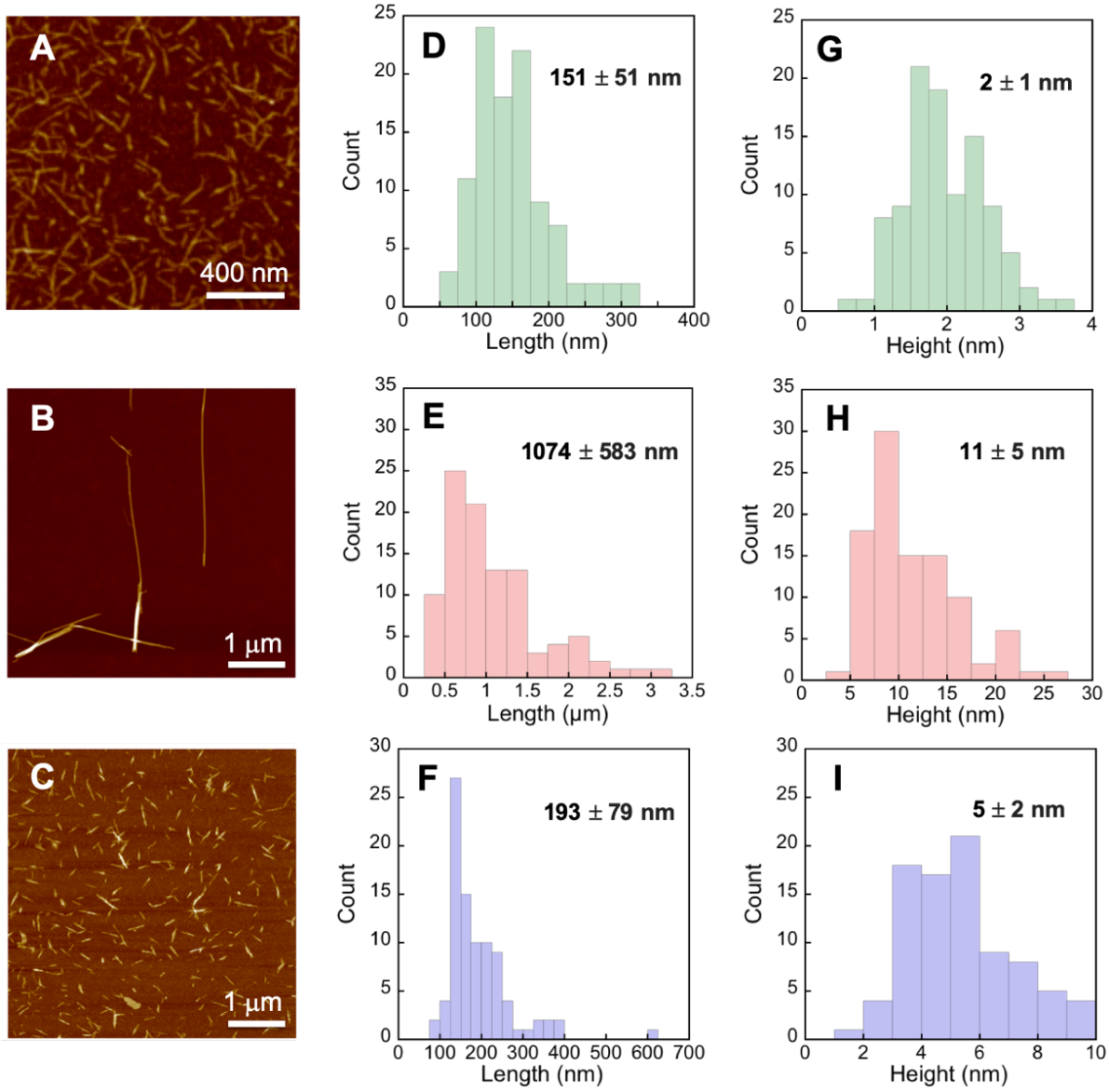

Figure 3.1: AFM images of (A) CNFs, (B) t-CNCs and (C) w-CNCs with the respective length (D, E, F) and height distributions (G, H, I).

The measurement of individual CNFs on AFM images revealed an average length of 151 ± 51 nm and an average height of 2 ± 1 nm (Figure 3.1(D) and 3.1(G)) resulting in an aspect ratio of about 75. These dimensions are lower than the ones reported in the literature but can be explained by the influence of the nanocellulose source and preparation protocol on the size of CNFs.[184] It was indeed impossible to see individual CNFs in the raw material which was organized in a very dense fibre network. Concerning cellulose nanocrystals, long CNCs extracted from tunicates with an aspect ratio of about 100 and short CNCs originating from wood pulp with an aspect ratio of about 40 could be observed on AFM images. Dimensions and aspect ratio values of

these cellulose nanocrystals were in good agreement with the ones reported in the literature.[85,88] The size and crystallinity of these CNCs are crucial factors when considering the preparation of reinforced nanocomposite materials.[184] In that perspective, using two types of CNCs with different sizes and crystallinity values is particularly interesting to target various mechanical properties.

The selected cellulose nanoparticles display various functional groups generated by chemical post-treatments during their production. CNFs bear negatively charged carboxymethylated groups ($-OCH_2COO^-$, pKa ~ 4.5) while t-CNCs and w-CNCs exhibit negatively charged sulfate ester groups ($-OSO_3^-$, pKa < 0) arising from the hydrolysis of hydroxyl groups with sulfuric acid. Zeta potential measurements were completed at 25°C to evaluate the surface charges of the different cellulose nanoparticles. Zeta potential values of -51 ± 5 mV, -53 ± 4 mV and -32 ± 3 mV were determined respectively for CNF, t-CNC and w-CNC suspensions at pH ~ 7. The obtained zeta potential values confirmed that all cellulose nanoparticles were highly negatively charged at pH ~ 7.

As the cellulose nanoparticles have been characterized, the fabrication of isotropic nanocellulose-based films will now be discussed.

3.2 Isotropic nanocellulose-based multilayer films

3.2.1 CNF-based films

Previous work in our team already showed the preparation of isotropic multilayer films by dip-assisted LbL assembly associating CNFs and poly(vinylamine) (PVAm), a polyelectrolyte known to improve the mechanical properties of cellulose-based materials.[185] The use of these flexible and long nanofibrils (aspect ratio ~260)[112] allowed the formation of strong films with a Young's modulus around 13 GPa at a relative humidity (RH) around 50% but the film strength was strongly dependent on the pH of the polyelectrolyte solution. As these long CNFs were not anymore commercially available we had to find new CNFs to continue our investigations. We will now study the preparation of similar films but with shorter nanofibrils characterized in Figure 3.1(A) and investigate their mechanical properties.

3.2.1.1 Influence of the pH

We first investigated the influence of the pH of the selected polyelectrolyte solution on the film build-up. As PVAm is a weak polyelectrolyte with a pKa ~10,[186] its ionization degree can be changed by tuning the pH of the solution.[187] That's why we prepared multi-layered $(CNF/PVAm)_n$ films from PVAm solutions prepared at two different pH values (pH = 8 and pH = 10). The film build-up was monitored by ellipsometry reporting the film thickness as function of the number of deposited layer pairs (Figure 3.2(A)).

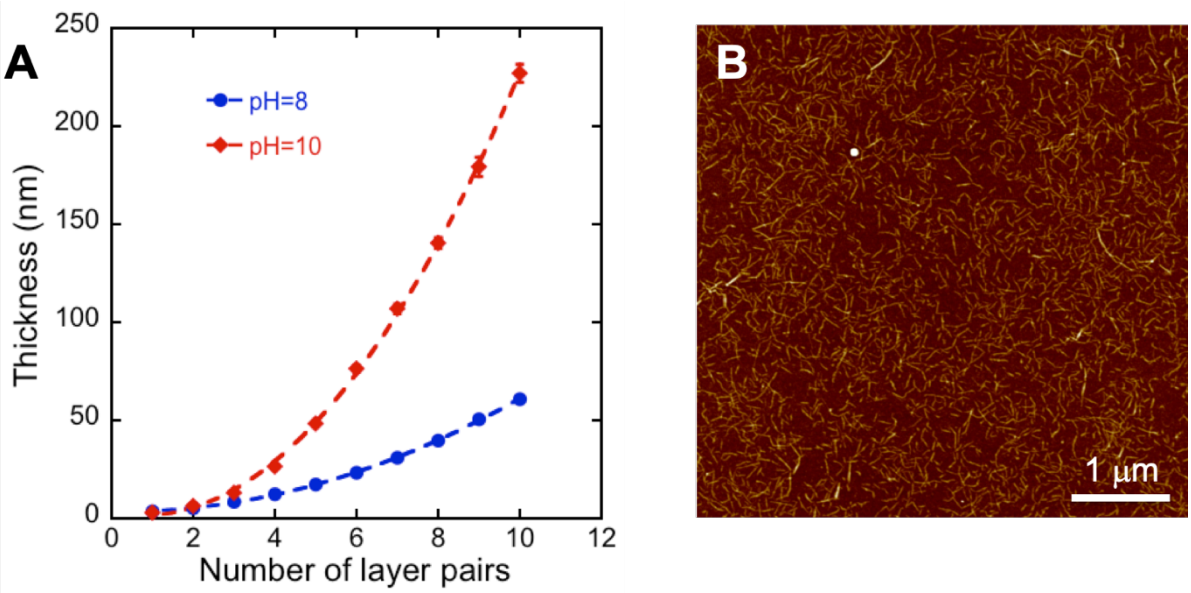

Figure 3.2: (A) Dip-assisted LbL assembly of CNF-based films as function of the pH of the PVAm solution monitored by ellipsometry. Dotted lines are only guides for the eye. (B) AFM height image of a CNF-monolayer deposited on a PEI-coated silicon wafer by dipping for 10 min.

The ellipsometry measurements revealed a significant film growth difference for films prepared with PVAm at pH = 8 and at pH = 10. Indeed, after the deposition of 10-layer pairs, the film thickness passed from 61 ± 2 nm at pH = 8 to 227 ± 5 nm at pH = 10. Meanwhile, the growth regime of the film changed from nearly linear at pH = 8 to super-linear at pH = 10. This behaviour was already reported in our team before for long CNFs.[178] This difference of growth regime was attributed to a charge decrease of the PVAm chains as the pH increased.[178] Consequently, the number of deposited PVAm molecules increases to compensate the negative charges of the cellulose nanofibrils resulting in a higher thickness increment. The use of a weak polyelectrolyte allowed the precisely tailoring of the film growth by changing the pH of the solution. AFM

imaging finally revealed a continuous random distribution of the fibrils after their deposition by dipping for 10 min on a PEI-coated silicon substrate arising from the random diffusion of the nanoparticles in solution (Figure 3.2(B)).

The build-up of isotropic films composed on CNFs was proved by ellipsometry and the nanofibrils were imaged. The preparation of thick CNF-based multi-layered films will now be discussed.

3.2.1.2 Preparation of thick films

The measurement of mechanical properties of supported films by tensile tests is a difficult task. It requires the preparation of self-supported micron-thick films as the resistance of the support masks the properties of the film that was deposited on it. It is also necessary to produce defect-free samples to limit the premature rupture of the film upon loading. Previous studies in the team showed that the use of hydrophobic substrates modified with a (PVAl/Clay) layer pair allows the build-up and detachment of micron-thick $(PVAm/CNF)_n$ multilayers.[177] We used the same procedure and prepared (PVAl/Clay)/$(PVAm/CNF)_{70}$ films on an octadecyltrichlorosilane coated silicon wafer (Figure 3.3(A)).

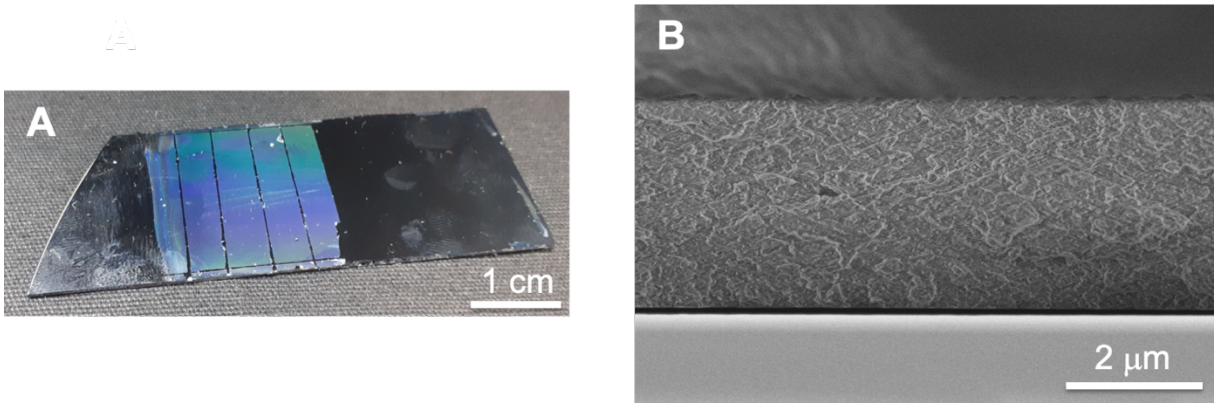

Figure 3.3: (A) Optical photograph of a thick $(PVAm/CNF)_{70}$ film built with PVAm at pH = 8 on an OTS/PVAl/Clay coated silicon wafer and (B) SEM cross-sectional image of the corresponding film after argon beam milling.

These films displayed green and blue colors arising from interferences observed for thin films with a uniform thickness. The film thickness was first estimated by spectroscopic ellipsometry providing a value of 3.2 ± 0.1 µm by setting the refractive

index of the multilayer film at 1.559. To confirm this thickness, the edge of one sample was imaged by SEM (Figure 3.3(B)) after argon beam milling and resulted in a thickness of 3.3 ± 0.1 μm which is in good agreement with the one measured by ellipsometry. Note that due to the heat produced during argon beam milling, morphology of soft objects may show considerable artefacts. The films built with PVAm solutions at pH = 8 were smooth, thick and transparent. The freestanding films could then be detached from substrates and attached in sample holders before conducting dynamic mechanical analysis (DMA) measurements. To speed up the film growth, a PVAm solution at pH = 10 was used but lead to the formation of opaque films after the deposition of around 10-layer pairs.

We demonstrated the preparation of transparent, smooth, thick and freestanding films composed of randomly distributed cellulose nanofibrils using LbL assembly. Beside cellulose nanofibrils, cellulose nanocrystals have recently attracted increasing interest due to their remarkable mechanical properties.[179] Moreover, a possible enhancement of the mechanical properties of cellulose-based materials using long and highly crystalline cellulose nanoparticles was suggested by Kan et al.[175] In that perspective, the next section will provide a study on the LbL assembly of isotropic CNC-based films especially with t-CNCs possessing the highest crystallinity and the highest aspect ratio of CNC sources.[179]

3.2.2 CNC-based films

As presented in chapter 1, CNCs display high stiffness and tensile strength[188] making them interesting building blocks towards the preparation of reinforced polymer nanocomposites.[189,190] A broad range of polyelectrolytes has been reported in association with CNCs using dip-assisted LbL assembly.[191] Nevertheless, no study has yet been reported on the combination of CNCs with PVAm to prepare thick freestanding films. In this part, we will employ two types of CNCs namely t-CNCs and w-CNCs extracted respectively from tunicate and wood pulp and investigate their assembly with PVAm. The microstructure of these films will then be studied and compared before preparing thick films to evaluate their mechanical properties.

3.2.2.1 Influence of the pH and the CNC source

We investigated the influence of the charge density of the PVAm solution on the build-up of isotropic films composed of CNCs extracted from wood (w-CNCs) and tunicates (t-CNCs). As for the preparation of CNF-based films discussed previously, $(CNC/PVAm)_n$ films were built by dip-assisted LbL assembly with PVAm at pH = 8 or pH = 10 and the growth of the multilayer films was monitored by ellipsometry (Figure 3.4(A) and 3.4(B)). Data presented in Figure 3.4 were obtained for a nanocellulose concentration of 0.4 g/L, a dipping time of 10 min and at room temperature. pH and nanocellulose source are the parameters that were varied on purpose and other conditions were kept fixed intentionally.

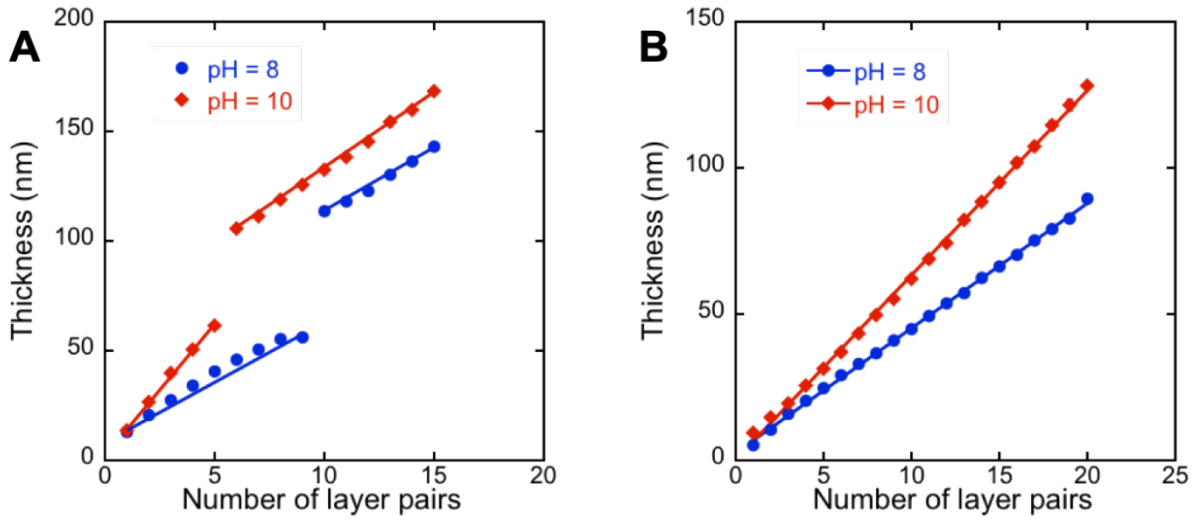

Figure 3.4: Variation of the thickness for CNC-based films prepared by dipping with t-CNCs (A) and w-CNCs (B) at the same concentration (0.4 g/L) as function of the pH of the PVAm solution monitored by ellipsometry. The sharp changes in thickness after the deposition of 5- and 9-layer pairs are discussed in the text.

For both types of CNCs, the build-up speed of the films increased when the pH was raised. However, a significant difference could be pointed out when comparing both systems. Indeed, the growth regime of films composed of w-CNCs was linear independently from the charge density of the PVAm solution with thickness increments of 4.3 and 6.3 nm/layer pair for films assembled at pH = 8 and pH = 10 respectively (Figure 3.4(B)). On the other hand, $(t\text{-}CNC/PVAm)_n$ multilayers displayed first a linear growth but a sudden thickness jump was observed for a thickness comprised between 50 and 60 nm (Figure 3.4(A)). Before the jump, especially at pH = 8, the film thickness

reached a plateau. Please note that this thickness jump appeared earlier and the plateau prior to the jump was less visible when the pH of the PVAm solution increased from 8 to 10. A similar behaviour was observed with an increasing concentration of t-CNCs for a given pH as depicted in Figure 3.5(A) for pH = 8. With PVAm at pH = 8, the thickness jump was observed earlier with an increase of the CNC concentration. Moreover, for each concentration, the slope was proved to be similar before and after the jump. Ellipsometry measurements carried out after the deposition of each layer (t-CNC and PVAm) during the film growth showed that the thickness jump occurred each time when a t-CNC layer is deposited. Similar results were obtained for commercial t-CNCs and t-CNCs provided by B. Jean from CERMAV in Grenoble (Figure 3.5(B)). The deposition of more layers permitted even to see a second jump (thickness increase ~20 nm) which was attenuated compared to the first one (thickness increase ~50 nm).

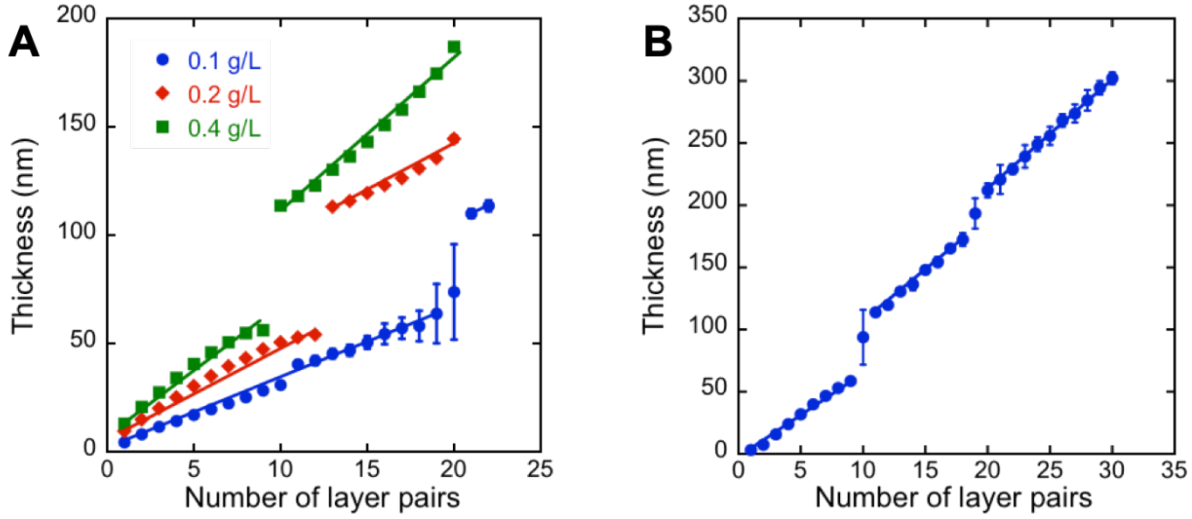

Figure 3.5: Variation of the thickness for CNC-based films prepared by dipping (A) with commercial t-CNCs as function of the CNC concentration and (B) with t-CNCs provided by CERMAV (Grenoble) monitored by ellipsometry after each deposited layer pair.

Nevertheless, when the thickness of these films during build-up is not reported after the deposition of each layer pair (Figure 3.5) but only after the deposition of every 10 layer-pairs, the growth regime of the different multilayers appeared linear (Figure 3.6) and does not display the thickness jump.

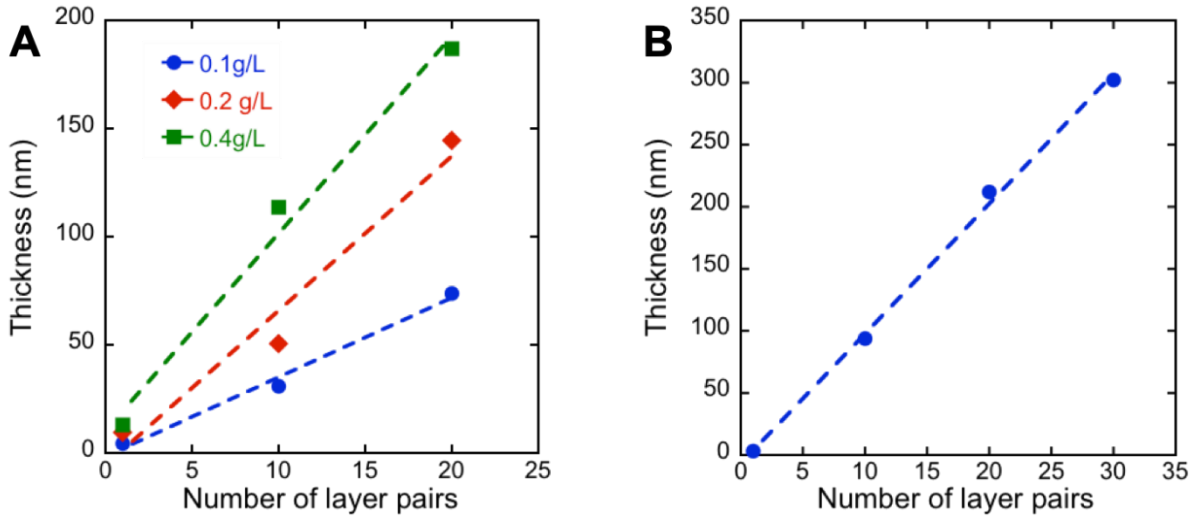

Figure 3.6: Variation of the thickness for CNC-based films prepared by dipping (A) with commercial t-CNCs as function of the CNC concentration and (B) with t-CNCs provided by CERMAV (Grenoble) monitored by ellipsometry after the deposition of every 10 layer-pairs.

The important thickness changes observed in Figures 3.4 and 3.5 are surprising and have never been reported so far in the literature. To verify the thickness values that have been determined by ellipsometry, AFM measurements were carried out during the film build-up by measuring the profile of the film edge (Figure 3.7).

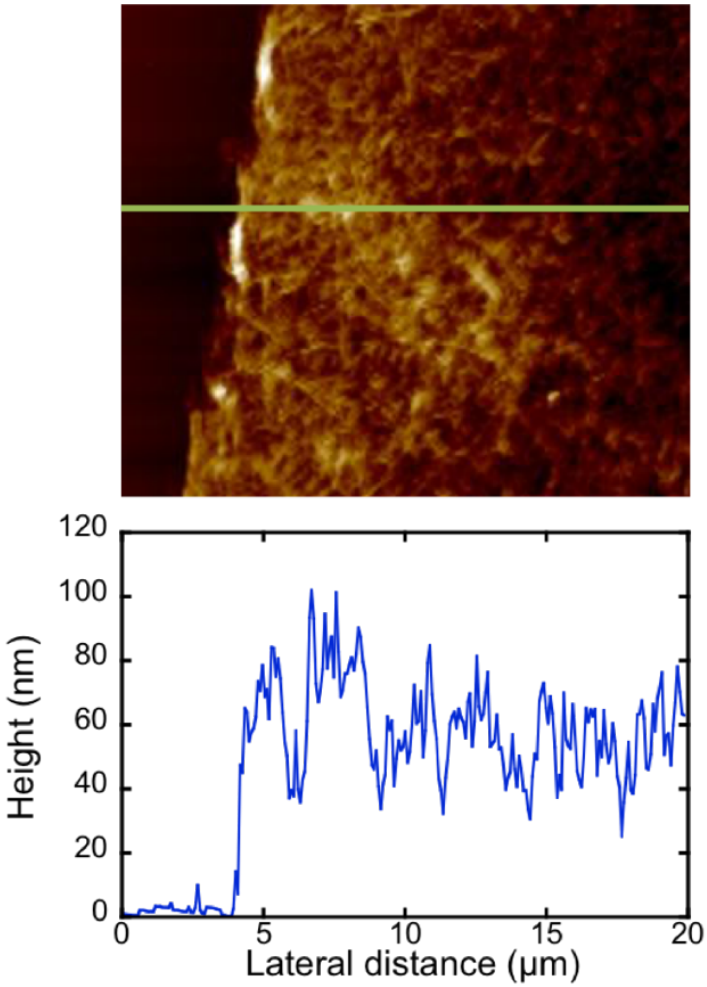

Figure 3.7: (top) Topographical AFM image of the (t-CNC/PVAm)$_9$ film prepared at pH = 8 and (bottom) the corresponding height profile (green line) resulting in a height of around 57 nm.

The analysis of the height variation as function of the lateral distance allowed the determination of a thickness of around 57 nm after the deposition of 9-layer pairs. These AFM measurements were carried out for different numbers of layer pairs and the corresponding results are given in Table 3.1. Analysis of results presented in Table 3.1 shows that thickness values determined by ellipsometry and AFM are in good agreement even if a slight deviation can be observed for 12 and 15 deposited layer pairs.

Table 3.1: Thickness of the (t-CNC/PVAm)$_n$ film monitored by ellipsometry and AFM during its build-up with PVAm at pH = 8.

Number of layer pairs	Ellipsometry	AFM
5	41 ± 1 nm	37 nm
7	51 ± 1 nm	50 nm
9	55 ± 1 nm	57 nm
12	123 ± 1 nm	133 nm
15	143 ± 2 nm	150 nm

Nevertheless, the general trend of the film growth is similar and confirms the abrupt thickness change that was observed previously by ellipsometry. To understand the reason lying behind this striking result, we decided to monitor the film build-up by quartz crystal microbalance (QCM) in order to verify if such behaviour could also be seen during film assembly in absence of drying steps. Unfortunately, QCM experiments were not successful due to tubing clogging after the deposition of few CNCs layers. Filtration of CNC solution to remove large particles did not help. The morphology of films determined by AFM before and after the jump was similar. Moreover, a similar thickness jump could also be seen using other polyelectrolytes like PEI (a weak polymeric base with pKa values between 8 and 10) and PDDA (a polyelectrolyte insensitive to pH) (Figure 3.8). The build-up speed of the films composed of PEI and PDDA was proved to be less important and the thickness jump was less visible.

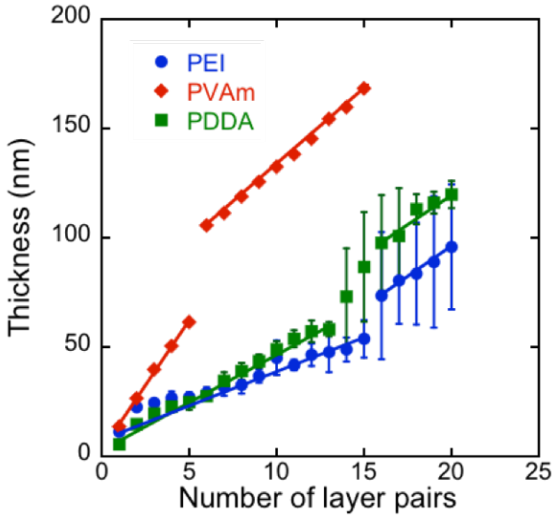

Figure 3.8: Variation of the thickness for CNC-based films prepared by dipping with commercial t-CNCs and different polyelectrolytes (PEI, PVAm and PDDA) monitored by ellipsometry.

As this behaviour was never observed when using w-CNCs, it seems that this thickness jump is related to the intrinsic properties of t-CNCs. Further studies and analyses will be required to provide an explanation of this surprising phenomenon. The preparation and structure of thick CNC-based films will be discussed in the next part.

3.2.2.2 Preparation of thick CNC-based films

The selected cellulose nanocrystals (w-CNCs and t-CNCs) present diameters of a few nanometers and lengths ranging from hundreds of nanometers to a few micrometers and can therefore be easily imaged by AFM. Monolayers of these CNCs deposited on PEI-coated silicon wafers by dipping are depicted in Figure 3.9(A) and 3.9(B).

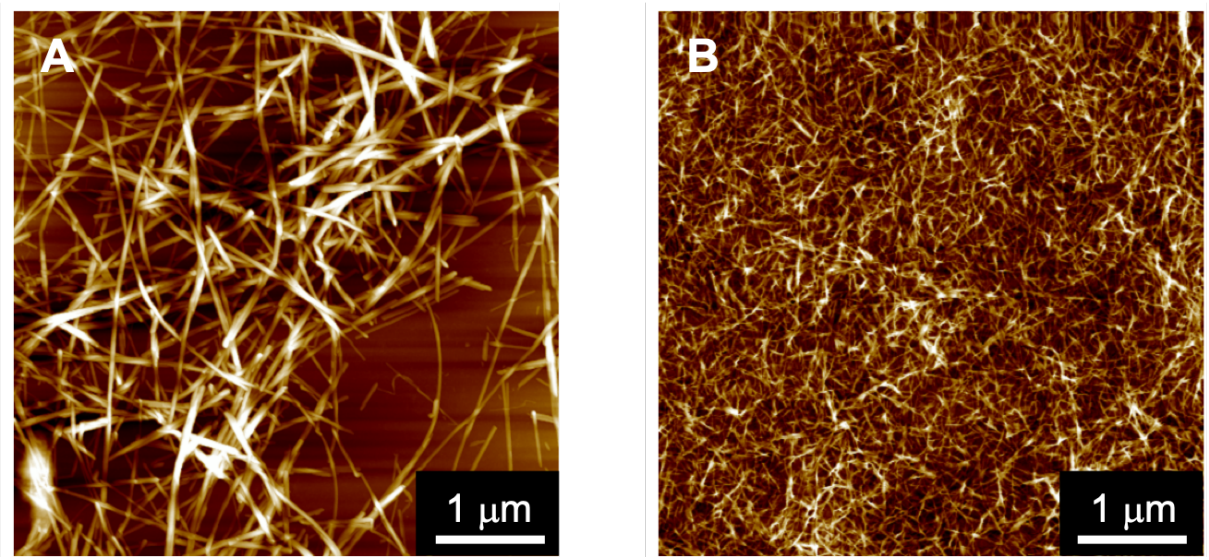

Figure 3.9: AFM height images of CNC monolayers deposited by dipping PEI-coated silicon wafers in (A) t-CNC and (B) w-CNC solutions at a concentration of 0.4 g/L for 10 min.

As expected obtained monolayers displayed cellulose nanocrystals with a random in-plane orientation. Nevertheless, films prepared with w-CNCs were continuous (Figure 3.9(B)) while films assembled with t-CNCs were discontinuous (Figure 3.9(A)). This structural difference can be attributed to the high aspect ratio of t-CNCs making them less favourable for compaction compared to low aspect ratio of w-CNCs.[192] To limit the agglomeration of t-CNCs and reduce the surface roughness of films, different treatments were completed including sonication, centrifugation and filtration steps to remove larger particles and favour t-CNC compaction. Despite these treatments no significant agglomeration difference could be observed by SEM. That's the reason why

in this work, we decided to use t-CNC solutions obtained by simple dilution of the commercial stock solution in Milli-Q water. When thicker films were built, we pointed out a significant difference in optical properties when using t-CNCs or w-CNCs. Indeed, films composed of t-CNCs started to become opaque for a thickness of about 600 nm (Figure 3.10(A)).

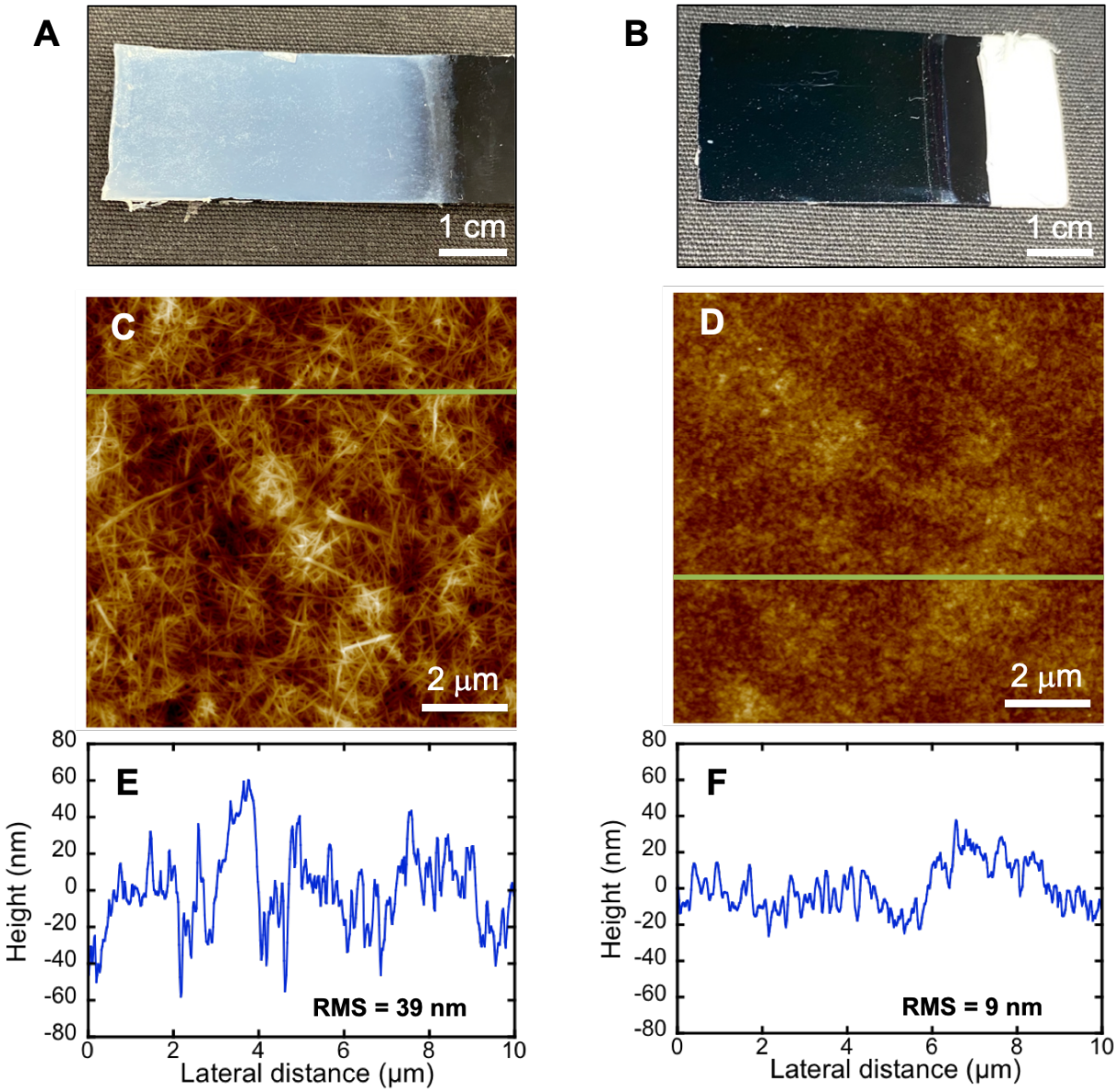

Figure 3.10: Optical photographs of isotropic $(CNC/PVAm)_n$ films prepared by dip-assisted LbL assembly with (A) t-CNCs (950 nm opaque thick film) and (B) w-CNCs (930 nm transparent thick film). (C, D) Topographical AFM images of A and B respectively. (E, F) Height profiles at the position of green lines in C and D respectively and calculated root mean square (RMS) roughness.

On the other hand, w-CNC-based films remained fully transparent suggesting a higher surface roughness and porosity for t-CNC films leading to an important light scattering. This assumption was confirmed by topographical AFM images (Figure 3.10(C) and 3.10(D)). Although the average thickness of both films was similar, the root mean square (RMS) roughness of films prepared with t-CNCs (39 nm) was more than four times larger than the one of the film composed of w-CNCs (9 nm) (Figure 3.10(E) and 3.10(F)). As CNF-based films we prepared thick CNC multilayers on hydrophobic substrates coated with the (PVAl/Clay) sequence. The structure and thickness of these films were also investigated by imaging the edge of thick samples by SEM (Figure 3.11). Cross-sectional SEM images revealed the formation of smooth films using both types of cellulose nanocrystals but with different internal morphologies. On the one hand, films consisting of long t-CNCs displayed pores that could be attributed to their high rigidity and length (Figure 3.11(A)). This type of porous structure, compared to a "flattened matchsticks pile", was already reported by the team of Kotov who built similar films composed of PEI and cellulose nanowires extracted from tunicates.[94] On the other hand, the use of w-CNCs resulted in a more dense and close-packed structure with short nanocrystals providing a lower porosity (Figure 3.11(B)).

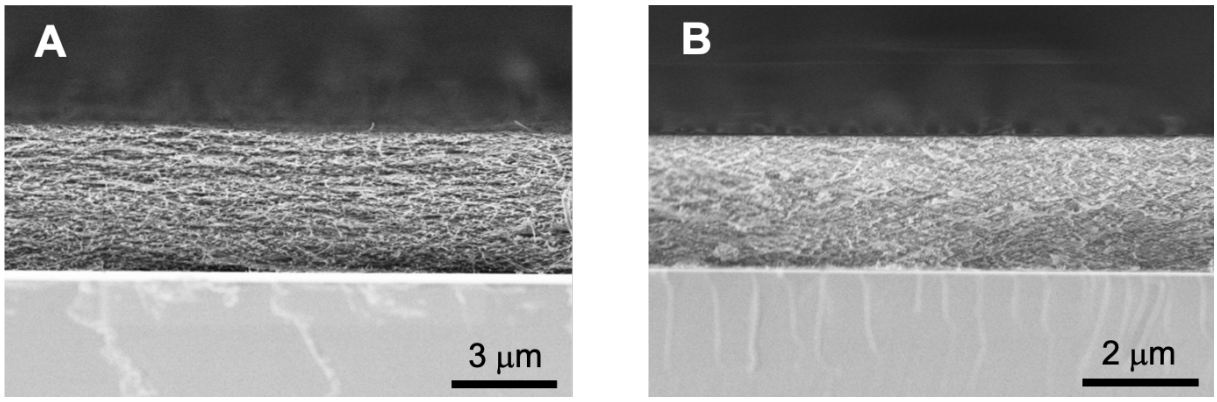

Figure 3.11: SEM cross-sectional images of $(t\text{-CNC/PVAm})_{300}$ (A) and $(w\text{-CNC/PVAm})_{380}$ (B) films prepared by dip-assisted LbL assembly with PVAm at pH = 10.

The SEM cross-sectional images also allowed the determination of the thickness of fabricated films. Indeed, this parameter is required for determining film mechanical properties by DMA as the measured modulus depends on the film thickness. SEM imaging resulted in a thickness of 4.3 ± 0.1 μm for the $(t\text{-CNC/PVAm})_{300}$ film (Figure 3.11(A)) and a thickness of 2.4 ± 0.1 μm (Figure 3.11(B)) for the $(w\text{-CNC/PVAm})_{380}$

film prepared at pH = 10. These films could then be cut and detached from the substrate before the characterization of their mechanical properties by DMA.

This first section demonstrated the possibility to prepare isotropic nanocellulose-based films using LbL assembly. The pH of the polyelectrolyte was proved to significantly affect the growth of CNF-based films while the aspect ratio and rigidity of cellulose nanocrystals had an influence on the morphology and surface roughness on the corresponding films. However, the remarkable mechanical properties of wood were proved to arise from the orientation of the cellulose units in the secondary cell walls.[3] In that perspective, many studies have already been completed on the alignment of CNCs[193] and CNFs[194] and demonstrated a significant enhancement of the mechanical properties of oriented films especially when using spin-assisted LbL assembly.[106]

3.3 Spin-assisted LbL assembly of cellulose-based films

The alignment of CNFs was first studied using spin-assisted assembly. Despite many attempts to orient them by changing the experimental conditions, it was not possible to image them by AFM. This could be due to the high shear forces generated during the spinning process that were probably too important for the flexible and small used cellulose nanoparticles. Spin-assisted LbL assembly has already been employed to prepare anisotropic CNC-multilayer films using binding polyelectrolytes such as PAH or xyloglucan.[105,195] Nevertheless, the mechanical properties of these oriented nanostructured films were not investigated intensively. As one aim of the present work was to obtain highly resistant materials, we decided to orient two types of crystalline cellulose nanoparticles, t-CNCs and w-CNCs. After the optimization of the alignment of these nanocrystals, thick films combining PVAm and CNCs were prepared and their mechanical properties were evaluated in the last section of this chapter.

3.3.1 Orientation of CNCs

The degree of alignment of t-CNCs was first characterized by AFM on monolayers deposited on PEI-coated silicon substrates (Figure 3.12).

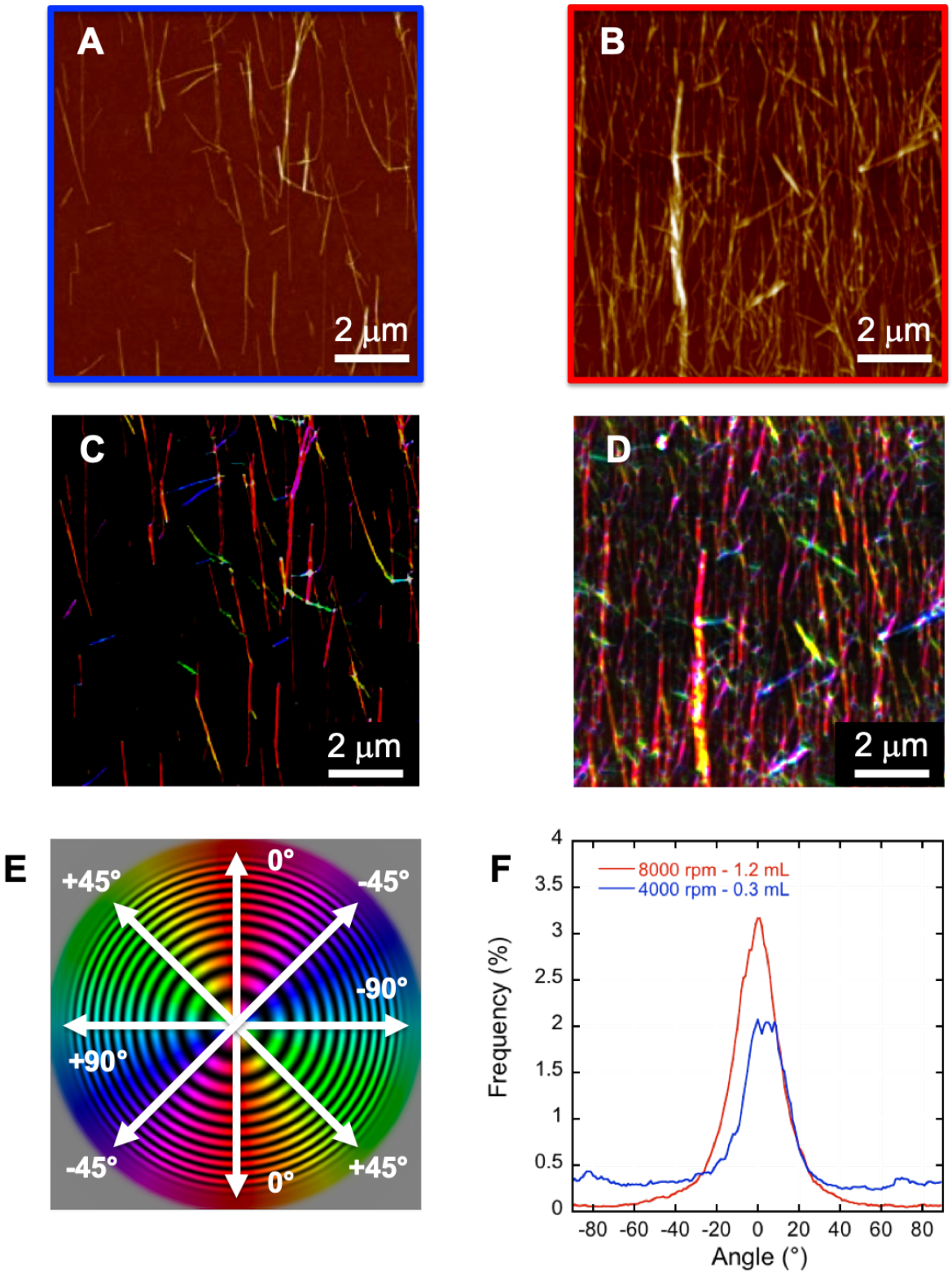

Figure 3.12: AFM height images t-CNC monolayers prepared with a spinning speed of 4000 rpm and a volume of 0.3 mL (A) and a spinning speed of 8000 rpm and a volume of 1.2 mL (B). Images were taken at 2 cm from the center. (C, D) Orientation analysis of A and B using the OrientationJ plugin. (E) Color-code used for the orientation analysis. (F) Orientation distribution of the CNC angle relative to the spraying direction extracted from (C) and (D).

The spinning speed and the deposited volume of CNC solutions were studied in that work in order to optimize the in-plane orientation of the cellulose nanocrystals. Three different spinning speeds (4000, 8000 and 10000 rpm) and two different volumes (0.3 and 1.2 mL) for solutions were selected for this optimization. Figure 3.12 shows AFM pictures of samples prepared with two different combinations of experimental conditions: (i) a rotation speed of 4000 rpm and a volume of 0.3 mL and (ii) a rotation speed of 8000 rpm and a volume of 1.2 mL. To quantify the degree of alignment of CNCs we analysed our samples using OrientationJ, a plugin of ImageJ software. After treatment we obtained images with a color code attributed to each pixel depending on its local orientation (Figure 3.12(C) and 3.12(D)). This allowed the visualization of the main direction of orientation. The distribution of the angle between each nanoparticle main axis and the main orientation of the sample can then be extracted. A 2D nematic order parameter (S_{2D}) can be calculated from this angular distribution by using Equation 3.1.

$$S_{2D} = \langle 2\ \cos^2(\theta) - 1 \rangle \qquad \textbf{Equation 3.1}$$

Where the chevrons denote the weighted average over the distribution of θ. S_{2D} is comprised between 0 and 1 with 0 corresponding to a random distribution (isotropic films) with all angles being equally represented and 1 corresponding to perfectly aligned nanoparticles (anisotropic films).

The order parameter significantly increased (Figure 3.13(A)) when the spinning speed switched from 4000 rpm to 8000 rpm. This observation is not surprising as the applied shear forces increased with the spinning speed. However, a spinning speed of 10000 rpm did not allow to improve the alignment quality further. Independently from the spinning speed, an increase of the deposited volume enabled an improvement of the orientation degree. This could be attributed to the first deposited crystals acting as a template and promoting a good alignment of the next ones. The order parameter reached a maximal value of about 0.8 with a spinning speed of 8000 rpm and a deposited volume of t-CNCs of 1.2 mL. As the aim of this work was to prepare highly oriented films with anisotropic properties, we decided to select these experimental conditions for all further experiments.

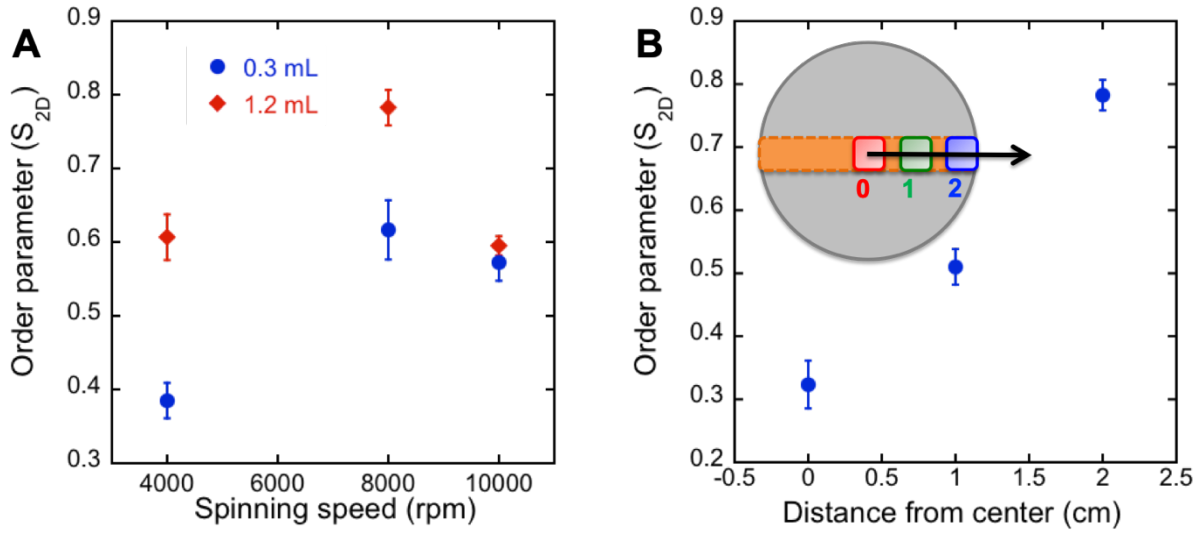

Figure 3.13: Evolution of the order parameter S_{2D} as function of (A) the spinning speed for 2 volumes of deposited t-CNCs (0.3 and 1.2 mL) and (B) the distance from the center of the sample with a spinning speed of 8000 rpm and a volume of 1.2 mL.

Moreover, the alignment of the cellulose nanocrystals was proved to be sensitive to the distance from the center. Indeed, as illustrated in Figure 3.13(B), the order parameter significantly increased from the center to the edge of the sample with a maximal value close to 0.8 measured at 2 cm away from the center. This result can be attributed to the increase of the shear forces created by the spinning from the center to the edge of the sample and leading to an increase of the degree of orientation.

Similarly, the orientation degree of w-CNCs was also studied on PEI-coated silicon substrates and characterized by AFM (Figure 3.14). The influence of the spinning speed on the degree of orientation and on the 2D order parameter is shown in Figure 3.14(E). As for t-CNCs, we observed a significant improvement of the alignment of the cellulose nanocrystals when the spinning speed increased. S_{2D} passed from ~0.1 at 4000 rpm to ~0.5 at 10000 rpm. Nevertheless, the maximal order parameter value was significantly lower than the one obtained when using t-CNCs. This difference in the quality of alignment can be attributed to the aspect ratio difference between both nanocrystals. Indeed, as the aspect ratio of t-CNCs (~100) is roughly twice than the one of w-CNCs (~40), t-CNCs are easier to align during the spinning process using the same conditions.

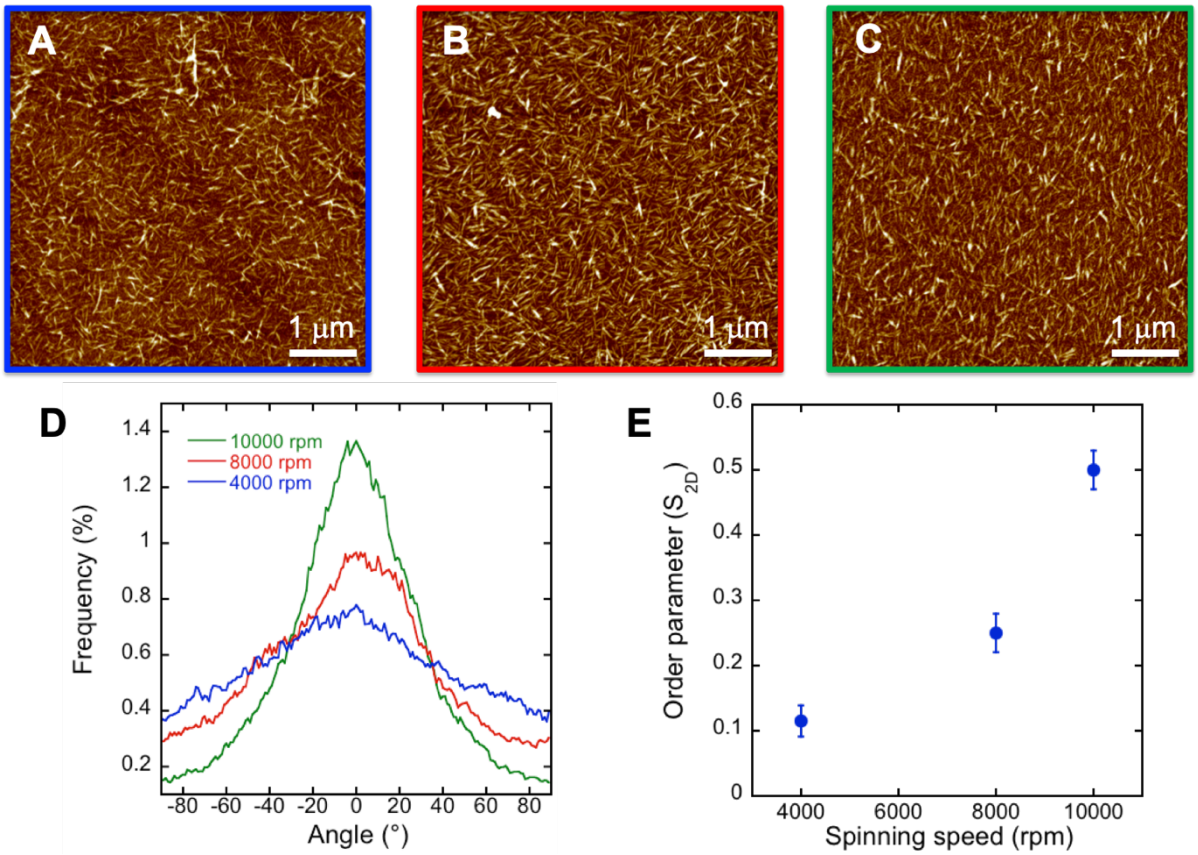

Figure 3.14: AFM height images samples prepared with a spinning speed of (A) 4000 rpm, (B) 8000 rpm and (C) 10000 rpm. Images were taken at 2 cm from the center. (D) Distribution of orientation for the three selected spinning speeds. (E) Order parameter S_{2D} as function of the spinning speed for 1.2 mL of deposited w-CNCs.

We prepared oriented monolayers of t-CNCs by spin-assisted assembly and optimized the experimental conditions for their alignment. This study also revealed the influence of the spinning speed, deposited volume and distance from the center on the orientation degree of the cellulose nanocrystals. Moreover, the aspect ratio had also an effect on the alignment quality as the long t-CNCs were easier to align compared to short w-CNCs. Due to the higher order parameter values obtained using t-CNCs, we will exclusively focus on the preparation of thick multilayer films composed of these nanocrystals in the next section.

3.3.2 Preparation of thick films

$(t\text{-CNC/PVAm})_n$ film growth was studied using the previous optimized conditions allowing the highest degree of orientation. The build-up of the film was monitored by

ellipsometry using PVAm solutions at pH = 8 and pH = 10 (Figure 3.15(A)). The multilayer growth was regular for these two pH values and the increase of the pH did not significantly raise the build-up speed. Thickness increments of 6.1 and 6.3 nm/layer-pair were determined at respectively pH = 8 and pH = 10. Similarly to t-CNC-based films built by dipping, these films also became hazy after a thickness of around 600 nm (Figure 3.15(B)).

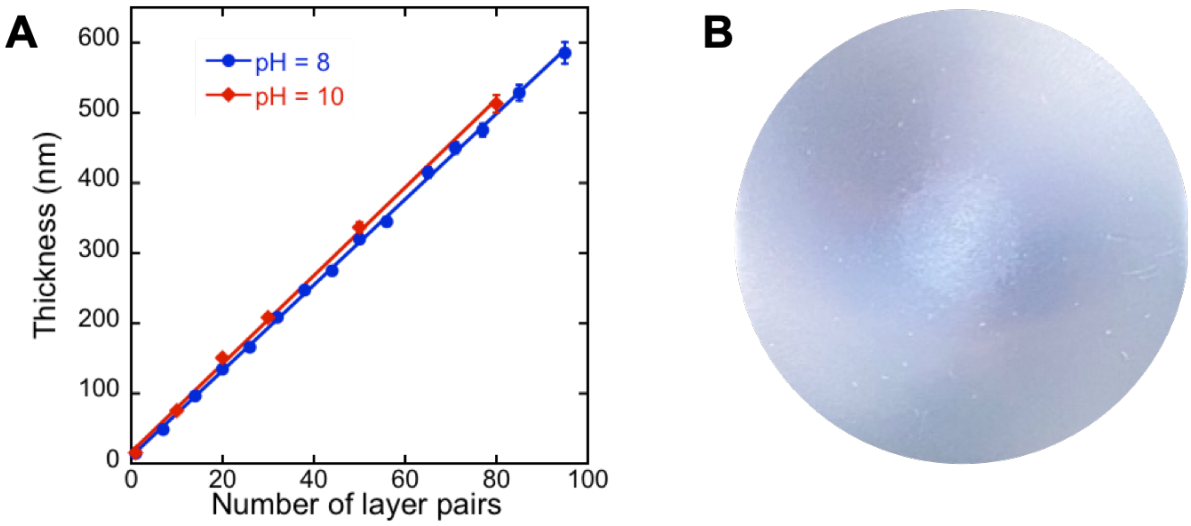

Figure 3.15: (A) Build-up of the (t-CNC/PVAm)$_n$ film prepared by spin-assisted LbL assembly monitored by ellipsometry as function of the pH of the PVAm solution. (B) Optical photograph of the opaque sample after the deposition of 95-layer pairs at pH = 8.

The microstructure of these films was then studied by microscopic investigations. SEM cross-sectional pictures revealed the formation of smooth films with a highly porous network as it can be seen in Figure 3.16(A) and 3.16(B). On the other hand, AFM measurements demonstrated a very important surface roughness (RMS = 212 nm) showing also large pores on the top of the sample and confirming the porous structure observed from the edge of the film by SEM. The important surface roughness of the film that is a direct consequence of the enhanced porosity can definitely explain the important light scattering of the prepared micron-thick samples making them hazy. SEM cross-sectional imaging also allowed the determination of the thickness of the prepared films during their build-up. Meanwhile, considering the ellipsometry measurements conducted before (Figure 3.15(A)) and predicting an increment of 6.1 nm/layer pair at pH = 8, we could estimate the thickness of the film. The estimated

thickness values from ellipsometry data and the measured thickness values extracted from SEM images are summarized in Table 3.2.

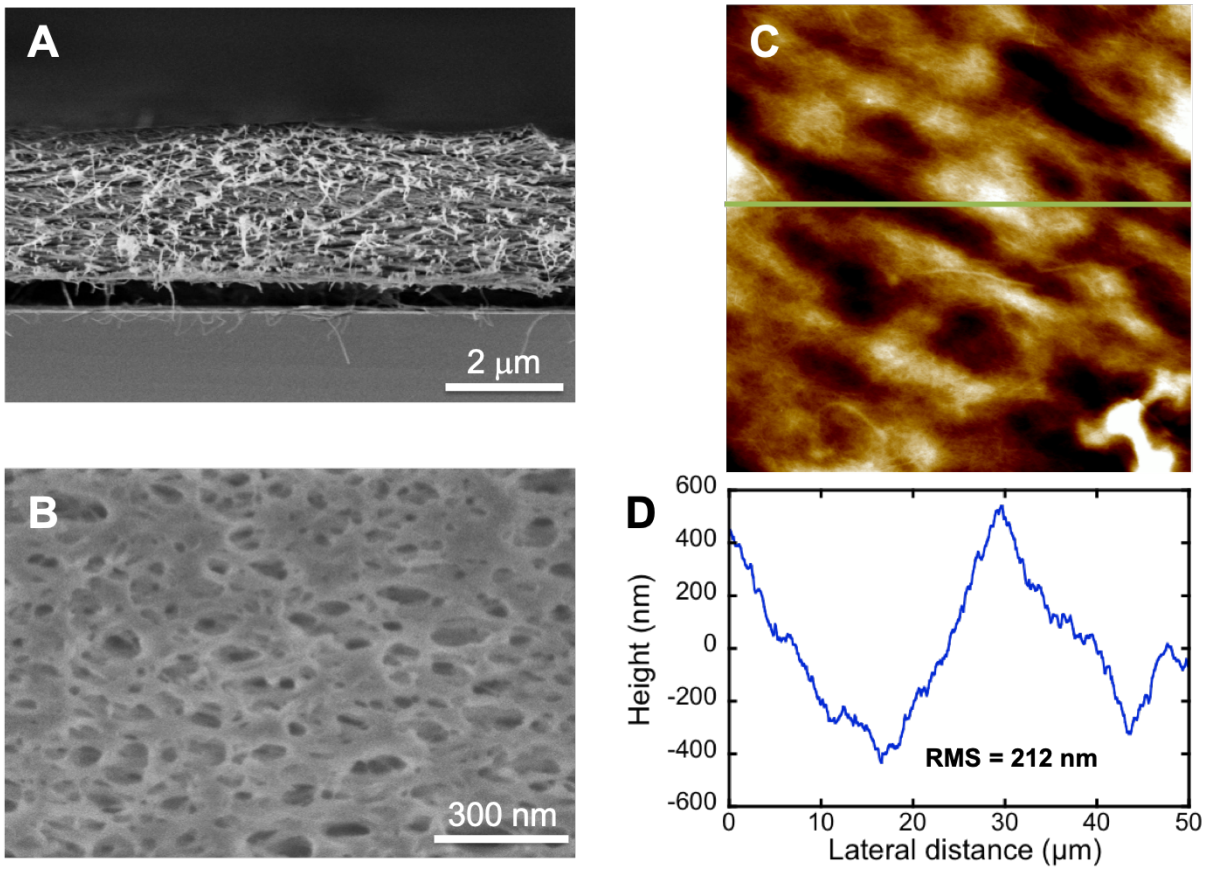

Figure 3.16: (A) SEM cross-sectional image of the (t-CNC/PVAm)$_{500}$ prepared by spin-assisted LbL assembly at pH = 8. (B) Close-up on the porous structure. (C) AFM topographical image of the film with the corresponding height profile at the position of green line and calculated root mean square (RMS) roughness (D).

Table 3.2: Estimated thickness values from ellipsometry data and measured thickness values from SEM cross-sectional imaging for (t-CNC/PVAm)$_n$ films prepared by spin-assisted LbL assembly at pH = 8.

Number of layer pairs	Ellipsometry	SEM
150	~915 nm	898 ± 38 nm
250	~1525 nm	1592 ± 75 nm
500	~ 3050 nm	2832 ± 286 nm

The thickness values estimated from ellipsometry are in good agreement with the ones measured by cross-sectional SEM imaging confirming the build-up of micron-thick films exhibiting a regular growth.

To verify the alignment of CNCs in thick samples, cross-polarized microscopy analyses were completed. Micrographs were acquired at different in-plane rotation angles on the edge of the sample and the relative brightness was determined for each angle by measuring the grey value of the images. Figure 3.17(C) shows the variation of the relative brightness as function of the rotation angle.

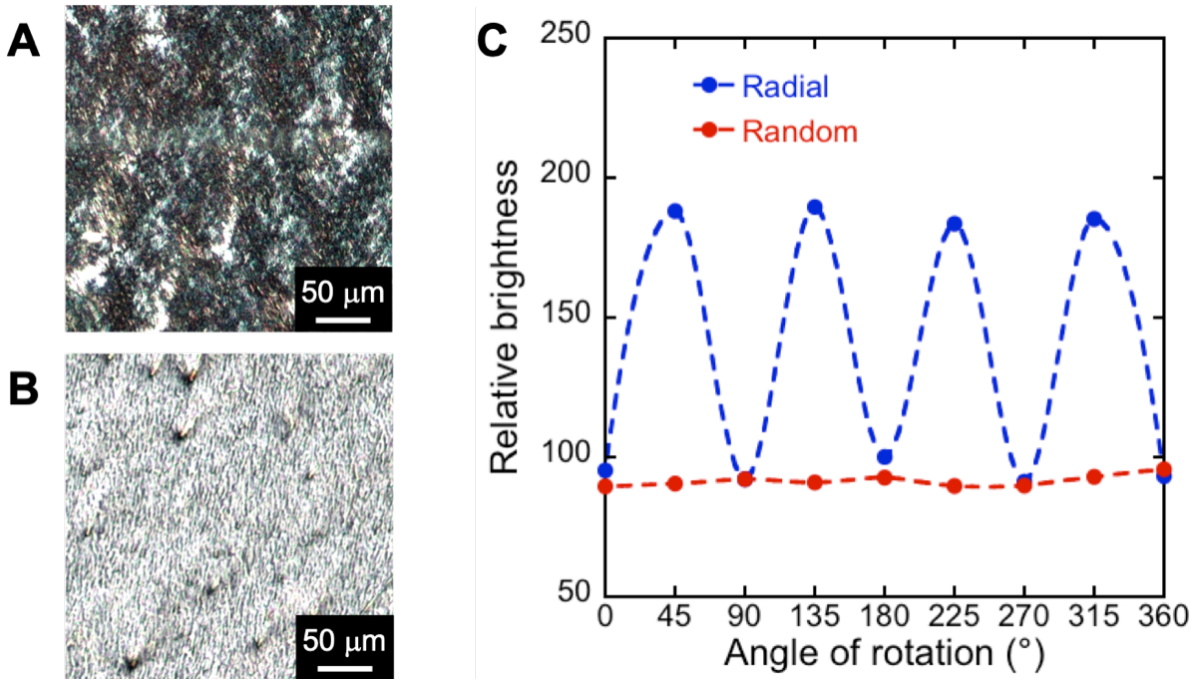

Figure 3.17: Relative brightness measured under cross polarizers on the edge of a (t-CNC/PVAm)$_{90}$ film prepared by spin-assisted LbL assembly with an angle between the CNC orientation and the polarizer of (A) 0° and (B) 45°. (C) Relative brightness variation as function of the in-plane rotation angle for random and radially oriented films.

As expected for an anisotropic sample, a minimum of light was reflected when the CNC alignment direction was parallel to the direction of one of the polarizers (0°, 90°, 180° and 360°). On the other hand, a maximum of light was reflected when the angle between the cellulose nanocrystals and the direction of the polarizers was 45°, 135°, 225° and 315°. Consequently, we observed either a maximum or a minimum of

brightness every 45°. The detection of this optical anisotropy is a proof of the anisotropic structure of the whole film confirming the local unidirectional alignment of CNCs in each layer at the edge of samples.

We demonstrated the possibility to prepare anisotropic and micron-thick films composed of highly oriented t-CNCs. Unfortunately, these films became opaque after reaching a thickness of about 600 nm due to their high surface roughness arising from their 3D-porous structure. Spin-assisted LbL assembly allowed the preparation of oriented films composed of CNCs with a fast deposition time compared to dipping. Nevertheless, all layers deposited within the multilayer film are aligned in the same direction limiting its use towards the fabrication of more complex structures. One key development to design more complex structures including helicoidal ones was introduced in chapter 1 and is referred as grazing incidence spraying (GIS).[11] This spraying technique combined with the LbL assembly allows the independent alignment of anisotropic nanoparticles in each layer and has already been utilized in our team to build helical architectures made of CNFs[112] and AgNWs. The next section will focus on the in-plane orientation of CNCs using GIS technique before presenting the preparation of thick unidirectionally and helicoidally aligned films.

3.4 Spray-assisted LbL assembly of cellulose-based films

3.4.1 Orientation studies on monolayers

Before the preparation of anisotropic thick films, the orientation of CNFs, t-CNCs and w-CNCs was first studied on monolayers deposited on PEI-coated silicon wafers using GIS. Figure 3.18 displays the GIS setup with the used experimental conditions including the concentration (*C*), the airflow rate (*A*), the liquid flow rate of the CNF or CNC solution (*L)*, the spraying time (t_{spray}), the incidence angle (α) and the distance between the nozzle and the sample (*d*). These experimental conditions were selected from previous studies performed in the team.

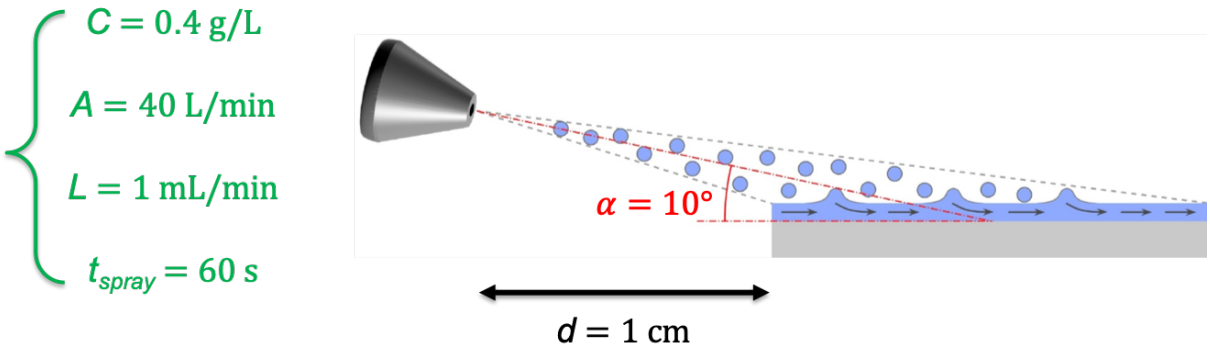

Figure 3.18: Schematic representation of the GIS setup and experimental conditions selected for the deposition of CNFs, t-CNCs and w-CNCs.[11]

The orientation of CNFs by GIS using the experimental conditions presented in Figure 3.18 was first studied. However, no nanofibril could be observed by AFM imaging. The optimization of these nanofibrils was not investigated further but the airflow rate was probably too high and generated shear forces that were too strong to cover them on the surface.

AFM pictures corresponding to the prepared samples using exactly the same experimental conditions with both types of cellulose nanocrystals are shown in Figure 3.19. The analysis of AFM images revealed a good in-plane alignment of t-CNCs (Figure 3.19(B)) with an order parameter close to 0.80 while w-CNCs (Figure 3.19(A)) were randomly distributed (S_{2D}~0.15). In addition, the density of w-CNCs deposited on the surface tends to be very poor compared to t-CNCs. Such behaviour can be explained by the removal of w-CNCs weakly attached by the harsh spraying jet acting as a “kärcher”. As the degree of alignment of t-CNCs was already high and considered as sufficient towards the preparation of anisotropic materials, we did not optimize their alignment further. On the other hand, as the orientation degree of w-CNCs was very low, different experimental conditions were tested but no improvement could be observed. The small aspect ratio of w-CNCs is probably too low to allow the alignment of the cellulose nanocrystals by the spraying shear forces. Indeed, it has already been demonstrated in our team that the quality of alignment increased with the length of the nanoparticles using different metallic nanowires.[196]

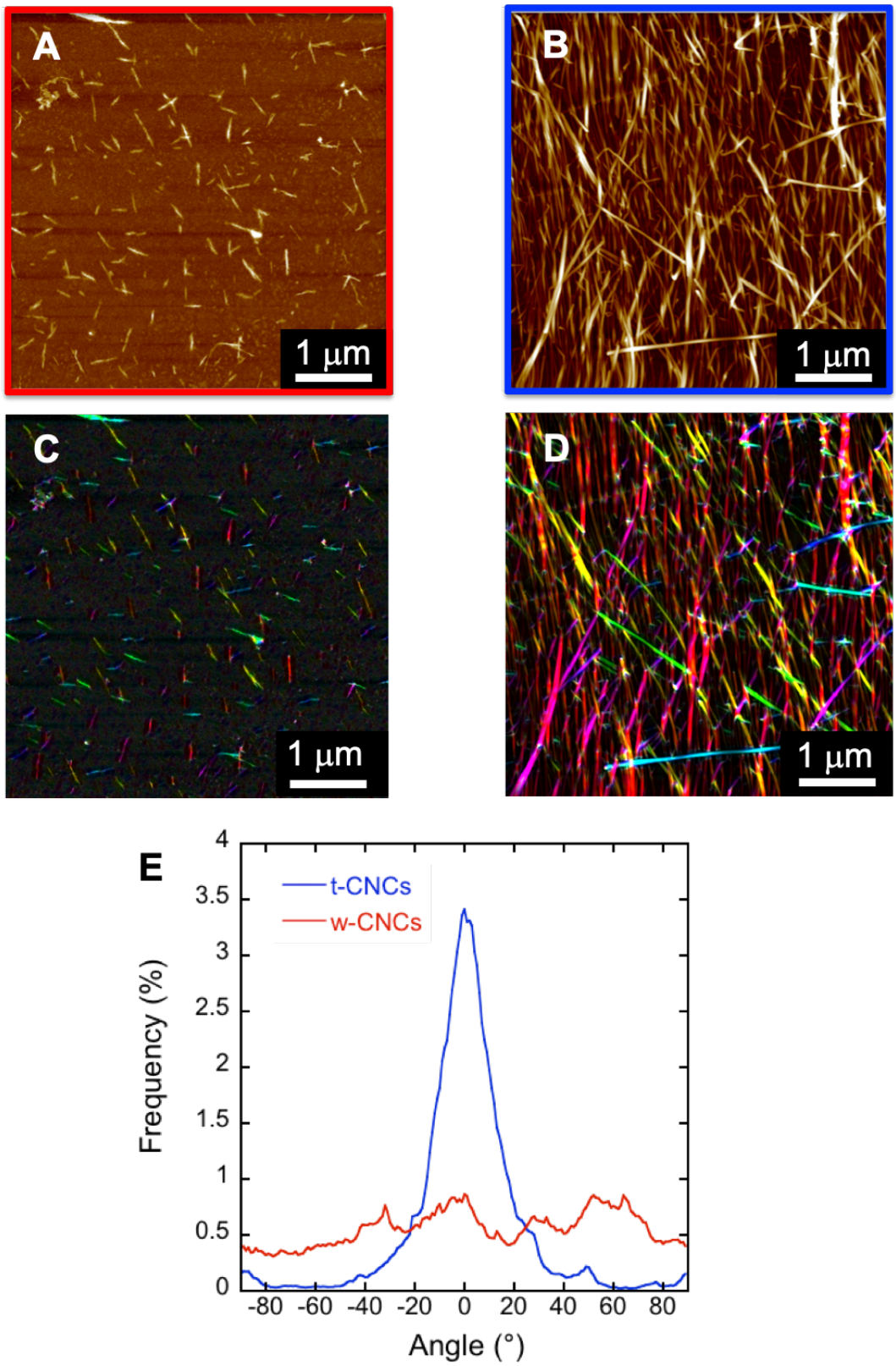

Figure 3.19: AFM height images of CNC monolayers prepared under the same experimental conditions by GIS with (A) w-CNCs and (B) t-CNCs. (C-D) Orientation analysis of images (A) and (B) respectively using OrientationJ plugin. (E) Orientation distributions of the CNC angle relative to the spraying direction extracted from (C) and (D).

We have seen that is was possible to efficiently orient t-CNCs in the plane. To prepare more complex anisotropic structures like the helical ones, the alignment of cellulose nanocrystals is needed in each deposited layer. In order to verify the independent alignment of nanocrystals in a multilayer film, we prepared samples by spraying two successive t-CNC layers in the same direction and samples with a rotation angle of 90° between them. A separating layer of PVAm at pH = 8 was sprayed in between CNC layers and the superposition of AFM images with one and two CNC layers are presented in Figure 3.20.

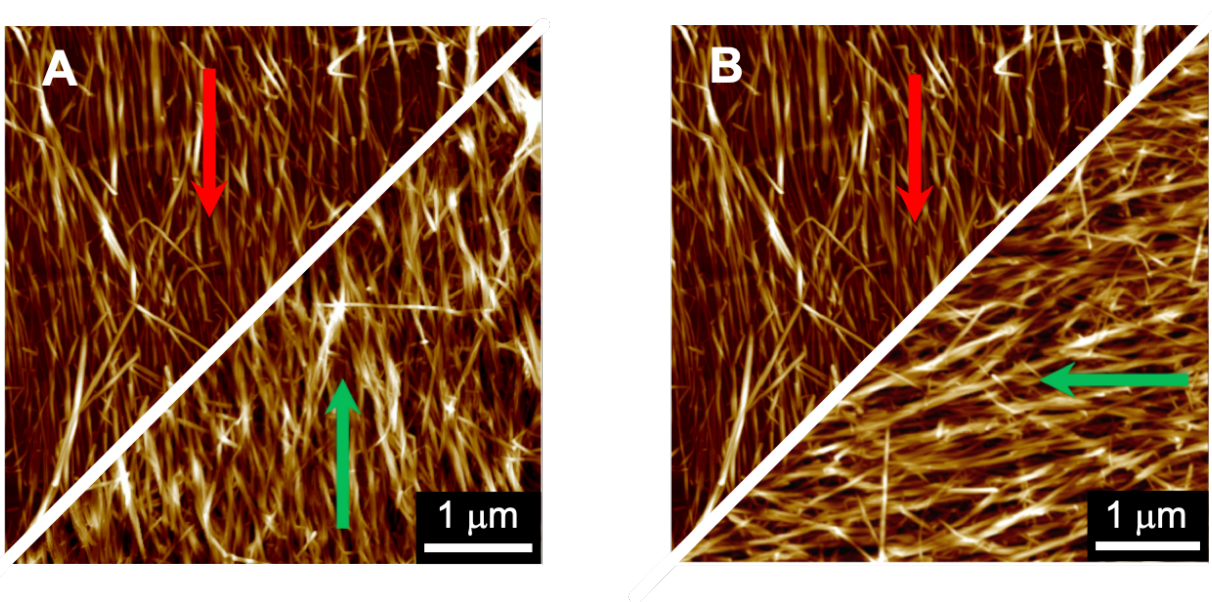

Figure 3.20: Superposition of AFM pictures of the first (red arrows) and second (green arrows) layers of t-CNCs sprayed by grazing incidence spraying in the same direction (A) and perpendicular to each other (B).

For each sample, an order parameter S_{2D} was calculated from obtained AFM images and results are depicted in Table 3.3.

Table 3.3: Evolution of the order parameter as function of the spraying direction (parallel or perpendicular) for the deposition of two alternated t-CNC layers.

Film structure	Order parameter S_{2D}
PEI/CNC	0.78 ± 0.03
PEI/CNC/PVAm/CNC (parallel)	0.74 ± 0.07
PEI/CNC/PVAm/CNC (perpendicular)	0.76 ± 0.07

The degree of alignment was proved to slightly decrease when a second t-CNC layer was sprayed on top of the first one. However, the order parameter values remained high (between 0.7 and 0.8) revealing that these cellulose nanocrystals could be oriented by GIS independently of the orientation of the underlying layer.

AFM analyses demonstrated the efficient alignment of t-CNCs by GIS on one and two deposited layers. We will now discuss the preparation of thick multi-layered CNC-based films exhibiting different structures.

3.4.2 Thick CNC-based multilayer films

3.4.2.1 Unidirectionally aligned films

After the study of the alignment of cellulose nanocrystals, we were interested into preparing thick unidirectionally aligned films to characterize their mechanical properties. $(t\text{-CNC/PVAm})_n$ thick films were prepared by spraying all cellulose nanocrystal layers in the same direction using the experimental conditions discussed previously. The film build-up was monitored by spectroscopic ellipsometry and revealed a regular behaviour with a growth rate of 12.4 nm/layer pair (Figure 3.21(A)).

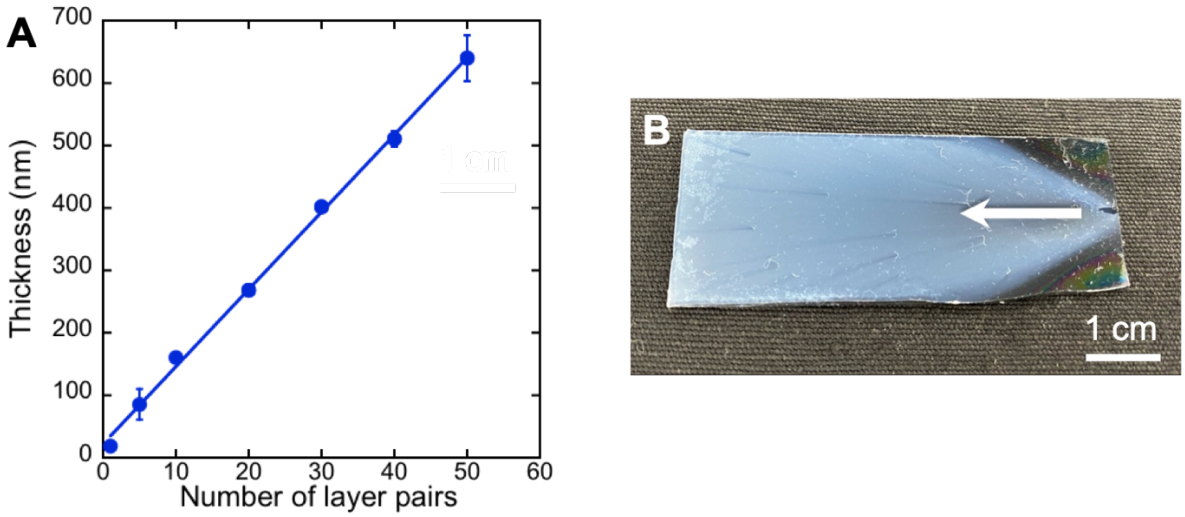

Figure 3.21: Thickness variation during the build-up of the unidirectionally aligned $(t\text{-CNC/PVAm})_n$ film prepared by spray-assisted LbL assembly monitored by ellipsometry. (B) Optical photograph of a $(t\text{-CNC/PVAm})_{240}$ film prepared with PVAm at pH = 10 in which the white arrow indicates the spraying direction.

However, the film became opaque after the deposition of 50-layer pairs corresponding to a thickness of around 640 nm. Meanwhile, the interference colors were hidden by a grey coloration certainly arising from an important light scattering (Figure 3.21(B)). During the film build-up, some dust particles were deposited on the surface and were responsible for the pattern observed in Figure 3.21(B).

To study and determine the opacity of these films, unidirectionally aligned films were built on quartz slides and the transmittance during their growth was monitored by UV-Visible spectroscopy (Figure 3.22(A)). As expected, the transparency of the films decreased from ~95% to ~75% in the visible range as the number of layer pairs increased from 10 to 90. This decrease of transparency during the film build-up was ascribed to an increase of the light scattering. Indeed, after the deposition of 240-layer pairs, the film displayed a thickness of 5.1 ± 0.3 μm with a root mean square (RMS) roughness of around 115 nm.

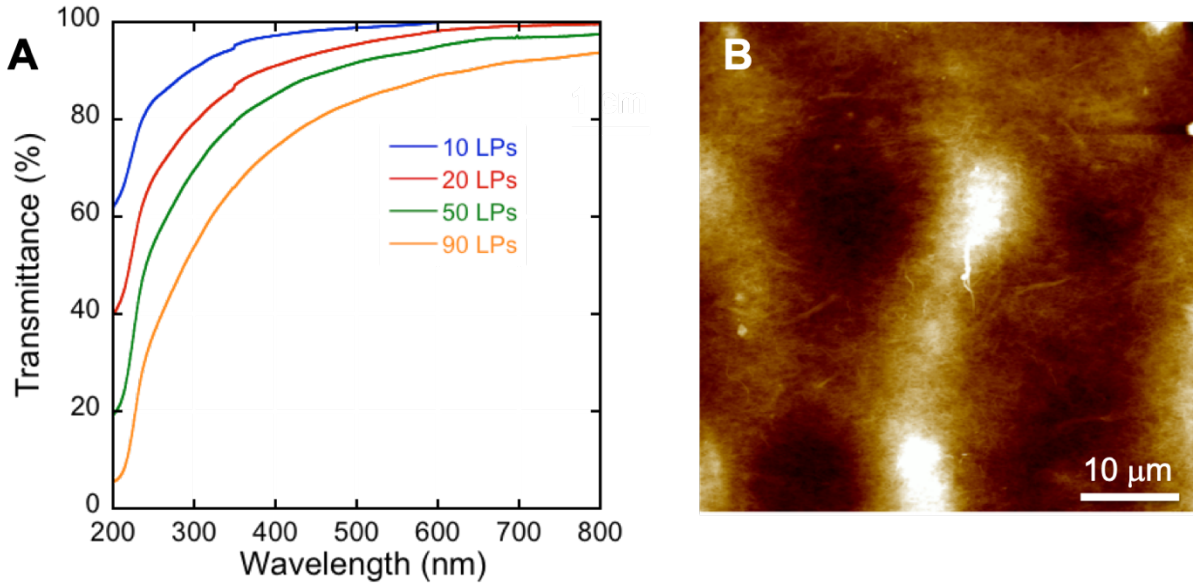

Figure 3.22: (A) UV-Visible transmittance spectra measured during the build-up of a unidirectionally oriented (t-CNC/PVAm)$_n$ film prepared by spray-assisted LbL assembly. (B) AFM height image of a unidirectionally oriented film composed of 240-layer pairs.

To verify the unidirectional alignment of the cellulose nanocrystals in the whole film, cross-polarized microscopy was used on a (t-CNC/PVAm)$_{30}$ film. Optical micrographs were acquired at different rotation angles at the center of the sample. An anisotropic optical response characterized by a minimum and a maximum of reflected light

alternating every 45° of rotation was observed (Figure 3.23). For comparison, results obtained for an isotropic sample prepared by dipping are represented and displayed an isotropic optical signal arising from the random distribution of cellulose nanocrystals.

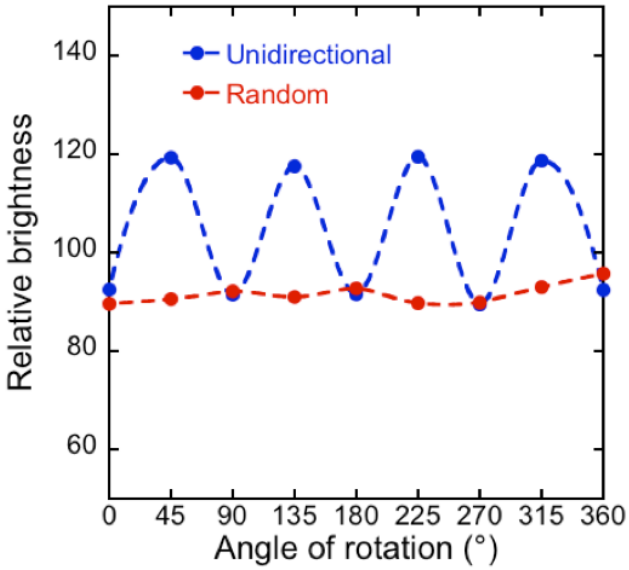

Figure 3.23: Angular dispersion of the in-plane relative brightness under crossed polarizers for random (red) and unidirectionally (blue) oriented CNC-based films.

3.4.2.2 Helicoidally structured films

We finally prepared $(t\text{-CNC/PVAm})_n$ films presenting a helicoidal architecture by spraying CNC layers with a constant angle of 30° between two consecutive CNC layers. A complete helical turn was consequently obtained after the deposition of 12-layer pairs. The films displayed circular interference colors when moving from the center to the edge of the silicon wafer (Figure 3.24(A) and 3.24(B)). The different colored areas observed on the optical photographs can be attributed to variations in the film thickness induced by the deposition process. However, these interference colours could not be seen anymore after a film thickness of about 600 nm and were hidden by a white color (Figure 3.24(C) and 3.24(D)).

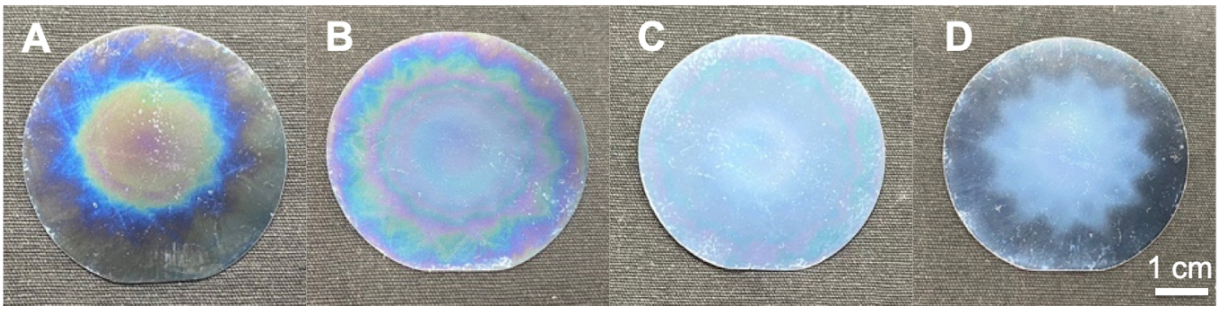

Figure 3.24: Optical photographs of left helicoidal (t-CNC/PVAm)$_n$ films with a rotation angle of 30° between two consecutive CNC layers and where n = 24 (A), n = 60 (B), n = 144 (C) and (D) n = 192.

To ascertain the helicoidal architecture of the cellulose nanocrystals in the film, the edge of a helicoidal sample with a rotation angle of 30° between two consecutive CNC layers was imaged by SEM. Unfortunately, the helical twisting of CNCs on the fracture plane could not be observed by SEM because of the small diameter of the cellulose nanocrystals and the possible structure damages induced by the mechanical fracture of the film.

To prove the helical structure, the chiral properties of the obtained films were investigated using circular dichroism (CD) spectroscopy. As optically active chiral species are expected to preferentially absorb one direction of circularly polarized light, we should observe chiral properties for the helical assembled structures depending on their handedness, the number of turns and the helical pitch.

In that perspective, different samples were prepared and analysed including a CNC solution, an isotropic film built by dipping and helical architectures with opposite handedness (Figure 3.25(A)). A CNC solution (0.4 g/L) (green curve) was first analysed and displayed a small signal at around 300 nm that was not visible for the isotropic film prepared by dipping (orange curve) (Figure 3.25(A)). This signal could be attributed to the formation of a chiral nematic structure as the CNCs tend to generate such structure in solution above a specific concentration. In comparison, as the nanocrystals were aligned in the same direction in the isotropic sample, no significant CD signal was observed.

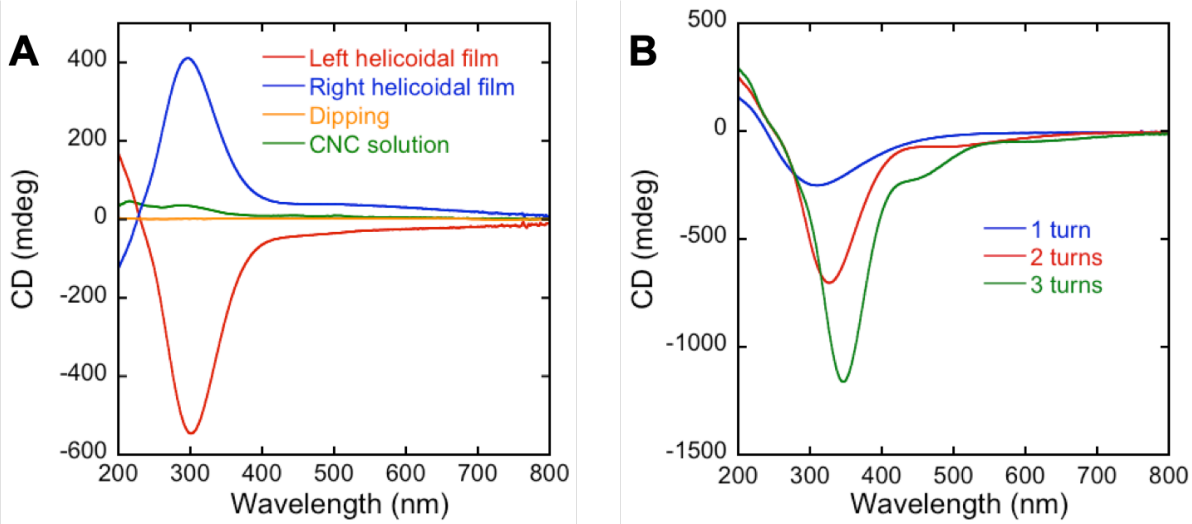

Figure 3.25: (A) CD spectra of left and right helicoidal (t-CNC/PVAm)$_{24}$ films compared to CD spectra of a CNC solution (0.4 g/L) and an isotropic film prepared by dipping. (B) CD spectra of a helicoidal sample with one, two and three helical turns.

Helical t-CNCs-based films with opposite handedness (blue and red curves) finally revealed an intense signal at around 300 nm that was significantly higher than the one observed for the CNC solution. The symmetrical optical response of these films prepared with opposite handedness demonstrated the helicoidal assembly of cellulose nanocrystals in the film with opposite chirality. The slight difference in the peak intensity between left and right helicoidal films with 2 turns can be ascribed to small structural differences as films are not exactly identical. Moreover, as CD measurements are not carried out exactly at the same spot, the analysed film composition can vary and consequently lead to variations in the signal intensity. These observations clearly demonstrated the presence of a helicoidal arrangement of the cellulose nanocrystals within the multilayer films.

We also observed an increase of the intensity of the structural peak with the number of turns (Figure 3.25(B)). This is not surprising as the CD signal is a measure of light absorption and is consequently proportional to the concentration of optically active species. Moreover, a redshift of the reflection wavelength can be observed when the number of helical turns increases (Figure 3.25(B)). This could be attributed to the fact that these helical structures were not exactly the same as they were prepared separately.

The preparation of films composed of various cellulose nanoparticles (CNF, w-CNCs and t-CNCs) has been discussed up to now. The build-up of these films was studied as well as the microstructure and optical properties.

3.5 Mechanical properties of nanocellulose-based films

In this chapter, we prepared multilayered films with different structures combining various cellulose nanoparticles (CNFs, w-CNCs and t-CNCs) and PVAm using LbL assembly and GIS. CNF-based films were proved to be flexible and relatively easy to peel off from the hydrophobic substrates. In contrast, many difficulties were encountered when detaching the films composed of CNCs. Indeed, the precise cutting of these films was difficult arising from their brittleness. Moreover, once it was possible to detach them, they often tended to roll up. After multiple attempts, stripes of t-CNC-based films could be prepared and used for dynamic mechanical analysis (DMA) measurements. For instance, stripes of isotropic CNC-based films that were cut and detached from hydrophobic silicon substrates can be seen in Figure 3.26.

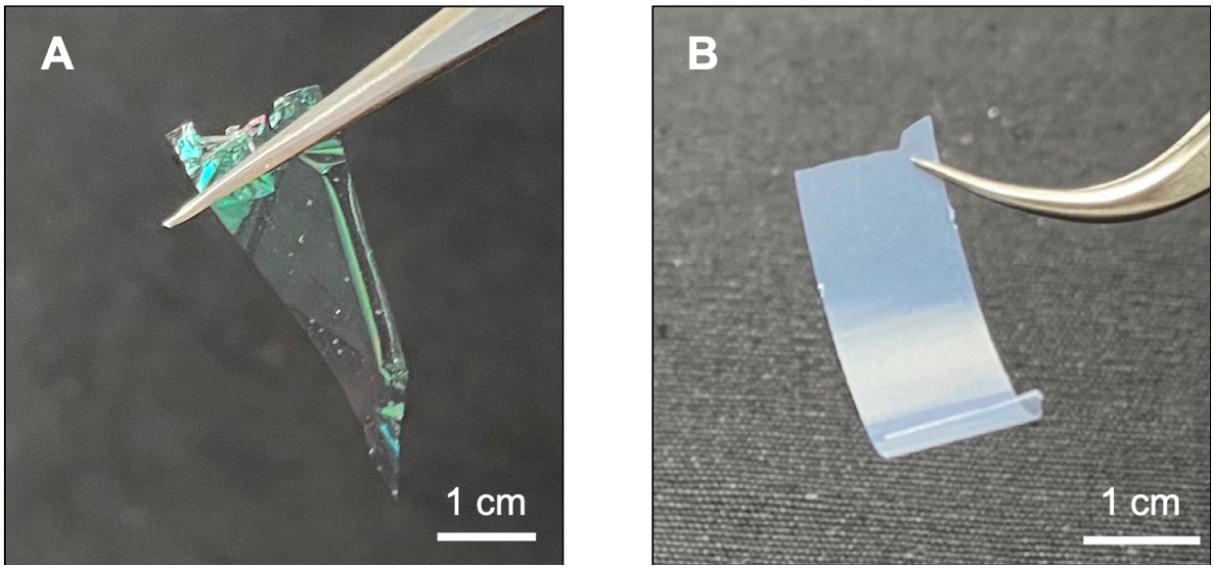

Figure 3.26: Optical photographs of transparent $(w\text{-}CNC/PVAm)_{380}$ (A) and opaque $(t\text{-}CNC/PVAm)_{300}$ (B) films prepared by dip-assisted LbL assembly.

For the DMA measurements, free-standing stripes of approximately 15 mm × 5 mm were required and were obtained by cutting and detaching films from the substrate. It should be pointed out that despite many attempts, helical structures composed of t-CNCs could not be characterized by DMA as the areas where the helical structures were formed were to small using the existing deposition process. The samples that have been prepared and successfully characterized by DMA are represented schematically in Figure 3.27.

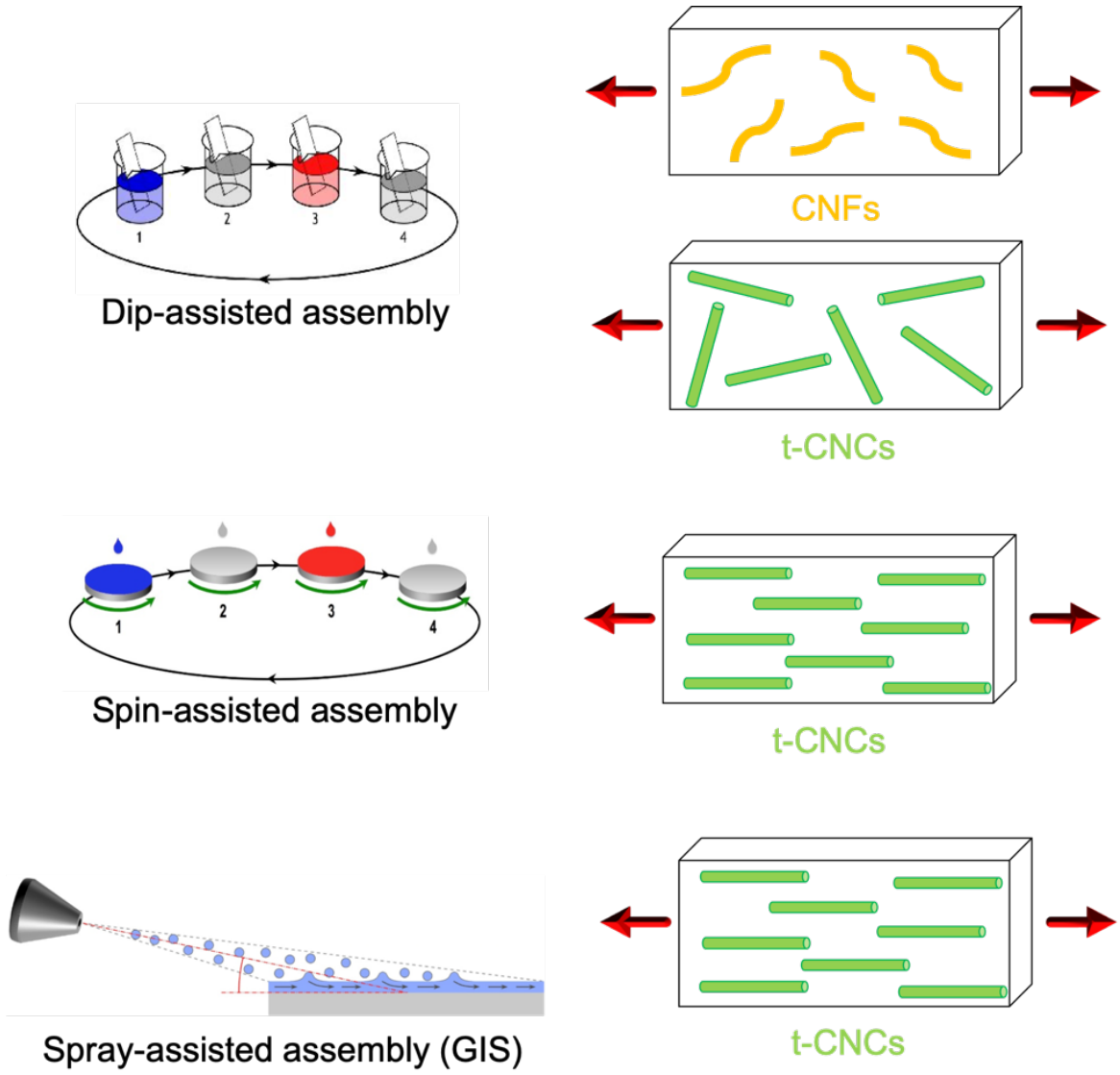

Figure 3.27: Schematic drawings of the films prepared by dipping, spin-assisted and spray-assisted (GIS) assembly using t-CNCs (green sticks) and CNFs (orange sticks) with the stretching direction applied during the DMA measurements represented by the red arrows.

Table 3.4 summarizes the values of complex modulus that have been determined by DMA.

Table 3.4: Complex modulus measured by DMA for different nanocellulose-based films prepared by various deposition methods at ambient conditions (RH∼50% and T∼22°C).

Nanocellulose	Deposition method	Thickness (μm)	pH of PVAm	E^*_{DMA} (GPa)
CNFs	Dip-assisted LbL	3.3 ± 0.1	8	∼9
t-CNCs	Dip-assisted LbL	4.3 ± 0.1	10	∼17
	Spin-assisted LbL	3.0 ± 0.3	8	∼15
	$GIS_{unidirectonal}$	5.0 ± 0.2	8	∼13
	$GIS_{unidirectional}$	5.1 ± 0.3	10	∼13

The films composed of CNCs were proved to show higher values of complex modulus compared to CNF-based films (Table 3.4). This difference could be explained by the fact that cellulose nanocrystals present a more important strength than cellulose nanofibrils coming from their higher crystallinity. A modulus of ∼15 GPa was determined by DMA measurements for t-CNC-based films. No significant influence of the film architecture on the mechanical properties was observed. This is surprising as we were expecting a significant enhancement of the mechanical properties by orienting the cellulose nanocrystals within the film.[197] The mechanical properties of these films are maybe more dependent on the porous structure than on the cellulose nanocrystals alignment and can thus explain the similar modulus obtained for these films. Further investigations would be required to find out a valid explanation.

These films were also characterized by nano-indentation to determine their elastic modulus values. Isotropic CNF-based films prepared by dipping displayed an elastic modulus ∼8 GPa, a value that is close to the modulus value determined by DMA

measurement (~9 GPa). The obtained value is in good agreement with the literature as we consider the characterization of a cellulose network.

Films composed of t-CNCs and prepared by dipping and GIS displayed elastic modulus values of 4 GPa and 5 GPa respectively. These values are significantly lower than the ones that have been measured by DMA (~15 GPa). This observation could be explained by the very important surface roughness of these t-CNC-based films that leads to inaccurate determinations of the area between the film and the indenter and thus to incorrect elastic modulus values. As the indentation depths were similar to the surface roughness of the films, significant differences could arise if the tip probes the sample or a valley or a peak of a rough feature. This phenomenon has already been observed in our group previously for rough $(CNF/PVAm)_n$ films.[112] The high porosity of these films could lead to a local collapse during the indentation (generating compression) being responsible for a underestimation of the elastic modulus determined by nano-indentation compared to DMA with a technique in traction.
That is why no conclusion can be drawn about the influence of the film architecture on the mechanical properties.

3.6 Conclusion and perspectives

The goal of this chapter was to use the LbL assembly and GIS to build cellulose-based nanocomposite materials with various structures and to study their mechanical properties. We first prepared isotropic wood-inspired multilayered films by combining different cellulose nanoparticles with a polymer matrix of poly(vinyl amine). The influence of the pH and deposition technique on the film build-up was first investigated and was proved to depend on the cellulose source. Moreover, isotropic films based on CNFs and short CNCs (w-CNCs) provided the formation of transparent and dense materials exhibiting a homogeneous dispersion of the nanoparticles. On the other hand, the use of long CNCs lead to opaque and highly porous structured films. In a second part, we used spin-assisted LbL assembly to produce oriented nanocomposite materials with high and anisotropic mechanical properties. A high degree of alignment was achieved using long CNCs whereas short CNCs and CNFs could not be oriented.

Micron-thick films composed of t-CNCs were then successfully prepared, detached from the substrates and displayed also a porous architecture. We also prepared unidirectionally and helicoidally aligned films composed of long CNCs by combining LbL assembly with the GIS methodology.

Mechanical properties of prepared multilayered films were finally characterized by DMA. Different conclusions can be drawn from obtained results. The aspect ratio and the rigidity of used cellulose nanoparticles have a significant impact on mechanical properties of films. Indeed, the use of flexible CNFs generally leads to the formation of a close-packed and low porous structure. Compared to previous results reported in our team,[178] isotropic CNF-based films displayed a lower modulus (~9 GPa) certainly arising from the use of shorter fibrils. Concerning CNC-based films, the use of long cellulose nanocrystals resulted in a porous network implying a high surface roughness. Moreover, no significant influence of the film structure on the mechanical properties could be pointed out (modulus between 13 and 17 GPa). It seems that mechanical properties of these films are mainly controlled by the foam structure and not by the orientation of cellulose nanocrystals.

As future prospects, other binding polyelectrolytes could be used in combination with these different nanocellulose particles. The interactions occurring between the polymer and nanocellulose would certainly change resulting in tunable mechanical properties. The combination of different cellulose nanoparticles within a single material could be another interesting idea in order to precisely tailor the mechanical properties. As CNC-based films appeared to be brittle, one possibility would be to combine them with flexible CNFs. In that perspective, multiple sequences of layers and also various structures can be completed by using different deposition techniques (dipping, spin-coating and GIS) within one single film. The mechanical properties of films composed of w-CNCs could also be determined and compared to the ones measured for other films. CNC-based films presenting helical structures could finally be studied further.

Chapter 4 – Development of an anisotropic strain sensor

As shown in chapter 1 there is an increasing interest in stretchable and wearable strain sensors for a wide variety of applications and especially for health monitoring.[12] Nevertheless, as the conventional sensors are not sensitive to the stretching direction, many efforts have recently been devoted to the development of multidimensional sensors that are highly demanded to detect stimuli in different directions.[198] In this respect, different strategies have been developed to align 1D-nanomaterials in the plane to prepare anisotropic architectures.[199] Among the broad range of sensing materials, silver nanowires (AgNWs) have been demonstrated to be very promising candidates for the preparation of multidimensional sensors due to their anisotropic physical properties.[200]

In the present work, the preparation of a multidimensional strain sensor composed of oriented AgNW monolayers will be presented. For this purpose, the metallic nanowires were first characterized and their alignment was carried out by grazing incidence spraying (GIS)[11] on a flexible and transparent substrate made of PDMS. The optical properties of the fabricated strain sensor were monitored by polarized UV-Visible-NIR spectroscopy and were shown to be dependent on both the stretching direction and light polarization. The development of a mathematical model based on the optical measurements finally allowed the determination of the extent and direction of a deformation.

4.1 Morphological characterization of AgNWs

AgNWs have been imaged by SEM in order to measure their size distribution. This distribution has been determined by depositing the nanowires on PEI-coated silicon wafers (Figure 4.1(A) and 4.1(B)). The size of 84 nanowires has been measured on multiple SEM images to get representative statistics. This analysis resulted in an average length of 3.3 ± 1.5 μm and an average diameter of 47 ± 7 nm (Figure 4.1(C) and 4.1(D)). The alignment of these long metallic nanowires with an aspect ratio of approximately 70 will be discussed in the next section.

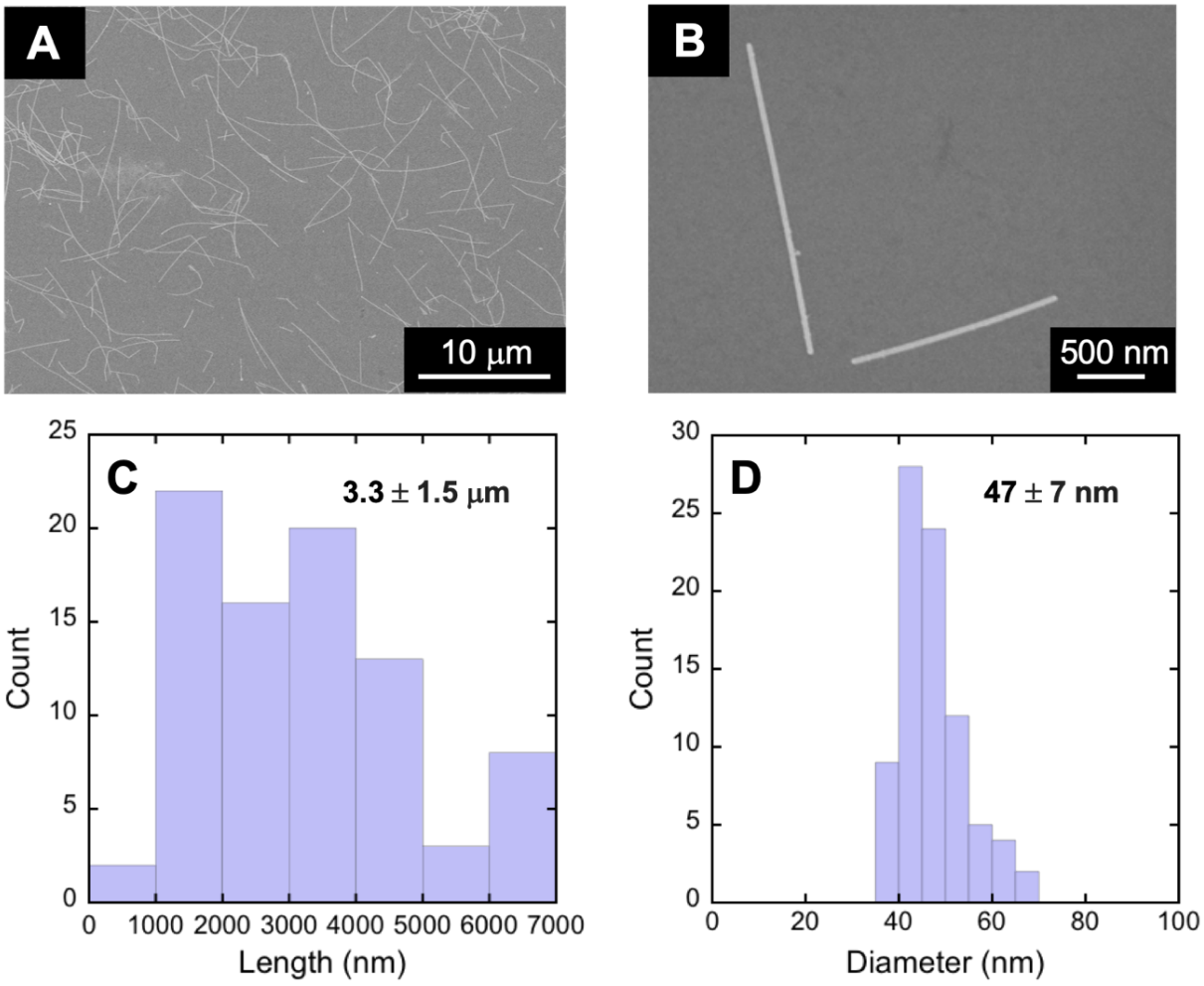

Figure 4.1: (A, B) SEM images of AgNWs deposited on PEI-coated silicon wafers at different magnifications. (C, D) Length and diameter distributions of AgNWs.

4.2 Oriented AgNW monolayers

To achieve the preparation of an anisotropic strain sensor, the in-plane alignment of the AgNWs is required. The deposition of oriented AgNW monolayers was carried out using the GIS technique on either silicon wafers or on PDMS sheets that were previously coated with an adhesion-promoting layer of PEI. The experimental conditions of the deposition were kept constants including the AgNWs concentration (C = 0.2 g/L), the liquid flow rate (L = 1 mL/min), the spraying time of the solution (t_{spray} = 50 s), the airflow rate (A = 30 L/min), the distance between the nozzle and the sample (d = 1 cm) and the incidence angle (α = 10°). SEM images of oriented AgNW monolayers prepared by GIS on a silicon wafer and on a PDMS substrate are shown in Figure 4.2.

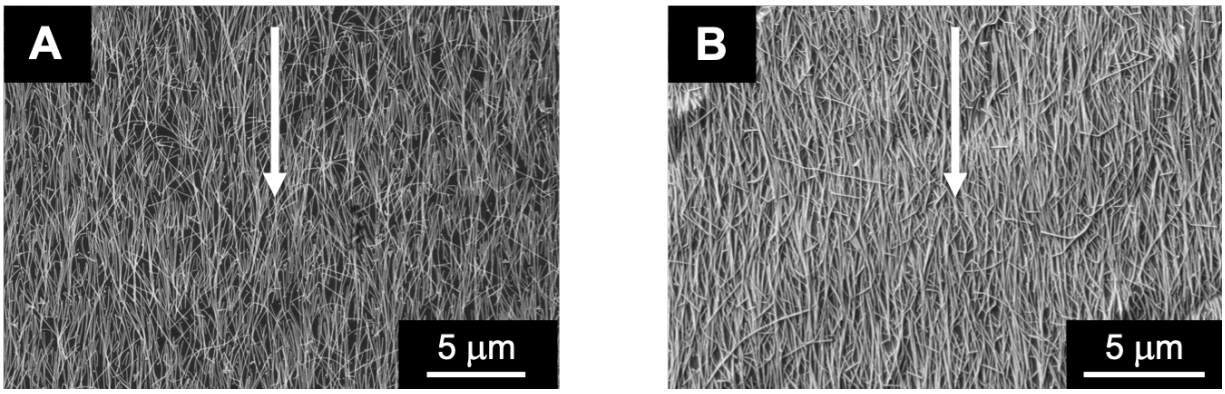

Figure 4.2: SEM images of oriented AgNW monolayers deposited by GIS for 50 s of spraying on a PEI-coated (A) silicon wafer and (B) PDMS substrate with the same experimental conditions. The white arrows indicate the spraying direction.

The degree of orientation of the deposited AgNWs was quantified using the plug-in OrientationJ[177] developed for ImageJ.[178] A local orientation is determined for each image pixel based on its local neighborhood. The images are color-coded according to the local orientation, and the distribution of the angle θ between each pixel and the main orientation in the sample can be determined. A 2D nematic order parameter (S_{2D}) can then be calculated from this angular distribution (Equation 4.1) for each sample.

$$S_{2D} = \langle 2\ \cos^2(\theta) - 1 \rangle \qquad \textbf{Equation 4.1}$$

The analysis of multiple SEM images using OrientationJ plug-in revealed a good in-plane alignment of the metallic nanowires on both surfaces with an order parameter S_{2D} of 0.78 ± 0.03 when deposited on silicon wafers (Figure 4.2(A)) and of 0.83 ± 0.02 when deposited on PDMS substrates (Figure 4.2(B)).

It is important to note that these pictures were not taken with the same microscope as the monolayers deposited on silicon wafers were imaged in our lab while the ones deposited on PDMS were imaged at the Leibniz-Institut für Polymerforschung in Dresden. Consequently, the acquisition time, the electron detectors and the applied voltage were not the same. The variation of these parameters can explain why AgNWs appear larger when deposited on PDMS.

AgNWs were efficiently aligned on PDMS substrates using the GIS technique. In addition to sensing materials, the preparation of a strain sensor also requires the

selection of a stretchable substrate. In the present work, we decided to use PDMS, a transparent elastomer, that has already been widely employed in strain sensors for a wide range of applications including human motion detection (heart rate, respiration, muscle movements), environment monitoring (humidity, temperature, pressure) or soft robotics.[202] The deformation of a material like PDMS in the direction perpendicular to the specific direction of loading is characterized by its Poisson's ratio. The determination of the Poisson's ratio of this elastomer will now be discussed.

4.3 Mechanical characterisation of the PDMS substrate

The Poisson's ratio of a material is a very important physical parameter as it defines its contraction perpendicular to the stretching direction as illustrated in Figure 4.3 in a plane view.

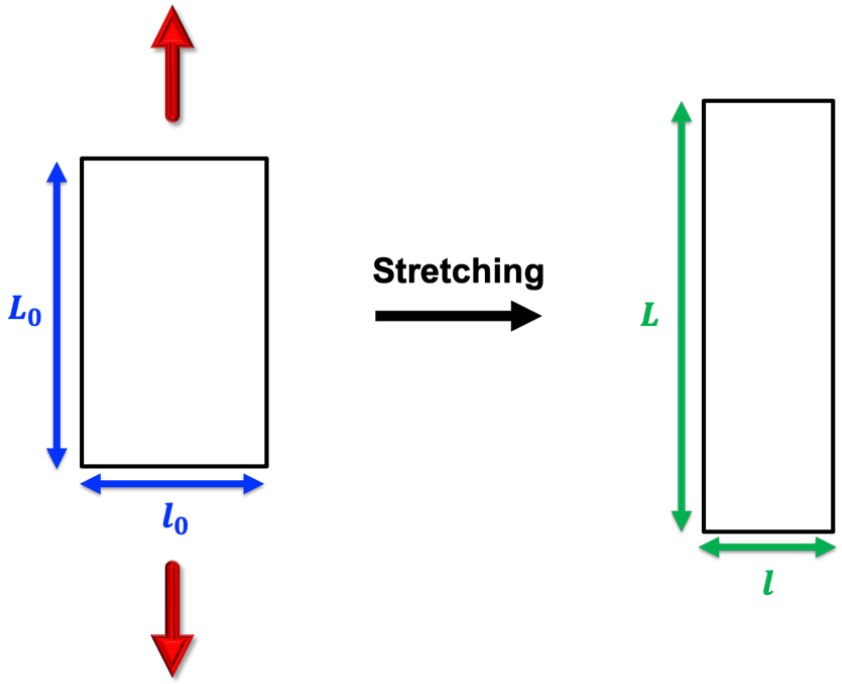

Figure 4.3: Simplified schematic drawing of a rectangular-shaped PDMS substrate before (l_0, L_0) and after (l, L) applying a uniaxial stretching represented by the red arrows and highlighting the contraction of the material in the direction perpendicular to the applied strain.

The Poisson's ratio is theoretically defined in all dimensions of space. However, as the thickness of the used PDMS sheets (~0.25 mm) is very low compared to their length and width (a few cm), the Poisson's ratio can be considered only in the plane.
In the case of PDMS, this ratio (ϑ_{PDMS}) has been reported to be close to 0.50[201] corresponding to an incompressible material and can be expressed as function of the dimensions of the substrate before and after stretching using Equation 4.2.

$$\vartheta_{PDMS} = -\frac{dl/l_0}{dL/L_0} = -\frac{(l-l_0)/l_0}{(L-L_0)/L_0} \qquad \textbf{Equation 4.2}$$

Nevertheless, whereas this Poisson's ratio is assumed to be constant in the small strain regime, it is usually defined as a function of the applied deformation in the large strain regime.[203] Different Poisson's ratios have been developed previously including the commonly used Hencky function that can be expressed by Equation 4.3.

$$\vartheta_{PDMS} = -\frac{ln\,(l/l_0)}{ln\,(L/L_0)} \qquad \textbf{Equation 4.3}$$

To determine the Poisson's ratio of the used PDMS experimentally, different PDMS sheets with different dimensions were prepared and points were marked on the surface of the elastomer to monitor its contraction during uniaxial stretching. The displacement of these points on a dog-bone shaped PDMS sheet during its stretching can be seen for instance in Figure 4.4.

To do so a home-made stretching device was developed with two metallic jaws whose movement was controlled by a single screw providing the same strain in both directions along the X-axis. The displacement of these points on a dog-bone shaped PDMS sheet during its stretching can for instance be seen in Figure 4.5. The distance between the points in the stretching direction (x_0, x) and perpendicular to it (y_0, y) for each applied strain was measured using the software ImageJ.

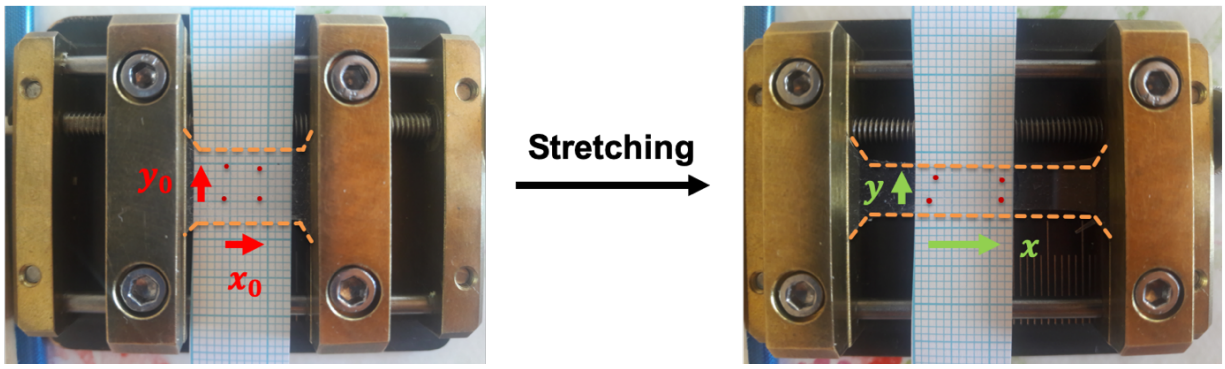

Figure 4.4: Optical photographs of a PDMS sheet with a dog-bone shape fixed at the two jaws of the homemade stretching device before and after uniaxial stretching. The orange dashed line highlights the shape of the transparent PDMS sheet. The position of the red points is measured as function of the strain applied to determine the Poisson's ratio.

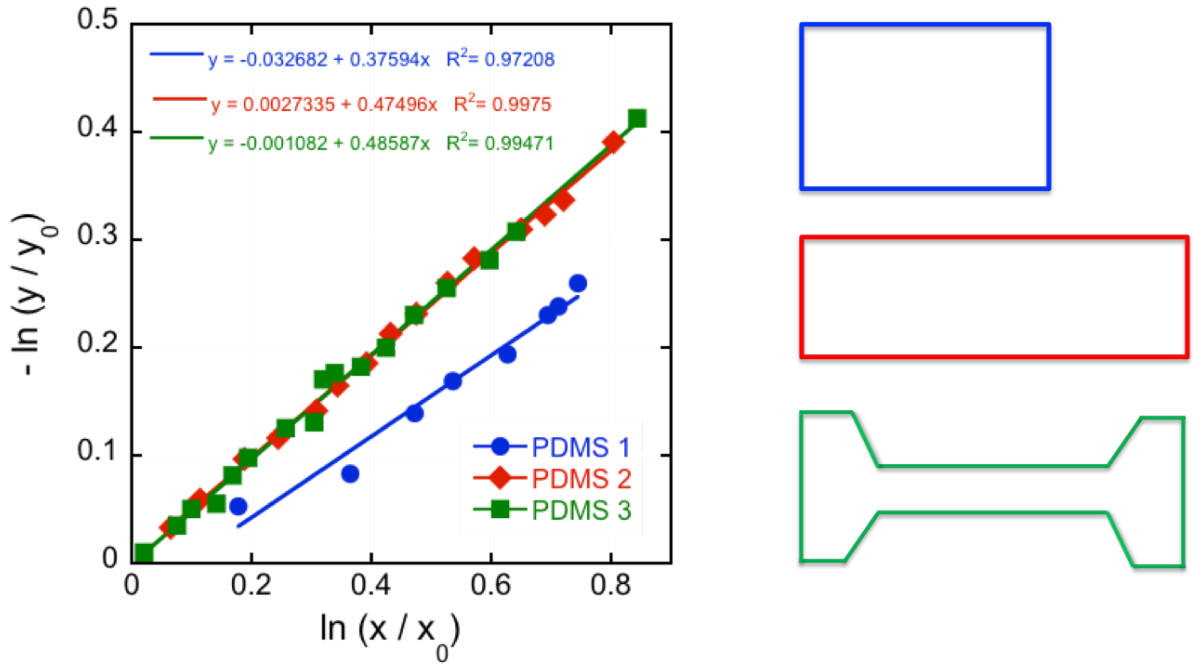

Figure 4.5: Transverse strain $-ln\,(^{y}/_{y_0})$ as function of the applied longitudinal strain $ln\,(^{x}/_{x_0})$ for three PDMS sheets. PDMS 1 and PDMS 2 correspond to rectangular-shaped sheets with respective initial length/width ratios of 1.5 and 3 while PDMS 3 corresponds to a dog-bone shaped sheet.

Equation 4.3 can now be rewritten as function of the distances measured between the points in the stretching direction and perpendicular to it (Equation 4.4).

$$\vartheta_{PDMS} = -\frac{ln\,(^{y}/_{y_0})}{ln\,(^{x}/_{x_0})} \qquad \textbf{Equation 4.4}$$

The Poisson's ratio can therefore be determined by plotting $-ln\,(^{y}/_{y_0})$ as function of $ln\,(^{x}/_{x_0})$ for PDMS sheets of different shapes (rectangular or dog-bone) and dimensions (Figure 4.5). Both PDMS 1 and PDMS 2 were rectangular-shaped but their dimensions were different. Indeed, the length/width ratio was about 1.5 for PDMS 1 and about 3 for PDMS 2. PDMS 3 was finally cut in a dog-bone shape as it is usually used for tensile tests, considering the narrowest calibrated section for measurements. Indeed, the sample is clamped between jaws that prevent the contraction of the sample in the transverse direction at the end of the sample. Analysis of the linear regressions of the different samples in Figure 6 leads to ϑ_{PDMS} values of 0.38, 0.47 and 0.49 for PDMS 1, PDMS 2 and PDMS 3 respectively. As PDMS 2 and 3 gave similar results which are in agreement with the expected value for ϑ_{PDMS} (close to 0.5), we decided in the following work to use PDMS sheets with a rectangular shape presenting a length/width ratio of 3 ($\vartheta_{PDMS} \approx 0.5$) as the manual cutting of the PDMS sheets in a dog-bone shape was difficult to reproduce precisely.

As the aim of this work consists in the preparation of an anisotropic strain sensor, the degree of orientation of the silver nanowires deposited on PDMS was also studied upon film stretching. We investigated the structure change of aligned metallic monolayers with a strain applied either parallel or perpendicular to the nanowire orientation (Figure 4.6(G)).

AgNW monolayers prepared on PDMS were stretched in-situ at a speed of 1 mm/min from 0% to 40% of its length with an intermediate step of 10% using a stretching device that was incorporated in a NEON 40 FIB-SEM workstation. This work was carried out in collaboration with the Leibniz-Institut für Polymerforschung in Dresden.

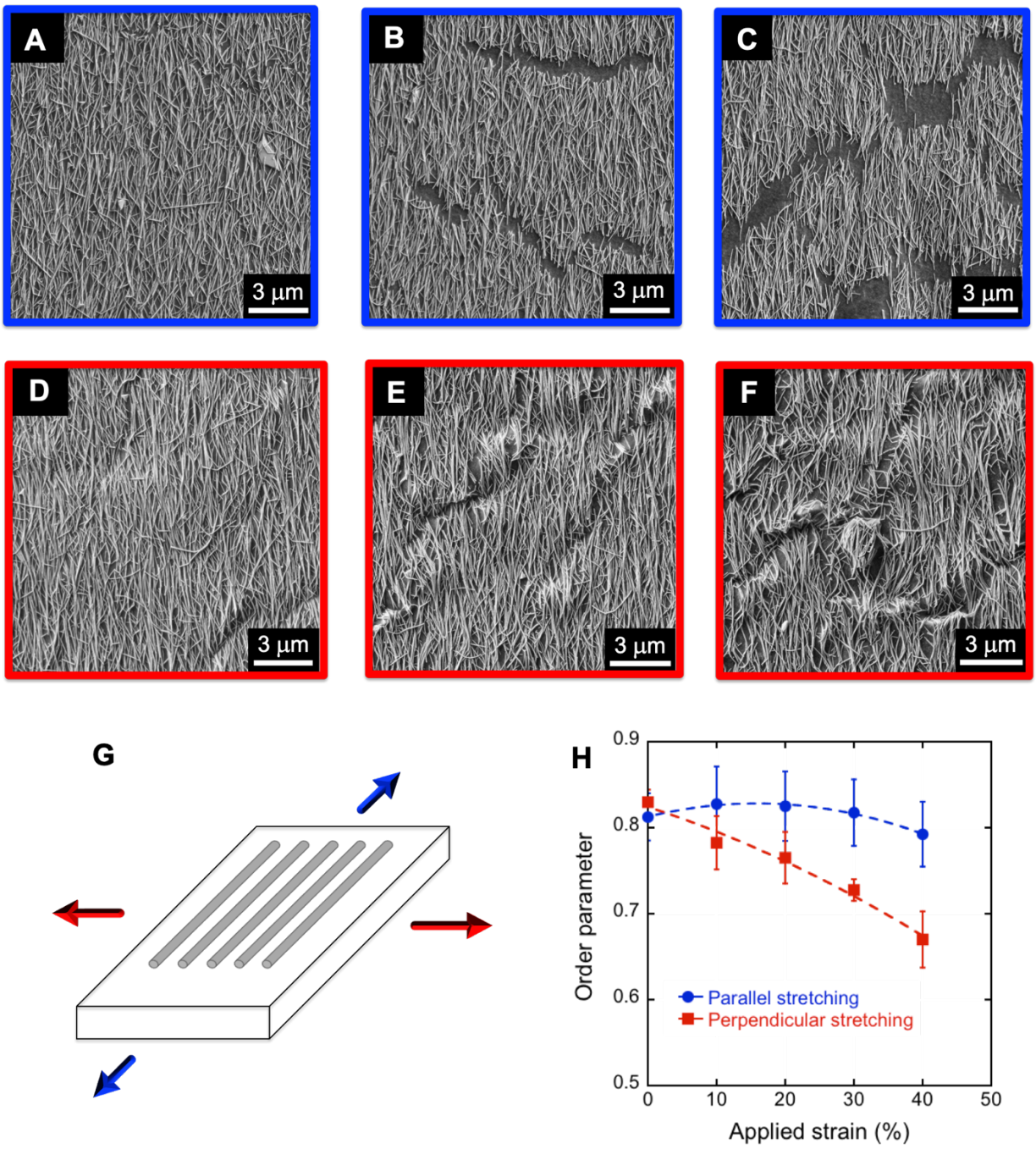

Figure 4.6: SEM images of aligned AgNW monolayers during a uniaxial stretching applied in the direction parallel to the nanowire orientation: (A) before strain, (B) after 10% and (C) after 30% of applied strain and in the direction perpendicular to the nanowire orientation: (D) before strain, (E) after 10% and (F) after 30% of applied strain. (G) Schematic illustration of a stretching applied perpendicular and parallel to the nanowire orientation. (H) Order parameter as function of applied strain for the two different stretching directions (parallel (blue dots) or perpendicular (red squares)) during the film stretching. Dashed curves are just a guide for the eye.

For a strain applied along the AgNW alignment direction (Figure 4.6(A), 4.6(B) and 4.6(C)), the order parameter remained close to 0.80 between 0% and 40% of applied strain meaning that the alignment quality was preserved during stretching (blue curve in Figure 4.6(H)). This is not surprising as the strain is applied in the same direction as the nanowire orientation. On the other hand, the degree of orientation decreased significantly upon stretching when the strain was applied perpendicular to the nanowire orientation (Figure 4.6(D), 4.6(E) and 4.6(F)). Indeed, the order parameter decreased from 0.83 to 0.65 as the applied strain increased from 0% to 40% (red curve in Figure 4.6(H)). This decrease can be attributed to the contraction of PDMS perpendicular to the stretching direction inducing a reorientation of some of the AgNWs.[204]

These microscopic investigations also revealed an influence of the stretching direction on the microstructure of the metallic oriented monolayers. For a strain applied in the same direction than AgNWs, a significant structure change was observed as cracks appeared perpendicular to the stretching direction (Figure 4.6(B) and 4.6(C)). The density and width of these cracks increased with the applied strain. This observation has already been reported in the literature for the preparation of strain sensors composed of oriented AgNW thin films on soft substrates.[204] The generation of these cracks was attributed to the low fracture strain (~2-4% for nanowire diameters ranging from 38 nm to 130 nm) of the single AgNWs in tensile mode.[205] The formation of these cracks also showed the good adhesion of the nanowires on PDMS as they were preferentially breaking than sliding on the substrate. For a strain applied in the direction perpendicular to the nanowire orientation, a buckling of the film can be observed especially for important applied strains (Figure 4.6(E) and 4.6(F)) and arise from the contraction in the direction perpendicular to the stretching direction.

Another important point is to verify that the strain applied to the PDMS substrate is transferred to the deposited oriented AgNW monolayers.
For a strain applied in the same direction as the nanowire orientation (Figure 4.7(A)), the average distance between 100 neighboring nanowires was measured manually on ImageJ and was proven to decrease upon stretching with a distance of 157 nm before the application of the strain and a distance of 128 nm after 40% of strain (Figure 4.7(B)). This decrease was expected as the strain was applied along the AgNW alignment direction and induced a contraction of the film in the perpendicular direction.

Consequently, as the nanowires are well attached to the substrate, they are expected to come closer to each other during stretching. By assuming a Poisson's ratio of ~0.5 for PDMS (value determined experimentally before), the expected distance decrease between AgNWs can be estimated and compared to the values obtained from microscopy measurements. A good agreement was observed between experimental and theoretical data.

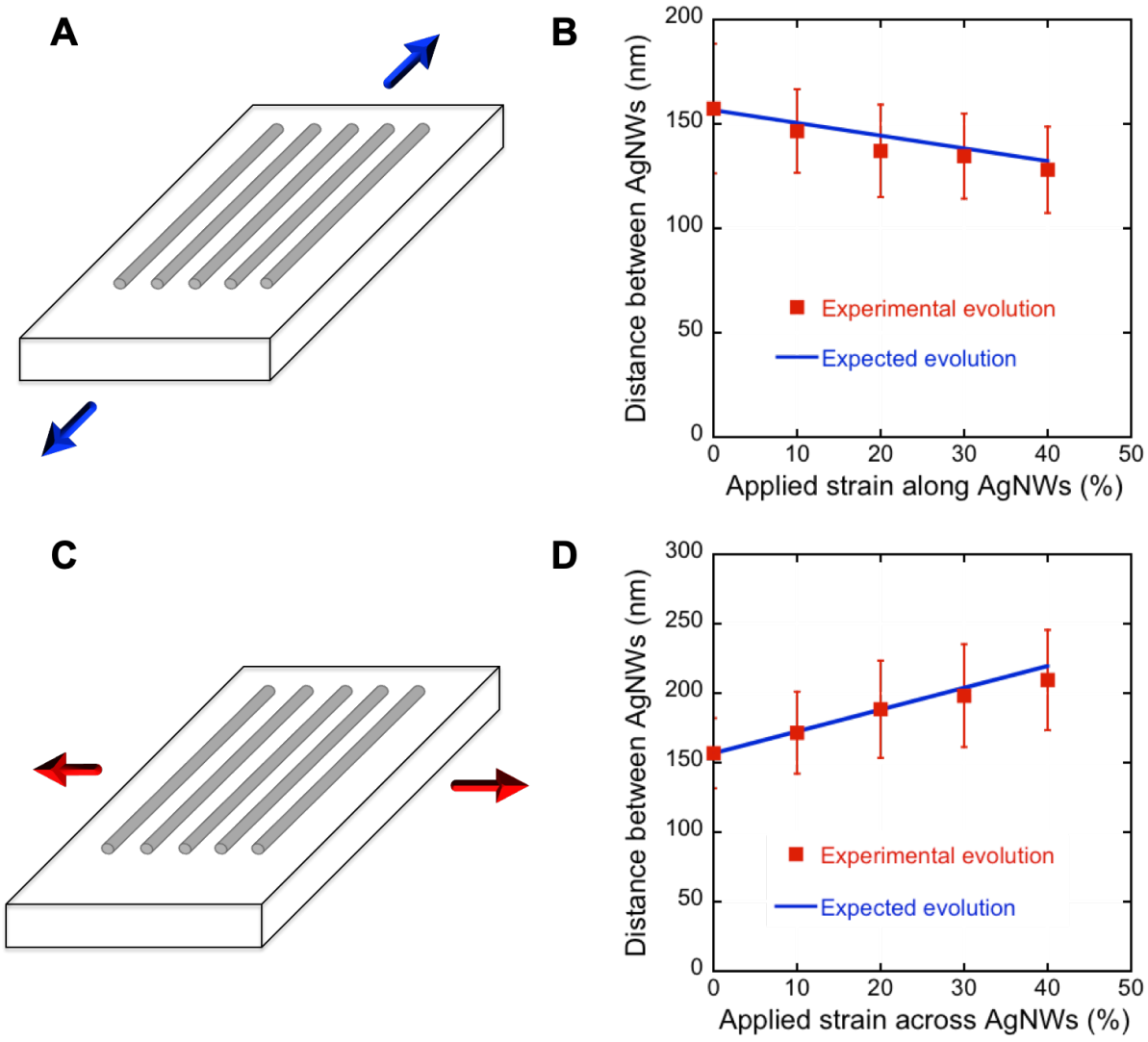

Figure 4.7: Schematic illustrations of a stretching applied parallel (A) and perpendicular (C) to the nanowire orientation. Variation of the distance between two neighboring AgNWs upon stretching for strains applied along (B) and across (D) AgNWs.

For a strain applied in the direction perpendicular to the stretching direction (Figure 4.7(C), the average distance between 100 neighboring nanowires increased from 157 nm before stretching to 210 nm at 40% of applied strain (Figure 4.7(D)). This increase

of the average distance between the nanowires was expected as the strain was applied perpendicular to them. Moreover, the variation of the interparticle distance can be expected by considering that the application of a specific strain to the sample will be transferred to the AgNWs. The comparison between the experimental and expected change (Figure 4.7(D)) revealed a good agreement proving the efficient strain transfer from the macro- to nanoscale level when the strain is applied perpendicular to the nanowire orientation direction.

These microscopic investigations showed the efficient transfer of the macroscopic applied strain at the nanoscale level and from the PDMS elastomeric substrate to the AgNW layer. Moreover, as previously reported in the literature, different deformation mechanisms could be pointed out.[204] Indeed, for a strain applied perpendicular to the AgNW alignment direction, nanowires were exposed to compressive stress coming from the contraction of PDMS in the perpendicular direction. On the other hand, they were subjected to tensile stress when the strain was applied in the same direction resulting in the appearance of cracks perpendicular to the stretching direction. Combined to the anisotropic optical response of oriented AgNW thin films, these results served as a basis for the development of a multidirectional strain sensor by using silver nanowires as an optical probe and PDMS as a transparent and deformable substrate. In the next section, a model will be developed to retrieve the direction and magnitude of the applied strain from the measured polarized absorbance spectra of an oriented AgNW layer deposited on a stretchable substrate that is stretched in an arbitrary direction.

4.4 Linking the anisotropic optical properties to the applied strain

The aim of this work is to prepare an anisotropic strain sensor which can measure any applied strain and its direction. The AgNWs can be sprayed on an arbitrary stretchable sample, and the anisotropic optical properties under linearly polarized light can be used to retrieve the direction at which the strain is locally applied with respect to the alignment direction and its magnitude. In working conditions, it will thus only be

necessary to know the direction of orientation of the nanowires, and to measure the polarized absorbance before and after stretching. However, to demonstrate the feasibility and investigate the accuracy of such a sensor, we will stretch the substrate at a known angle with respect to the AgNW orientation direction.

Let's assume an arbitrary angle α between the stretching direction and the AgNW alignment direction (Figure 4.8).

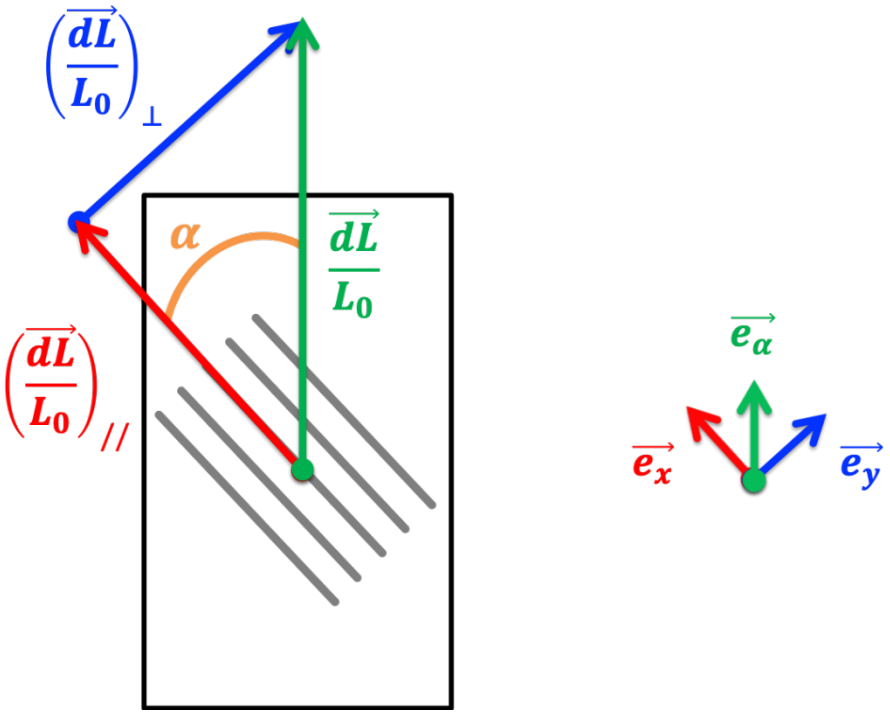

Figure 4.8: (left) Schematic drawing of an oriented AgNW monolayer (grey sticks) on PDMS subjected to a strain $\frac{\overrightarrow{dL}}{L_0}$ (green vector) with an angle α between the stretching direction and the nanowire orientation. (right) Corresponding unit vectors $\overrightarrow{e_\alpha}$, $\overrightarrow{e_x}$ and $\overrightarrow{e_y}$.

In that case, the applied strain $\frac{\overrightarrow{dL}}{L_0}$ can be geometrically decomposed into a strain applied parallel to the AgNW alignment direction $\left(\frac{\overrightarrow{dL}}{L_0}\right)_{//}$ and a strain applied perpendicular to the AgNW alignment direction $\left(\frac{\overrightarrow{dL}}{L_0}\right)_{\perp}$ (Equation 4.5).

$$\frac{\overrightarrow{dL}}{L_0} = \left(\frac{\overrightarrow{dL}}{L_0}\right)_{//} + \left(\frac{\overrightarrow{dL}}{L_0}\right)_{\perp} \qquad \textbf{Equation 4.5}$$

These vectors can be expressed using the unit vectors $\overrightarrow{e_\alpha}$, $\overrightarrow{e_x}$ and $\overrightarrow{e_y}$ (Equation 4.6).

$$\frac{dL}{L_0}\overrightarrow{e_\alpha} = \left(\frac{dL}{L_0}\right)_{//}\overrightarrow{e_x} + \left(\frac{dL}{L_0}\right)_{\perp}\overrightarrow{e_y} \qquad \textbf{Equation 4.6}$$

$\left(\frac{dL}{L_0}\right)_{//}\overrightarrow{e_x}$ and $\left(\frac{dL}{L_0}\right)_{\perp}\overrightarrow{e_y}$ can then be expressed along one single unit vector $\overrightarrow{e_\alpha}$ by projection (Equation 4.7).

$$\frac{dL}{L_0}\overrightarrow{e_\alpha} = cos(\alpha) \times \left(\frac{dL}{L_0}\right)_{//}\overrightarrow{e_\alpha} + sin(\alpha) \times \left(\frac{dL}{L_0}\right)_{\perp}\overrightarrow{e_\alpha} \qquad \textbf{Equation 4.7}$$

The strain sensor is based on the measurement of the optical properties of the anisotropic metallic network during stretching. We will use the extinction in the following expressions, which includes the reflection, absorption and scattering of the thin films. The extinction change measured upon stretching at a specific angle α can be decomposed into an extinction change due to the stretching along the nanowires and an extinction change due to the stretching across the nanowires (Figure 4.9).

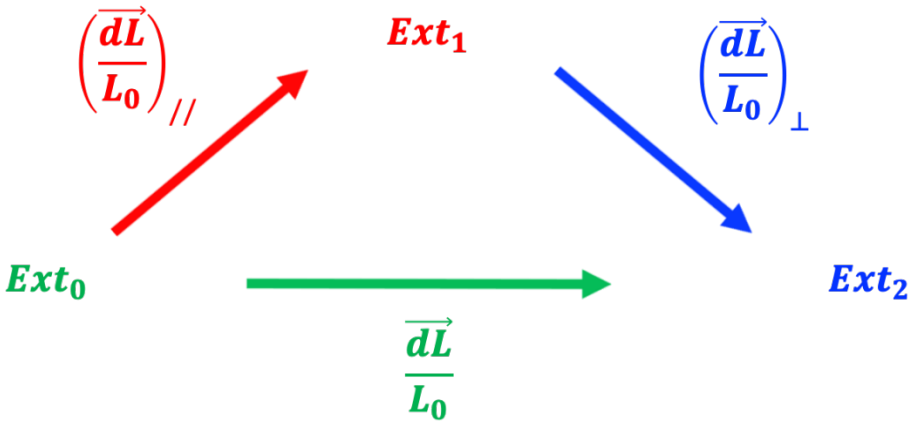

Figure 4.9: Schematic drawing of the extinctions during the stretching of an oriented AgNW monolayer with an angle α between the nanowire orientation and the stretching direction.

The extinction variation at an angle α can therefore be expressed using Equation 4.8 with Ext_0 the extinction of the sample before the application of the strain, Ext_1 the extinction after the stretching along the AgNWs and Ext_2 the extinction after the stretching across the AgNWs.

$$\frac{Ext_2}{Ext_0} = \frac{Ext_1}{Ext_0} \times \frac{Ext_2}{Ext_1} \qquad \textbf{Equation 4.8}$$

Equation 4.8 can be rewritten in Equation 4.9 to show more clearly the extinction variation due to a strain applied parallel to the nanowire orientation $\left(\frac{Ext}{Ext_0}\right)_{//}$ and the extinction variation due to a strain applied perpendicular to the nanowire orientation $\left(\frac{Ext}{Ext_0}\right)_{\perp}$.

$$\frac{Ext}{Ext_0} = \left(\frac{Ext}{Ext_0}\right)_{//} \times \left(\frac{Ext}{Ext_0}\right)_{\perp} \qquad \textbf{Equation 4.9}$$

The aim of this work is to find out the applied strain $\frac{dL}{L_0}$ and its direction given by the orientation angle α from the extinction change $\frac{Ext}{Ext_0}$ of the sample measured by spectroscopy. To do so, we will use the polarization-dependent optical properties of oriented AgNWs and study them upon stretching in the direction parallel and perpendicular to the silver nanowire orientation.

4.5 Optical properties of aligned AgNWs

The optical properties of oriented AgNW monolayers on PDMS substrates were investigated by UV-Visible-NIR spectroscopy. The extinction spectra of oriented silver nanowires on PDMS measured with unpolarized light displayed three characteristic features due to the localized surface plasmon resonances (LSPR) of AgNWs (green spectrum in Figure 4.10(B)). While the two peaks in the UV range (350 and 380 nm) are assigned to the transverse LSPR modes, the broad band starting at around 650 nm and extending towards the near infrared region can be attributed to the longitudinal LSPR mode.[164]

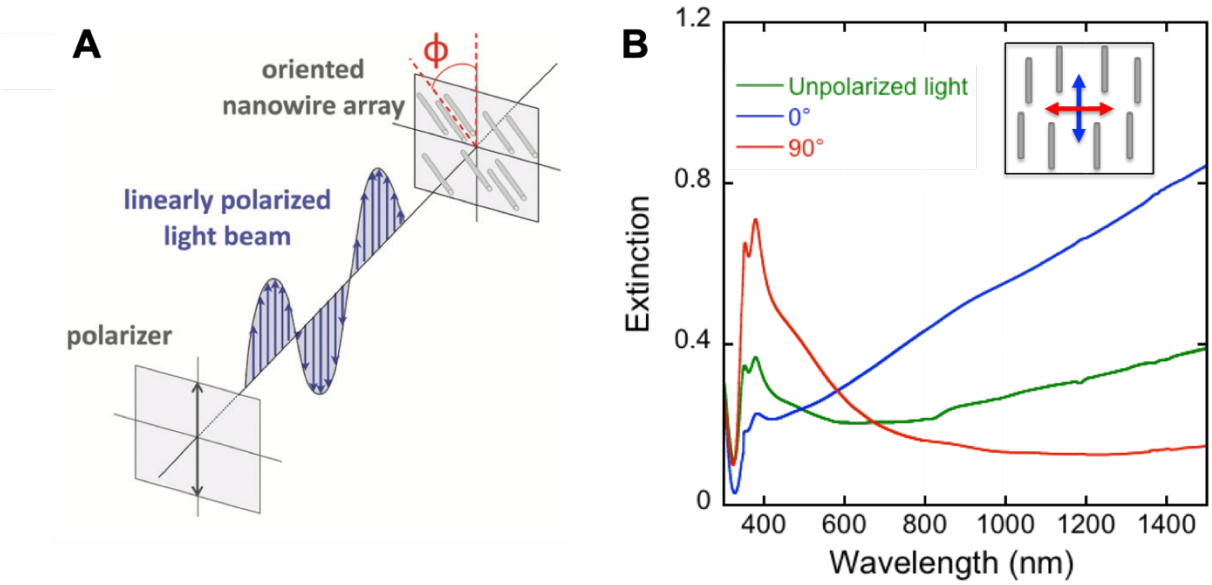

Figure 4.10: (A) Schematic illustration of polarized UV-Visible-NIR measurements highlighting the angle ϕ between the nanowire orientation direction and the light polarization plane.[163] (B) UV-Visible-NIR spectra of an oriented AgNW monolayer on PDMS (grey sticks) with unpolarized light (green), with light polarized along the nanowire orientation (blue) and across the nanowire orientation (red).

The use of linearly polarized light allows the selective excitation of the transverse and longitudinal LSPR modes of AgNWs. Indeed, oriented AgNWs display important light polarization effects that depend on the direction of the transverse and longitudinal LSPR modes of the nanowires. When the light polarization is parallel to the nanowire alignment direction, the longitudinal plasmon band is excited and is associated to a high extinction in the near infrared region (blue spectrum in Figure 4.10(B)). On the other hand, the transverse mode is excited when the polarization is perpendicular to the AgNW orientation and provides extinction peaks between 350 and 380 nm (red spectrum in Figure 4.10(B)). The anisotropic optical properties of oriented AgNW monolayers were used in the present work to develop a direction-sensitive strain sensor. In that perspective, the influence of the stretching direction and the light polarization on the optical properties of AgNW monolayers were studied (Figure 4.11). The stretching (S) and light polarization (P) were defined with respect to the nanowire orientation (parallel (//) or perpendicular (⊥)) and can be described by four configurations reported as S//P//, S//P⊥, S⊥P// and S⊥P⊥.

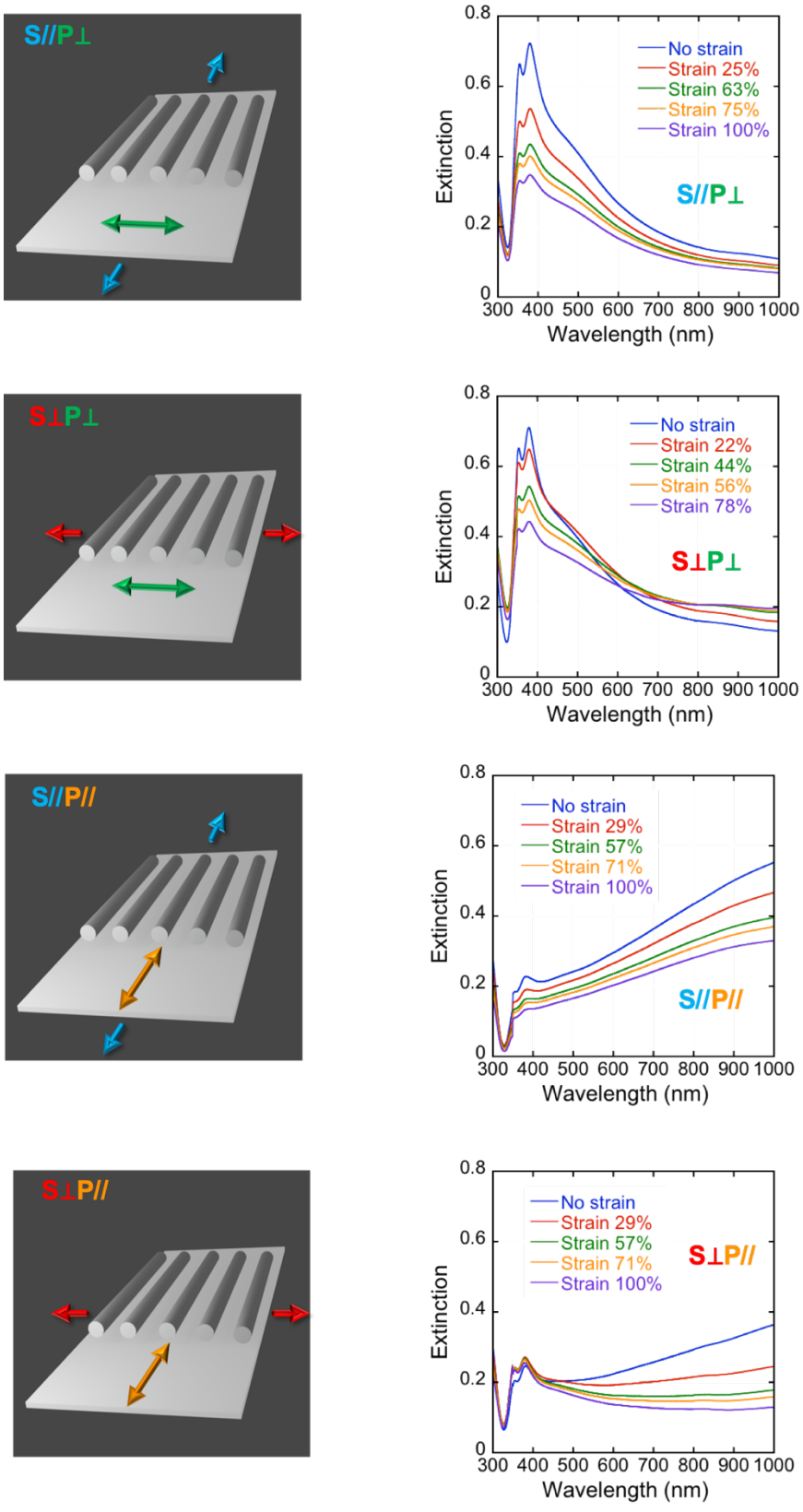

Figure 4.11: Schematic illustrations (left) and corresponding UV-Visible-NIR extinction spectra upon film stretching (right) for each configuration (S//P⊥, S⊥P⊥, S//P// and S⊥P//) with the stretching directions (S) represented by blue and red arrows and the polarization directions (P) with the green and orange double arrows.

For each configuration, the measured extinction decreased progressively upon film stretching. This decrease was attributed at first sight to a decrease of the density of nanowires per unit area induced by the geometric structure change of PDMS during stretching. Indeed, it is known that during uniaxial deformation, PDMS stretches around two times more in the stretching direction than it contracts in the perpendicular direction as quantified by its Poisson's ratio. This provided an increase of the PDMS surface, and as the number of AgNWs remained constant, their density consequently decreased during stretching.

In order to ascertain if these extinction decreases were only due to a density variation, the extinction change of a model sample of PDMS colored with a red dye was monitored as function of the applied strain in the next section.

4.6 Optical properties of a colored PDMS upon stretching

To ascertain the density change during stretching, a red silicone-based dye (Holcosil) was added during PDMS curing providing a homogeneous bulk coloring of the film (Figure 4.12(A)).

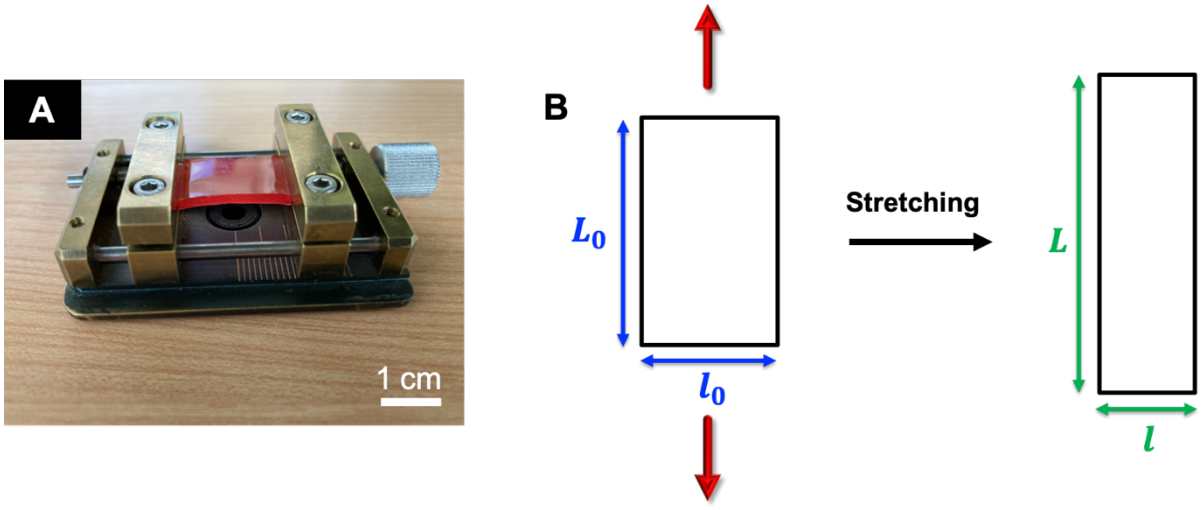

Figure 4.12: (A) Optical photograph of the red-colored PDMS film fixed at the two jaws of the homemade stretching device. (B) Schematic illustration of the uniaxial stretching of a PDMS film showing the transformation of the dimensions before (l_0, L_0) and after stretching (l, L).

The extinction change of the colored elastomeric film can be evaluated by geometrical considerations. As illustrated in Figure 4.12(B), the surface area of the film before (S_0) and after applying a uniaxial strain (S) can first be respectively calculated using Equations 4.10 and 4.11.

$$S_0 = L_0 \times l_0 \qquad \textbf{Equation 4.10}$$

$$S = L \times l \qquad \textbf{Equation 4.11}$$

As the measured extinction of the film is inversely proportional to the surface area, we can express the ratio between the extinction at a stretched state (Ext) and the extinction before stretching (Ext_0) using Equation 4.12.

$$\frac{Ext}{Ext_0} = \frac{L_0 \times l_0}{L \times l} \qquad \textbf{Equation 4.12}$$

By using the relation of the Poisson's ratio $(\vartheta_{PDMS} = -\frac{ln\,(l/l_0)}{ln\,(L/L_0)})$, we can express the ratio l/l_0 as function of ϑ_{PDMS} (Equation 4.13).

$$\frac{l}{l_0} = \left(\frac{L}{L_0}\right)^{-\vartheta_{PDMS}} \qquad \textbf{Equation 4.13}$$

The extinction change can be finally expressed as function of the applied strain and the Poisson's ratio (Equation 4.14).

$$\frac{Ext}{Ext_0} = \frac{L_0}{L} \times \left(\frac{L}{L_0}\right)^{\vartheta_{PDMS}} = \left(1 + \frac{dL}{L_0}\right)^{\vartheta_{PDMS}\,-\,1} \qquad \textbf{Equation 4.14}$$

To verify this relation between the extinction change and the applied strain, the colored film was stretched progressively and the corresponding visible extinction spectra upon stretching was acquired using unpolarized light (Figure 4.13(A)). The recorded spectra showed a progressive decrease of the maximal extinction measured at 584 nm with

the applied strain. As the density of dye molecules decreased upon stretching it was expected to observe an extinction decrease. This extinction decrease was proved to be in good agreement with the theoretical change considering Equation 4.14 (Figure 4.13(B)). The good agreement between the experimental and expected variations also validate our hypothesis on the small thickness change of the film during stretching. Indeed, if the thickness change had been significant, we would have observed a differences between the two extinction changes.

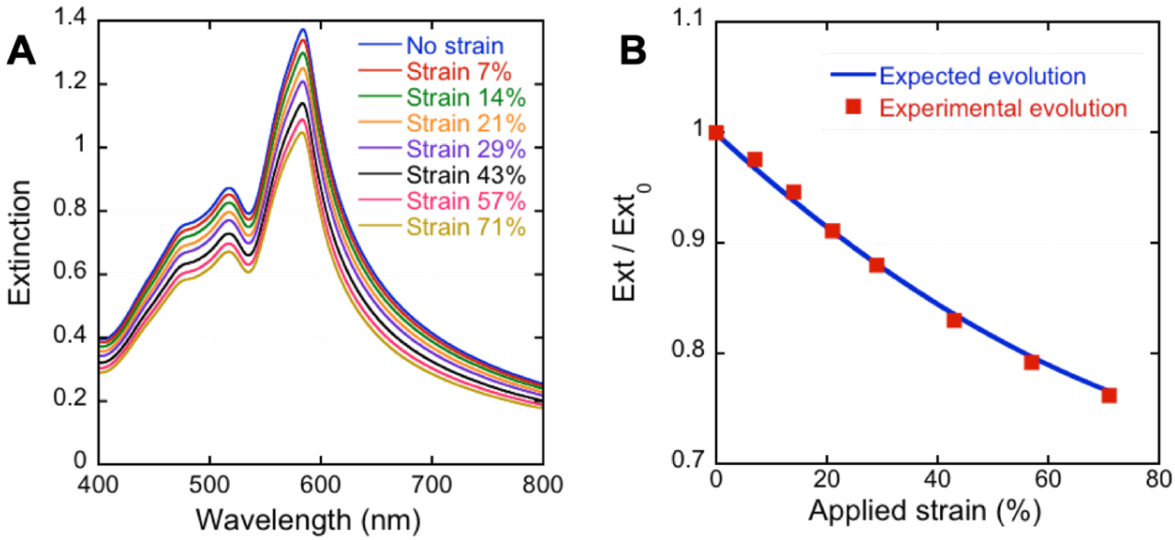

Figure 4.13: (A) Visible extinction spectra of the red-colored PDMS film upon stretching. (B) Comparison between the theoretical and experimental extinction changes upon stretching.

The extinction change measured for the colored PDMS film was compared to the one measured for AgNW monolayers. An isotropic monolayer was first prepared by spraying the nanowire solution on a PEI-coated PDMS substrate by orthogonal spraying. The optical properties of the sample upon stretching were monitored by spectroscopy with unpolarized light at 380 nm and 1000 nm (Figure 4.14(A)). The extinction change of the sample was proved to decrease similarly for both wavelengths and more importantly than the extinction of a colored PDMS.

The extinction change of the oriented AgNW monolayers (Figure 4.11) during stretching was then investigated by spectroscopy using polarized light (Figure 4.14(B)). The extinction change was monitored at 380 nm when the transverse modes of the nanowires were preferentially excited (S//P⊥, S⊥P⊥) and at 1000 nm when the longitudinal mode of the nanowires was preferentially excited (S//P//, S⊥P//).

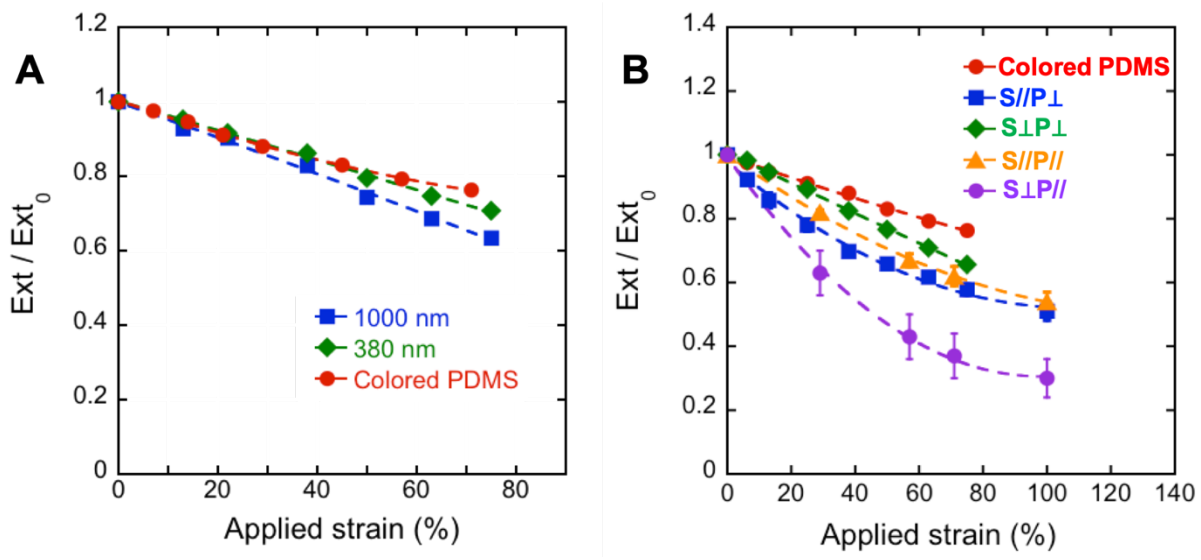

Figure 4.14: Extinction change as function of the applied strain for a colored PDMS film and for (A) an isotropic AgNW monolayer at 380 nm and 1000 nm (unpolarized light) and for (B) oriented AgNW monolayers with different stretching directions and light polarizations (S//P⊥, S⊥P⊥, S//P// and S⊥P//). The extinction change of the oriented AgNW monolayers was extracted from the UV-Visible-NIR extinction spectra presented in Figure 4.11. The extinction change was measured at 380 nm for configurations S//P⊥ and S⊥P⊥ and at 1000 nm for configurations S//P// and S⊥P//.

Different conclusions can be drawn from the results presented in Figure 4.14. As the extinction decrease was more important for all PDMS films coated with AgNW monolayers than for the colored PDMS, we can conclude that the optical properties of AgNW monolayers upon deformation are not exclusively due to a density change. The extinction decrease was observed for non-oriented AgNWs (Figure 4.14(A)) with unpolarized light but also for oriented AgNWs with unpolarized and polarized light (Figure 4.14(B)). This decrease could be attributed to a reflectance change of the metallic network induced by the stretching. For oriented AgNW monolayers, the variation of the alignment degree of the nanowires, the formation of microcracks or the contraction of PDMS in the direction perpendicular to the stretching direction could explain the significant change of the measured extinction (Figure 4.14(B)).
Moreover, the extinction change was proved to be dependent on both the stretching direction and light polarization as 4 different evolutions of the optical properties were observed (Figure 4.14(B)).

We decided to exploit the optical anisotropy of the oriented AgNWs during stretching to prepare an anisotropic strain sensor sensitive to the deformation and its direction.

4.7 Development of an anisotropic strain sensor

As discussed previously, the aim of this work is to build a strain sensor capable of detecting any applied deformation and its direction. The determination of the silver nanowire orientation will first be discussed. When an unknown strain is not applied along (α = 0°) or across (α = 90°) the AgNW alignment direction, α has a value comprised between 0° and 90°. In that case, the deformation of the sample transforms l_0 in l, L_0 in L and α in α' with $\alpha' < \alpha$ as illustrated in Figure 4.15.

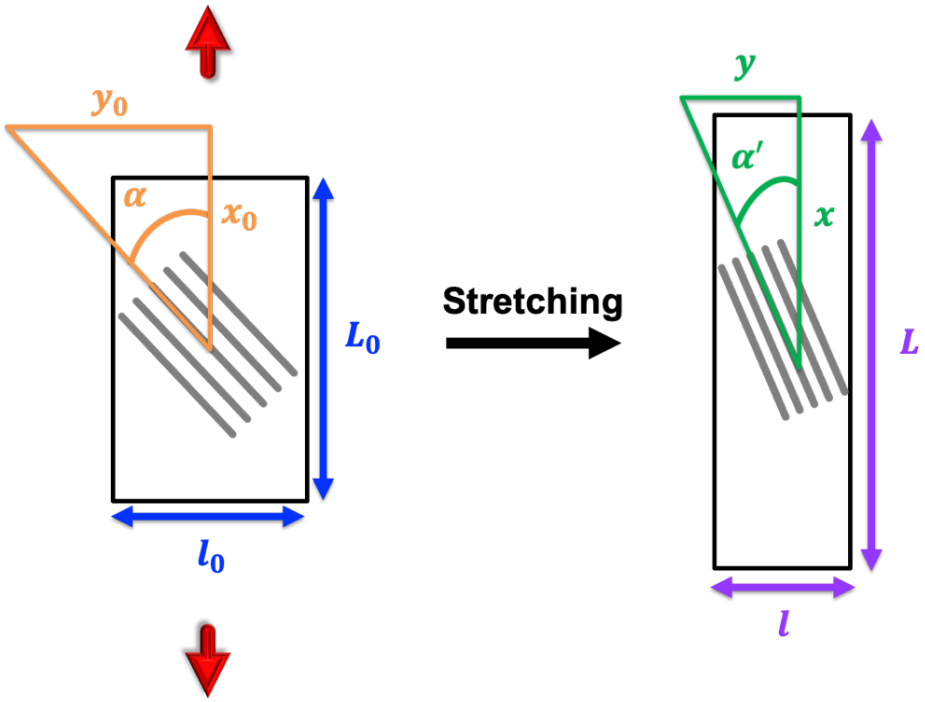

Figure 4.15: Schematic drawing of the uniaxial stretching (red arrows) of an oriented AgNW monolayer (grey sticks) on PDMS with an initial angle α between the stretching direction and the nanowire orientation.

Based on geometrical considerations, the expected change of the nanowire orientation angle from α to α' can be expressed as function of the applied strain. From the orange and green triangles formed by the stretching direction and the nanowire orientation (Figure 4.15), we can first express the orientation angle before (α) and after (α') stretching using Equations 4.15 and 4.16.

$$tan(\alpha) = {}^{y_0}/_{x_0} \qquad \textbf{Equation 4.15}$$

$$tan(\alpha') = {}^{y}/_{x} \qquad \textbf{Equation 4.16}$$

By using the Poisson's ratio definition (Equation 4.17), it is possible to relate the angles before and after stretching as function of the applied strain (Equation 4.20).

$$\frac{y}{y_0} = \left(\frac{x}{x_0}\right)^{-\vartheta_{PDMS}} \qquad \textbf{Equation 4.17}$$

$$\frac{tan(\alpha')}{tan(\alpha)} = \frac{y}{y_0} \times \frac{x_0}{x} \qquad \textbf{Equation 4.18}$$

$$\frac{tan(\alpha')}{tan(\alpha)} = \left(\frac{x}{x_0}\right)^{-\vartheta_{PDMS}} \times \frac{x_0}{x} \qquad \textbf{Equation 4.19}$$

$$tan(\alpha') = tan(\alpha) \times \left(1 + \frac{dx}{x_0}\right)^{-\vartheta_{PDMS} - 1} \qquad \textbf{Equation 4.20}$$

Regarding this equation, the angle change was dependent on the applied deformation and the Poisson's ratio of PDMS, translating the contraction of the material in the direction perpendicular compared to the stretching direction. Experimentally, the angle between the stretching direction and the nanowire orientation can be determined easily by monitoring the extinction change of the film at a specific wavelength as function of the polarizer angle. In the following study, we decided to monitor the optical properties at 380 nm. The extinction at this wavelength was maximum when the AgNW orientation and the polarization direction were perpendicular.

To validate our approach three films composed of oriented AgNW monolayers were prepared with different initial orientation angles with respect to the stretching direction (25°, 50° and 70°). The extinction measured at 380 nm as function of the angle between the stretching direction and the polarization direction (reported as polarizer angle ϕ) can be seen for each film in Figure 4.16. The extinction measured at 380 nm was maximal when the nanowire orientation angle α and the polarizer angle ϕ were perpendicular meaning that $\phi - \alpha = 90°$ (Figure 4.16(A), 4.16(B) and 4.16(C)). The maximum value of the extinction measured by spectroscopy in Figure 4.16 allowed the determination of the polarizer angle and consequently the orientation angle for each applied strain. The monitoring of the extinction upon film stretching demonstrated a

progressive decrease of the polarizer angle at which the maximum extinction is reached for the three films as predicted by Equation 4.20.

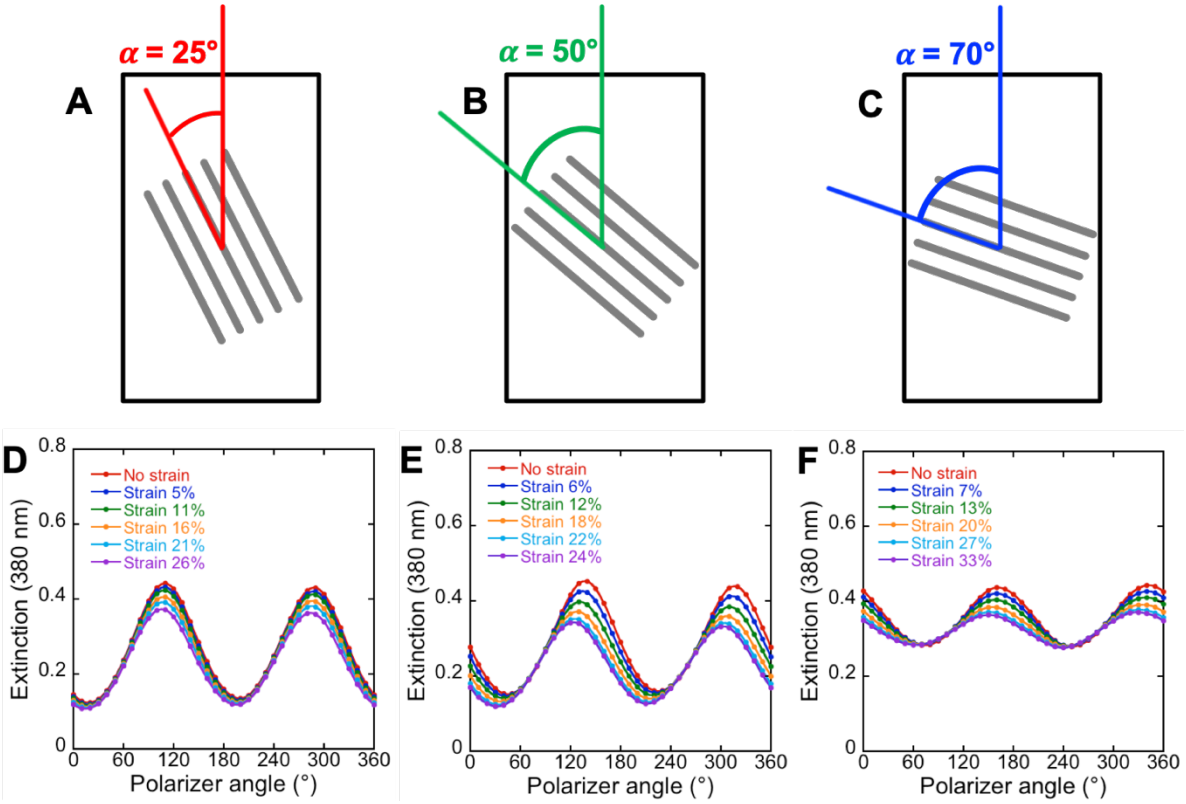

Figure 4.16: Schematic drawings of the oriented AgNW monolayers with orientation angles α set during the GIS deposition at (A) 25°, (B) 50°, (C) 70° and with the polarizer direction ϕ (in orange) and the nanowire orientation α being perpendicular when a maximum extinction is reached at 380 nm. (D, E, F) Extinction spectra measured at 380 nm as function of the polarizer angle ϕ during the respective stretching of films A, B and C.

Table 4.1 summarizes the orientation angle values that have been set during the deposition of the AgNW monolayers on PDMS and determined by spectroscopy.

Table 4.1: Comparison between the initial orientation angles α set during the GIS deposition and the ones determined by polarized spectroscopy at 380 nm on the unstretched films.

$\alpha_{set\ during\ deposition}$ (°)	$\phi_{spectroscopy}$ (°)	$\alpha_{spectroscopy}$ (°)
25	113.9	23.9
50	137.1	47.1
70	161.3	71.3

The small difference observed between the initial orientation angles set during the deposition and the ones determined by spectroscopy could be attributed to slight imprecisions on the angles set during the deposition and the fact that the samples were not perfectly vertically aligned when attached on the stretching device during the spectroscopic measurements.

The variation of the different orientation angles was then investigated upon stretching for different films and can be seen in Figure 4.17. Meanwhile, these experimental evolutions were compared to the expected ones corresponding to Equation 4.20.

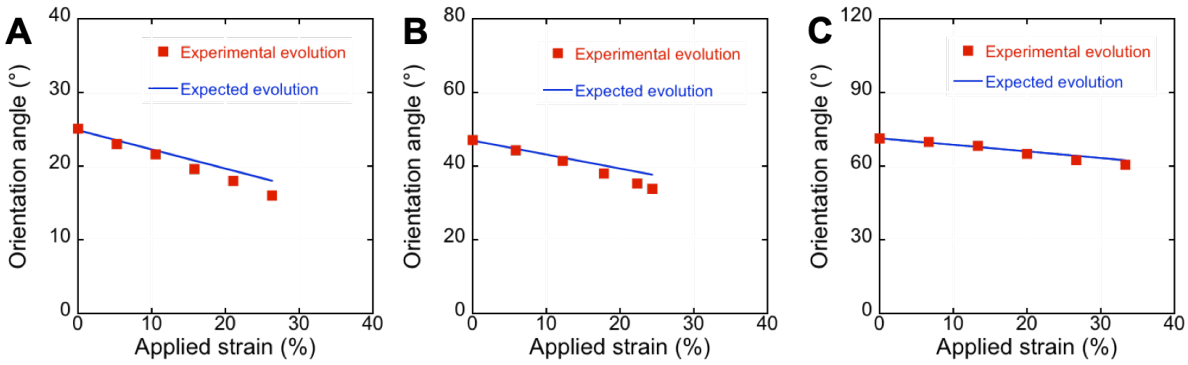

Figure 4.17: Orientation angle α' as function of the applied strain for three films with different initial orientation angles of 25° (A), 50° (B) and 70° (C).

The theoretical and experimental evolutions were proved to be in good agreement even if deviations could be pointed out when the applied strain increased (Figure 4.17). This study allowed to determine accurately the orientation angle of the AgNWs for every applied strain.

The last point was to link the extinction change measured for the film at a specific angle to the applied strain. To do so, the extinction change measured parallel and perpendicular with respect to the nanowire orientation could be determined at 380 nm upon stretching thanks to the extinction spectra determined with a light polarization applied perpendicular to the nanowire orientation.
The extinction changes at 380 nm of metallic oriented monolayers upon stretching for a strain applied perpendicular and parallel to the AgNW alignment direction are depicted in Figure 4.18.

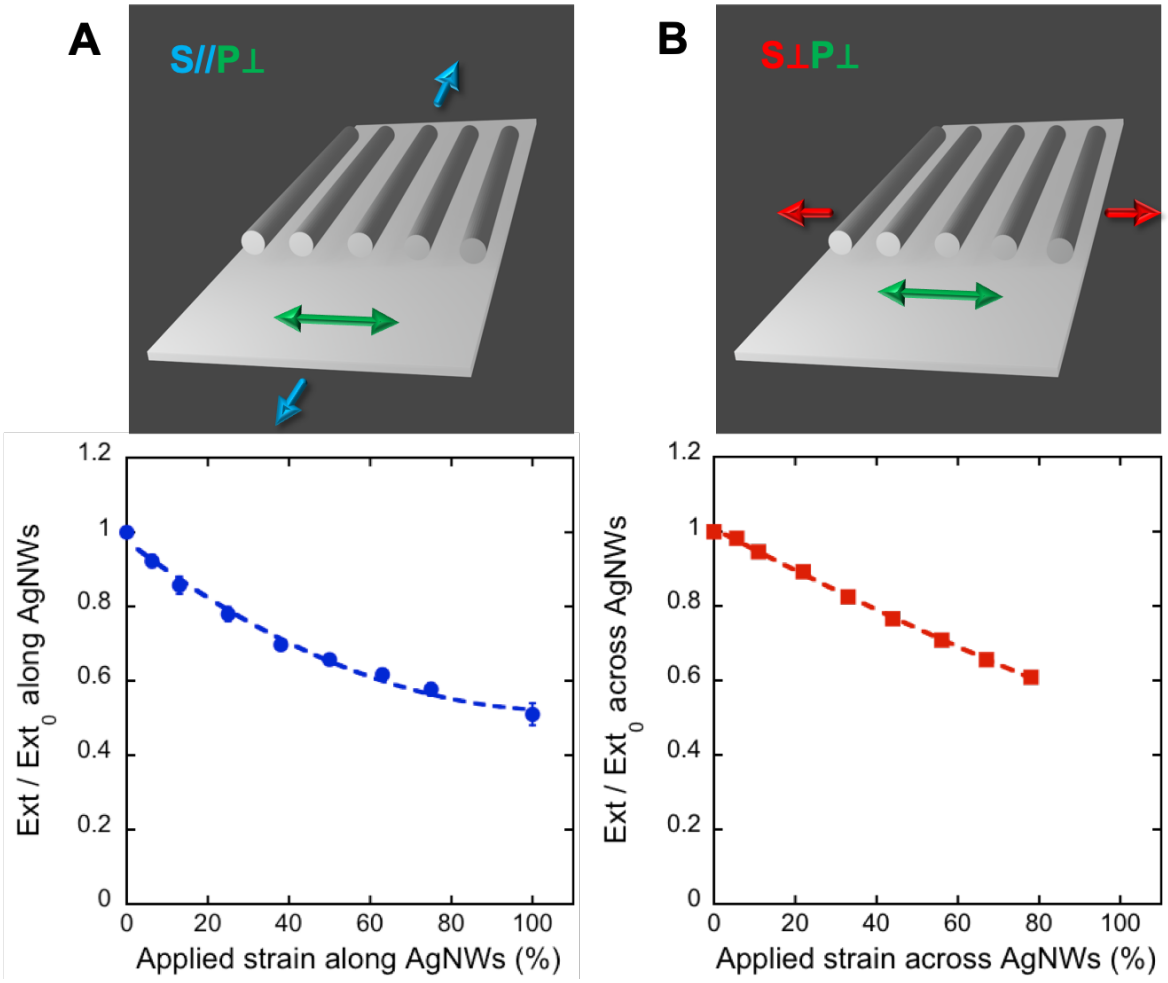

Figure 4.18: Schematic illustrations of the stretching of oriented AgNW monolayers with the corresponding evolutions of the extinction change for a strain applied parallel (A) and perpendicular (B) to the nanowire orientation and the light polarized perpendicular to the nanowire orientation (at 380 nm). Red and blue dotted lines correspond to second-order polynomial fits.

Data presented in Figure 4.17 were fitted with second-order polynoms. For both stretching directions, the extinction changes $\left(\frac{Ext}{Ext_0}\right)_{//}$ and $\left(\frac{Ext}{Ext_0}\right)_{\perp}$ could be expressed as function of the applied strain (Equations 4.21 and 4.22).

$$\left(\frac{Ext}{Ext_0}\right)_{//} = 0.388 \times \left(\frac{dL}{L_0}\right)_{//}^2 - 0.842 \times \left(\frac{dL}{L_0}\right)_{//} + 0.977 \qquad \textbf{Equation 4.21}$$

$$\left(\frac{Ext}{Ext_0}\right)_{\perp} = 0.0765 \times \left(\frac{dL}{L_0}\right)_{\perp}^2 - 0.574 \times \left(\frac{dL}{L_0}\right)_{\perp} + 1.008 \qquad \textbf{Equation 4.22}$$

Meanwhile, the extinction change $\frac{Ext}{Ext_0}$ of the oriented AgNW monolayers with an angle α between the stretching direction and the nanowire orientation can be expressed as $\frac{Ext}{Ext_0} = \left(\frac{Ext}{Ext_0}\right)_{//} \times \left(\frac{Ext}{Ext_0}\right)_{\perp}$ (Equation 4.9).

The measured extinction of the sample $\frac{Ext}{Ext_0}$ can therefore be expressed as function of two parameters that are the strains $\left(\frac{dL}{L_0}\right)_{//}$ and $\left(\frac{dL}{L_0}\right)_{\perp}$. In order to relate directly the extinction change of the sample to one single parameter, the strain applied perpendicular to the nanowire orientation $\left(\frac{dL}{L_0}\right)_{\perp}$ can be expressed as function of the strain applied parallel to the nanowire orientation $\left(\frac{dL}{L_0}\right)_{//}$ thanks to Equation 4.23.

$$tan(\alpha) = \frac{\left(\frac{dL}{L_0}\right)_{\perp}}{\left(\frac{dL}{L_0}\right)_{//}} \qquad \textbf{Equation 4.23}$$

The extinction change can consequently be expressed as function of $\left(\frac{dL}{L_0}\right)_{//}$ as a fourth-degree polynomial equation (Equation 4.24).

$$\frac{Ext}{Ext_0} = A \times \left(\frac{dL}{L_0}\right)_{//}^4 + B \times \left(\frac{dL}{L_0}\right)_{//}^3 + C \times \left(\frac{dL}{L_0}\right)_{//}^2 + D \times \left(\frac{dL}{L_0}\right)_{//} + E \qquad \textbf{Equation 4.24}$$

The coefficients A, B, C, D and E depend on the orientation angle α. A one fourth-degree polynomial equation will be obtained for each sample at a specific applied strain as the orientation angle depends on the applied strain. In order to solve this fourth-degree polynomial equation for each measured extinction change $\frac{Ext}{Ext_0}$, we developed an Excel VBA Macro.

The values of $\frac{Ext}{Ext_0}$ measured during spectroscopic measurements were set as the goal seek value in this macro (Table 4.2). For each sample and applied strain, the macro was calculating the value of the extinction change step by step for different values of $\left(\frac{dL}{L_0}\right)_{//}$ until it reached the goal seek value.

The use of this Excel macro allowed the determination of the solution of each fourth-degree polynomial equation. For instance, a strain $\left(\frac{dL}{L_0}\right)_{//}$ of 24% (0.24) was determined by the macro for an extinction change of 0.77 (Table 4.2) measured by spectroscopy for an oriented AgNW monolayer with an initial orientation angle of 23.9°.

Table 4.2: Solving of the fourth-degree polynomial equations using an Excel VBA macro on an oriented AgNW monolayer with an initial orientation angle of 23.9°. A, B, C, D and E correspond to the coefficients of the fourth-degree polynomial equations and $\frac{Ext}{Ext_0}$ to the extinction change measured by spectroscopy and set as the goal seek value.

$\frac{Ext}{Ext_0}$	Angle	A	B	C	D	E	$\left(\frac{dL}{L_0}\right)_{//}$
1	23.9	0.0058	-0.110	0.62	-1.10	0.98	-0.014
0.95	21.7	0.0047	-0.010	0.60	-1.07	0.98	0.034
0.89	19.7	0.0038	-0.088	0.57	-1.05	0.98	0.091
0.87	18.7	0.0034	-0.083	0.56	-1.04	0.98	0.110
0.82	17.0	0.0028	-0.074	0.55	-1.02	0.98	0.180
0.77	14.9	0.0021	-0.064	0.52	-0.99	0.98	0.240

The strain applied in the perpendicular direction to the nanowire orientation $\left(\frac{dL}{L_0}\right)_{\perp}$ was then determined using Equation 4.23.

The applied strain $\frac{dL}{L_0}$ was finally calculated using Equation 4.7 that was already presented before.

$$\frac{dL}{L_0}\overrightarrow{e_\alpha} = cos(\alpha) \times \left(\frac{dL}{L_0}\right)_{//} \overrightarrow{e_\alpha} + sin(\alpha) \times \left(\frac{dL}{L_0}\right)_{\perp} \overrightarrow{e_\alpha} \qquad \textbf{Equation 4.7}$$

For each applied strain, the orientation angle α of AgNWs and the strains applied along and across the nanowire alignment direction can be determined by spectroscopy.

This mathematical model was checked for the three oriented AgNW monolayers having an initial orientation angle α of about 25°, 50° and 70° in triplicate. The extinction changes $\frac{Ext}{Ext_0}$ of these monolayers upon stretching were monitored by UV-Visible-

spectroscopy at 380 nm with light polarized perpendicular to the nanowire direction and the applied strain $\frac{dL}{L_0}$ was then calculated using the previous Excel macro. The calculated strain values were then compared with the strains applied physically with the stretching device (Figure 4.19).

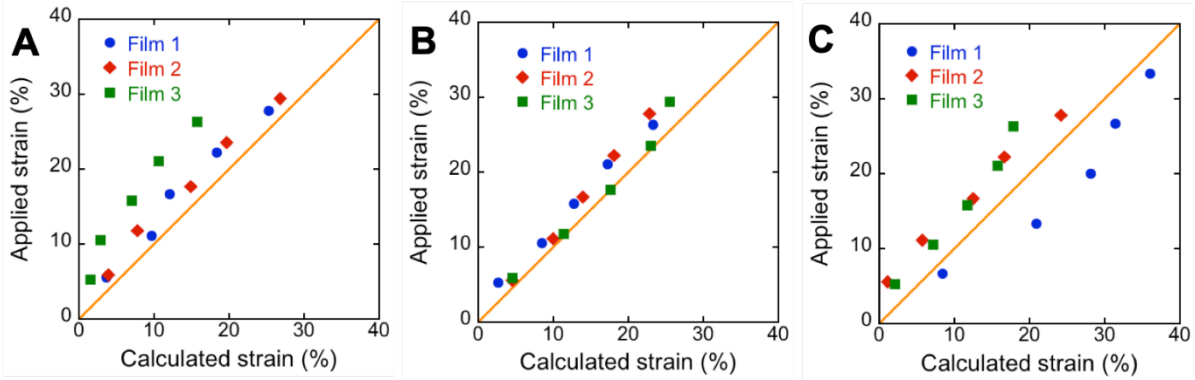

Figure 4.19: Variation of the applied strain as function of the calculated strain for films with initial orientation angles close to 25° (A), 50° (B) and 70° (C). Applied and calculated strains are identical on the orange lines of graphs.

The applied and calculated strains were proven to be in good agreement for all films presenting an initial orientation angle of about 50° (Figure 4.19(B)). Indeed, the reported points were located close to the orange line corresponding to the case for which the applied and calculated strains are identical.

The developed model was based on the measurements of the optical properties of the oriented AgNW monolayers at a single wavelength (380 nm). However, when the transverse modes of the metallic nanowires are preferentially excited, we can observe that the extinction of the longitudinal mode (at 1000 nm) is also affected (Figure 4.11). The extinction variations observed at this wavelength were not considered in our model and can explain the discrepancies between the applied and calculated strains. Moreover, we did not consider that the extinction change due to a stretching along AgNWs depends on the strain applied along but also across the nanowires that is induced by the Poisson's ratio.

Finally, the model does not consider the variation of the nanowire orientation and the formation of cracks during the film stretching. These structural changes that were

observed during the microscopic investigations can definitely have an influence on the corresponding optical properties of the metallic monolayers during the stretching.

4.8 Conclusion

Oriented AgNW monolayers were successfully deposited on PEI-coated PDMS and silicon-based substrates using GIS, a versatile and easy technique. The alignment of these metallic nanowires was characterized by electronic microscopy and a 2D nematic order parameter of about 0.80 was determined. The resulting AgNW monolayers displayed highly anisotropic optical properties that were used to prepare a multidimensional strain sensor. UV-Visible-NIR spectroscopy measurements conducted on a colored PDMS film demonstrated that the optical properties of the metallic thin films upon stretching were not only attributed to a density change. Spectroscopic studies performed with linearly polarized light during stretching showed that the optical properties of AgNW monolayers were highly dependent on the stretching direction and the light polarization. A mathematical model was developed by integrating parameters including the sample dimensions, the orientation angle, the measured extinction, the applied strain and the Poisson's ratio of the PDMS substrate. This model allowed the determination of the applied strain and its direction from the optical measurements. The designed anisotropic strain sensor was sensitive to small strains (< 10%) and could be applied in different applications where the measurement of multidimensional strains is required.

General conclusions and perspectives

In the current environmental context, bio-sourced composite materials composed of nanocellulose have attracted tremendous attraction thanks to the remarkable physical properties of cellulose (strength, lightness, biodegradability). The aim of this work was firstly to prepare wood-inspired nanocomposite materials using various cellulose nanoparticles (CNCs and CNFs) and study their mechanical and optical properties.

Multilayer $(CNF/PVAm)_n$ and $(CNC/PVAm)_n$ films with different architectures were prepared using various deposition methods. The growth and microstructure of these nanocomposite films prepared by dip-assisted LbL assembly were proved to be highly dependent on the selected cellulose nanoparticles. Long and stiff CNCs resulted in the formation of highly porous, rough and opaque materials while short CNCs and CNFs provided transparent, smooth and densely packed films (Figure C.1).

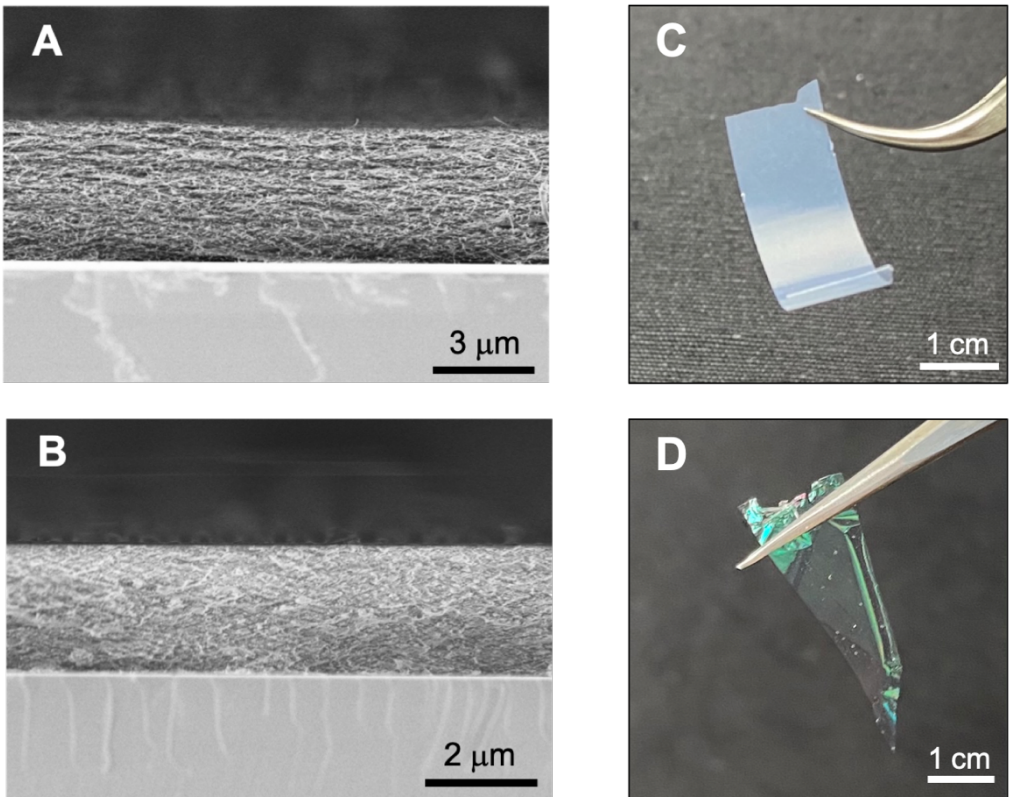

Figure C.1: Cross-sectional SEM images and optical photographs of thick multilayer films with a porous structure and opaque films using t-CNCs (A, C) and with a densely packed structure and transparent films using w-CNCs (B, D).

Spin-assisted LbL assembly was then employed to obtain materials with physical anisotropic properties. It turned out that only long CNCs could be oriented by spin-assisted assembly. The orientation degree of long CNCs was first optimized on monolayers deposited on silicon wafers and resulted in a high degree of alignment (S_{2D}~0.80). Thick, freestanding and highly oriented multilayers were then fabricated and displayed enhanced birefringent properties. Helical structures that are responsible for the high impact resistant exoskeletons of crustaceans or the selective filtration of circularly polarized light in beetles have been successfully prepared by combining LbL assembly with the GIS methodology. This specific structure was evidenced by circular dichroism (CD) spectroscopy on CNC-based films with the observation of a characteristic Bragg reflection peak (Figure C.2). The mechanical properties of the cellulose-based multi-layered films were finally characterized by DMA and nano-indentation measurements. Surprisingly CNC-based films presented a modulus of ~15 GPa that was independent of the film structure while isotropic CNF-based films displayed a modulus of ~9 GPa.

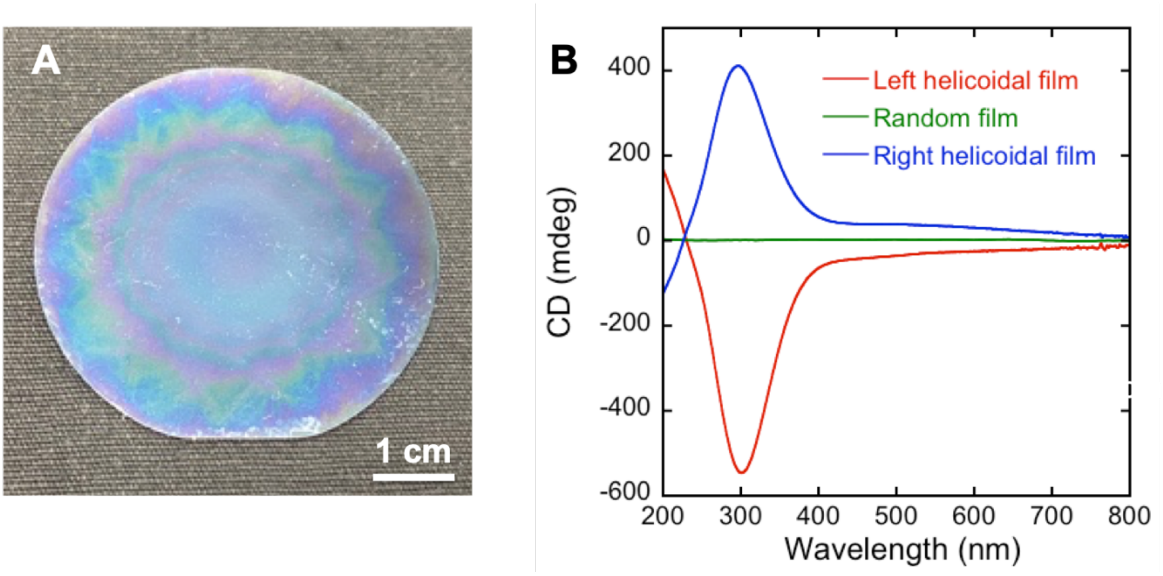

Figure C.2: (A) Optical photograph of a t-CNC-based multilayer film presenting a helicoidal structure and (B) CD spectra of left and right helicoidal films displaying an intense reflection peak that is not visible in the random film.

This study paves the way for the preparation of nanocomposite films with well-controlled internal structures of the reinforcing agent, which can be exploited for

conferring enhanced mechanical and optical functionalities to the resulting films. In this work we have extended our approach to short and long nanocellulose nanocrystals in order improve the mechanical resistance of the nanocellulose-based LbL films and their efficiency in the filtration of circularly-polarized light. The high porosity and brittleness observed for thick films composed of long CNCs may be reduced by combining CNFs and CNCs in the same films and by adjusting the number of oriented CNC layers. Moreover, other polyelectrolytes like chitosan and xyloglycan could be employed for building different structures (random, unidirectional, cross-ply, helicoidal). Despite the recent development of approaches for the assembly of nanocellulose-based helical structures, the combination of LbL assembly and GIS represents an alternative highly appealing by its flexibility and its nanoscale precision. For instance, it provides the possibility to incorporate various sub-structures within the film, e.g. the combination of opposite handedness of the chiral assembly, the alternation with unidirectional segments, the staking of various pitches or the creation of gradients. In addition, it offers plenty of room for improvement, optimization, and scale-up possibilities. One important aspect to be developed may be the preparation of large-area helical samples which are required for tensile strength measurements. It is indeed expected to measure similar stress and Young modulus independently from the in-plane direction. One could think to use this approach for the fabrication of damage resistant optical filtering coatings/thin films, which will be competitive for future applications (e.g. counterfeiting protection, flexible displays, …). Such applications require resistant thin films transparent in the visible range that can control the polarization state (linear or circular) of the reflected and transmitted light, which is allowed by our bio-sourced and non-toxic system.

In a second part, the aim was to build a multidimensional optical strain sensor. Indeed, stretchable and wearable strain sensors have recently attracted enormous attention due to their numerous possible applications. However, traditional strain sensors are generally not sensitive to the stretching direction. To prepare a direction-sensitive strain sensor, GIS technique was employed and allowed the successful orientation of AgNW monolayers on deformable PDMS substrates. Microscopic investigations revealed an anisotropy of the mechanical properties of the metallic nanowires upon stretching with the formation of microcracks perpendicular to the stretching direction when the strain was applied along the nanowire orientation. On the other hand, a strain

applied across the nanowire alignment direction did not induce any fracture but lead to a decrease of the alignment degree of the nanowires. The optical properties of oriented AgNW monolayers on PDMS were then investigated with linearly polarized light allowing the selective excitation of transverse and longitudinal resonance modes of AgNWs. The measured extinction of these aligned metallic films decreased progressively upon stretching and its variation was proved to be highly dependent on the stretching direction but also on the light polarization (Figure C.3).

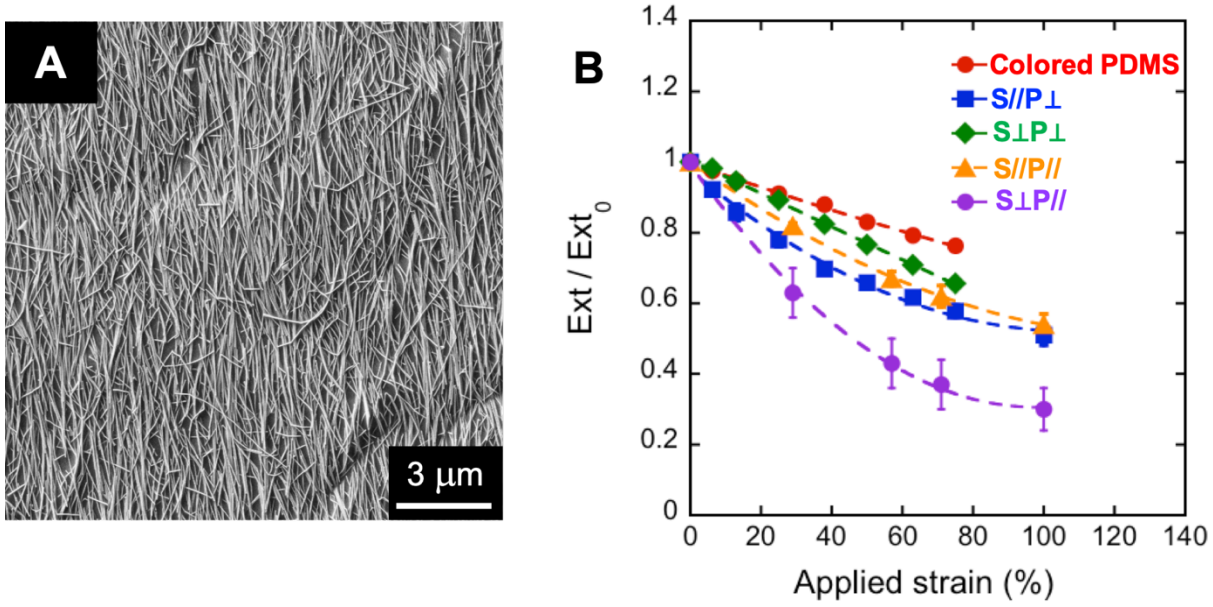

Figure C.3: (A) SEM image of an oriented AgNW monolayer deposited by GIS on a PDMS substrate and (B) extinction change of a colored PDMS film and oriented AgNW monolayers upon stretching with different light polarizations and stretching directions.

Meanwhile, the monitoring of the optical properties of a colored PDMS film confirmed that the change of the optical properties of AgNW monolayers was not only the result of an AgNW density change.

These anisotropic optical properties were then used to prepare the multidimensional strain sensor. To do so, we developed a mathematical model that allowed to link the measured extinction of the sample to the applied strain (Figure C.4). The obtained sensor was working efficiently for different nanowire orientation angles and for different applied strains. This sensor could be very useful for applications necessitating the measurement of multidimensional strains. Moreover, the developed strategy is simple, fast and efficient as the sensor requires only the spraying of a monolayer of AgNWs

during 50 s. No heating or additional treatment is needed after the deposition of the metallic nanowires and the size of the film can be easily modified. This strategy could be applied to different surfaces including sticky objects that could be stuck on any object.

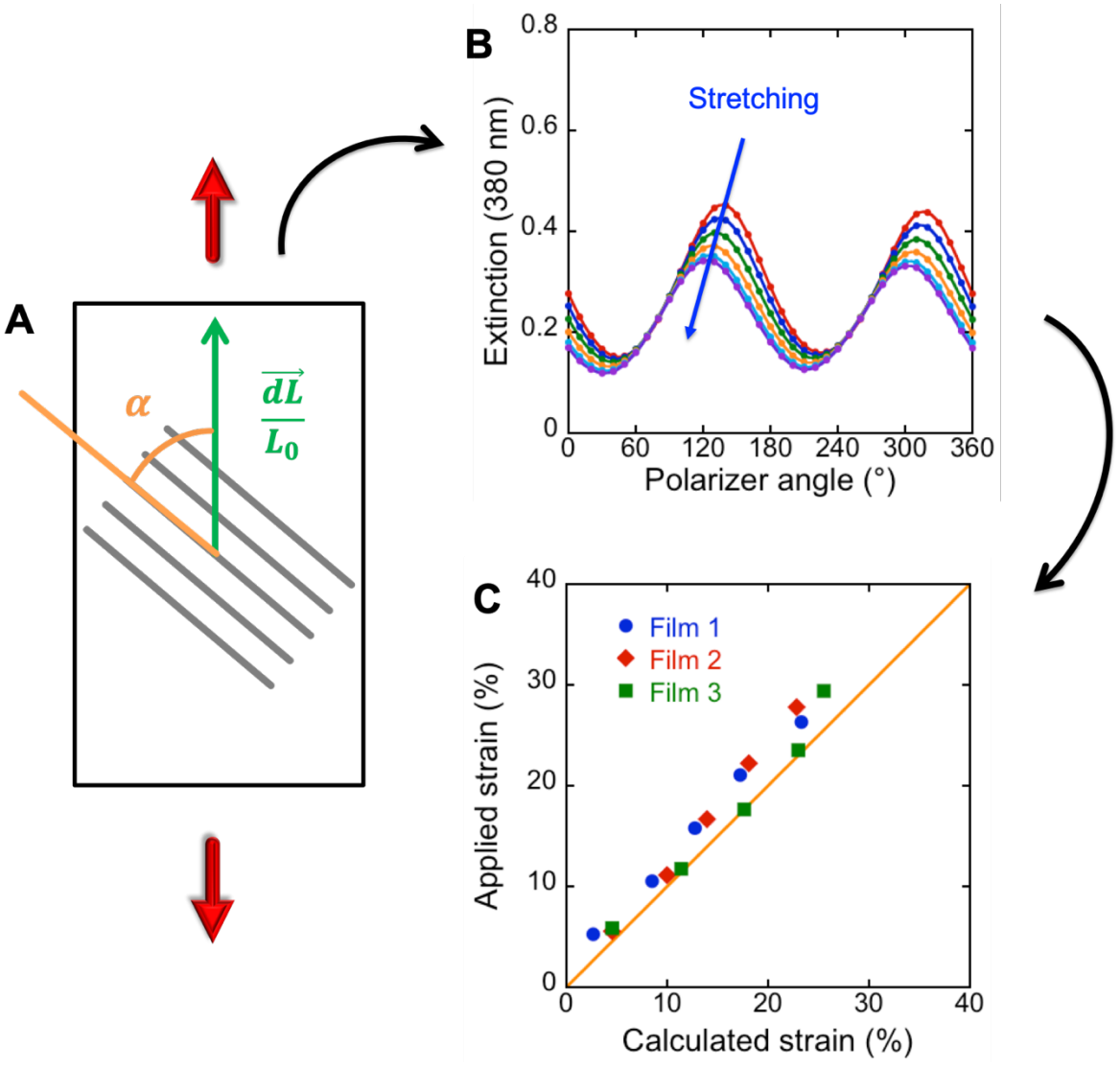

Figure C.4: (A) Schematic drawing of the stretching of an oriented AgNW monolayer with an unknown orientation angle and applied strain. (B) Extinction change of the sample upon stretching allowing the determination of the orientation angle for each applied strain. (C) Determination of the applied strain from the spectroscopic measurements by using the developed mathematical model.

This study lays the groundwork for the development of an anisotropic multidirectional sensor based on an AgNW monolayer. In a future work it would be interesting to investigate the sensitivity of the sensor and the influence of the nanowire density on

the sensitivity of this sensor as this study focused on a specific density. The confrontation of these experimental results with simulated data on a model monolayer upon stretching could also be completed. Furthermore, the developed model considers the variation of the optical properties at a single wavelength. This model could be changed in order to improve the performances of this sensor by considering the optical properties at different wavelengths for instance. Additional investigations will be required for the determination of the mechanical parameters of a sample upon stretching from the optical measurements (calibration curve).

Finally it would be interesting to see if our anisotropic optical sensor could be applied for the determination of mechanical parameters of a nanocellulose-based films deposited on a PDMS substrates. The sequence of the deposited layers as well as the structure of the film could be modified and their influence on the optical properties could be studied.

References

1. Fratzl, P. & Weinkamer, R. Nature's hierarchical materials. *Progress in Materials Science* **52**, 1263–1334 (2007).
2. Bouligand, Y. Twisted fibrous arrangements in biological materials and cholesteric mesophases. *Tissue and Cell* **4**, 189–217 (1972).
3. Gibson, L. J. The hierarchical structure and mechanics of plant materials. *Journal of The Royal Society Interface* **9**, 2749–2766 (2012).
4. Weaver James C. *et al.* The Stomatopod Dactyl Club: A Formidable Damage-Tolerant Biological Hammer. *Science* **336**, 1275–1280 (2012).
5. Okumura, K. Simple Model for the Toughness of a Helical Structure Inspired by the Exoskeleton of Lobsters. *Journal of the Physical Society of Japan* **82**, 124802 (2013).
6. Nikolov, S., Fabritius, H.-O., Friák, M. & Raabe, D. Integrated multiscale modeling approach for hierarchical biological nanocomposites applied to lobster cuticle. **47**, 423–432 (2016).
7. Vignolini, S. *et al.* Structural colour from helicoidal cell-wall architecture in fruits of Margaritaria nobilis. *Journal of The Royal Society Interface* **13**, 20160645 (2016).
8. Finlayson, E. D., McDonald, L. T. & Vukusic, P. Optically ambidextrous circularly polarized reflection from the chiral cuticle of the scarab beetle Chrysina resplendens. *Journal of The Royal Society Interface* **14**, 20170129 (2017).
9. Lakes, R. Materials with structural hierarchy. *Nature* **361**, 511–515 (1993).
10. Decher, G. Fuzzy Nanoassemblies: Toward Layered Polymeric Multicomposites. *Science* **277**, 1232 (1997).
11. Blell, R. *et al.* Generating in-Plane Orientational Order in Multilayer Films Prepared by Spray-Assisted Layer-by-Layer Assembly. *ACS Nano* **11**, 84–94 (2017).
12. Souri, H. *et al.* Wearable and Stretchable Strain Sensors: Materials, Sensing Mechanisms, and Applications. *Advanced Intelligent Systems* **2**, 2000039 (2020).
13. Amjadi, M., Kyung, K.-U., Park, I. & Sitti, M. Stretchable, Skin-Mountable, and Wearable Strain Sensors and Their Potential Applications: A Review. *Advanced Functional Materials* **26**, 1678–1698 (2016).
14. NEINHUIS, C. & BARTHLOTT, W. Characterization and Distribution of Water-repellent, Self-cleaning Plant Surfaces. *Annals of Botany* **79**, 667–677 (1997).

15. NEINHUIS, C. & BARTHLOTT, W. Characterization and Distribution of Water-repellent, Self-cleaning Plant Surfaces. *Annals of Botany* **79**, 667–677 (1997).

16. Zhang, J. *et al.* How does the leaf margin make the lotus surface dry as the lotus leaf floats on water? *Soft Matter* **4**, 2232–2237 (2008).

17. Ensikat, H. J., Boese, M., Mader, W., Barthlott, W. & Koch, K. Crystallinity of plant epicuticular waxes: electron and X-ray diffraction studies. *Chemistry and Physics of Lipids* **144**, 45–59 (2006).

18. Römer, L. & Scheibel, T. The elaborate structure of spider silk: structure and function of a natural high performance fiber. *Prion* **2**, 154–161 (2008).

19. Gosline, J. M., Guerette, P. A., Ortlepp, C. S. & Savage, K. N. The mechanical design of spider silks: from fibroin sequence to mechanical function. *Journal of Experimental Biology* **202**, 3295–3303 (1999).

20. Schneider, D. *et al.* Nonlinear control of high-frequency phonons in spider silk. *Nature Materials* **15**, 1079–1083 (2016).

21. Naghilou, A. *et al.* Correlating the secondary protein structure of natural spider silk with its guiding properties for Schwann cells. *Materials Science and Engineering: C* **116**, 111219 (2020).

22. Ghiradella, H. Light and color on the wing: structural colors in butterflies and moths. *Appl. Opt.* **30**, 3492–3500 (1991).

23. Song, B., Johansen, V. E., Sigmund, O. & Shin, J. H. Reproducing the hierarchy of disorder for Morpho-inspired, broad-angle color reflection. *Scientific Reports* **7**, 46023 (2017).

24. Sun, J. & Bhushan, B. Hierarchical structure and mechanical properties of nacre: a review. *RSC Adv.* **2**, 7617–7632 (2012).

25. Seki, Y., Schneider, M. S. & Meyers, M. A. Structure and mechanical behavior of a toucan beak. *Acta Materialia* **53**, 5281–5296 (2005).

26. Fabritius, H.-O. *et al.* Functional adaptation of crustacean exoskeletal elements through structural and compositional diversity: a combined experimental and theoretical study. *Bioinspir Biomim* **11**, 055006 (2016).

27. Raabe, D. *et al.* Discovery of a honeycomb structure in the twisted plywood patterns of fibrous biological nanocomposite tissue. *Journal of Crystal Growth* **283**, 1–7 (2005).

28. Giraud-Guille, M.-M. Plywood structures in nature. *Current Opinion in Solid State and Materials Science* **3**, 221–227 (1998).

29. Raabe, D. & Sachs, C. Mechanical Properties of the Lobster Cuticle. *MRS Proceedings* **874**, L5.3 (2005).

30. Gibson, L. J. The hierarchical structure and mechanics of plant materials. *Journal of The Royal Society Interface* **9**, 2749–2766 (2012).

31. Liu, C. *et al.* Bio-polymers Derived from Trees as Sustainable Multifunctional Materials: A Review. *Advanced Materials* (2020) doi:10.1002/adma.202001654.

32. Feldman, D. Wood—chemistry, ultrastructure, reactions, by D. Fengel and G. Wegener, Walter de Gruyter, Berlin and New York, 1984, 613 pp. Price: 245 DM. *Journal of Polymer Science: Polymer Letters Edition* **23**, 601–602 (1985).

33. Cave, I. D. Theory of X-ray measurement of microfibril angle in wood. *Wood Science and Technology* **31**, 143–152 (1997).

34. Peng, H. B. & Jaffe, L. F. Cell-wall formation in Pelvetia embryos. A freeze-fracture study. *Planta* **133**, 57–71 (1976).

35. Cave, I. D. A theory of the shrinkage of wood. *Wood Science and Technology* **6**, 284–292 (1972).

36. Gibson, L. J. Biomechanics of cellular solids. *Journal of Biomechanics* **38**, 377–399 (2005).

37. Lu, Y., Weng, L. & Zhang, L. Morphology and Properties of Soy Protein Isolate Thermoplastics Reinforced with Chitin Whiskers. *Biomacromolecules* **5**, 1046–1051 (2004).

38. Ifuku, S. *et al.* Preparation of high-strength transparent chitosan film reinforced with surface-deacetylated chitin nanofibers. *Carbohydrate Polymers* **98**, 1198–1202 (2013).

39. Uddin, A. J., Fujie, M., Sembo, S. & Gotoh, Y. Outstanding reinforcing effect of highly oriented chitin whiskers in PVA nanocomposites. *Carbohydrate Polymers* **87**, 799–805 (2012).

40. Oh, D. X. *et al.* Chiral nematic self-assembly of minimally surface damaged chitin nanofibrils and its load bearing functions. *Scientific Reports* **6**, 23245 (2016).

41. Sehaqui, H., Zhou, Q., Ikkala, O. & Berglund, L. A. Strong and tough cellulose nanopaper with high specific surface area and porosity. *Biomacromolecules* **12**, 3638–3644 (2011).

42. Merk, V., Chanana, M., Keplinger, T., Gaan, S. & Burgert, I. Hybrid wood materials with improved fire retardance by bio-inspired mineralisation on the nano- and submicron level. *Green Chem.* **17**, 1423–1428 (2015).

43. Chen, Y. *et al.* Wood-Inspired Anisotropic Cellulose Nanofibril Composite Sponges for Multifunctional Applications. *ACS Appl. Mater. Interfaces* **12**, 35513–35522 (2020).

44. Mittal, N. *et al.* Multiscale Control of Nanocellulose Assembly: Transferring Remarkable Nanoscale Fibril Mechanics to Macroscale Fibers. *ACS Nano* **12**, 6378–6388 (2018).

45. Shamshina, J. L. *et al.* In Search of Stronger/Cheaper Chitin Nanofibers through Electrospinning of Chitin–Cellulose Composites Using an Ionic Liquid Platform. *ACS Sustainable Chem. Eng.* **6**, 14713–14722 (2018).

46. Rawat, R. S. Dense Plasma Focus - From Alternative Fusion Source to Versatile High Energy Density Plasma Source for Plasma Nanotechnology. *Journal of Physics: Conference Series* **591**, 012021 (2015).

47. Feynman, R. P. There's plenty of room at the bottom. *Resonance* **16**, 890 (2011).

48. Kim, D.-E. & Sung, I.-H. Lithography. in *Encyclopedia of Tribology* (eds. Wang, Q. J. & Chung, Y.-W.) 1994–2007 (Springer US, 2013). doi:10.1007/978-0-387-92897-5_1051.

49. Broers, A. N., Hoole, A. C. F. & Ryan, J. M. Electron beam lithography—Resolution limits. *Microelectronic Engineering* **32**, 131–142 (1996).

50. Cumming, D. R. S., Thoms, S., Beaumont, S. P. & Weaver, J. M. R. Fabrication of 3 nm wires using 100 keV electron beam lithography and poly(methyl methacrylate) resist. *Appl. Phys. Lett.* **68**, 322–324 (1996).

51. Gundiah, G. *et al.* Dip-pen nanolithography with magnetic Fe2O3 nanocrystals. *Appl. Phys. Lett.* **84**, 5341–5343 (2004).

52. Yang, Y., Mielczarek, K., Aryal, M., Zakhidov, A. & Hu, W. Nanoimprinted Polymer Solar Cell. *ACS Nano* **6**, 2877–2892 (2012).

53. Fratzl, P. & Weinkamer, R. Nature's hierarchical materials. *Progress in Materials Science* **52**, 1263–1334 (2007).

54. Hench, L. L. & West, J. K. The sol-gel process. *Chem. Rev.* **90**, 33–72 (1990).

55. Marikkannan, M., Vishnukanthan, V., Vijayshankar, A., Mayandi, J. & Pearce, J. M. A novel synthesis of tin oxide thin films by the sol-gel process for optoelectronic applications. *AIP Advances* **5**, 027122 (2015).

56. Cheung, C. L., Hafner, J. H. & Lieber, C. M. Carbon nanotube atomic force microscopy tips: Direct growth by chemical vapor deposition and application to high-resolution imaging. *Proc Natl Acad Sci USA* **97**, 3809 (2000).

57. Yao, B. *et al.* Efficient 3D Printed Pseudocapacitive Electrodes with Ultrahigh MnO2 Loading. *Joule* **3**, 459–470 (2019).

58. Torelli, E. *et al.* A DNA origami nanorobot controlled by nucleic acid hybridization. *Small* **10**, 2918–2926 (2014).

59. Iler, R. Multilayers of colloidal particles. *Journal of Colloid and Interface Science* **21**, 569–594 (1966).

60. FROMHERZ, P. Electron Microscopic Studies of Lipid Protein Films. *Nature* **231**, 267–268 (1971).

61. Decher, G. & Hong, J.-D. Buildup of ultrathin multilayer films by a self-assembly process, 1 consecutive adsorption of anionic and cationic bipolar amphiphiles on charged surfaces. *Makromolekulare Chemie. Macromolecular Symposia* **46**, 321–327 (1991).

62. Schlenoff, J. B., Dubas, S. T. & Farhat, T. Sprayed Polyelectrolyte Multilayers. *Langmuir* **16**, 9968–9969 (2000).

63. Cho, J., Char, K., Hong, J.-D. & Lee, K.-B. Fabrication of Highly Ordered Multilayer Films Using a Spin Self-Assembly Method. *Advanced Materials* **13**, 1076–1078 (2001).

64. Schlenoff, J. Multilayer Thin Films: Sequential Assembly of Nanocomposite Materials, Second Edition. in 99–132 (2003). doi:10.1002/3527600574.ch4.

65. Merindol, R. *et al.* Bio-Inspired Multiproperty Materials: Strong, Self-Healing, and Transparent Artificial Wood Nanostructures. *ACS Nano* **9**, 1127–1136 (2015).

66. Dodoo, S., Steitz, R., Laschewsky, A. & von Klitzing, R. Effect of ionic strength and type of ions on the structure of water swollen polyelectrolyte multilayers. *Phys. Chem. Chem. Phys.* **13**, 10318–10325 (2011).

67. Poptoshev, E., Schoeler, B. & Caruso, F. Influence of solvent quality on the growth of polyelectrolyte multilayers. *Langmuir* **20**, 829–834 (2004).

68. Zhang, X., Chen, H. & Zhang, H. Layer-by-layer assembly: from conventional to unconventional methods. *Chem. Commun.* 1395–1405 (2007) doi:10.1039/B615590A.

69. Podsiadlo, P. *et al.* Ultrastrong and Stiff Layered Polymer Nanocomposites. *Science* **318**, 80 (2007).

70. Lee, H., Mensire, R., Cohen, R. E. & Rubner, M. F. Strategies for Hydrogen Bonding Based Layer-by-Layer Assembly of Poly(vinyl alcohol) with Weak Polyacids. *Macromolecules* **45**, 347–355 (2012).

71. Kotov, N. A. Layer-by-layer self-assembly: The contribution of hydrophobic interactions. *Nanostructured Materials* **12**, 789–796 (1999).

72. Zhang, J. *et al.* Layer-by-Layer Assembly of Azulene-Based Supra-Amphiphiles: Reversible Encapsulation of Organic Molecules in Water by Charge-Transfer Interaction. *Langmuir* **29**, 6348–6353 (2013).

73. Seo, J. *et al.* Covalently Bonded Layer-by-Layer Assembly of Multifunctional Thin Films Based on Activated Esters. *Langmuir* **26**, 1830–1836 (2010).

74. Van der Heyden, A., Wilczewski, M., Labbé, P. & Auzély, R. Multilayer films based on host–guest interactions between biocompatible polymers. *Chem. Commun.* 3220–3222 (2006) doi:10.1039/B604672J.

75. Marszalek, T., Li, M. & Pisula, W. Design directed self-assembly of donor–acceptor polymers. *Chem. Commun.* **52**, 10938–10947 (2016).

76. Jawaid, M. & Abdul Khalil, H. P. S. Cellulosic/synthetic fibre reinforced polymer hybrid composites: A review. *Carbohydrate Polymers* **86**, 1–18 (2011).

77. Lee, S.-Y., Chun, S.-J., Kang, I.-A. & Park, J.-Y. Preparation of cellulose nanofibrils by high-pressure homogenizer and cellulose-based composite films. *Journal of Industrial and Engineering Chemistry* **15**, 50–55 (2009).

78. Dilamian, M. & Noroozi, B. A combined homogenization-high intensity ultrasonication process for individualizaion of cellulose micro-nano fibers from rice straw. *Cellulose* **26**, 5831–5849 (2019).

79. Nair, S., Zhu, J. Y., Yulin, bullet, bullet, D. & Ragauskas, A. Charaterization of cellulose nanofibrillation by micro grinding. *Journal of Nanoparticle Research* **16**, 2349 (2014).

80. Pääkkö, M. *et al.* Enzymatic Hydrolysis Combined with Mechanical Shearing and High-Pressure Homogenization for Nanoscale Cellulose Fibrils and Strong Gels. *Biomacromolecules* **8**, 1934–1941 (2007).

81. Rånby, B. G. Fibrous macromolecular systems. Cellulose and muscle. The colloidal properties of cellulose micelles. *Discuss. Faraday Soc.* **11**, 158–164 (1951).

82. Moon, R. J., Martini, A., Nairn, J., Simonsen, J. & Youngblood, J. Cellulose nanomaterials review: structure, properties and nanocomposites. *Chem. Soc. Rev.* **40**, 3941–3994 (2011).

83. Junior de Menezes, A., Siqueira, G., Curvelo, A. A. S. & Dufresne, A. Extrusion and characterization of functionalized cellulose whiskers reinforced polyethylene nanocomposites. *Polymer* **50**, 4552–4563 (2009).

84. Araki, J., Wada, M. & Kuga, S. Steric Stabilization of a Cellulose Microcrystal Suspension by Poly(ethylene glycol) Grafting. *Langmuir* **17**, 21–27 (2001).

85. Beck-Candanedo, S., Roman, M. & Gray, D. G. Effect of Reaction Conditions on the Properties and Behavior of Wood Cellulose Nanocrystal Suspensions. *Biomacromolecules* **6**, 1048–1054 (2005).

86. Garcia de Rodriguez, N. L., Thielemans, W. & Dufresne, A. Sisal cellulose whiskers reinforced polyvinyl acetate nanocomposites. *Cellulose* **13**, 261–270 (2006).

87. George, J., Bawa, A. S., & Siddaramaiah. Synthesis and Characterization of Bacterial Cellulose Nanocrystals and their PVA Nanocomposites. *Advanced Materials Research* **123–125**, 383–386 (2010).

88. Kimura, F. *et al.* Magnetic Alignment of the Chiral Nematic Phase of a Cellulose Microfibril Suspension. *Langmuir* **21**, 2034–2037 (2005).

89. Lin, N., Huang, J. & Dufresne, A. Preparation, properties and applications of polysaccharide nanocrystals in advanced functional nanomaterials: a review. *Nanoscale* **4**, 3274–3294 (2012).

90. Klemm, D. *et al.* Nanocelluloses: A New Family of Nature-Based Materials. *Angewandte Chemie International Edition* **50**, 5438–5466 (2011).

91. Revol, J.-F., Bradford, H., Giasson, J., Marchessault, R. H. & Gray, D. G. Helicoidal self-ordering of cellulose microfibrils in aqueous suspension. *International Journal of Biological Macromolecules* **14**, 170–172 (1992).

92. Podsiadlo, P. *et al.* Molecularly Engineered Nanocomposites: Layer-by-Layer Assembly of Cellulose Nanocrystals. *Biomacromolecules* **6**, 2914–8 (2005).

93. Wågberg, L. *et al.* The build-up of polyelectrolyte multilayers of microfibrillated cellulose and cationic polyelectrolytes. *Langmuir* **24**, 784–795 (2008).

94. Podsiadlo, P. *et al.* Layer-by-Layer Assembled Films of Cellulose Nanowires with Antireflective Properties. *Langmuir : the ACS journal of surfaces and colloids* **23**, 7901–6 (2007).

95. Dammak, A. *et al.* Influence of cellulose nanocrystals concentration and ionic strength on the elaboration of cellulose nanocrystals–xyloglucan multilayered thin films. *Journal of Colloid and Interface Science* **460**, 214–220 (2015).

96. Moreau, C., Beury, N., Delorme, N. & Cathala, B. Tuning the architecture of cellulose nanocrystal-poly(allylamine hydrochloride) multilayered thin films: influence of dipping parameters. *Langmuir* **28**, 10425–10436 (2012).

97. Cranston, E. D. *et al.* Determination of Young's modulus for nanofibrillated cellulose multilayer thin films using buckling mechanics. *Biomacromolecules* **12**, 961–969 (2011).

98. Eita, M., Arwin, H., Granberg, H. & Wågberg, L. Addition of silica nanoparticles to tailor the mechanical properties of nanofibrillated cellulose thin films. *J Colloid Interface Sci* **363**, 566–572 (2011).

99. Karabulut, E. & Wågberg, L. Design and characterization of cellulose nanofibril-based freestanding films prepared by layer-by-layer deposition technique. *Soft Matter* **7**, 3467–3474 (2011).

100. Ghanadpour, M., Carosio, F. & Wågberg, L. Ultrastrong and flame-resistant freestanding films from nanocelluloses, self-assembled using a layer-by-layer approach. *Applied Materials Today* **9**, 229–239 (2017).

101. Karabulut, E., Pettersson, T., Ankerfors, M. & Wågberg, L. Adhesive Layer-by-Layer Films of Carboxymethylated Cellulose Nanofibril–Dopamine Covalent Bioconjugates Inspired by Marine Mussel Threads. *ACS Nano* **6**, 4731–4739 (2012).

102. Utsel, S., Malmström, E. E., Carlmark, A. & Wågberg, L. Thermoresponsive nanocomposites from multilayers of nanofibrillated cellulose and specially designed N-isopropylacrylamide based polymers. *Soft Matter* **6**, 342–352 (2010).

103. Aulin, C., Karabulut, E., Tran, A., Wågberg, L. & Lindström, T. Transparent nanocellulosic multilayer thin films on polylactic acid with tunable gas barrier properties. *ACS Appl Mater Interfaces* **5**, 7352–7359 (2013).

104. Kwiat, M., Cohen, S., Pevzner, A. & Patolsky, F. Large-scale ordered 1D-nanomaterials arrays: Assembly or not? *Nano Today* **8**, 677–694 (2013).

105. Cranston, E. D. & Gray, D. G. Birefringence in spin-coated films containing cellulose nanocrystals. *Colloids and Surfaces A: Physicochemical and Engineering Aspects* **325**, 44–51 (2008).

106. Merindol, R. *et al.* Assembly of Anisotropic Nanocellulose Films Stronger than the Original Tree. *ACS Nano* **14**, 16525–16534 (2020).

107. Jean, B., Dubreuil, F., Heux, L. & Cousin, F. Structural Details of Cellulose Nanocrystals/Polyelectrolytes Multilayers Probed by Neutron Reflectivity and AFM. *Langmuir* **24**, 3452–3458 (2008).

108. Cranston, E. D. & Gray, D. G. Formation of cellulose-based electrostatic layer-by-layer films in a magnetic field. *null* **7**, 319–321 (2006).

109. Wu, K. *et al.* Discontinuous fibrous Bouligand architecture enabling formidable fracture resistance with crack orientation insensitivity. *Proc Natl Acad Sci U S A* **117**, 15465–15472 (2020).

110. Yang Yang *et al.* Electrically assisted 3D printing of nacre-inspired structures with self-sensing capability. *Science Advances* **5**, eaau9490.

111. Chen, S.-M. *et al.* Biomimetic twisted plywood structural materials. *National Science Review* **5**, 703–714 (2018).

112. Mujica, R. Layer-by-Layer assembly of nanocellulose composite films with bio-inspired helicoidal superstructures. (2020).

113. Gao, Y., Yu, L., Yeo, J. C. & Lim, C. T. Flexible Hybrid Sensors for Health Monitoring: Materials and Mechanisms to Render Wearability. *Advanced Materials* **32**, 1902133 (2020).

114. Amjadi, M., Pichitpajongkit, A., Lee, S., Ryu, S. & Park, I. Highly Stretchable and Sensitive Strain Sensor Based on Silver Nanowire–Elastomer Nanocomposite. *ACS Nano* **8**, 5154–5163 (2014).

115. J. Chossat, Yiwei Tao, V. Duchaine, & Y. Park. Wearable soft artificial skin for hand motion detection with embedded microfluidic strain sensing. in *2015 IEEE International Conference on Robotics and Automation (ICRA)* 2568–2573 (2015). doi:10.1109/ICRA.2015.7139544.

116. Rus, D. & Tolley, M. T. Design, fabrication and control of soft robots. *Nature* **521**, 467–475 (2015).

117. Wang, Y. *et al.* Flexible electrically resistive-type strain sensors based on reduced graphene oxide-decorated electrospun polymer fibrous mats for human motion monitoring. *Carbon* **126**, 360–371 (2018).

118. Nur, R. *et al.* A Highly Sensitive Capacitive-type Strain Sensor Using Wrinkled Ultrathin Gold Films. *Nano Lett.* **18**, 5610–5617 (2018).

119. Gu, J., Kwon, D., Ahn, J. & Park, I. Wearable Strain Sensors Using Light Transmittance Change of Carbon Nanotube-Embedded Elastomers with Microcracks. *ACS Appl. Mater. Interfaces* **12**, 10908–10917 (2020).

120. Lang, C., Liu, Y., Cao, K. & Qu, S. Temperature-insensitive optical fiber strain sensor with ultra-low detection limit based on capillary-taper temperature compensation structure. *Opt. Express* **26**, 477–487 (2018).

121. Sabri, N., Aljunid, S., Salim, M., Ahmad, R. B. & Kamaruddin, R. Toward Optical Sensors: Review and Applications. *Journal of Physics Conference Series* **423**, 2064 (2013).

122. Liu, X. *et al.* A highly sensitive graphene woven fabric strain sensor for wearable wireless musical instruments. *Mater. Horiz.* **4**, 477–486 (2017).

123. Xu, H. *et al.* An ultra-stretchable, highly sensitive and biocompatible capacitive strain sensor from an ionic nanocomposite for on-skin monitoring. *Nanoscale* **11**, 1570–1578 (2019).

124. Liu, H. *et al.* Electrically conductive polymer composites for smart flexible strain sensors: a critical review. *J. Mater. Chem. C* **6**, 12121–12141 (2018).

125. Seyedin, S. *et al.* Textile strain sensors: a review of the fabrication technologies, performance evaluation and applications. *Mater. Horiz.* **6**, 219–249 (2019).

126. Kim, K.-H., Jang, N.-S., Ha, S.-H., Cho, J. H. & Kim, J.-M. Highly Sensitive and Stretchable Resistive Strain Sensors Based on Microstructured Metal Nanowire/Elastomer Composite Films. *Small* **14**, e1704232 (2018).

127. Wang, Z. *et al.* Polyurethane/Cotton/Carbon Nanotubes Core-Spun Yarn as High Reliability Stretchable Strain Sensor for Human Motion Detection. *ACS Appl. Mater. Interfaces* **8**, 24837–24843 (2016).

128. Dejace, L., Laubeuf, N., Furfaro, I. & Lacour, S. P. Gallium-Based Thin Films for Wearable Human Motion Sensors. *Advanced Intelligent Systems* **1**, 1900079 (2019).

129. Zhao, H., O'Brien, K., Li, S. & Shepherd, R. F. Optoelectronically innervated soft prosthetic hand via stretchable optical waveguides. *Sci. Robotics* **1**, eaai7529 (2016).

130. Guo, J., Niu, M. & Yang, C. Highly flexible and stretchable optical strain sensing for human motion detection. *Optica* **4**, 1285–1288 (2017).

131. Wang, S. *et al.* Network cracks-based wearable strain sensors for subtle and large strain detection of human motions. *J. Mater. Chem. C* **6**, 5140–5147 (2018).

132. Amjadi, M., Turan, M., Clementson, C. P. & Sitti, M. Parallel Microcracks-based Ultrasensitive and Highly Stretchable Strain Sensors. *ACS Appl Mater Interfaces* **8**, 5618–5626 (2016).

133. Zhou, J. *et al.* Flexible piezotronic strain sensor. *Nano Lett* **8**, 3035–3040 (2008).

134. Gu, J., Kwon, D., Ahn, J. & Park, I. Wearable Strain Sensors Using Light Transmittance Change of Carbon Nanotube-Embedded Elastomers with Microcracks. *ACS Appl. Mater. Interfaces* **12**, 10908–10917 (2020).

135. Bae, S.-H. *et al.* Graphene-based transparent strain sensor. *Carbon* **51**, 236–242 (2013).

136. Lu, Y. *et al.* Ultrastretchable Conductive Polymer Complex as a Strain Sensor with a Repeatable Autonomous Self-Healing Ability. *ACS Appl. Mater. Interfaces* **11**, 20453–20464 (2019).

137. Huang, C.-B. *et al.* Highly Sensitive Strain Sensors Based on Molecules–Gold Nanoparticles Networks for High-Resolution Human Pulse Analysis. *Small* **17**, 2007593 (2021).

138. Gong, S. *et al.* Tattoolike Polyaniline Microparticle-Doped Gold Nanowire Patches as Highly Durable Wearable Sensors. *ACS Appl. Mater. Interfaces* **7**, 19700–19708 (2015).

139. Liu, X., Li, D., Chen, X., Lai, W.-Y. & Huang, W. Highly Transparent and Flexible All-Solid-State Supercapacitors Based on Ultralong Silver Nanowire Conductive Networks. *ACS Appl. Mater. Interfaces* **10**, 32536–32542 (2018).

140. Wang, T., Wang, R., Cheng, Y. & Sun, J. Quasi In Situ Polymerization To Fabricate Copper Nanowire-Based Stretchable Conductor and Its Applications. *ACS Appl. Mater. Interfaces* **8**, 9297–9304 (2016).

141. Wang, S. *et al.* Network cracks-based wearable strain sensors for subtle and large strain detection of human motions. *J. Mater. Chem. C* **6**, 5140–5147 (2018).

142. Xu, M., Qi, J., Li, F. & Zhang, Y. Highly stretchable strain sensors with reduced graphene oxide sensing liquids for wearable electronics. *Nanoscale* **10**, 5264–5271 (2018).

143. Cai, G. *et al.* Large-Scale Production of Highly Stretchable CNT/Cotton/Spandex Composite Yarn for Wearable Applications. *ACS Appl. Mater. Interfaces* **10**, 32726–32735 (2018).

144. Wang, C. *et al.* Carbonized Silk Fabric for Ultrastretchable, Highly Sensitive, and Wearable Strain Sensors. *Advanced Materials* **28**, 6640–6648 (2016).

145. Cai, Y. *et al.* Stretchable Ti(3)C(2)T(x) MXene/Carbon Nanotube Composite Based Strain Sensor with Ultrahigh Sensitivity and Tunable Sensing Range. *ACS Nano* **12**, 56–62 (2018).

146. Liu, X. *et al.* A highly sensitive graphene woven fabric strain sensor for wearable wireless musical instruments. *Mater. Horiz.* **4**, 477–486 (2017).

147. Gao, Y. *et al.* Laser Direct Writing of Ultrahigh Sensitive SiC-Based Strain Sensor Arrays on Elastomer toward Electronic Skins. *Advanced Functional Materials* **29**, 1806786 (2019).

148. Zhang, S. *et al.* Fully Printed Silver-Nanoparticle-Based Strain Gauges with Record High Sensitivity. *Advanced Electronic Materials* **3**, 1700067 (2017).

149. Zeng, Z. *et al.* Lightweight and Anisotropic Porous MWCNT/WPU Composites for Ultrahigh Performance Electromagnetic Interference Shielding. *Advanced Functional Materials* **26**, 303–310 (2016).

150. Lee, J.-H. *et al.* Highly Aligned, Anisotropic Carbon Nanofiber Films for Multidirectional Strain Sensors with Exceptional Selectivity. *Advanced Functional Materials* **29**, 1901623 (2019).

151. Mousavi, S., Howard, D., Zhang, F., Leng, J. & Wang, C. H. Direct 3D Printing of Highly Anisotropic, Flexible, Constriction-Resistive Sensors for Multidirectional Proprioception in Soft Robots. *ACS Appl. Mater. Interfaces* **12**, 15631–15643 (2020).

152. Jain, P. K., Huang, X., El-Sayed, I. H. & El-Sayed, M. A. Noble metals on the nanoscale: optical and photothermal properties and some applications in imaging, sensing, biology, and medicine. *Acc Chem Res* **41**, 1578–1586 (2008).

153. Halas, N. J., Lal, S., Chang, W.-S., Link, S. & Nordlander, P. Plasmons in Strongly Coupled Metallic Nanostructures. *Chem. Rev.* **111**, 3913–3961 (2011).

154. Peiris, S., McMurtrie, J. & Zhu, H. Metal nanoparticle photocatalysts: Emerging processes for green organic synthesis. *Catal. Sci. Technol.* **6**, (2015).

155. Eustis, S. & El-Sayed, M. A. Why gold nanoparticles are more precious than pretty gold: Noble metal surface plasmon resonance and its enhancement of the radiative and nonradiative properties of nanocrystals of different shapes. *Chem. Soc. Rev.* **35**, 209–217 (2006).

156. Chen, H., Kou, X., Yang, Z., Ni, W. & Wang, J. Shape- and Size-Dependent Refractive Index Sensitivity of Gold Nanoparticles. *Langmuir* **24**, 5233–5237 (2008).

157. Li, N., Zhao, P. & Astruc, D. Anisotropic Gold Nanoparticles: Synthesis, Properties, Applications, and Toxicity. *Angewandte Chemie International Edition* **53**, 1756–1789 (2014).

158. Langley, D. *et al.* Flexible transparent conductive materials based on silver nanowire networks: A review. *Nanotechnology* **24**, 452001 (2013).

159. Lee, J.-Y., Connor, S. T., Cui, Y. & Peumans, P. Solution-Processed Metal Nanowire Mesh Transparent Electrodes. *Nano Lett.* **8**, 689–692 (2008).

160. Madaria, A. R., Kumar, A. & Zhou, C. Large scale, highly conductive and patterned transparent films of silver nanowires on arbitrary substrates and their application in touch screens. *Nanotechnology* **22**, 245201 (2011).

161. Jung, E. *et al.* Roll-to-roll preparation of silver-nanowire transparent electrode and its application to large-area organic light-emitting diodes. *Organic Electronics* **41**, 190–197 (2017).

162. Selzer, F. *et al.* A spray-coating process for highly conductive silver nanowire networks as the transparent top-electrode for small molecule organic photovoltaics. *Nanoscale* **7**, 2777–2783 (2015).

163. Liu, C.-H. & Yu, X. Silver nanowire-based transparent, flexible, and conductive thin film. *Nanoscale Research Letters* **6**, 75 (2011).

164. Dong, J., Abukhdeir, N. & Goldthorpe, I. Simple assembly of long nanowires through substrate stretching. *Nanotechnology* **26**, 485302 (2015).

165. Kang, S. *et al.* Capillary Printing of Highly Aligned Silver Nanowire Transparent Electrodes for High-Performance Optoelectronic Devices. *Nano Lett.* **15**, 7933–7942 (2015).

166. Shin, M. G., Choi, C. J., Jung, Y., Choi, J. H. & Ko, J. S. Alignment of silver nanowires using heat-assisted dip-coating method. *AIP Advances* **10**, 035101 (2020).

167. Cao, Y. *et al.* A technique for controlling the alignment of silver NWs with an electric field. *NANOTECHNOLOGY Nanotechnology* **17**, 2378–2380 (2006).

168. Sekar, S., Lemaire, V., Hu, H., Decher, G. & Pauly, M. Anisotropic optical and conductive properties of oriented 1D-nanoparticle thin films made by spray-assisted self-assembly. *Faraday Discuss.* **191**, 373–389 (2016).

169. Hu, H., Pauly, M., Felix, O. & Decher, G. Spray-assisted alignment of Layer-by-Layer assembled silver nanowires: a general approach for the preparation of highly anisotropic nano-composite films. *Nanoscale* **9**, 1307–1314 (2017).

170. Ogieglo, W., Wormeester, H., Eichhorn, K., Wessling, M. & Benes, N. In situ ellipsometry studies on swelling of thin polymer films: A review. *Progress in Polymer Science* **42**, (2014).

171. Greenfield, N. J. Using circular dichroism spectra to estimate protein secondary structure. *Nat Protoc* **1**, 2876–2890 (2006).

172. V. Mittal. Characterization techniques for polymer nanocomposites. Wiley-VCH Verlag, Weinheim, Germany (2012).

173. Xu, K. *et al.* Recent development of PeakForce Tapping mode atomic force microscopy and its applications on nanoscience. *Nanotechnology Reviews* **7**, 605–621 (2018).

174. "Scanning-electron microscopy," can be found under https://fakultaeten.hu-berlin.de/en/mnf/forschung_internationales/grs/salsa/p-a-labs/application lab/instrumentation/a-labs-sem

175. P. C. Robinson, M. W. Davidson, "Polarized Light Microscopy," can be found under www.microscopyu.com/techniques/polarized-light/polarized-light-microscopy.

176. Rezakhaniha, R. *et al.* Experimental investigation of collagen waviness and orientation in the arterial adventitia using confocal laser scanning microscopy. *Biomech Model Mechanobiol* **11**, 461–473 (2012).

177. Schneider, C. A., Rasband, W. S. & Eliceiri, K. W. NIH Image to ImageJ: 25 years of image analysis. *Nat Methods* **9**, 671–675 (2012).

178. Oliver, W. C. & Pharr, G. M. An improved technique for determining hardness and elastic modulus using load and displacement sensing indentation experiments. *Journal of Materials Research* **7**, 1564–1583 (1992).

179. Zhang, H. *et al.* Characterization of mechanical properties of epoxy/nanohybrid composites by nanoindentation: *Nanotechnology Reviews* **9**, 28–40 (2020).

180. Sun, Y., Bell, T. & Zheng, S. Finite element analysis of the critical ratio of coating thickness to indentation depth for coating property measurements by nanoindentation. *Thin Solid Films* **258**, 198–204 (1995).

181. Menard, K. Dynamic Mechanical Analysis: A Practical Introduction. **02**, (2008).

182. "RSA-G2 Solids Analyzer," can be found under www.tainstruments.com/rsa-g2/.

183. Nechyporchuk, O., Belgacem, M. N. & Bras, J. Production of cellulose nanofibrils: A review of recent advances. *Industrial Crops and Products* **93**, 2–25 (2016).

184. Kan, K. & Cranston, E. Mechanical testing of thin film nanocellulose composites using buckling mechanics. *Tappi Journal* **12**, 9–17 (2013).

185. Marais, A. & Wågberg, L. The use of polymeric amines to enhance the mechanical properties of lignocellulosic fibrous networks. *Cellulose* **19**, 1437–1447 (2012).

186. Sumaru, K., Matsuoka, H. & Yamaoka, H. Exact Evaluation of Characteristic Protonation of Poly(vinylamine) in Aqueous Solution. *J. Phys. Chem.* **100**, 9000–9005

(1996).

187. Feng, X., Pelton, R., Leduc, M. & Champ, S. Colloidal Complexes from Poly(vinyl amine) and Carboxymethyl Cellulose Mixtures. *Langmuir* **23**, 2970–2976 (2007).

188. George, J. & Sabapathi, S. N. Cellulose nanocrystals: synthesis, functional properties, and applications. *Nanotechnol Sci Appl* **8**, 45–54 (2015).

189. Kargarzadeh, H. *et al.* Recent developments on nanocellulose reinforced polymer nanocomposites: A review. *Polymer* **132**, 368–393 (2017).

190. Miao, C. & Hamad, W. Y. Critical insights into the reinforcement potential of cellulose nanocrystals in polymer nanocomposites. *Current Opinion in Solid State and Materials Science* **23**, 100761 (2019).

191. Martin, C. & Jean, B. Nanocellulose/polymer multilayered thin films: Tunable architectures towards tailored physical properties. *Nordic Pulp and Paper Research Journal* **29**, (2014).

192. Dunlop, M. J. *et al.* Towards the scalable isolation of cellulose nanocrystals from tunicates. *Scientific Reports* **10**, 19090 (2020).

193. Prathapan, R., Tabor, R. F., Garnier, G. & Hu, J. Recent Progress in Cellulose Nanocrystal Alignment and Its Applications. *ACS Appl. Bio Mater.* **3**, 1828–1844 (2020).

194. Li, K. *et al.* Alignment of Cellulose Nanofibers: Harnessing Nanoscale Properties to Macroscale Benefits. *ACS Nano* **15**, (2021).

195. Cerclier, C. V. *et al.* Xyloglucan–Cellulose Nanocrystal Multilayered Films: Effect of Film Architecture on Enzymatic Hydrolysis. *Biomacromolecules* **14**, 3599–3609 (2013).

196. Sekar, S., Lemaire, V., Hu, H., Decher, G. & Pauly, M. Anisotropic optical and conductive properties of oriented 1D-nanoparticle thin films made by spray-assisted self-assembly. *Faraday Discuss.* **191**, 373–389 (2016).

197. Reising, A., Moon, R. & Youngblood, J. Effect of particle alignment on mechanical properties of neat cellulose nanocrystal films. *J. Sci. Technol. For. Prod. Processes* **2**, 32–41 (2012).

198. Zhang, F. *et al.* Anisotropic conductive networks for multidimensional sensing. *Mater. Horiz.* (2021) doi:10.1039/D1MH00615K.

199. Hu, H. *et al.* In-plane aligned assemblies of 1D-nanoobjects: recent approaches and applications. *Chem. Soc. Rev.* **49**, 509–553 (2020).

200. Dong, J. & Goldthorpe, I. Exploiting both Optical and Electrical Anisotropy in Nanowire Electrodes for Higher Transparency. *Nanotechnology* **29**, (2017).

201. Chen, J. *et al.* Polydimethylsiloxane (PDMS)-Based Flexible Resistive Strain Sensors for Wearable Applications. *Applied Sciences* **8**, (2018).

202. Johnston, I. D., McCluskey, D. K., Tan, C. K. L. & Tracey, M. C. Mechanical characterization of bulk Sylgard 184 for microfluidics and microengineering. *Journal of Micromechanics and Microengineering* **24**, 035017 (2014).

203. Mihai, L. A. & Goriely, A. How to characterize a nonlinear elastic material? A review on nonlinear constitutive parameters in isotropic finite elasticity. *Proceedings of the Royal Society A: Mathematical, Physical and Engineering Sciences* **473**, 20170607 (2017).

204. Schrenker, N. J. *et al.* Microscopic Deformation Modes and Impact of Network Anisotropy on the Mechanical and Electrical Performance of Five-fold Twinned Silver Nanowire Electrodes. *ACS Nano* **15**, 362–376 (2021).

205. Narayanan, S., Cheng, G., Zeng, Z., Zhu, Y. & Zhu, T. Strain Hardening and Size Effect in Five-fold Twinned Ag Nanowires. *Nano Lett.* **15**, 4037–4044 (2015).

1. Introduction

Au cours de l'évolution, la nature a développé des matériaux nanocomposites présentant des structures complexes et hiérarchiques ayant des propriétés mécaniques et optiques remarquables.[1,2] Étonnamment, l'architecture hélicoïdale, probablement l'une des structures les plus compliquées à assembler, est largement utilisée dans le règne animal et le règne végétal. Cet arrangement hélicoïdal de fibres orientées, aussi connu sous le nom de structure de Bouligand[3] (Figure R.1(A)), est présent par exemple dans les couches secondaires de la paroi cellulaire (Figure R.1(B) et R.1(C)) du bois et lui confère ses propriétés mécaniques exceptionnelles.[4]

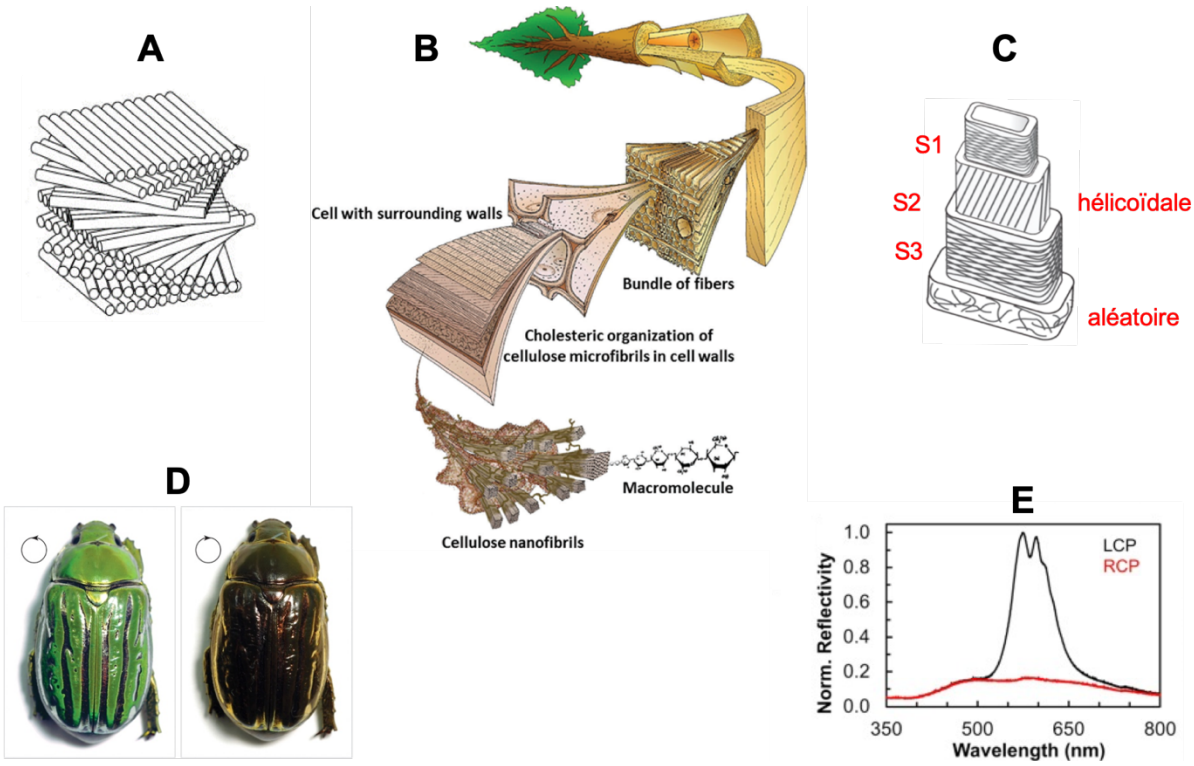

Figure R.1 : (A) Représentation schématique de la structure de Bouligand. (B) Structure hiérarchique du bois. (C) Structure de la paroi cellulaire du bois mettant en évidence l'arrangement des nanofibres de cellulose au sein des couches secondaires en particulier l'arrangement hélicoïdal dans la couche S2. (D) Photographies de l'exosquelette d'un scarabée *Chrysina gloriosa* illuminé avec de la lumière polarisée circulairement gauche (LCP) et droite (RCP). (E) Spectres de réflectivité de l'exosquelette du scarabée pour de la lumière LCP et RCP montrant une réflectivité préférentielle de la LCP.[5]

Cette structure spécifique permet également à certains fruits ou à certains animaux de pouvoir réfléchir sélectivement de la lumière polarisée (Figure R.1(D) et R.1(E)) et de produire des couleurs structurelles.[6] Les propriétés remarquables de ces matériaux naturels ont inspiré les chercheurs pour le développement de matériaux nanocomposites synthétiques avec des performances supérieures.

Différentes techniques ont été développées afin de concevoir des matériaux nanocomposites mais la plupart d'entre elles présente des inconvénients comme une résolution spatiale limitée ou encore l'utilisation d'équipements coûteux. Afin de surmonter ces limitations, une approche simple et polyvalente, connue sous le nom d'assemblage couche-par-couche (LbL)[7] a été développée dans notre équipe et est utilisée pour la préparation de matériaux nanocomposites multifonctionnels avec un haut contrôle sur le positionnement spatial des constituants. Cette technique consiste à déposer alternativement des objets de charges opposées sur une surface (Figure R.2(A)) avec des étapes intermédiaires de rinçage. La croissance du film ainsi que les propriétés correspondantes peuvent être ajustées par différents paramètres comme par exemple le pH et la concentration des solutions utilisées, la nature des polyélectrolytes ou la méthode de dépôt. Alors que le trempage (Figure R.2(B)) et la pulvérisation orthogonale[8] (Figure R.2(C)) génèrent une distribution aléatoire des nanoparticules anisotropes, le spin-coating[9] (Figure R.2(D)) permet un alignement local radial de ces nano-objets par l'intermédiaire de forces centrifuges lors du dépôt.

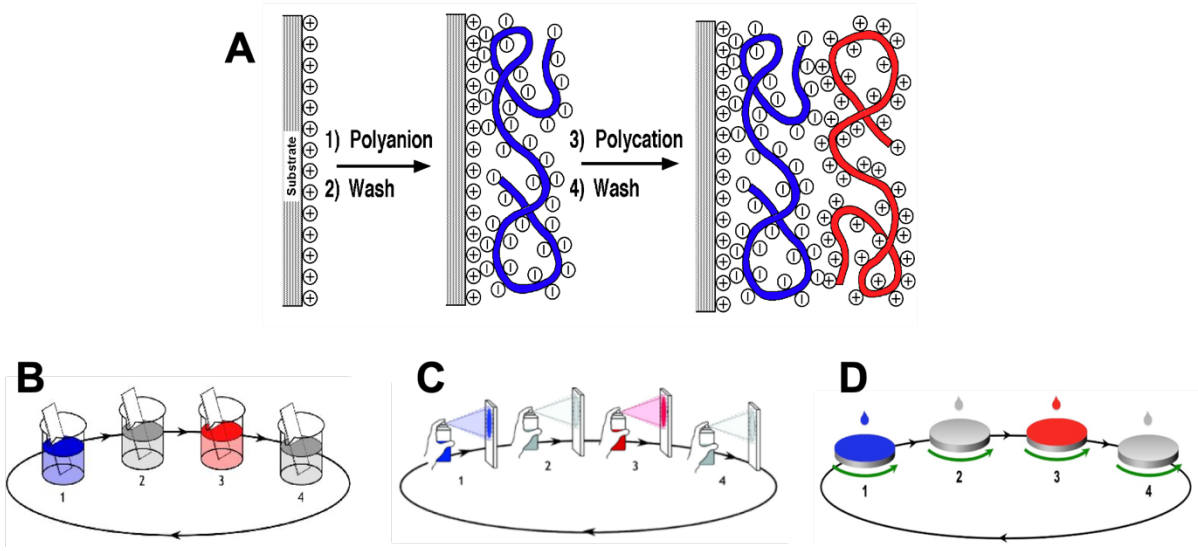

Figure R.2 : (A) Représentation schématique de la technique d'assemblage couche-par-couche (LbL) utilisée pour construire par (B) trempage, (C) pulvérisation orthogonale ou (D) spin-coating des films multicouches à partir d'un polyanion (en bleu) et d'un polycation (en rouge) sur une surface chargée positivement. Les étapes 2 et 4 représentent les étapes de rinçage.[7]

Pour préparer des architectures plus complexes comme les structures hélicoïdales, notre groupe a développé récemment une méthode, la pulvérisation à incidence rasante (GIS),[10] afin de contrôler l'alignement unidirectionnel des nano-objets anisotropes dans le plan pour chaque couche (Figure R.3(A)). Cette méthode a notamment permis d'aligner efficacement dans le plan des nanofibrilles de cellulose (CNFs) et des nanofils d'argent (AgNWs) (Figure R.3(B) et R.3(C)). Sa combinaison avec l'approche LbL permet de concevoir des films multicouches complexes (par exemple, hélicoïdaux) dans lesquels la composition et l'orientation peuvent être contrôlées indépendamment dans chaque couche.

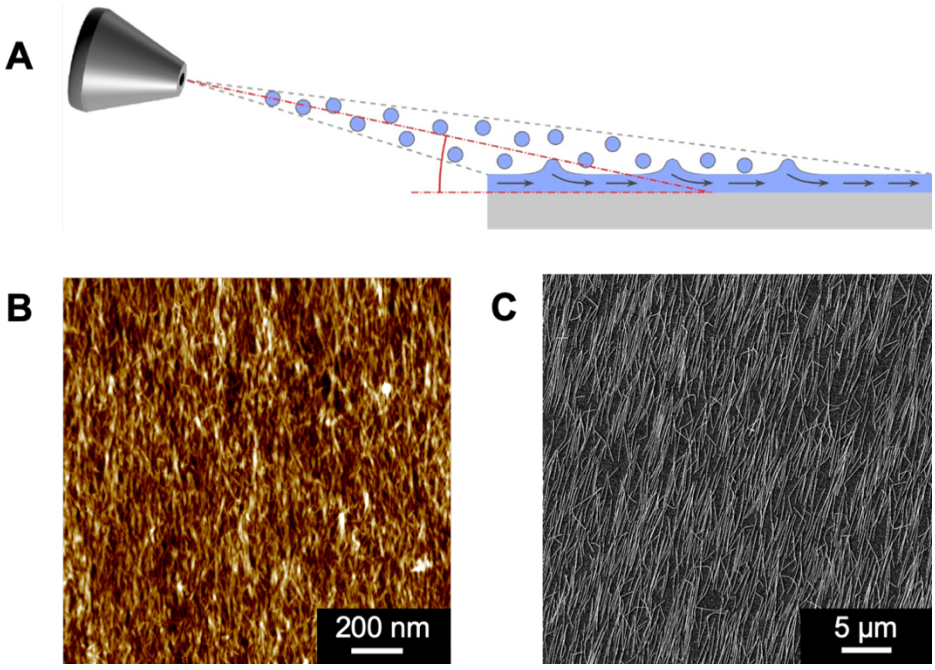

Figure R.3 : (A) Illustration de la technique de pulvérisation à incidence rasante (GIS).[10] (B) Image de microscopie à force atomique (AFM) de nanofibrilles de cellulose (CNFs) orientées par GIS[10] et (C) image de microscopie électronique à balayage (MEB) de nanofils d'argent (AgNWs) alignés par GIS.[11]

2. Objectifs de la thèse

Le premier objectif de cette thèse est de préparer des films multicouches à base de nanocellulose avec des propriétés mécaniques et optiques intéressantes. Dans cette optique, des nanocristaux de cellulose (CNCs) extraits de différentes sources ont été utilisés pour préparer des matériaux bio-inspirés. Des films isotropes ont d'abord été construits par trempage avant de préparer des films orientés par enduction centrifuge.

Afin de préparer des architectures plus complexes comme des structures hélicoïdales, l'assemblage couche-par-couche a été combinée à la pulvérisation à incidence rasante (GIS) permettant de contrôler de façon indépendante l'alignement des nanoparticules de cellulose dans le plan de chaque couche. Les propriétés optiques et mécaniques de ces films à base de nanocelluloses ont finalement été déterminées par spectroscopie par dichroïsme circulaire, par nano-indentation et par analyse mécanique dynamique (DMA).

D'autre part, dans le cadre de ce travail, nous nous sommes également intéressés au développement d'un capteur de déformation multidirectionnel. La recherche portant sur les capteurs de déformation portables a pris un essor considérable récemment du fait de leur intérêt dans de nombreuses applications comme le suivi médical ou la détection de mouvements.[12] Cependant, la plupart de ces capteurs ne sont pas sensibles à la direction d'étirement. Pour pallier à cette limitation majeure, la fabrication de capteurs avec des propriétés anisotropes est nécessaire. Parmi les possibles matériaux avec des propriétés anisotropes, les nanofils d'argent (AgNWs) sont des candidats prometteurs. Lors de cette thèse, les AgNWs ont été alignés par GIS et déposés sur un film élastomère de PDMS. L'influence de la direction d'étirement et de la polarisation de la lumière a été étudiée par spectroscopie UV-Visible-IR. A partir d'un modèle que nous avons développé, nous avons été capable de déterminer la déformation appliquée ainsi que sa direction à partir des propriétés optiques des AgNWs orientés mesurés sous lumière polarisée linéairement. Cette étude démontre le potentiel de ce capteur de déformation optique capable de détecter la déformation mécanique appliquée et sa direction.

3. Préparation de nanocomposites à base de nanocellulose

Ayant comme objectif de mimer les propriétés mécaniques remarquables du bois, nous avons préparé des films multicouches à base de cellulose par trempage. L'influence de la densité de charge du polyélectrolyte utilisé (poly(vinyl amine), PVAm) sur la croissance de films $(CNC/PVAm)_n$ isotropes composés de nanocristaux de cellulose extraits du tunicier (t-CNCs) et du bois (w-CNCs) a été étudiée par

ellipsométrie (Figure R.4). Les données présentées dans la Figure R.4 ont été obtenues pour une concentration en nanocristaux de cellulose de 0.4 g/L, un temps de trempage de 10 min et à température ambiante. Le pH de la solution de PVAm et la source de nanocellulose sont les paramètres qui ont été variés alors que les autres conditions expérimentales ont été maintenues constantes. La variation du pH permet de modifier la densité de charge des chaînes de polymère et d'ajuster la croissance du film.

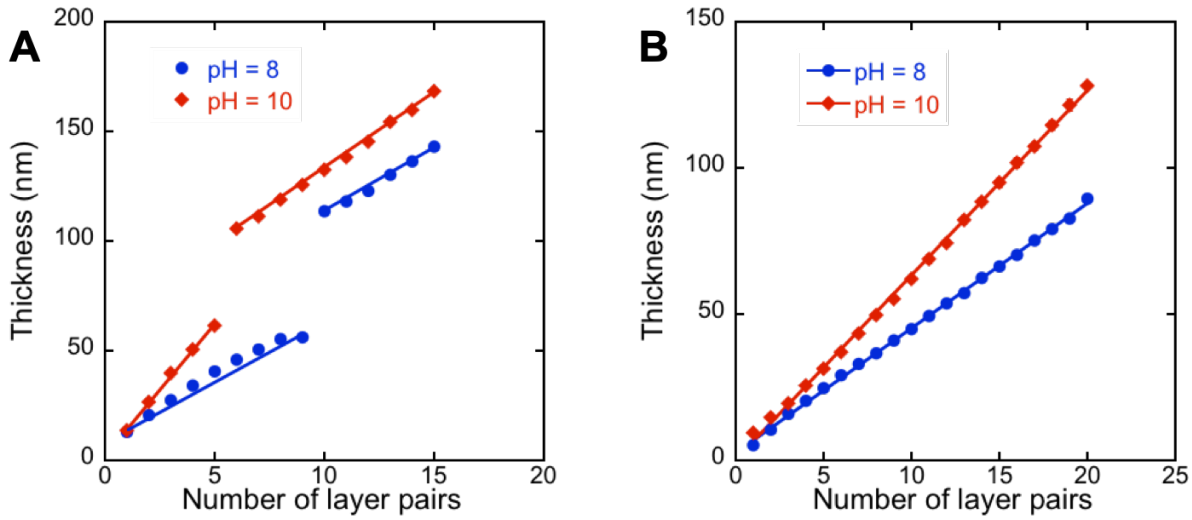

Figure R.4 : Variation de l'épaisseur de films multicouches $(CNC/PVAm)_n$ suivie par ellipsométrie en fonction du pH de la solution de PVAm avec des (A) CNCs extraits du tunicier (t-CNCs) et (B) des CNCs extraits du bois (w-CNCs) pour une concentration de 0.4 g/L.

Pour les deux types de CNCs, la vitesse de croissance des films augmente avec le pH de la solution de PVAm. Cependant, une différence significative peut être notée entre les deux systèmes. En effet, le régime de croissance des films composés de w-CNCs est régulier indépendamment de la densité de charge de la solution de PVAm (Figure R.4(B)) alors que les films composés de t-CNCs présentent un régime de croissance initialement régulier avant de montrer un changement d'épaisseur soudain pour une épaisseur comprise entre 50 et 60 nm (Figure R.4(A)). Ce saut d'épaisseur a été confirmé par des mesures par AFM durant la croissance du film. Comme ce comportement n'a jamais été observé en utilisant les w-CNCs, il semble que ce saut d'épaisseur provienne des propriétés intrinsèques des t-CNCs. Des études complémentaires devront être menées afin de trouver une explication à ce phénomène surprenant qui n'a jamais été reporté dans la littérature. Des films multicouches épais à base de t-CNCs et w-CNCs ont ensuite été construits par trempage. Les propriétés

optiques des films obtenus étaient significativement différentes dans la mesure où les films composés de t-CNCs deviennent opaques pour une épaisseur supérieure à environ 600 nm (Figure R.5(A)).

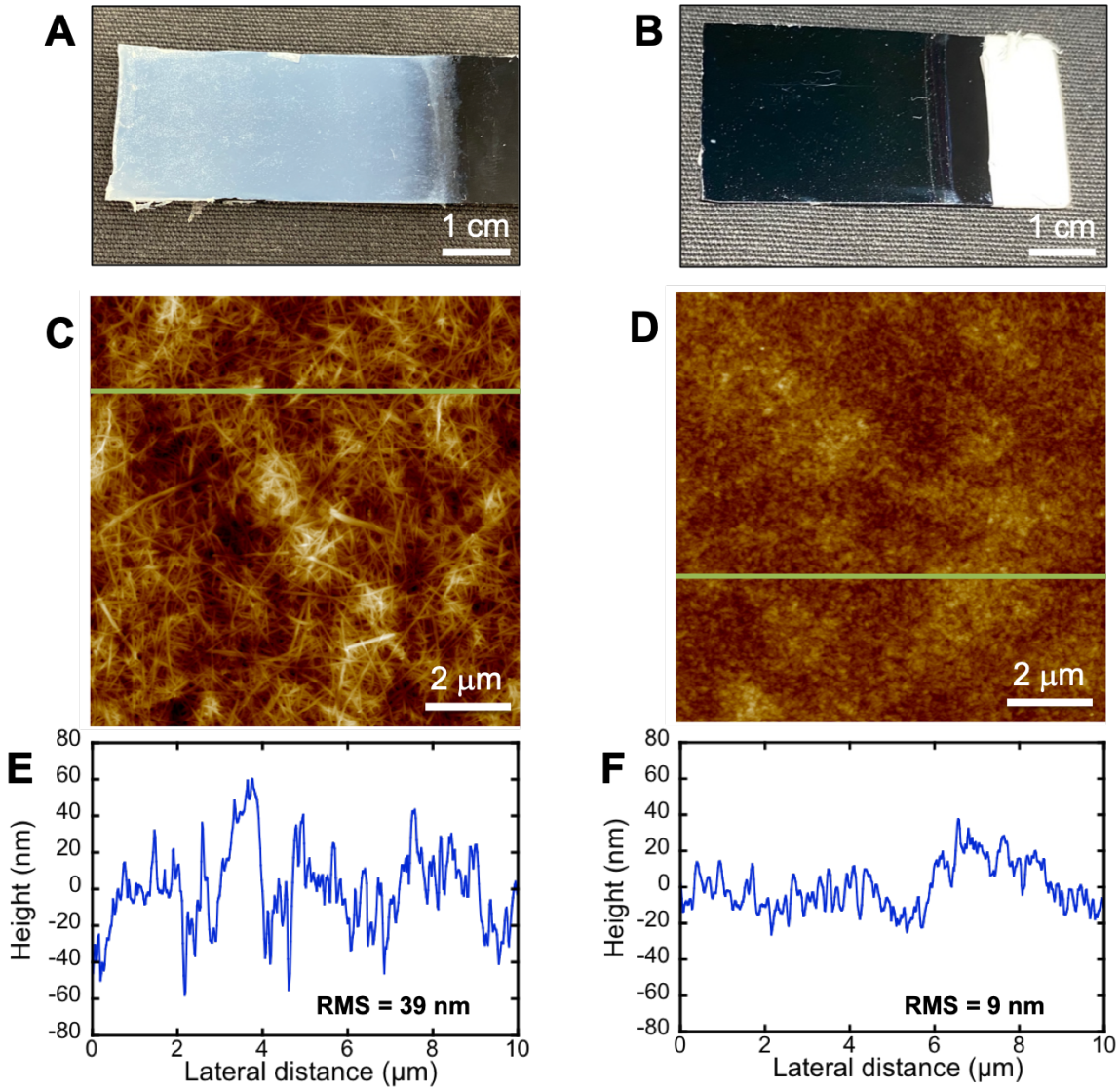

Figure R.5 : Photographies optiques de films $(CNC/PVAm)_n$ préparés par trempage avec (A) des t-CNCs (film opaque d'une épaisseur de 950 nm) et avec (B) des w-CNCs (film transparent d'une épaisseur de 930 nm). (C, D) Images AFM des échantillons A et B avec leurs profils de hauteurs (lignes vertes) et la valeur moyenne quadratique de la rugosité de surface (RMS) (E, F).

Les films composés de w-CNCs sont restés totalement transparents y compris aux plus grandes épaisseurs (Figure R.5(B)), ce qui suggère une rugosité de surface plus importante pour les films t-CNCs conduisant certainement à une diffusion de la lumière plus importante. Cette hypothèse a été confirmée par des analyses par AFM (Figure R.5(C) et R.5(D)). Alors que l'épaisseur des films était similaire, la valeur moyenne quadratique de la rugosité de surface des films préparés avec des t-CNCs (39 nm)

était plus de 4 fois plus importante que celle des films préparés avec des w-CNCs (9 nm) (Figure R.5(E) et R.5(F)).

Des films épais à base de CNCs ont ensuite été préparés sur des substrats hydrophobes afin de pouvoir les détacher pour caractériser leurs propriétés mécaniques par DMA. La structure et l'épaisseur des films ont été déterminés par MEB sur des coupes transversales. Les images de microscopie ont révélé l'obtention de films lisses pour les deux types de CNCs mais avec des morphologies différentes. D'une part, les films se composant de t-CNCs présentaient des pores qui pouvaient être attribués à leur rigidité et leur longueur importante (Figure R.6(A)). D'autre part, l'utilisation des w-CNCs, des nanocristaux plus courts, a conduit à des structures plus denses et compactes ; ce qui explique l'obtention de films avec une plus faible porosité (Figure R.6(B)).

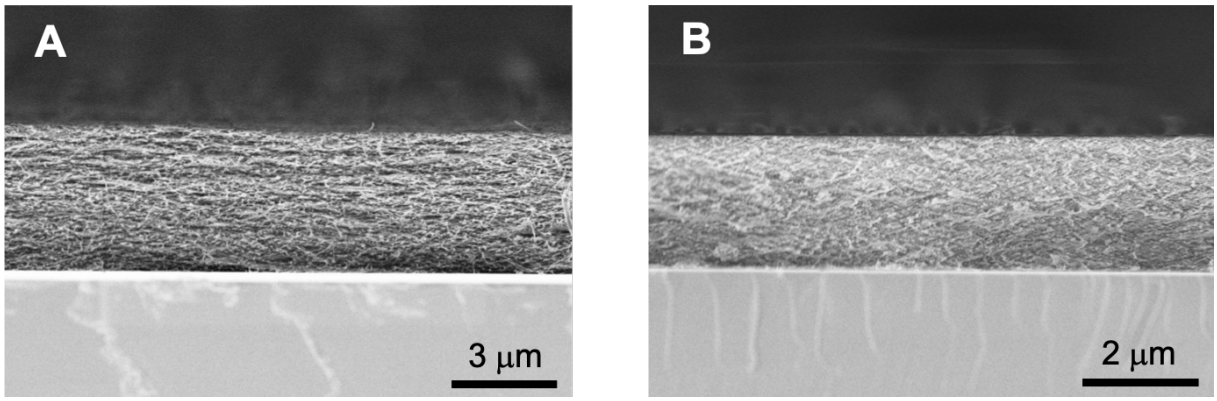

Figure R.6 : Images de microscopie électronique en coupe des films (A) $(t\text{-CNC/PVAm})_{300}$ et (B) $(w\text{-CNC/PVAm})_{380}$ préparés par trempage à pH = 10.

Afin d'obtenir des matériaux bio-inspirés anisotropes très résistants, nous avons décidé d'orienter les CNCs par enduction centrifuge. L'alignement unidirectionnel local de ces cristaux a été caractérisé par AFM sur des monocouches déposées sur des substrats de silicium recouverts d'une couche de poly(éthylène imine) (PEI). L'influence de la vitesse de rotation et du volume de CNCs déposé sur l'alignement ont été étudiés dans ce travail. La Figure R.7 montre les images AFM des échantillons préparés avec 2 combinaisons différentes de conditions expérimentales : (i) une vitesse de rotation de 4000 tr/min et un volume de 0.3 mL et (ii) une vitesse de rotation de 8000 tr/min et un volume de 1.2 mL. Pour quantifier le degré d'alignement des nanocristaux de cellulose, nous avons utilisé le plugin OrientationJ du logiciel ImageJ. Cela nous a permis de visualiser la direction principale d'alignement des nano-objets

et de calculer un paramètre d'ordre 2D que nous avons utilisé pour quantifier la qualité de l'alignement des nanocristaux pour chaque échantillon.

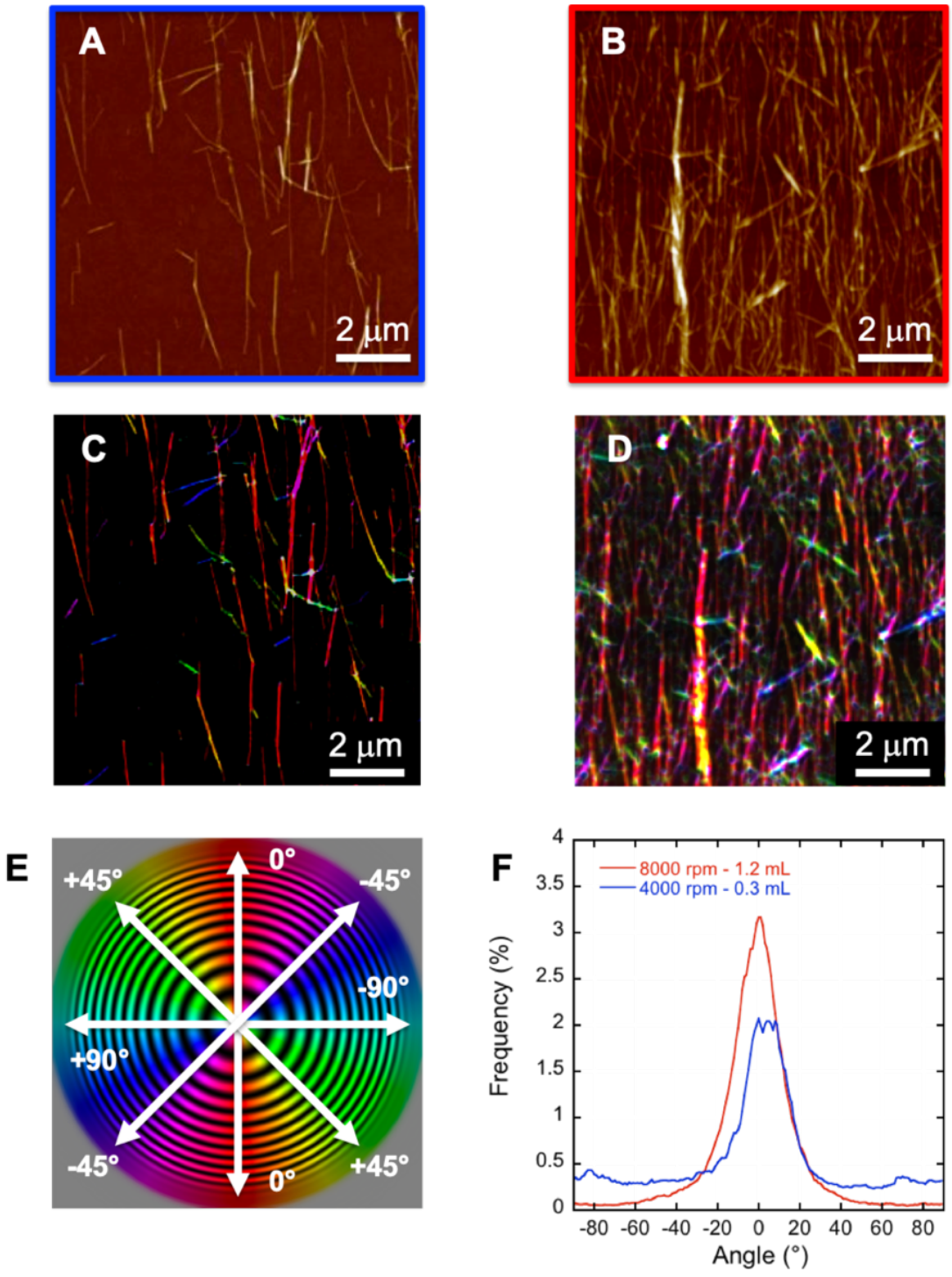

Figure R.7 : Images AFM de monocouches de t-CNCs préparées avec une vitesse de rotation de 4000 tr/min et un volume de 0.3 mL (A) et une vitesse de rotation de 8000 tr/min et un volume de 1.2 mL (B). Les images ont été prises à 2 cm du centre de l'échantillon. (C, D) Analyse de l'orientation de (A) et (B) en utilisant le plugin OrientationJ. (E) Code couleur utilisé pour l'analyse de l'orientation. (F) Distributions de l'orientation des t-CNCs extraites des image (C) et (D).

Une augmentation du paramètre d'ordre a été observée quand la vitesse de rotation passait de 4000 à 8000 tr/min. Cette observation n'est pas surprenante dans la mesure où les forces de cisaillement augmentent avec la vitesse de rotation. Indépendamment de la vitesse de rotation, une augmentation du volume déposé a permis une amélioration de la qualité d'alignement. Le paramètre d'ordre a atteint une valeur maximale de 0.8 avec une vitesse de rotation de 8000 tr/min et un volume déposé de 1.2 mL. L'alignement des t-CNCs dépendait aussi de la distance par rapport au centre de l'échantillon. En effet, le paramètre d'ordre augmentait du centre au bord de l'échantillon avec une valeur maximale mesurée à 2 cm du centre.

L'alignement a aussi été étudié pour les w-CNCs. Comme pour les t-CNCs, nous avons observé une amélioration significative de l'alignement quand la vitesse de rotation a été augmenté. Cependant, la valeur maximale du paramètre d'ordre était bien inférieure (S_{2D} ~0.5) à celle obtenue avec les t-CNCs (S_{2D} ~0.8). Cette différence est certainement due à la différence importante de rapport d'aspect entre les deux CNCs. En effet, ce rapport d'aspect est plus de deux fois plus important pour les t-CNCs que pour les w-CNCs et peut expliquer que les t-CNCs s'alignent plus facilement en utilisant les mêmes conditions de dépôt.

Après avoir optimisé l'alignement des t-CNCs sur une monocouche déposée par enduction centrifuge, la construction de film épais avec une orientation unidirectionnelle des CNCs a été réalisée. La microstructure des films préparés a ensuite été étudiée. Des images MEB réalisées en coupe ont montré la formation de films lisses avec une structure très poreuse (Figure R.9(B)). De plus, des mesures par AFM ont démontré une rugosité de surface importante (RMS = 212 nm) et la présence de larges pores sur le dessus du film. L'importante rugosité de surface du film est une conséquence directe de la porosité et peut expliquer la diffusion de lumière importante du matériau pour des épaisseurs élevées.

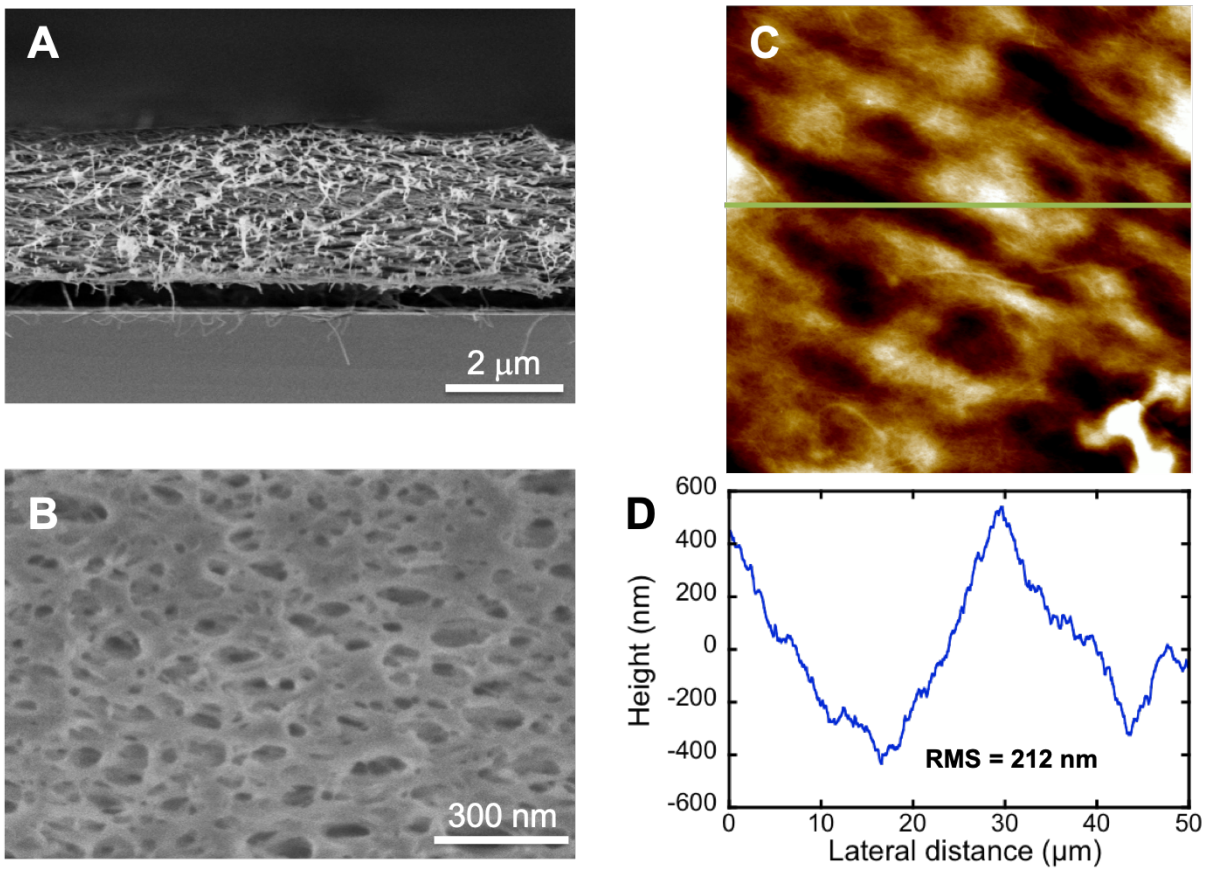

Figure R.8 : (A) Image MEB en coupe transverse du film (t-CNC/PVAm)$_{500}$ préparé par spin-coating à pH = 8. (B) Agrandissement d'une vue en coupe sur le film faisant apparaître la structure poreuse. (C) Image AFM du film avec le profil de hauteur correspondant à la position de la ligne verte et la rugosité de surface (D).

L'assemblage couche-par-couche a enfin été combiné à la pulvérisation à incidence rasante pour la préparation de matériaux avec des structures plus complexes, en particulier hélicoïdales. La première étape a consisté à optimiser les conditions expérimentales pour déposer des monocouches orientés de CNCs par GIS sur des substrats de silicium recouverts d'une couche de poly(éthylène imine) (PEI). Seuls les t-CNCs ont pu être orientés par GIS. Ensuite, l'influence de l'orientation des t-CNCs de la couche précédente sur l'orientation de la couche déposée a été étudiée en pulvérisant 2 couches successives de nanocristaux dans la même direction ou perpendiculairement. Une couche séparatrice de PVAm à pH = 8 a été déposée entre les 2 couches de CNCs. La superposition des images AFM avec une et deux couches de t-CNCs sont présentées en Figure R.9. Les résultats montrent que l'orientation de la couche précédente n'influence pas ou peu l'orientation de la couche déposée.

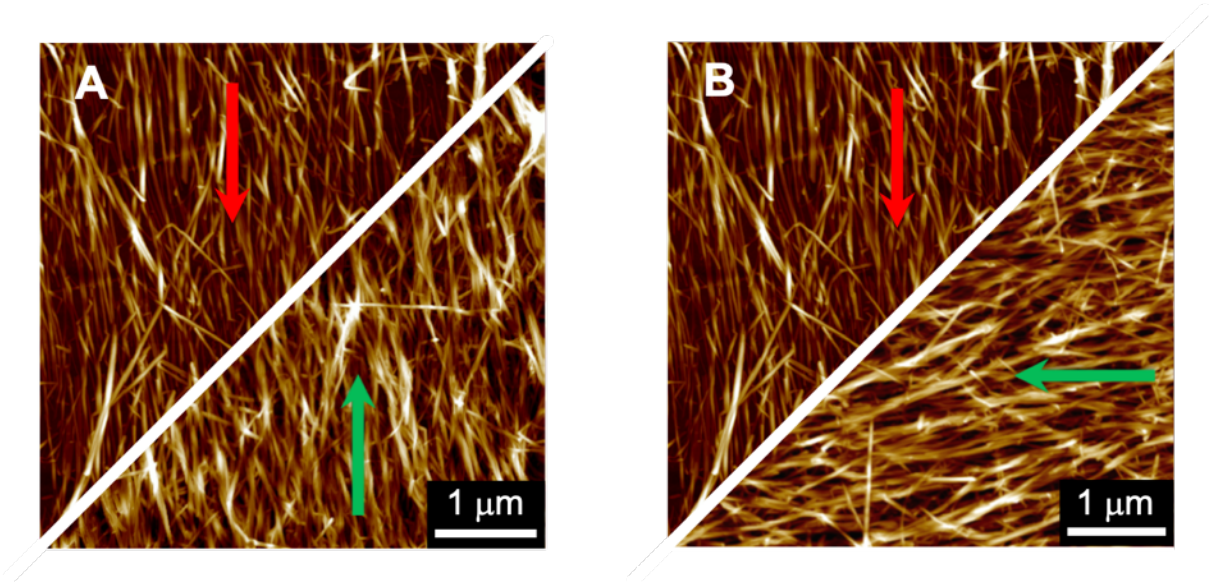

Figure R.9 : Superposition des images AFM de la première couche (flèches rouges) et de la deuxième couche (flèches vertes) de t-CNCs pulvérisées dans la même direction (A) et perpendiculairement (B).

Des films $(t\text{-CNC/PVAm})_n$ présentant une architecture hélicoïdale ont ensuite été construits en déposant les couches de CNCs avec un angle constant de 30° entre deux couches consécutives. Comme la microscopie électronique ne nous a pas permis de confirmer la structure hélicoïdale des nanocristaux au sein du film, les propriétés chirales de ces films ont été étudiées par spectroscopie par dichroïsme circulaire (CD).

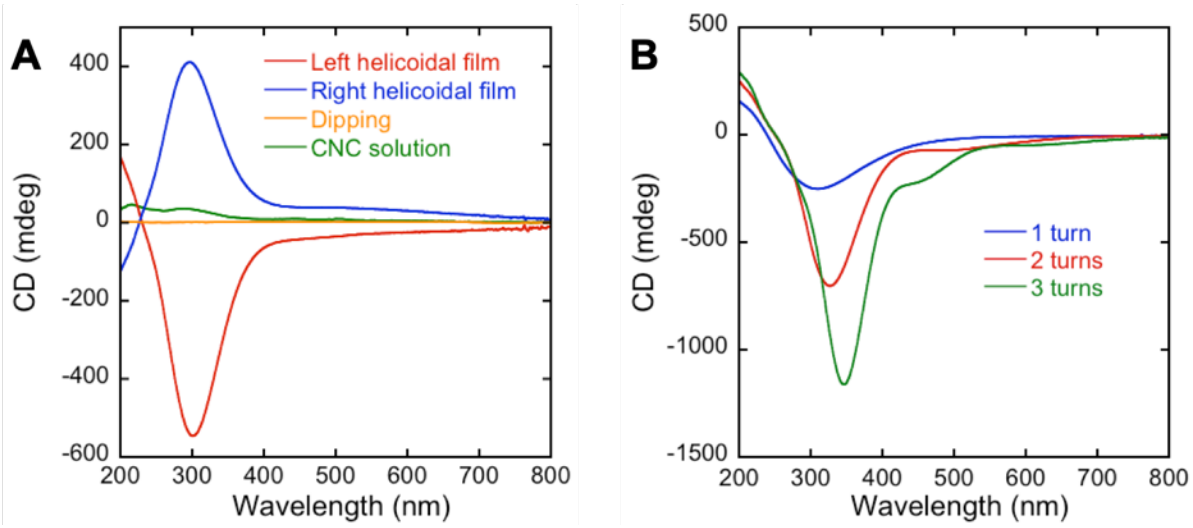

Figure R.10 : (A) Spectres CD de films hélicoïdaux $(t\text{-CNC/PVAm})_{24}$ gauche et droit comparés aux spectres CD d'une solution de t-CNCs (0.4 g/L) et d'un film isotrope préparé par trempage. (B) Spectres CD d'une structure hélicoïdale gauche avec 1, 2 et 3 tours d'hélice.

Les films présentant une structure hélicoïdale avec des chiralités opposées ont révélé un signal intense vers 300 nm qui était très peu intense pour le film isotrope (Figure R.10(A)). La symétrie des spectres pour ces films énantiomorphes confirme l'assemblage hélicoïdal des nanocristaux avec des chiralités opposées. D'autre part, il a également été montré que l'intensité de ce pic de CD d'origine structurale augmente avec le nombre de tours d'hélices (Figure R.10(B)).

Des films épais composés de t-CNCs orientés de manière aléatoire (trempage) et unidirectionnelle (préparés par spin-coating et GIS) ont été caractérisés par DMA et un module compris entre 13 et 17 GPa a été déterminé. L'absence de différence significative au niveau du module en fonction de la structure des films est vraisemblablement liée à la porosité importante des films.

4. Développement d'un capteur de déformation anisotrope

En parallèle à l'étude de films complexes à base de nanocellulose, nous avons également investigué le développement d'un capteur de déformation multidirectionnel. La recherche portant sur les capteurs de déformation portables a pris un essor considérable ces dernières années puisqu'ils peuvent être utilisés dans de nombreuses applications notamment pour du suivi médical.[12] L'objectif de cette partie consiste à préparer un capteur de déformation anisotrope composé de nanofils d'argent (AgNWs) orientés qui soit sensible à la direction d'étirement et la déformation appliquée. Pour cela, l'alignement des nanofils métalliques a été réalisé par GIS soit sur un wafer de silicium soit sur un substrat de PDMS. Les images MEB correspondant aux monocouches orientées d'AgNWs préparées par GIS sont présentées dans la Figure R.11.

L'analyse de plusieurs images MEB en utilisant OrientationJ a démontré un alignement efficace des nanofils métalliques sur les 2 surfaces avec un paramètre d'ordre S_{2D} de 0.78 ± 0.03 quand ils étaient déposés sur des wafers de silicium (Figure R.11(A)) et de 0.83 ± 0.02 quand ils étaient déposés sur des substrats de PDMS (Figure R.11(B)). Le degré d'orientation des AgNWs et la structure du film métallique ont ensuite été

étudiés au cours de la déformation du film par MEB. Ce travail a été effectué en collaboration avec le Leibniz-Institut für Polymerforschung de Dresden qui a permis de déformer les films orientés de AgNWs au sein du microscope.

Pour une déformation appliquée perpendiculairement à la direction d'alignement des AgNWs, une baisse du paramètre d'ordre et une augmentation de la distance entre nanofils voisins ont été observés. Lorsque la déformation était par contre appliquée dans la direction des AgNWs, la qualité d'alignement était préservée mais la formation de fractures dans la direction perpendiculaire à la direction d'étirement a été observée.

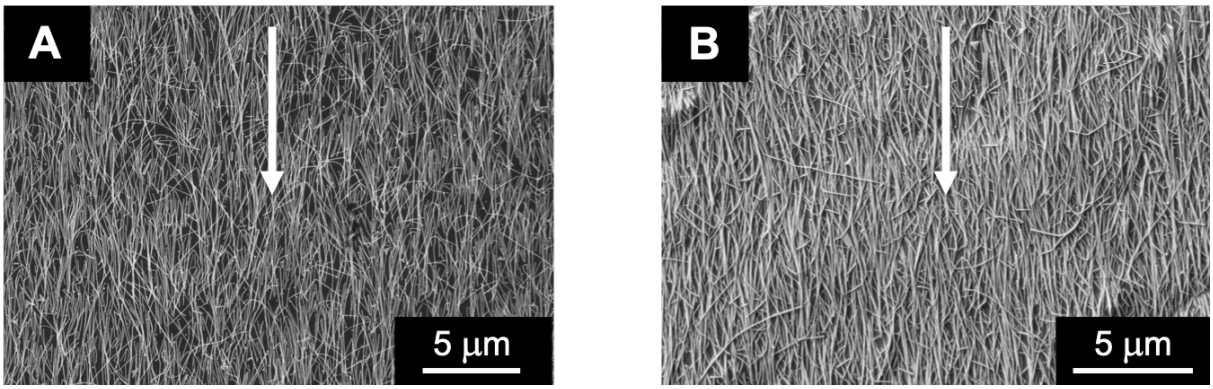

Figure R.11 : Images MEB d'AgNWs orientés par GIS pendant 50 s sur (A) un wafer de silicium et (B) un substrat de PDMS recouverts d'une couche de PEI dans les mêmes conditions expérimentales. Les flèches blanches indiquent les directions de pulvérisation.

Les propriétés optiques de monocouches orientées de AgNWs ont ensuite été étudiées par spectroscopie UV-Visible-IR. Les spectres d'extinction des nanofils métalliques orientés sur PDMS mesurés avec de la lumière non polarisée présentaient 3 signaux caractéristiques provenant des résonances de plasmons de surfaces localisés (LSPR) (Figure R.12(B)). Alors que les 2 pics observés dans le domaine UV (350-380 nm) sont attribués aux modes transverses, la bande large commençant vers 650 nm et s'étendant vers le proche infra-rouge peut être attribué au mode longitudinal.[11]

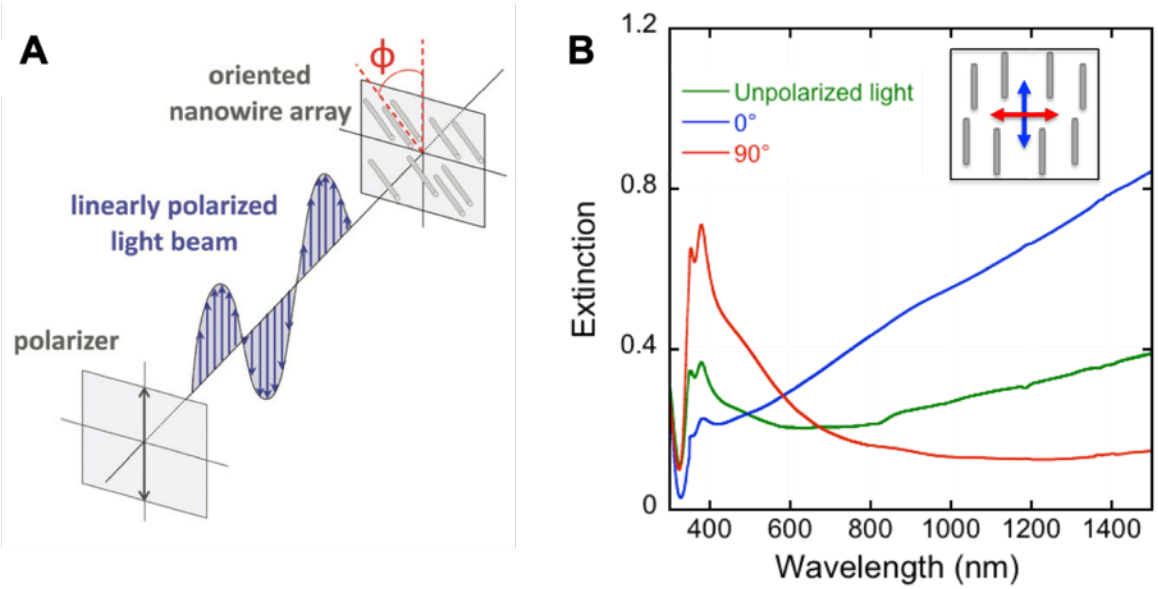

Figure R.12 : (A) Illustration schématique des mesures de spectroscopie UV-Visible-IR en lumière polarisée avec l'angle ϕ entre la direction d'alignement des AgNWs et la direction de polarisation de la lumière.[11] (B) Spectres UV-Visible-IR de monocouches orientées de AgNWs (bâtons gris) sur un substrat de PDMS en lumière non polarisée (vert), avec de la lumière polarisée le long de la direction d'orientation (bleu) et perpendiculairement à la direction d'orientation des AgNWs (rouge).

Les propriétés optiques anisotropes des AgNWs alignés ont été utilisées dans ce travail afin de développer un capteur de déformation sensible à la direction d'étirement. Dans cette perspective, l'influence de la direction d'étirement et de la polarisation de la lumière sur les propriétés optiques a été étudiée (Figure R.13). La direction d'étirement (S) et la polarisation de la lumière (P) sont définies par rapport à la direction d'alignement des AgNWs (parallèlement (//) ou perpendiculairement (⊥)) et peuvent être décrites par 4 configurations : S//P//, S//P⊥, S⊥P// and S⊥P⊥.

Pour chaque configuration, l'extinction mesurée diminue progressivement durant la déformation du film. Cette diminution a d'abord été attribuée à une diminution de la densité en AgNWs provenant du changement de géométrie du PDMS pendant la déformation. En effet, il est admis que durant une déformation uniaxiale, le PDMS est étiré environ 2 fois plus qu'il n'est contraint dans la direction perpendiculaire. Cela induit une augmentation de la surface du PDMS, et comme le nombre de AgNWs reste constant, leur densité diminue pendant la déformation.

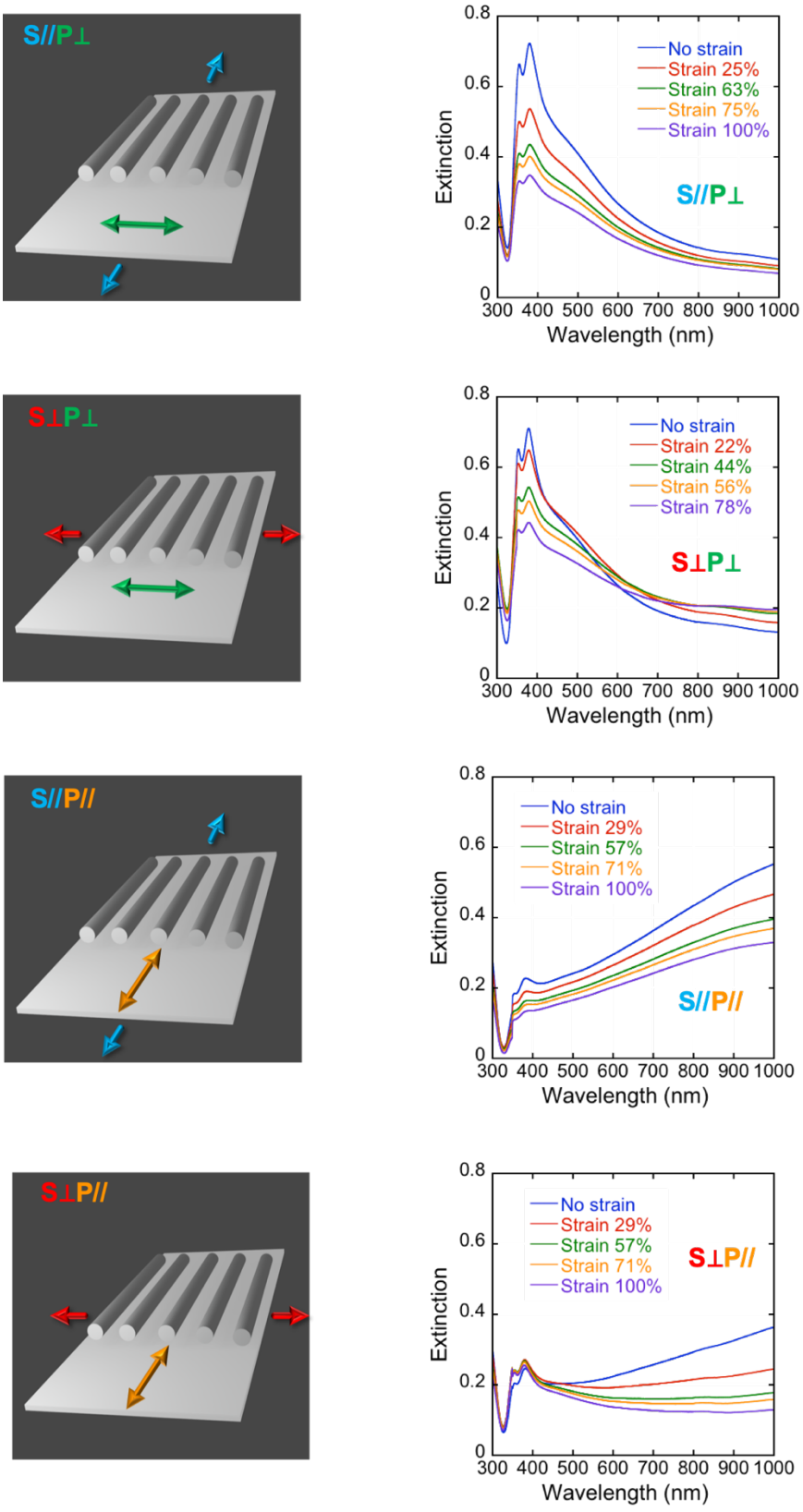

Figure R.13 : Illustrations schématiques et spectres UV-Vis-IR pendant la déformation pour chaque configuration (S//P⊥, S⊥P⊥, S//P// and S⊥P//) avec les directions d'étirement (S) représentées par les flèches bleues et rouges et les directions de polarisation de la lumière (P) avec les doubles flèches vertes et oranges.

Afin de vérifier que cette diminution de l'extinction était due à un changement de densité en AgNWs, l'extinction d'un film de PDMS coloré en masse avec un colorant (Holcosil) a été suivie en fonction de la déformation appliquée (Figure R.14). Il a été montré que la variation d'extinction du film de PDMS coloré était conforme à ce qui était attendu à cause de l'augmentation de la surface pendant l'étirement, et que de surcroit elle était moins importante que celle observée pour les films orientés de AgNWs. Nous avons donc pu en conclure que le changement des propriétés optiques des monocouches orientées de AgNWs n'était pas exclusivement dû à un changement de densité mais peut être également à un changement de la structure du film qui induit une modification de la réflectance du réseau métallique au cours de la déformation du film.

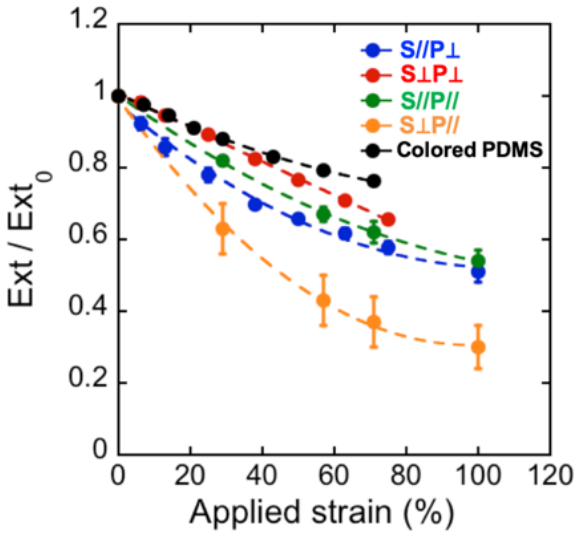

Figure R.14 : Changement d'extinction en fonction de la déformation appliquée pour un film de PDMS coloré dans la masse en lumière non polarisée et pour des monocouches orientées de AgNWs déposées sur un film de PDMS pour différentes directions d'étirement et polarisation de la lumière (S//P⊥, S⊥P⊥, S//P// and S⊥P//).

Nous avons alors décidé d'exploiter l'anisotropie optique de ces monocouches orientées de AgNWs pendant la déformation pour préparer un capteur de déformation sensible à la direction d'étirement valable pour n'importe quel angle α entre la direction d'étirement et la direction d'alignement des AgNWs (Figure R.15).

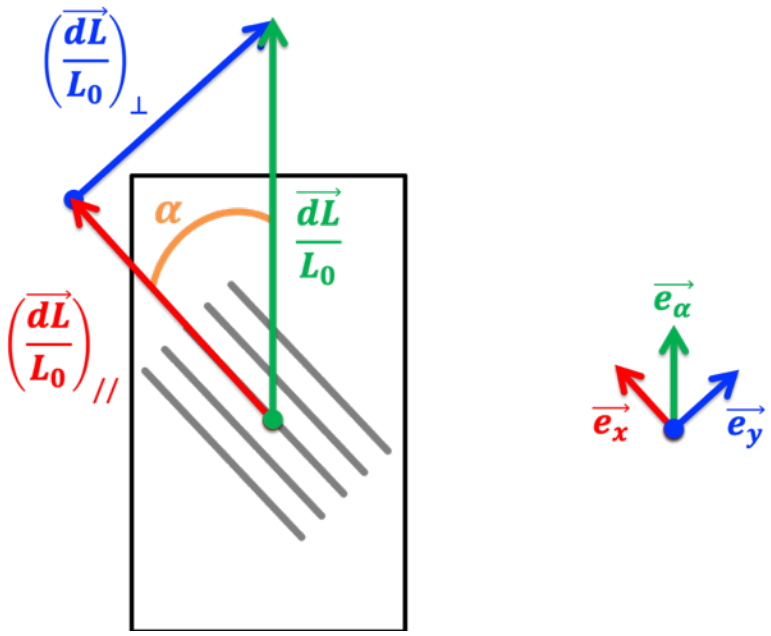

Figure R.15 : (Gauche) Dessin schématique d'une monocouche orientée d'AgNWs (bâtons gris) déposée sur PDMS et sous la déformation $\frac{\overrightarrow{dL}}{L_0}$ (vecteur vert) avec un angle α entre la direction d'étirement et l'orientation des AgNWs. (Droite) Vecteurs unitaires correspondants $\overrightarrow{e_\alpha}$, $\overrightarrow{e_x}$ and $\overrightarrow{e_y}$.

Ce capteur de déformation se base sur l'utilisation d'un modèle mathématique qui permet de relier le changement d'extinction mesuré par spectroscopie polarisée sur une monocouche orientée d'AgNWs (dont l'orientation et la déformation appliquée sont inconnues) à la contrainte appliquée au film.

Afin de valider notre approche, trois films composés d'AgNWs orientés ont été préparés avec divers angles d'orientation initiaux (25°, 50° et 70°) pendant le dépôt des nanofils métalliques par GIS. L'extinction mesurée à 380 nm en fonction de l'angle entre la direction de polarisation de la lumière et la direction d'étirement peut être observée pour chaque film dans la Figure R.16. L'extinction mesurée à 380 nm était maximale lorsque la direction d'alignement des AgNWs et la direction de polarisation étaient perpendiculaires. La valeur maximale de l'extinction mesurée par spectroscopie a permis de déterminer l'angle de polarisation et donc l'angle d'orientation pour chaque déformation appliquée. Le suivi de l'extinction en fonction de la déformation du film a démontré une progressive diminution de l'angle de polarisation pour les trois films (Figure R.16(A), (B) et (C)) comme cela pouvait être

attendu du fait de la contraction du film dans la direction perpendiculaire à la direction d'étirement.

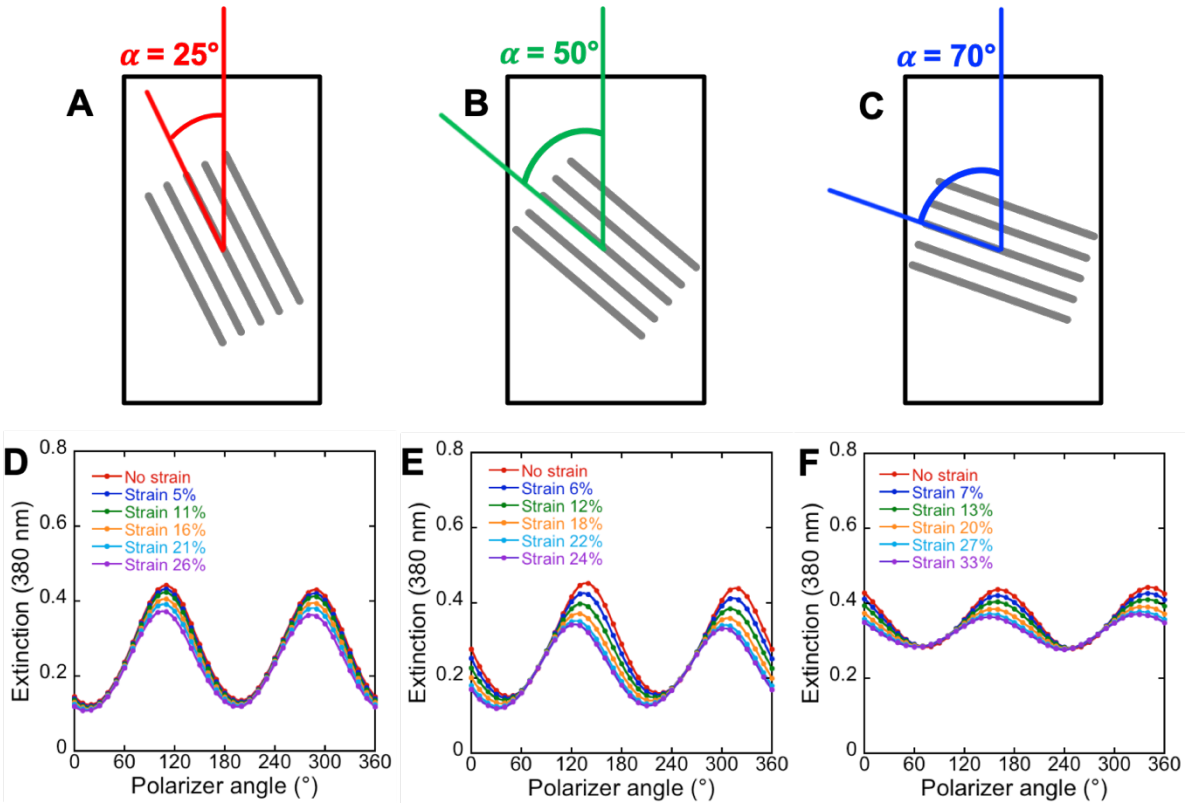

Figure R.16 : Dessins schématiques des AgNWs orientés avec des angles d'orientations α fixés pendant le dépôt par GIS à (A) 25°, (B) 50° et (C) 70°. (D, E, F) Extinctions mesurées à 380 nm en fonction de l'angle de polarisation ϕ pendant l'étirement respectif des films (A, B, C).

Pour chaque déformation appliquée, l'angle d'orientation α des AgNWs et les déformations appliquées parallèlement et perpendiculairement à la direction d'alignement des AgNWs peuvent être déterminés par spectroscopie (Figure R.16). Un modèle mathématique a ensuite été développé et utilisé pour trois monocouches orientées de AgNWs avec des angles initiaux d'orientations α d'environ 25°, 50° et 70°. Les changements d'extinction $\frac{Ext}{Ext_0}$ ont d'abord été mesurés pour un étirement appliqué parallèlement et perpendiculairement à la direction d'alignement des AgNWs à une longueur d'onde de 380 nm (Figure R.14). Le modèle mathématique a ensuite permis de relier $\frac{Ext}{Ext_0}$ mesuré pour un angle α quelconque (Figure R.16) aux changements d'extinction $\frac{Ext}{Ext_0}$ mesurés parallèlement et perpendiculairement à l'orientation des nanofils. Les déformations mesurées ont ensuite été comparées avec

les déformations appliquées macroscopiquement à l'aide du dispositif d'étirement (Figure R.17).

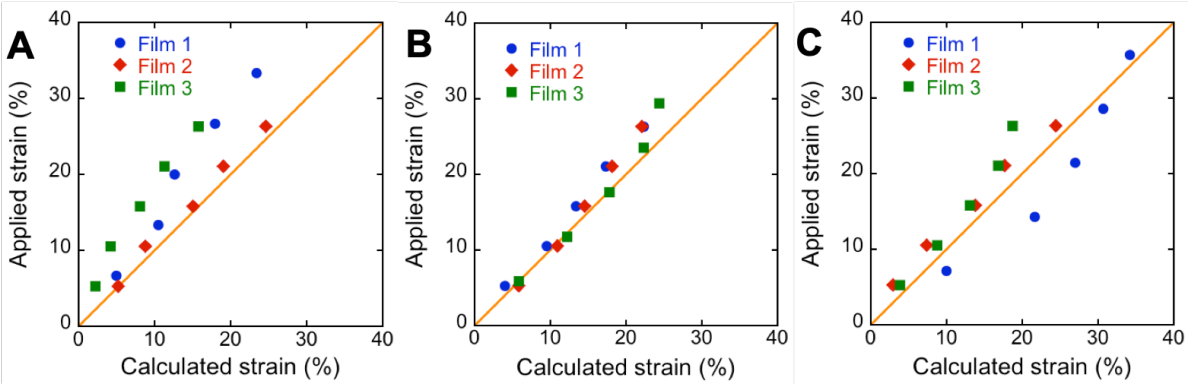

Figure R.17 : Évolution de la déformation appliquée en fonction de la déformation calculée pour des films orientés d'AgNWs sur PDMS avec des angles d'orientation initiaux proches de 25° (A), 50° (B) et 70° (C). Les déformations appliquées et calculées sont identiques sur les lignes orange représentées sur les graphiques.

Les déformations appliquées et calculées étaient en accord pour les films présentant un angle d'orientation d'environ 50° (Figure R.17(B)). Pour les films avec des angles d'orientation d'environ 25° et 70° (Figure R.17(A) and R.17(C)), des différences sont observées entre les valeurs calculées et celles appliquées réellement et peuvent être dues aux incertitudes de mesures de la déformation appliquée à l'aide du dispositif d'étirement.

5. Conclusions

Lors de ce travail, la préparation de films nanocomposites multicouches composés de différents types de nanoparticules de cellulose (CNFs, CNCs) a été abordée. Des films isotropes ont d'abord été fabriqués par trempage en combinant diverses nanoparticules de cellulose avec une matrice polymère de PVAm. Il a été démontré que le pH de la solution de polymère ainsi que la source de cellulose avaient une influence sur la croissance de ces films. De plus, des films isotropes composés de CNFs et de CNCs courts (w-CNCs) ont donné lieu à la formation de matériaux denses et transparents avec une dispersion homogène des nanoparticules. D'un autre côté, l'utilisation de long CNCs (t-CNCs) a mené à des films opaques présentant une structure poreuse. Dans un second temps, nous avons utilisé le spin-coating afin de

produire des matériaux nanocomposites avec des propriétés mécaniques anisotropes. Un haut degré d'alignement a été atteint en utilisant des longs CNCs alors que les CNCs courts et les CNFs n'ont pas pu être orientés. Des films orientés de manière unidirectionnelle et hélicoïdale composés de CNCs longs ont été construits en combinant l'assemblage couche-par-couche (LbL) et la méthodologie de pulvérisation à incidence rasante (GIS). Les propriétés mécaniques des films obtenus ont enfin été caractérisées par DMA. Le rapport d'aspect et la rigidité des nanoparticules de cellulose utilisées a montré un impact significatif sur les propriétés mécaniques. En effet, l'utilisation de CNFs flexibles conduisent à une formation de films avec une structure dense et peu poreuse. Concernant les films à base de CNCs, l'utilisation de longs CNCs résulte en un réseau poreux induisant une rugosité de surface importante. D'autre part, aucune influence significative de la structure du film sur les propriétés mécaniques n'a pu être observée (modules déterminés par DMA entre 13 et 17 GPa). Il semble que les propriétés mécaniques de ces films sont majoritairement contrôlées par la structure poreuse et non par l'orientation des nanocristaux.

Dans une deuxième partie, des AgNWs ont été orientés sur des substrats de PDMS par GIS. L'alignement de ces nanofils métalliques a été caractérisé par microscopie électronique et le paramètre d'ordre d'environ 0.80 a été déterminé. Les monocouches orientés d'AgNWs présentaient des propriétés optiques anisotropes qui ont été exploitées pour fabriquer un capteur de déformation multidimensionnel. Il a également été montré que ces propriétés optiques ne variaient pas uniquement à cause du changement de densité. Des études spectroscopiques réalisées avec de la lumière polarisée linéairement pendant la déformation montrent que les propriétés optiques des AgNWs orientés étaient fortement dépendantes de la direction d'étirement et de la polarisation de la lumière. Un modèle mathématique a ensuite été développé en intégrant divers paramètres incluant l'angle d'orientation des AgNWs, l'extinction mesurée, la déformation appliquée et le coefficient de Poisson du PDMS utilisé. Ce modèle a permis la détermination de la déformation appliquée et de sa direction à partir des mesures optiques. Le capteur de déformation anisotrope obtenu était sensible à de faibles déformations et pourrait certainement être utilisé dans différentes applications nécessitant la mesure de déformations multidirectionnelles.

Références

1. Fratzl, P. & Weinkamer, R. Nature's hierarchical materials. *Prog. Mater. Sci.* **52**, 1263–1334 (2007).
2. Lakes, R. Materials with structural hierarchy. *Nature* **361**, 511–515 (1993).
3. Bouligand, Y. Twisted fibrous arrangements in biological materials and cholesteric mesophases. *Tissue Cell* **4**, 189–217 (1972).
4. Gibson, L. J. The hierarchical structure and mechanics of plant materials. *J. R. Soc. Interface* **9**, 2749–2766 (2012).
5. Sharma, V., Crne, M., Park, J. & Srinivasarao, M. Structural Origin of Circularly Polarized Iridescence in Jeweled Beetles. *Science (New York, N.Y.)* **325**, 449–51 (2009).
6. Vignolini, S. *et al.* Structural colour from helicoidal cell-wall architecture in fruits of Margaritaria nobilis. *J. R. Soc. Interface* **13**, 20160645 (2016).
7. Decher, G. Fuzzy Nanoassemblies: Toward Layered Polymeric Multicomposites. *Science* **277**, 1232 (1997).
8. Schlenoff, J. B., Dubas, S. T. & Farhat, T. Sprayed Polyelectrolyte Multilayers. *Langmuir* **16**, 9968–9969 (2000).
9. Cho, J., Char, K., Hong, J.-D. & Lee, K.-B. Fabrication of Highly Ordered Multilayer Films Using a Spin Self-Assembly Method. *Adv. Mater.* **13**, 1076–1078 (2001).
10. Blell, R. *et al.* Generating in-Plane Orientational Order in Multilayer Films Prepared by Spray-Assisted Layer-by-Layer Assembly. *ACS Nano* **11**, 84–94 (2017).
11. Hu, H., Pauly, M., Felix, O. & Decher, G. Spray-assisted alignment of Layer-by-Layer assembled silver nanowires: a general approach for the preparation of highly anisotropic nano-composite films. *Nanoscale* **9**, 1307–1314 (2017).
12. Souri, H. *et al.* Wearable and Stretchable Strain Sensors: Materials, Sensing Mechanisms, and Applications. *Adv. Intell. Syst.* **2**, 2000039 (2020).

Jean MULLER

Self-assembly and properties of nano-organized multimaterial films with complex anisotropies

Résumé

La nature a développé au cours de l'évolution des matériaux nanocomposites avec des structures complexes comme l'architecture hélicoïdale dans les parois cellulaires du bois et de l'exosquelette des arthropodes. Les propriétés remarquables de ces matériaux ont inspiré notre équipe de recherche à développer des matériaux à hautes performances. Nous avons d'abord préparé des films multicouches composés de nanocellulose et de poly(vinylamine) en combinant l'assemblage couche-par-couche et la pulvérisation à incidence rasante (GIS). Des matériaux nanocomposites avec une orientation aléatoire, unidirectionnelle ou hélicoïdale des nanoparticules de cellulose ont été assemblés. La structure des films obtenus a été étudiée par microscopie tandis que leurs propriétés mécaniques et optiques ont été déterminées par analyse mécanique dynamique et spectroscopie par dichroïsme circulaire. Dans un second temps, nous avons exploité les propriétés optiques anisotropes de nanofils d'argent (AgNWs) orientés afin de construire un capteur de déformation sensible à la direction de déformation. Dans ce travail, nous avons aligné ces nanofils par GIS sur un substrat étirable et transparent de poly(diméthylsiloxane). Des mesures réalisées par spectroscopie UV-Visible-IR en lumière polarisée ont pu mettre en évidence que la variation des propriétés optiques de la monocouche alignée de AgNWs au cours de la déformation dépendait à la fois de la polarisation de la lumière mais également de la direction d'étirement. Un modèle a été développé pour déterminer la direction et l'amplitude de la déformation appliquée à partir des mesures optiques au cours de l'étirement du film.

Mots clés : Assemblage couche-par-couche, matériaux bio-inspirés, nanocellulose, nanofils d'argent, anisotropies complexes, propriétés mécaniques, capteur de déformation.

Résumé en anglais

Through evolution Nature has succeeded to form nanocomposite materials with complex anisotropies structures including the helical architectures found in cell walls of wood or in the exoskeleton of Arthropods. The remarkable properties of these materials have inspired our research team to reproduce similar high-performance materials synthetically. We first prepared multilayer films composed of nanocellulose and poly(vinylamine) combining the layer-by-layer assembly and grazing incidence spraying (GIS). Nanocomposite materials with random, unidirectional or helical orientation of cellulose nanoparticles were assembled. The structure and morphology of the resulting films was investigated by electron microscopy while their mechanical and optical properties were determined using dynamic mechanical analysis and circular dichroism spectroscopy. In a second part, we utilized the anisotropic optical properties of oriented silver nanowires (AgNWs) to fabricate a direction-sensitive strain sensor. For this purpose, monolayers of AgNWs were aligned on a stretchable and transparent substrate of poly(dimethylsiloxane). UV-Visible-IR spectroscopy measurements with polarized light revealed that the variation of the optical properties of the oriented AgNW monolayer upon stretching was depending on both the light polarization and stretching direction. A mathematical model was developed for analyzing the optical data and for calculating the applied strain and its direction during linear deformation.

Keywords: Layer-by-Layer assembly, bio-inspired materials, nanocellulose, silver nanowires, complex anisotropies, mechanical properties, strain sensor.